Imperial College London

The application of autofluorescence lifetime metrology to the study of heart failure models and heart disease

Benjamin Thomas Dyer

Heart Failure & Therapeutics Group
Myocardial Function
National Heart & Lung Institute
Imperial College London

Thesis submitted in partial fulfilment of the requirements for the degree of Doctor of Philosophy (Ph.D.)
Imperial College of Science, Technology and Medicine

Abstract

Autofluorescence spectroscopy offers a promising label-free approach to characterise biological samples and has already shown diagnostic potential in a number of medical applications, although study of myocardium has been relatively limited. A number of myocardial molecules display autofluorescence, including those involved in energetics, e.g. NADH and flavoproteins, as well as structural molecules, e.g. collagen. This thesis discusses the application of a custom-built single point fibre-optic probe-based instrumentation for time-resolved spectrofluorometry utilising spectrally resolved time-correlated single photon counting detection (TCSPC) and white light reflectometry to the investigation of models of heart failure, both *ex vivo* and *in vivo*.

Heart failure (HF) is a pathophysiological state in which an abnormality of cardiac function causes failure of the heart to pump blood at a rate commensurate with the requirements of the metabolising tissues. It affects 1-2% of the population rising to greater than 10% aged over 70 years. Despite recent therapeutic advances, annualized mortality can still approach 10%. HF results from a myocardial injury (e.g. myocardial infarction, chemotherapy) causing loss of myocytes, and maladaptive changes in surviving myocytes and extracellular matrix by 'pathological remodelling'. That HF is characterized by structural and energetic changes was the principal motivation for the creation of an instrument to investigate changes in myocardial autofluorescence signature in disease states *in vivo*. If the signatures associated with known pathological diagnoses could be ascertained, such a technique could perform 'virtual biopsy' to aid diagnosis.

This thesis describes the application of autofluorescence technique to an *ex vivo* Langendorff-heart to characterise the changes in autofluorescence signature with controlled insults of glucose deprivation and hypoxia. Additionally, it reports for the first-time the characterization of the autofluorescence lifetime signature *in vivo* at different time points in an established rat post-myocardial infarction heart failure. The thesis describes development of *in vivo* intravenous doxorubicin chemotherapy-cardiomyopathy heart failure model (DOX-HF) and subsequent characterization of *in vivo* autofluorescence signature. This investigation prompted development of a clinically viable instrument and the progress to date is described.

Author declaration

All the work in this thesis was performed by the author, with the following exceptions:

- In Chapter 3 *ex vivo* Langendorff isolated perfused heart measurements and analysis were realised in collaboration with Dr João Lagarto
- In Chapter 4, myocardial infarction induction surgeries were realised by Dr Markus Sikkel and Dr Adam Mills
- In Chapter 4, *in vivo* myocardial infarction-heart failure measurements and analysis were realised in collaboration with Dr João Lagarto
- In Chapter 5, animal work for the development of the intravenous doxorubicin heart failure model, and *in vivo* measurements were realised in collaboration with Maeve Elder

Copyright declaration

The copyright of this thesis rests with the author and is made available under a Creative Commons Attribution Non-Commercial No Derivatives licence. Researchers are free to copy, distribute or transmit the thesis on the condition that they attribute it, that they do not use it for commercial purposes and that they do not alter, transform or build upon it. For any reuse or redistribution, researchers must make clear to others the licence terms of this work

Acknowledgements

Firstly, I would like to thank my outstanding supervisors Alex, Chris, Nick and Paul for giving me the opportunity to work on this project and for their understanding, invaluable guidance and advice.

I would like to thank Dr João Lagarto for his assistance, support and collaboration on this project from the Photonics Group side of the project. A big 'thank you' to other friends and colleagues within the Photonics Group for their friendship, knowledge and advice.

Within the National Heart and Lung Institute, I would particularly like to thank Professor Sian Harding and her group for their friendship and support and to particularly acknowledge the help of Markus, Maeve, Laura, Matt, Adam, Rasheda, and Pravina during this project.

I would like to thank my Mum and Dad for their love, support and for everything that they have done for me.

Finally, a big thank you to my beautiful family – my wife Clare, and children Rosie & Ted - for their love, support, encouragement and patience.

To Clare, Rosie & Ted

Table of Contents

Abstract **2**

Author declaration *3*

Copyright declaration *3*

Acknowledgements *4*

List of figures *10*

List of tables *18*

Publications and published abstracts *19*

1 Introduction **21**

1.1 Overview *21*

1.2 Use of Optical techniques in the heart *21*

1.3 Fluorescence *25*

1.4 Properties of fluorescence *27*

1.4.1 Intensity and quantum yield 27

1.4.2 Excitation and emission spectra 27

1.4.3 Fluorescence lifetime 28

1.4.4 Fluorescence polarisation 29

1.5 Fluorescence lifetime measurement techniques *30*

1.5.1 Time-domain fluorescence lifetime determination 30

1.5.2 Time-correlated single photon counting 31

1.6 Analysis of fluorescence lifetime data *33*

1.7 Autofluorescence and tissue spectroscopy of the heart *33*

1.7.1 Amino acid autofluorescence 34

1.7.2 Nicotinamide adenine dinucleotide – NAD(P)H 35

1.7.3 Flavin adenine dinucleotide – FAD 37

1.7.4 Extracellular matrix autofluorescence – collagens and elastins 38

1.8 Diffuse reflectance of cardiac tissue *39*

1.9 Structure, physiology and energetics of the heart in health *40*

1.10 Structure, physiology and energetics of the heart in disease *50*

1.11 Summary, hypothesis and aims *51*

2 Methods and Materials **53**

2.1 Autofluorescence lifetime and diffuse reflectance spectroscopy custom-built single-point fibre-optic probe based instrument *53*

2.1.1 Optical setup and fibre optic probe 53
2.1.2 Data acquisition 58
2.1.3 Data analysis 59
2.2 Surgery protocols 61
2.2.1 Animals 62
2.2.2 Anaesthesia, endotracheal intubation and pre-operative management for surgery protocols 62
2.2.3 Myocardial infarction induction surgery 63
2.2.4 *In vivo* autofluorescence lifetime measurements 64
2.3 Echocardiography 64
2.4 Ex vivo isolated perfused heart 65
2.4.1 Background 65
2.4.2 Langendorff perfusion apparatus 66
2.4.3 Isolated heart protocol 67
2.5 Myocardial histology: PSR staining 69
2.6 Statistical analysis 70
3 Autofluorescence in an *ex vivo* Langendorff heart model 71
3.1 Introduction 71
3.2 Methods 72
3.2.1 Animals 72
3.2.2 Langendorff apparatus 72
3.2.3 *Ex vivo* heart protocol 73
3.2.4 Data analysis: spectral analysis, fluorescence lifetime data analysis and diffuse reflectance data analysis 75
3.3 Results 76
3.3.1 Preliminary 'no-flow ischaemia' experiments 76
3.3.2 Diffuse reflectance measurements 76
3.3.3 Autofluorescence spectral measurements 79
3.3.4 Autofluorescence lifetime measurements 81
3.4 Discussion 86
3.4.1 Diffuse reflectance measurements 86
3.4.2 Autofluorescence spectral measurements 87
3.4.3 Autofluorescence lifetime measurements 88
3.5 Summary 93
4 Autofluorescence in a myocardial infarction-heart failure model 94

4.1 Introduction *94*
4.2 Experimental methods *97*
4.2.1 Myocardial infarction induction surgery, *in vivo* autofluorescence lifetime measurements and histology 97
4.2.2 Data collection 98
4.2.3 Spectral analysis, fluorescence lifetime data analysis and diffuse reflectance data analysis 98
4.2.4 Principal component analysis and linear discriminant analysis 99
4.2.5 Statistical analysis 99
4.3 Results *100*
4.3.1 1 week-post myocardial infarction induction 100
4.3.2 2 weeks-post myocardial infarction induction 105
4.3.3 4 weeks-post myocardial infarction induction 110
4.3.4 16 weeks-post myocardial infarction induction 115
4.4 Discussion *127*
4.5 Summary *132*

5 Autofluorescence in a preclinical doxorubicin chemotherapy cardiomyopathy heart failure model 133
5.1 Introduction *133*
5.2 Methods *135*
5.2.1 Animals 135
5.2.2 Doxorubicin heart failure model 135
5.2.3 Echocardiography 137
5.2.4 *In vivo* autofluorescence lifetime measurements 137
5.2.5 Data collection 137
5.2.6 Spectral analysis and fluorescence lifetime data analysis 137
5.2.7 Principal component analysis and linear discriminant analysis 137
5.3 Results *138*
5.3.1 Intraperitoneal doxorubicin treatment models 138
5.3.2 Intravenous doxorubicin treatment model 141
5.4 Discussion *155*
5.5 Summary *160*

6 Conclusions 161
6.1 Summary *161*
6.2 Background *161*

6.3 Ex vivo Langendorff heart model 163
6.4 Preclinical doxorubicin chemotherapy cardiomyopathy heart failure model 163
6.5 Myocardial infarction-heart failure model 165
6.6 Towards in vivo measurements in man 166
6.7 Limitations 169
6.8 Final remarks 170

List of figures

Figure 1.1 Simplified Jabłoński diagram showing potential transitions between molecular energy states – adapted from (Lakowicz 2006) 26

Figure 1.2 Schematic representation of TCSPC method. Photons are detected one at a time relative to the excitation pulse (T, T+1, … T+n) and a histogram of photon arrival times is constructed, to which can be fitted an exponential function to the decay determine the lifetime parameters. (After (Becker 2010)) 32

Figure 1.3 Chemical structure of NADH. In the oxidized form NAD^+, the two protons shown in green are lost. In $NADP^+$/NADPH the hydroxyl group shown in red is replaced by the phosphate group shown in the dashed box. After (Lakowicz 2006) 35

Figure 1.4 Chemical structure of FAD. The reduced form, $FADH_2$ has a proton couple to the nitrogen atoms shown in green. After (Lakowicz 2006) 37

Figure 1.5 Absorbance spectra of key chromophores in cardiac tissue – haemoglobin (Hb), myoglobin (Mb) and cytochrome c in their oxidized and reduced states. Paired oxidized and reduced state of each molecule scaled by normalization of the larger of each curve to 1. Absorption curves obtained from literature: Human Hb and HBO2(Prahl 1999), horse cytochrome c (Arai et al. 1999), horse Mb and Mb02 (Margoliash & Frohwirt 1959). 40

Figure 1.6 Simplified schematic beta-oxidation pathways of a fatty acid, where *n* represents the number of carbon atoms in the fatty acid. The cycle ends when all carbons are converted into acetyl-CoA, i.e. with n = 2. For each cycle, one molecule of NADH and $FADH_2$ are produced. Reproduced with permission from Dr João Lagarto. 44

Figure 1.7 Simplified schematic of the aerobic glucose metabolic pathway to generate acetyl-CoA. Glycolysis occurs in the cytosol of the cells (left) and pyruvate is oxidised to acetyl-CoA in mitochondria (right). Reproduced with permission from Dr João Lagarto. 45

Figure 1.8 A schematic representation of the Krebs (citric acid) cycle, including by-products of electron carriers and CO2 (in red) and enzyme complexes that catalyse each reaction (in blue). Reproduced with permission from Dr João Lagarto 46

Figure 1.9 Summary of aerobic metabolic pathways for production of ATP. Reproduced with permission from Dr João Lagarto. 48

Figure 2.1 (A) Experimental layout of the autofluorescence lifetime & diffuse reflectance spectroscopy custom-built single-point fibre-optic probe based instrument and its optical fibre configuration at the excitation (proximal) and sample (distal) ends. Optical fibre cores

are coloured blue for excitation fibres, white for fibres delivering white light and collecting the diffuse reflected light and green for fibres collecting returned fluorescence. (B) Portable trolley mounting of the system allows ease of deployment in clinical settings. (C) Distal end of the fibre-optic probe with ruler for scale. 54

Figure 2.2 Detail of the fibre optic bundle with (A) detail of the cross-section (left) and en-face (right) views of the proximal end of the fibre-bundle, at the fluorescence excitation branch where it is coupled to the lasers (B) Colour-coded cross-section en-face view showing arrangement of delivery and collection fibres at the distal end of the probe: blue - fluorescence excitation fibres; green - fluorescence collection fibres; and white - light delivery and collection fibres. (C) Photograph of the distal end of the fibre bundle with ruler for scale. 55

Figure 2.3 Emission spectra of endogenous fluorophores of interest excited at 375 nm and plotted to show their relation to the spectral range of the detection channels of the fluorescence lifetime point probe system. Curves are normalized to their maximum amplitude. Solutions of β-NADH (N1161, Sigma-Aldrich, Germany) and FAD (F6625, Sigma-Aldrich, Germany) were prepared by diluting the respective powder in phosphate buffered saline (PBS) solution. Collagen type-I from rat tail was from Sigma (C8897, Sigma-Aldrich, Germany) and was used directly without further preparation. Measurements of the fluorescence emission spectra is carried out on a spectrofluorophotometer (RF-5301PC, Shimadzu, Japan) using 375 nm excitation. Emission spectra were recorded from 400 to 700 nm. A 390 nm long-pass filter was placed at the entrance slit of the monochromator to prevent contamination of the fluorescence signal by the excitation light. 57

Figure 2.4 LabVIEW graphical user interface (GUI) – an update of the code, previously developed in our laboratory, by Dr João Lagarto 58

Figure 2.5 Example left ventricular M-mode tracing from a control animal, from which can be calculated end-diastolic and systolic interventricular septum dimensions (IVSd and IVSs), left ventricular internal diameter (LVIDd and LVIDs), and end-diastolic and systolic left ventricular posterior wall dimensions (LVPWd and LVPWs), M-mode velocity and heart rate. 65

Figure 2.6 Langendorff perfusion apparatus (figure reproduced with permission from Dr M Debney) 69

Figure 3.1 Schematic representation of the Langendorff system with three-way tap to permit switching between two different perfusate solutions and / or gas mixtures 73

Figure 3.2 From left to right: initial results of 'No-flow ischaemia' method. Mean fluorescence lifetime for channel 2 (NADH), mean fluorescence lifetime for channel 4 (FAD), and redox

ratio (Ch2 I / Ch2 + Ch3 I = [NADH]/(a[NADH] + b[FAD])). Black arrows show the duration of 'no flow ischaemia'. Blue indicates control, red indicates ischaemia, solid lines indicate mean, and pale dashed lines indicate ± 1 s.d. 77

Figure 3.3 Mean fluorescence lifetime for channel 2 (NADH) on 'no-flow ischaemia' (A) against time, and temperature measurement just proximal to the aortic cannula against time (B) showing a high degree of correlation (r = 0.905). In (A) blue indicates control, red indicates ischaemia, solid lines indicate mean, and pale dashed line indicate ± 1 s.d..... 77

Figure 3.4 Variation of NADH in solution mean lifetime with temperature measured in cuvette system..... 78

Figure 3.5 Absorbance spectra at baseline (blue) and on hypoxia (red) obtained from the Langendorff hypoxia model. Difference between the two states is summarised as Δabsorbance (green). Black arrows are positioned at position of maximum difference in absorbance in oxygenated and deoxygenated states - 578nm and 600nm 78

Figure 3.6 Variation of tissue oxygenation derived from tissue absorbance [A(578 nm)/A(600 nm) a.u.] in control (blue, n=4), hypoxia (red, n=5) and mannitol (green, n=4) protocols (solid line = mean, dashed lines = 1 .s.d.). Column switches shown by vertical dashed lines.79

Figure 3.7 Normalised fluorescence intensity during protocols: control (blue, n=4), hypoxia (red, n=5) and mannitol (green, n=4) (solid line = mean, pale dashed lines = 1 .s.d.) Switch of perfusate shown by grey vertical dashed line..... 80

Figure 3.8 Relative fluorescence intensity in each detection channel using UV excitation – (Ch X / (CH1+CH2+CH3)): control (blue, n=4), hypoxia (red, n=5) and mannitol (green, n=4) (solid line = mean, pale dashed lines = 1 .s.d.) Switch of perfusate shown by grey vertical dashed line..... 81

Figure 3.9 Redox ratio (ratio CH2 : CH3 fluorescence : control (blue, n=4), hypoxia (red, n=5) and mannitol (green, n=4) (solid line = mean, pale dashed lines = 1 .s.d.) Switch of perfusate shown by grey vertical dashed line..... 81

Figure 3.10 Channel 1 autofluorescence lifetime (single exponential decay model) during protocols: control (blue, n=4), hypoxia (red, n=5) and mannitol (green, n=4) (solid line = mean, pale dashed lines = 1 .s.d.) Switch of perfusate shown by grey vertical dashed line.... 83

Figure 3.11 Channel 2 ('NADH' - 375nm excitation, 430nm – 480nm emission) autofluorescence lifetime parameters (double exponential model) during protocols: control (blue, n=4), hypoxia (red, n=5) and mannitol (green, n=4) (solid line = mean, pale dashed lines = 1 s.d.) Switch of perfusate shown by grey vertical dashed line 84

Figure 3.12 Channel 3 ('NADH' & 'FAD' - 4375nm excitation, 500nm – 550nm emission) autofluorescence lifetime parameters (double exponential model) during protocols: control (blue, n=4), hypoxia (red, n=5) and mannitol (green, n=4) (solid line = mean, pale dashed lines = 1 s.d.) Switch of perfusate shown by grey vertical dashed line. 85

Figure 3.13 Channel 4 ('FAD' - 440nm excitation, 500nm – 550nm emission) autofluorescence lifetime parameters (double exponential model) during protocols: control (blue, n=4), hypoxia (red, n=5) and mannitol (green, n=4) (solid line = mean, pale dashed lines = 1 s.d.) Switch of perfusate shown by grey vertical dashed line. 86

Figure 4.1 Figurative diagram of regions of interests (ROI) for *in vivo* epicardial measurements in the MI-HF model studies. (A) anterior view; (B) posterior view; left ventricle (LV) anterior ('scar'); interventricular septum ('border zone'); right ventricle; LV posterior 98

Figure 4.2 1 week timepoint diffuse reflectance data for MI-HF model in MI-HF and AMC, displayed by region of interest (ROI): A – RV; B – LV posterior; C – Interventricular septum / 'border zone'; D – LV anterior / 'scar'. Pale dashed lines indicate ± 1 SD. 101

Figure 4.3 1 week timepoint relative contribution of each spectral channel to total autofluorescence from UV excitation in MI-HF and AMC, displayed by ROI. * $p < 0.05$; ** $p < 0.01$ 102

Figure 4.4 1 week timepoint relative autofluorescence in each ROI in MI-HF and AMC 102

Figure 4.5 1 week timepoint autofluorescence lifetime parameters for each spectral channel for MI-HF and AMC, displayed by ROI. * $p < 0.05$; ** $p < 0.01$; *** $p < 0.001$; **** $p < 0.0001$.....103

Figure 4.6 1 week timepoint scores of first 2 principal components from classification algorithm for MI-HF and AMC, displayed by ROI: A – RV; B – LV posterior; C – Interventricular septum / 'border zone'; D – LV anterior / 'scar'. Decision line shown as black line. 104

Figure 4.7 2 weeks timepoint diffuse reflectance data for MI-HF model in MI-HF and AMC, displayed by region of interest (ROI): A – RV; B – LV posterior; C – Interventricular septum / 'border zone'; D – LV anterior / 'scar'. Pale dashed lines indicate ± 1 SD. 106

Figure 4.8 2 weeks timepoint relative contribution of each spectral channel to total autofluorescence from UV excitation in MI-HF and AMC, displayed by ROI. * $p < 0.05$; ** $p < 0.01$ 107

Figure 4.9 2 weeks timepoint relative autofluorescence in each ROI in MI-HF and AMC 107

Figure 4.10 2 weeks timepoint autofluorescence lifetime parameters for each spectral channel for MI-HF and AMC, displayed by ROI. * $p < 0.05$; ** $p < 0.01$; *** $p < 0.001$; **** $p < 0.0001$.....108

Figure 4.11 2 weeks timepoint scores of first 2 principal components from classification algorithm for MI-HF and AMC, displayed by ROI: A – RV; B – LV posterior; C – Interventricular septum / 'border zone'; D – LV anterior / 'scar'. Decision line shown as black line.....109

Figure 4.12 4 weeks timepoint diffuse reflectance data for MI-HF model in MI-HF and AMC, displayed by region of interest (ROI): A – RV; B – LV posterior; C – Interventricular septum / 'border zone'; D – LV anterior / 'scar'. Pale dashed lines indicate ± 1 SD.....111

Figure 4.13 4 weeks timepoint relative contribution of each spectral channel to total autofluorescence from UV excitation in MI-HF and AMC, displayed by ROI. * $p < 0.05$; ** $p < 0.01$.....112

Figure 4.14 4 weeks timepoint relative autofluorescence in each ROI in MI-HF and AMC.....112

Figure 4.15 4 weeks timepoint autofluorescence lifetime parameters for each spectral channel for MI-HF and AMC, displayed by ROI. * $p < 0.05$; ** $p < 0.01$; *** $p < 0.001$; **** $p < 0.0001$.....113

Figure 4.16 4 weeks timepoint scores of first 2 principal components from classification algorithm for MI-HF and AMC, displayed by ROI: A – RV; B – LV posterior; C – Interventricular septum / 'border zone'; D – LV anterior / 'scar'. Decision line shown as black line.....114

Figure 4.17 Representative histology images from AMC (left column) and MI-HF (right column) hearts. (A, E) RV; (B, F) LV posterior; (C, G) Interventricular septum / Border zone; (D, H) LV anterior / 'scar'.....118

Figure 4.18 16 weeks timepoint diffuse reflectance data for MI-HF model in MI-HF and AMC, displayed by region of interest (ROI): A – RV; B – LV posterior; C – Interventricular septum / 'border zone'; D – LV anterior / 'scar'. Pale dashed lines indicate ± 1 SD.....119

Figure 4.19 16 weeks timepoint relative contribution of each spectral channel to total autofluorescence from UV excitation in MI-HF and AMC, displayed by ROI * $p < 0.05$; ** $p < 0.01$; *** $p < 0.001$; **** $p < 0.0001$.....120

Figure 4.20 16 weeks timepoint relative autofluorescence in each ROI in MI-HF and AMC.....120

Figure 4.21 16 weeks timepoint autofluorescence lifetime parameters for each spectral channel for MI-HF and AMC, displayed by ROI. * $p < 0.05$; ** $p < 0.01$; *** $p < 0.001$; **** $p < 0.0001$.....121

Figure 4.22 16 weeks timepoint scores of first 2 principal components from classification algorithm for MI-HF and AMC, displayed by ROI: A – RV; B – LV posterior; C –

Interventricular septum / 'border zone'; D – LV anterior / 'scar'. Decision line shown as black line.....122

Figure 4.23 Relative channel 1 (400 – 420 nm) autofluorescence in MI-HF to AMC hearts in each ROI against time point after MI induction surgery 126

Figure 4.24 Variation of short lifetime component $\tau 1$ of detection channel 4 (500 – 550 nm) in MI-HF to AMC hearts in each ROI against time point after MI induction surgery.....126

Figure 5.1 Body weight (g) in animals treated with 10 mg / kg intraperitoneal doxorubicin or intraperitoneal saline control at 2 weeks and 4 weeks post last injection. * $p < 0.05$; ** $p < 0.01$.....139

Figure 5.2 Ejection fraction (%) assessed by echocardiography in animals treated with 10 mg / kg intraperitoneal doxorubicin or intraperitoneal saline control at 2 weeks and 4 weeks post last injection. ** $p < 0.01$.....139

Figure 5.3 Mortality (%) in animals treated with 10 mg / kg intraperitoneal doxorubicin or intraperitoneal saline control and treated or control drinking water: Control - control i.p. injection + control drinking water (n = 5); DOX - doxorubicin 10mg/kg i.p. + control drinking water (n = 5); E50 - doxorubicin 10mg/kg i.p. + enalapril 50mg/kg drinking water (n = 5); C50 - doxorubicin 10mg/kg i.p. + carvedilol 50mg/kg drinking water (n = 5); EC50 - doxorubicin 10mg/kg i.p. + enalapril 50mg/kg + carvedilol 50mg/kg drinking water (n = 5); E200 – doxorubicin 10mg/kg i.p. + enalapril 200mg/kg drinking water (n = 5).....140

Figure 5.4 Mortality (%) in animals treated with 10 mg / kg intraperitoneal doxorubicin (DOX) or intraperitoneal saline control (Control) and treated drinking water (Treated) or control drinking water (control) (* $p = 0.01$) 140

Figure 5.5 Mean lifetime (τ) of LV anterior wall (LV) by channel in animals treated with 10 mg / kg intraperitoneal doxorubicin or intraperitoneal saline control and treated or control drinking water: Control - control i.p. injection + control drinking water (n = 5); DOX - doxorubicin 10mg/kg i.p. + control drinking water (n = 1); E50 - doxorubicin 10mg/kg i.p. + enalapril 50mg/kg drinking water (n = 4); C50 - doxorubicin 10mg/kg i.p. + carvedilol 50mg/kg drinking water (n = 3); EC50 - doxorubicin 10mg/kg i.p. + enalapril 50mg/kg + carvedilol 50mg/kg drinking water (n = 4); E200 – doxorubicin 10mg/kg i.p. + enalapril 200mg/kg drinking water (n = 4). 141

Figure 5.6 Body weight (g) in control (solid line, n=4) and 10 mg/kg IV doxorubicin treated (dashed line, n = 7-9) * $p < 0.0042$ Bonferroni-adjusted alpha level (0.05/12).....142

Figure 5.7 Ejection fraction calculated from M-mode echocardiography in control (solid line, n = 4) and 10 mg/kg IV doxorubicin treated (dashed line, n = 7-9) * p < 0.01 Bonferroni-adjusted alpha level (0.05/5) 143

Figure 5.8 - Anterior left ventricle (LV) autofluorescence lifetime parameters for spectral channel 1 (Ch1) in IV doxorubicin (n = 6) and control (n = 3) animals (n.s.) 145

Figure 5.9 - Anterior left ventricle (LV) autofluorescence lifetime parameters for spectral channel 2 (Ch2) in IV doxorubicin (n = 6) and control (n = 3) animals (n.s.) 145

Figure 5.10 Anterior left ventricle (LV) autofluorescence lifetime parameters for spectral channel 3 (Ch3) in IV doxorubicin (n = 6) and control (n = 3) animals (n.s.) 146

Figure 5.11 Anterior left ventricle (LV) autofluorescence lifetime parameters for spectral channel 4 (Ch4) in IV doxorubicin (n = 6) and control (n = 3) animals (n.s.) 147

Figure 5.12 Right ventricle (RV) autofluorescence lifetime parameters for spectral channel 1 (Ch1) in IV doxorubicin (n = 6) and control (n = 3) animals ** p < 0.01. 147

Figure 5.13 Right ventricle (RV) autofluorescence lifetime parameters for spectral channel 2 (Ch2) in IV doxorubicin (n = 6) and control (n = 3) animals. * p < 0.05. 148

Figure 5.14 Right ventricle (RV) autofluorescence lifetime parameters for spectral channel 3 (Ch3) in IV doxorubicin (n = 6) and control (n = 3) animals. * p < 0.05; ** p < 0.01. 149

Figure 5.15 Right ventricle autofluorescence lifetime parameters for spectral channel 4 (Ch4) in IV doxorubicin (n = 6) and control (n = 3) animals. ** p < 0.01. 150

Figure 5.16 Posterior aspect of left ventricle (Posterior) autofluorescence lifetime parameters for spectral channel 1 (Ch1) in IV doxorubicin (n = 6) and control (n = 3) animals. * p < 0.05.150

Figure 5.17 Posterior aspect of left ventricle (Posterior) autofluorescence lifetime parameters for spectral channel 2 (Ch2) in IV doxorubicin (n = 6) and control (n = 3) animals. * p < 0.05.151

Figure 5.18 Posterior aspect of left ventricle (Posterior) autofluorescence lifetime parameters for spectral channel 3 (Ch3) in IV doxorubicin (n = 6) and control (n = 3) animals. * p < 0.05.152

Figure 5.19 Posterior aspect of left ventricle (Posterior) autofluorescence lifetime parameters for spectral channel 4 (Ch4) in IV doxorubicin (n = 6) and control (n = 3) animals. ** p < 0.01. 153

Figure 5.20 Example PSR positive staining to show collagen content of tissue (superimposed on histology image in red) in control (A) compared to IV doxorubicin treated DOX-HF hearts (B & C) 154

Figure 5.21 Histological quantification of collagen content by % tissue PSR-positive staining by region of interest in IV doxorubicin DOX-HF (n = 9) and control (n = 4) animals. ** p < 0.01. 154

Figure 5.22 Scores of first 2 principal components from classification algorithm for IV doxorubicin (DOX) (blue) and control (red) for the LV region of interest. Decision line shown as green line. 155

Figure 6.1 Photograph of the fibre optic probe stainless steel sheath 168

List of tables

Table 1.1 Energetic yield of aerobic cellular respiration through glucose ($C_6H_{12}O_6$) metabolism (in moles) 49

Table 1.2 Energetic yield of aerobic cellular respiration through beta-oxidation of an example fatty acid, e.g.16-C fatty acid (palmitate) (in moles) 49

Table 1.3 Energetic yield of anaerobic metabolism of glucose (in moles) 50

Table 2.1 List of spectroscopic parameters that are extracted from an acquisition 61

Table 3.1 Summary of trend in autofluorescence lifetime parameters during hypoxia and glucose deprivation (mannitol) protocols compared to control: increase (+), decrease (-) or no change observed (0) 92

Table 4.1 Summary of numbers of myocardial-infarction heart failure (MI-HF) and age-matched control (AMC) animals studied by timepoint 97

Table 4.2 1 week timepoint LDA-PCA algorithm classification results (using 5 most significant principal components) 104

Table 4.3 2 weeks timepoint LDA-PCA algorithm classification results (using 5 most significant principal components) 109

Table 4.4 4 weeks timepoint LDA-PCA algorithm classification results (using 5 most significant principal components) 114

Table 4.5 Collagen content calculated from representative histology images in MI-HF hearts and AMC hearts. (two-tailed Student t-test, n=3) 119

Table 4.6 16 weeks timepoint LDA-PCA algorithm classification results by ROI using autofluorescence intensity and/or lifetime and diffuse reflectance parameters, and a combination of both autofluorescence intensity and/or lifetime and diffuse reflectance parameters 124

Table 4.7 16 weeks timepoint autofluorescence parameters calculated for LDA-PCA algorithm classification method ranked by Cohen's d coefficient. 125

Publications and published abstracts

Publications

Lagarto J*, **Dyer BT***, Talbot C, Sikkel MB, Peters NS, French PMW, Lyon AR, Dunsby C, 2015, Application of time-resolved autofluorescence to label-free in vivo optical mapping of changes in tissue matrix and metabolism associated with myocardial infarction and heart failure, *BIOMEDICAL OPTICS EXPRESS*, Vol: 6, Pages: 324-346, ISSN: 2156-7085 [**Joint first author*]

Dyer BT and Lyon AR. 2013, Cardiovascular complications of breast cancer therapy, Association of Breast Surgery Yearbook 2013, Publisher: Association of Breast Surgery at the Royal College of Surgeons (8th edition), ISBN 978-0-9567937-3-7

Kelly DJ, Warren SC, Kumar S, Lagarto JL, **Dyer BT**, Margineanu A, Lam EW-F, Dunsby C, French PMW et al., 2014, An automated multiwell plate reading film microscope for live cell autofluorescence lifetime assays, JOURNAL OF INNOVATIVE OPTICAL HEALTH SCIENCES, Vol: 7, ISSN: 1793-5458

Published abstracts and presentations

Dyer BT, Elder JM, Lagarto J, Harding SE, French PMW, Peters NS, Dunsby C, Lyon AR et al., 2015, Application of label-free autofluorescence lifetime in vivo to measure changes in myocardial fibrosis and metabolism in a doxorubicin cardiomyopathy heart failure model, Congress of the European-Society-of-Cardiology (ESC), Publisher: OXFORD UNIV PRESS, Pages: 151-151, ISSN: 0195-668X [*European Society of Cardiology, Congress 2015, London, U.K.*]

Dyer BT, Elder JM, Lagarto J, Harding SE, French PMW, Peters NS, Dunsby C, Lyon AR et al., 2015, LABEL-FREE AUTOFLUORESCENCE LIFETIME TO ASSESS CHANGES IN MYOCARDIAL FIBROSIS AND METABOLISM IN VIVO IN A DOXORUBICIN CARDIOMYOPATHY HEART FAILURE MODEL, British-Cardiac-Society (BCS) Annual Conference on Hearts and Genes, Publisher: BMJ PUBLISHING GROUP, Pages: A94-A94, ISSN: 1355-6037 [*British Cardiovascular Society Annual Conference 2015, Manchester, U.K.*]

Dyer BT, de Jesus Reis Lagarto J, Sikkel M, Mills A, French P, Peters NS, Dunsby C, Lyon AR et al., 2015, Application of label-free autofluorescence lifetime in vivo to measure changes in myocardial fibrosis and metabolism associated with myocardial infarction and heart failure, EUROPEAN JOURNAL OF HEART FAILURE, Vol: 17, Pages: 367-367, ISSN: 1388-9842 [*European Society of Cardiology Heart Failure Association Winter Meeting 2015, Les Diaberelets, Switzerland. & European Society of Cardiology, Heart Failure 2015 & 2nd World Congress on Acute Heart Failure, Seville, Spain.*]

Dyer BT, Lagarto J, Sikkel M, French P, Dunsby C, Peters N, Lyon A et al., 2014, THE APPLICATION OF AUTOFLUORESCENCE LIFETIME METROLOGY AS A NOVEL LABEL-FREE TECHNIQUE FOR THE ASSESSMENT OF CARDIAC DISEASE, HEART, Vol: 100, Pages: A104-A104, ISSN: 1355-6037 [*British Cardiovascular Society Annual Conference 2014, Manchester, U.K.]*

Dyer BT, Lagarto J, French P, Peters NS, Dunsby C, Lyon AR et al., 2014, TIME-RESOLVED AUTOFLUORESCENCE SPECTROSCOPY AS LABEL-FREE METHOD TO CHARACTERISE ACUTE CHANGES IN EX VIVO MODELS OF CARDIAC DISEASE, Autumn Meeting of the British-Society-for-Cardiovascular-Research (BSCR) on Cardiovascular Signalling in Health and Disease, Publisher: BMJ PUBLISHING GROUP, ISSN: 1355-6037 [British Society for Cardiovascular Research (BSCR) Autumn Meeting , 2014, Reading, U.K.]

Benjamin T. Dyer, J. Lagarto, M. B. Sikkel, C. B. Talbot, N. S. Peters, A. R. Lyon, P. M. French, C. Dunsby, "Application of autofluorescence lifetime metrology as a label-free technique to assess heart disease", [BiOS 2014 SPIE Photonics West, San Francisco, California, United States.]

BT Dyer, J Lagarto, P French, Dunsby, NS Peters, C Dunsby, AR Lyon (2014). Time-resolved autofluorescence spectroscopy as a label-free method to characterise acute changes in ex vivo models of cardiac disease. Heart, 100 (Suppl 4), A13–A13. [*British Cardiovascular Society Annual Conference 2013, Manchester, U.K.]*

1 Introduction

1.1 Overview

The work described in this thesis concerns an investigation of autofluorescence lifetime metrology as a novel technique to assess heart disease utilizing a custom-built single-point fibre-optic probe based instrument developed in the Photonics Group of the Department of Physics at Imperial College London. This chapter provides an introduction to the key concepts including fluorescence, fluorescence lifetime, and autofluorescence in the context of the heart. It describes the key autofluorescent molecules in cardiac tissue and gives the background to the role the molecules play in physiology and disease. Finally, there is consideration of the concept of heart failure as a clinical syndrome that represents the end-point of disease processes of myocardium of different aetiologies and that having new tools to look particularly at the early deleterious changes in the asymptomatic phases of these conditions would represent a tremendous clinical advance.

1.2 Use of Optical techniques in the heart

The widespread availability of cardiac imaging techniques has revolutionised the practice of cardiovascular medicine. The diagnostic and prognostic assessment of patients with known or suspected cardiac disease has become increasingly dependent on the use of these technologies to detect either structural or functional changes in the heart. The most commonly-used cardiac imaging modalities in current practice include echocardiography; coronary angiography with cardiac catheterisation; intravascular ultrasound (IVUS); nuclear cardiology tests (myocardial perfusion scintigraphy (MPS), multi-gated acquisition scan (MUGA) and positron emission tomography (PET); computed tomography (CT) calcium scoring and angiography; and cardiac magnetic resonance (CMR) imaging. (Camm et al. 2009) It is worth discussing these established imaging techniques before looking at the use of novel optical techniques in medical applications and their use to date in the heart.

Echocardiography remains the most important diagnostic imaging tool in clinical practice and like all forms of ultrasonic imaging it is based on generation of high frequency acoustic pressure waves from a transducer comprised of one or more piezoelectric crystals, which also act as a receiver from returning waves from insonified objects (e.g. heart walls and heart valves). As the velocity of sound is constant, the object location can be determined based on the timing of the returning signal. (Ramrakha & Hill 2008) Echocardiography can be performed transthoracic or transoesophageal and can incorporate a number of different techniques including M-mode, 2D imaging, 3D imaging, pulsed Doppler, continuous wave Doppler, colour flow Doppler, tissue

Doppler imaging and strain rate imaging. With the use of these techniques echocardiography can provide information on heart structure, dimensions, valve structure and function, assessment of wall motion and assessment of systolic and diastolic function.

Cardiac catheterization involves insertion of catheters into the heart via arteries in the arm or leg, which permits pressure monitoring and blood sampling through the catheter. Coronary angiography entails injection of radio contrast dye, imaged using X-ray fluoroscopy, which permits assessment of the patency and configuration of the coronary artery lumens and this imaging can be used to guide the use of catheter-based interventional techniques such as coronary artery stent insertion during percutaneous coronary intervention (PCI). Intravascular ultrasound (IVUS) is an ultrasound-based technique that allows direct visualization of atherosclerotic plaque and the vessel lumen. Unlike coronary angiography, it allows visualization of the full circumference of the vessel wall and is therefore the method of choice to determine vessel luminal area. (Ramrakha & Hill 2008)

Nuclear cardiology techniques incorporate three main types of scan: myocardial perfusion scintigraphy (MPS); multi-gated acquisition scan (MUGA); and positron emission tomography (PET). The principle of all of these tests is the use of a radionuclide tracer e.g. technetium-99m (^{99m}Tc) or thallium-201 (^{201}Tl), which is then imaged by a gamma camera designed to detect the gamma radiation emitted from the radionuclide. The technetium is bound to a compound e.g. tetrofosmin which means that it is retained in intact cardiomyocytes. MPS is a well validated technique for the diagnosis and assessment of coronary artery disease and utilises rest and physical- or pharmaceutical-induced stress images to determine resting myocardial perfusion, and evidence of inducible defects of perfusion. MUGA scans work by labelling the blood pool with radio nucleotide and taking images of multiple gated cardiac cycles, which gives an accurate and reproducible assessment of overall LV function. PET uses ^{18}F-deoxyglucose to detect changes in glucose metabolism, which is an indicator of myocardial viability. (Khavandi (ed) 2014)

Multi-detector computer tomography (CT) uses X ray images from multiple angles to produce cross sectional imaging. Its use in cardiology is principally in producing non-contrast coronary calcium scores to screen for development of calcified atherosclerotic plaque, and in producing contrast-enhanced CT angiography images of the coronary arteries, allowing multi-plane reconstruction of the images along the length of the arteries to allow interrogation of all coronary segments. (Khavandi (ed) 2014)

CMR is an imaging methodology based on aligning the spin axis of nuclei within molecules of the object being visualized by applying a powerful magnetic field. The scanner produces a radiofrequency electromagnetic wave with a varying magnetic field. The protons absorb the energy from the variable field and flip their spins. When the field is turned off, the protons gradually return to their normal spin, a process called precession, which is different in different tissues. The scanner settings can be adjusted to produce contrast between different body tissues

permitting the production of an image. CMR offers high spatial and temporal resolution imaging of the heart as it has excellent differentiation of soft tissues. Assessment of left and right ventricular function is highly accurate and reproducible, and velocity encoded imaging can measure blood flow to quantify intra-cardiac shunts and valvular abnormalities. In terms of anatomical imaging, unlike echocardiography, it can study the heart in any plane and it is not limited by imaging windows. It is particularly invaluable in the assessment of congenital heart disease where accurate anatomical information is paramount. The use of a contrast agent, gadolinium, can be used to assess perfusion and delayed contrast enhancement can also be used to assess viability as gadolinium collects in areas of increased extracellular space e.g. fibrosis or infarction, differentiating it from normal myocardium by a phenomenon called late-gadolinium enhancement. (Khavandi (ed) 2014)

Many optical techniques have been investigated and shown promise in biomedical applications as potential diagnostic techniques. These include diffuse reflectance, autofluorescence spectroscopy and imaging (Talbot et al. 2010; McGinty et al. 2010; Schneckenburger 1992), pump-probe spectroscopy (Matthews et al. 2011), optical coherence tomography (Jang 2015) and Raman spectroscopy (Kallaway et al. 2013). In principle, the aim of the use of a given optical technique is that of obtaining an optical fingerprint associated with a given disease state to permit categorization of a sample. Optical techniques have been used in a wide variety of clinical applications including blood oxygen saturation (Häggblad et al. 2008), oncology (Kallaway et al. 2013; P. A. A. De Beule et al. 2007; Thompson et al. 2012; Pu et al. 2013; Weber et al. 2012), osteoarthritis (Johansson et al. 2011), atherosclerosis (L Marcu, MC, Maarek, & Grundfest, 2001, Fatakdawala et al., 2015), and to a much lesser extent heart disease (Ti et al. 2010; Ranji et al. 2009; Ranji et al. 2006; Lindbergh et al. 2011; Venius, Bagdonas, Žurauskas, et al. 2011; Venius, Bagdonas, Zurauskas, et al. 2011). The growing interest in optical tools is driven by the potential for immediate biochemical, morphological and physiological information as real time and *in situ* measurements to create a 'virtual biopsy' to guide physicians. Overall, with the exception of optical coherence tomography, there has been relatively limited application to date of other optical spectroscopic techniques to study of the heart but some examples of applications are detailed below.

Optical coherence tomography (OCT) is an optical analogue of intravascular ultrasound (IVUS) that was described above and is used to examine the coronary arteries during cardiac catheterization. OCT uses light in the infrared region of the electromagnetic spectrum, typically with a central wavelength of between 1250 nm and 1300 nm. In terms of novel optical techniques in use in cardiology, optical coherence tomography is the only technique that is regulatory body-approved and commercially available for use in clinical settings although research is on-going as to how to interpret the morphological findings that OCT provides. OCT has 10-fold higher resolution than IVUS giving almost histological cross-sectional coronary imaging with axial resolution of 10-20 micron compared to 100-200 microns for IVUS. However,

the penetration is considerably less than IVUS and therefore some vessel structures e.g. external elastic lamina cannot be visualized in the case of a large atherosclerotic plaque. OCT can differentiate different tissue characteristics (fibrous, calcified, or lipid-rich plaque) as high birefringence identifies fibrous tissue, collagen, and lipid composition, whereas low birefringence is linked to calcium-based plaques and may identify thin-cap fibroatheroma. Because of the strong attenuation of light by blood due to absorption by haemoglobin and scattering by red blood cells, OCT systems therefore originally required the removal of blood during the acquisition by use of an occlusion balloon and flushing of the artery during the acquisition. More recently, non-occlusive techniques requiring only flushing have been developed with a move from time-domain to frequency-domain systems that have increased the frame rates and scanning speeds. The main applications of OCT are in assessment of atherosclerotic plaque characteristics, coronary stent strut coverage and apposition assessment, evaluation of in-stent restenosis and to guide PCI as it can provide detailed information on dissection, tissue prolapse, thrombi, and to detect incomplete stent apposition.

Cazmara *et al* described the use of Raman spectroscopy to characterize *ex vivo* the biochemical tissue alterations in aortic valves associated with the development of aortic stenosis, in which they reported that the lipid-to-protein ratio decreased with disease progression. (Czamara et al. 2015) Brazhe *et al* detailed the use of Raman spectroscopy *ex vivo* on a Langendorff-perfused rat heart to simultaneous study of redox changes in c-and b-type cytochromes with treatment with mitochondrial uncoupling agent FCCP and for a semi quantitative estimation of the amount of oxygenated myoglobin upon hypoxia, although the heart was not contracting as an arrested heart was necessary to permit a stable focus. (Brazhe et al. 2013)

The use of diffuse reflectance measurements has been used *in vivo* during coronary artery bypass graft surgery to measure myocardium tissue oxygenation during surgery and this confirmed that tissue oxygenation could be tracked and was noted to decreases during cardiac arrest and to increase following reperfusion as would be expected. (Häggblad et al. 2008)

Autofluorescence spectroscopy has been applied to studies in the heart, although the number of reports is limited. The Marcu group from University of California, Davis described the ability of label-free autofluorescence lifetime imaging (FLIM) to complement intravascular ultrasound (IVUS) for concurrent visualization of human coronary vessel composition, structure, and pathology in an *ex vivo* model. The use of co-registered FLIM with the morphological IVUS data gave further information about plaque composition, including classification of the plaque as thick or thin-capped, and the presence or not of macrophages, which are features associated with vulnerable plaques more prone to rupture causing myocardial infarction. (Fatakdawala et al. 2015) Chorvat *et al* reported that the metabolic status of isolated rat cardiomyocytes could be determined directly without the use of labels by investigating the autofluorescence resulting from mitochondrial flavoprotein and reduced NAD(P)H after excitation with UV light. (Chorvat,

Kirchnerova, Cagalinec, Smolka, A. Mateasik, et al. 2005; Chorvat & Chorvatova 2006) Additionally, they reported altered NAD(P)H autofluorescence lifetime components in human cardiomyocytes from myocardial biopsies from paediatric heart transplant recipients suffering mild graft rejection compared to no rejection. (Chorvat et al. 2010) Swift *et al* reported visualization of epicardial cryoablation lesions by endogenous tissue fluorescence as either blood-perfused or saline-perfused Langendorff perfused hearts was associated with a marked decrease in nicotinamide adenine dinucleotide (NADH) fluorescence within approximately 30 seconds, leading to a 60% to 70% loss of signal intensity at the lesion site, which they suggest could be used during ablation procedures to confirm successful ablation and avoid ablation gaps. (Swift et al. 2014)

Autofluorescence spectroscopy is a promising tool for the characterization of biological tissues without the use of exogenous labels and it is already shown potential for *in* vivo clinical diagnosis in a number of applications. Furthermore, the Photonics Group of the Department of Physics, Imperial College London has a research interest in the use of autofluorescence lifetime spectroscopic techniques in the development of biomedical applications. An EPSRC project grant was awarded to the group for a project in collaboration with the National Heart and Lung Institute, Imperial College London and the Kennedy Institute of Rheumatology, formerly at Imperial College London, to develop a compact and portable fibre-optic probe-based instrumentation for time-resolved spectroscopy to report on structural and metabolic alterations associated with osteoarthritis and heart disease. This project grant funded my studentship.

1.3 Fluorescence

Fluorescence is the phenomenon by which certain molecules absorb light at a specific wavelengths and subsequently emit at different longer wavelengths.(Lakowicz 2006) It was Sir Frederich William Herschel who first reported the phenomenon in 1845 upon observing a blue colour emitting from a colourless quinine solution when observed under “certain incidences of light”.(J.F.W. Herschel 1845) The difference in wavelength between the absorbed and emitted light is known as the *Stokes shift*. (Lakowicz 2006) This can be explained with reference to the *Jabłoński diagram*, which schematically represents the processes occurring between absorption and emission where the horizontal lines correspond to different molecular energy levels, while the vertical arrows represent transitions between the levels.

Excitation of a molecule occurs when it absorbs a photon causing it to be promoted from its ground electronic energy state (S0) into a higher energy state (S1, S2…) depending on the energy of the absorbed photon. Once excited, the molecule can return to ground state through a number of different processes: non-radiative decay where energy is lost as heat; intersystem crossing to a triplet state followed by radiative decay via phosphorescence; or by fluorescence on transition from the lowest vibrational state of S1 (i.e. j = 0) to the ground electronic state S0 via release of a

photon. The energy of the emission is typically lower than that of absorption and therefore has a longer wavelength – see equation 1.1, where λ is the wavelength of light, ΔE is the energy change by the transition, *h* is Plank's constant and *c* is the speed of light.

Equation 1.1

$$\lambda = \frac{hc}{\Delta E}$$

The contribution that these various processes make can be influenced by the molecule itself, and the environment in which the molecule finds itself.

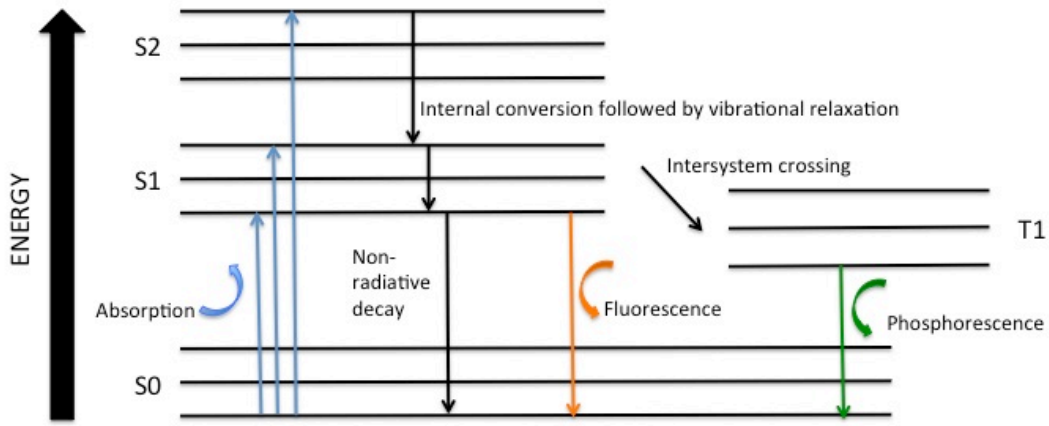


Figure 1.1 Simplified Jabłoński diagram showing potential transitions between molecular energy states – adapted from (Lakowicz 2006)

Scientists have long been exploiting the property of fluorescence to label specific molecules of interest permitting study of the localisation of molecules within cells or tissue, or quantification of a biological parameter e.g. cell membrane potential.(Lakowicz 2006) This has traditionally involved the use of exogenous molecules, which exhibit the property of fluorescence, to label targets of interest. Such compounds are referred to as 'probes' or 'fluorophores'. There are a number of limitations of the use of such compounds including the introduction of an extrinsic molecule, which itself can affect the system under investigation, as well as issues of toxicity to the cell, tissue, or organ under investigation.

1.4 Properties of fluorescence

Fluorescence is characterised by several inherent physical properties: intensity and quantum yield, excitation and emission spectra, fluorescence lifetime and polarisation.

1.4.1 Intensity and quantum yield

The intensity of fluorescence is the most readily determined characteristic that can be measured. The quantum yield (Φ) of a specimen being investigated is described by the number of fluorescent photons emitted (N_c) relative to the number of photons absorbed (N_a) as described in equation 1.2. Substances with the highest quantum yields therefore demonstrate the brightest emissions. (Lakowicz 2006)

Equation 1.2

$$\phi = \frac{N_c}{N_a}$$

However, the intensity of fluorescence can be affected by a number of experimental factors as well as by the physical properties of the tissue or sample being studied. These include the concentration of the molecule present, the power of the excitation laser, and other experimental artefacts in the biological sample including quenching, scattering properties, bleaching, excitation light geometry and absorption. (Lakowicz 2006; Talbot et al. 2010; Islam et al. 2013b)

Although fluorescence intensity is easy to measure, it remains difficult to produce reproducible quantitative fluorescence intensity measurements of fluorophores in tissue and to compare measurements between instruments and samples, particularly in biological specimens.

1.4.2 Excitation and emission spectra

As discussed earlier, every energy transition involving absorption or emission of a photon as described in the Jabłoński diagram is described by the photon energy equation 1.1. Since not all transitions occur with equal likelihood, a fluorophore will absorb and emit light at some wavelengths more efficiently than others. As discussed above, after excitation the electron may undergo a series of non-radiative processes by which energy is lost, before the emission of a fluorescence-photon occurs. Therefore, the emitted photon is always of lower energy and thus the fluorescence emission wavelength is red-shifted relative to the excitation wavelength. This phenomenon is called the Stokes' shift. The emission spectrum is independent of the fluorescence excitation wavelength since it results from the transition from the lowest vibrational energy level in first-excited state (S_1) to ground state (S_0), following the completion of vibrational relaxation.

Furthermore, the excitation and emission spectra are typically 'mirror images', owing to the similar vibrational energies and levels of the ground and first-excited states. The wavelength at which excitation and emission of fluorescence light occurs depends on the electronic configuration of the molecules and this in turn depends on the chemical structure and local milieu. Measurements reporting changes in these parameters have been used in biomedical research to differentiate disease and healthy tissue. (Onizawa et al. 1999; Pu et al. 2013)

1.4.3 Fluorescence lifetime

Fluorescence lifetime represents the amount of time on average that the molecule spends in the excited state (S_1) before returning to the ground state (S_0) and, as such, gives information of the kinetics of the transition from the excited state. The assumption that S_1 (excited state) is exponentially decaying with intensity *I(t)* is as described mathematically in equation 1.3, where I_0 is the initial intensity, t is the time since excitation and τ is the fluorescence lifetime, which is defined as the average time an electron remains in an excited state before decaying back to the ground state.

Equation 1.3

$$I(t) = I_0 \mathrm{e}\left(-\frac{t}{\tau_1}\right)$$

The temporal decay for many samples is multi-exponential and is due to the presence of multiple fluorophores. In this case, the multi-exponential decay would be described by equation 1.4, where *n* is the number of decay components.

Equation 1.4

$$I(t) = \sum_{i=1}^{n} I_i \; e^{\left(-\frac{t}{\tau_i}\right)}$$

If the decay can be described by a bi-exponential decay model with time constants τ_1 and τ_2 for the two components, it would be described by the equation 1.5.

Equation 1.5

$$I(t) = I_1 \, e^{\frac{-t}{\tau_1}} + I_2 \, e^{\frac{-t}{\tau_2}}$$

Fluorescence lifetime measurements are inherently ratiometric as the decay parameters are recovered by comparing the signal level at different points in time. They are therefore relatively insensitive to artefacts affecting intensity measurements such as uneven fluorophore concentration and heterogeneous absorption and scattering within the sample. The lifetimes observed in biological tissues range from hundreds to thousands of picoseconds and lifetime measurements can be used to differentiate molecules that emit their fluorescence at overlapping

emission wavelengths or different structural configurations or protein-binding states of a molecule. For example, NADH has a short fluorescence lifetime of approximately 0.4 ns, attributed to a balance between the extended and folded confirmations of the free molecule. NADH exhibits a much longer lifetime (approximately 1.5 ns (Blacker et al. 2014; Lakowicz 2006)) when bound to an enzyme. As well as changes in structural configuration or binding state, fluorescence lifetime is sensitive to changes in the milieu of the molecule that affect the radiative or non-radiative decay rates, which can include viscosity (Blatt et al. 1981), temperature (Blatt et al. 1981), and pH (Nakabayashi et al. 2012) amongst others. Overall, given the sensitivity to changes in the microenvironment of the fluorophore and relative insensitivity to the artefacts that trouble intensity-based techniques, there has been increasing interest in application of fluorescence lifetime-based techniques to read out contrast associated with disease processes including cancer (Pu et al. 2013; Mycek et al. 1998; Tadrous et al. 2003; Uehlinger et al. 2009; P. a a De Beule et al. 2007; Ardeshirpour et al. 2014; Thompson et al. 2012; Sun et al. 2012; Weber et al. 2012) and cardiovascular diseases. (Phipps et al. 2012; Phipps et al. 2009; Phipps et al. 2011; Park et al. 2012)

1.4.4 Fluorescence polarisation

Excitation of a fluorophore by a linearly polarized light can result in a fluorescence emission that can be polarized parallel (I∥) or perpendicular (I⊥) with respect to the excitation. The ratio of both components is described by fluorescence anisotropy, *r,* which is defined by the equation 1.6.

Equation 1.6

$$r = \frac{I_{\parallel} - I_{\perp}}{I_{\parallel} + 2I_{\perp}}$$

Each fluorophore has an excitation and emission dipole with a fixed relative orientation that is characteristic to that fluorescent molecule. It can be shown that the fluorescence anisotropy, *r*, for a molecule with an excitation dipole orientated with respect to the excitation polarization by angle θ is given by the equation 1.7.

Equation 1.7

$$r = \frac{3\ \cos^2\theta - 1}{2}$$

A phenomenon referred to as photoselection results from an absorption probability proportional to $\cos^2\theta$ such that not all molecules are excited with equal probability. If the molecules are isotropically distributed, the fluorescence anisotropy r is equal to 0.4 (Lakowicz 2006). This is only valid if excitation and emission dipoles are parallel and there are no other means of depolarization. Fluorophore rotation results in a time-dependant anisotropy after excitation with an ultrafast laser pulse given by the equation 1.8.

Equation 1.8

$$r(t) = \frac{I_{\parallel}(t) - I_{\perp}(t)}{I_{\parallel}(t) + 2I_{\perp}(t)} = r_0 e^{\frac{-t}{\Theta}}$$

If the molecule can be represented as a rotating sphere then Θ is given by the equation 1.9 and the time-dependant anisotropy decays with a mono-exponential profile.

Equation 1.9

$$\Theta = \frac{\eta V}{RT}$$

Where η is the viscosity, T is the temperature, R is the universal gas constant and V is the volume of the rotating unit. This explains how anisotropy decays can be used to report on fluorophore size, solvent viscosity, molecular conformations, and why anisotropy studies are widely used in protein studies (Lakowicz 2006).

1.5 Fluorescence lifetime measurement techniques

Fluorescence lifetime can be measured using two distinct techniques characterized by their fluorescence excitation and detection strategies. Frequency-domain fluorescence lifetime determination uses periodically modulated excitation light, usually a sinusoidal waveform together with periodic modulation, again usually sinusoidal, of the gain of the detector. The lifetime information is derived from the difference in phase and amplitude between the excitation signal and the demodulated fluorescence emission. The technique employed in our work is time-domain fluorescence lifetime determination which uses ultra-short laser pulses and the detection of fluorescence light evolving over time through the time-correlated single photon counting (TCSPC) approach. Time-domain techniques offer higher temporal resolution although historically were more expensive than frequency domain systems owing to the need for ultrafast lasers and complex detection devices, although the relative cost of these technologies is coming down.

1.5.1 Time-domain fluorescence lifetime determination

Time-domain fluorescence lifetime measurement can be categorized as either photon-counting based techniques, such as time-correlated single photon counting (TCSPC) - in which the time of arrival of single photons is recorded with respect to the excitation pulse - or sampling techniques - in which the fluorescence emission is recorded in two or more time gates following the excitation signal. Photon counting techniques are considered to offer greater temporal precision at the expense of acquisition time, given that detection is typically limited to one photon per excitation period and is made on a point-by-point basis, which can make it very time-consuming for imaging. Wide-field time-gated methods offer faster acquisition times, allowing simultaneous

acquisition over multiple pixels. This may be an acceptable trade-off where faster acquisition times would represent considerable advantage e.g. for clinical imaging modalities, such as endoscopy.

1.5.2 Time-correlated single photon counting

Time-correlated single photon counting (TCSPC) is the most common and well-established method for fluorescence lifetime measurements. In simple terms, it works by exciting the sample with high-repetition rate laser excitation pulses and detecting the arrival time of single photons of fluorescence with a fast photomultiplier tube (PMT). It is based on the principle that, at sufficiently low fluorescence rates, individual photons can be detected and their respective arrival times compared to the laser excitation pulse can be measured. TCSPC uses ultra-short excitation pulses at high repetition rates (MHz frequency), photon-counting detectors - typically photomultiplier tubes (PMT) - and sophisticated high-speed counting electronics to accurately allocate a time of arrival to each detected fluorescence photon. The TCSPC module determines the time delay, Δt, between the excitation of the fluorophore (i.e. the laser pulse) and the detection of the emitted fluorescence photon. After many photon detection events a histogram can be constructed depicting the probability of photon detection as a function of time (see figure 1.2) from which the fluorescence lifetime parameters can be calculated by fitting an exponential function to the acquired histogram.

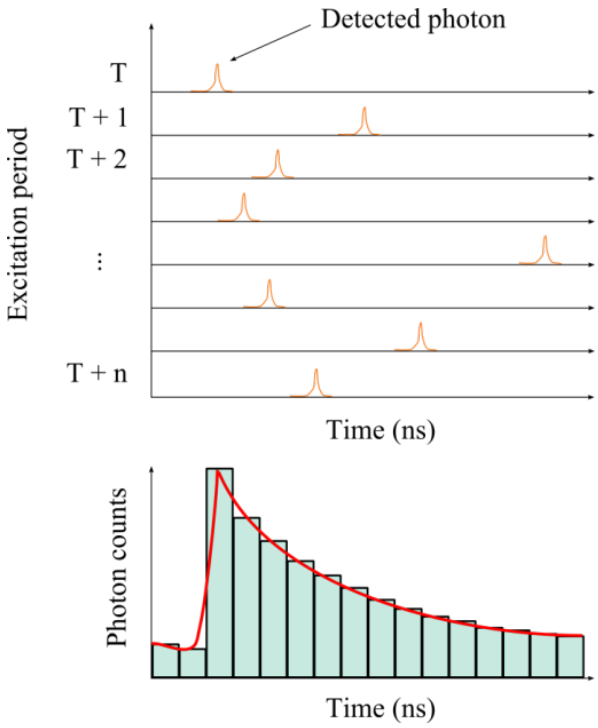


Figure 1.2 Schematic representation of TCSPC method. Photons are detected one at a time relative to the excitation pulse (T, T+1, ... T+n) and a histogram of photon arrival times is constructed, to which can be fitted an exponential function to the decay determine the lifetime parameters. (After (Becker 2010))

The TCSPC method offers high photon efficiency at low count rates, high temporal precision (down to 3 ps at 80 MHz) and its accuracy means that it is widely regarded as a gold standard for determination of fluorescence lifetime. (Becker et al. 2004; Lakowicz 2006) The major limitation is the relatively low count rate and consequently the longer acquisition times imposed by the dead times of the electronics (typically 100 ns) following the detection of a single photon. This dead time reduces the effective detection efficiency of the system as the count rate increases. There is also the need to reduce the probability of more than one photon being detected following a laser pulse and this necessitates that the fluorescence signal needs to be kept at a low level (ideally less than 1 – 5 % of the laser repetition rate) to minimise the probability of multiple photons arriving during the detection period. This is a problem because photons arriving closer to the excitation pulse are preferentially counted by the TCSPC compared to late-arriving photons. The resultant 'photon pile up' biases the fluorescence lifetime measurements towards shorter values. Therefore, the intensity of the laser excitation needs to be adjusted for a given type of sample such that the photon detection rate obtained is below 1-5% of the laser repetition rate.

Laser scanning fluorescence microscopes utilising TCSPC collect fluorescence lifetime on a pixel-by-pixel basis and typically have long image acquisition times compared to wide-field fluorescence lifetime imaging (FLIM) technologies. TCSPC can also be implemented for single-point detection, which considerably decreases acquisition time by integrating the fluorescence intensity arising from a volume of a sample, e.g. using a point-probe approach when spatial

information is not required. (Coda et al. 2014; Thompson et al. 2012; Thompson 2012; Chorvat & Chorvatova 2006)

1.6 Analysis of fluorescence lifetime data

The analysis of fluorescence lifetime in this thesis was undertaken using a non-linear least squares fitting routine from MATLAB (lsqnonlin function, R2011b, The Mathworks Inc., USA) implemented in custom software written by our group. The autofluorescence decays from biological tissue are complex and fitted with a multi-exponential decay model. There are a number of methods to analyse the fluorescence decay and calculate the lifetime: rapid lifetime determination (RLD); Laguerre expansion, phasor analysis and most commonly, and as used in our work, non-linear least squares fitting to minimise the goodness of fit chi-square value (χ^2) expressed as indicated in equation 1.10, where n is the number of bins in the decay, I is the measured intensity at each time delay, and I_{model} is the fit model convolved with the measured instrument response function (IRF).

Equation 1.10

$$\chi^2 = \sum_{k=1}^{n} \frac{(I(t_k) - I_{model}(t_k))^2}{I(t_k)}$$

It is important to note that the number of exponential components used in the fitting model is not necessarily the same as the number of fluorophores giving rise to the fluorescence signal, especially in complex samples such as biological tissue. This is because problems with signal-to-noise ratio are encountered as the number of lifetimes attempted to be fitted increases. Köllner *et al* (Köllner & Wolfrum 1992) calculated that only 185 photons would be required to resolve a single exponential lifetime of 2.5 ns with 10% accuracy using 8 ns as the acquisition window and 256 bins. A double exponential decay with two individual lifetimes of 2 ns and 4 ns using the same other parameters would require 400,000 photons to achieve the same accuracy. Therefore, the fluorescence decay used can depend on the number of photons collected during the acquisition.

1.7 Autofluorescence and tissue spectroscopy of the heart

As discussed above, there are a number of ways to quantify fluorescence and these have been widely utilized in biomedical research. Contrast in biological samples can be either achieved by employing exogenous markers that tag specific molecules in a specimen or by exciting intrinsically fluorescent molecules within the sample. There are a number of such molecules occurring naturally in tissue. This phenomenon is referred to as autofluorescence. According to their chemical structure and biological function, these autofluorescent compounds can be divided in amino acids (tryptophan, tyrosine and phenylalanine); proteins e.g. collagen; protein cofactors

e.g. NADH; and pigments e.g. melanin. Commonly occurring autofluorescent molecules in the heart include molecules involved in fundamental biological mechanisms, including energetics cofactors NADH and flavoproteins FAD, and structural extracellular matrix proteins such as collagen and elastin. One of the key advantages of using autofluorescence is that it avoids the use of exogenous compounds, which could be toxic if used in vivo, or could affect the system under investigation. As such autofluorescence has been increasingly used as a diagnostic tool to provide label-free differentiation between healthy and diseased states. (Tang et al. 1989; Pradhan et al. 1995; Mycek et al. 1998; P. A. A. De Beule et al. 2007; Thompson et al. 2012; Coda et al. 2014; Gill et al. 2003; Konig et al. 2004; Chorvat, Kirchnerova, Cagalinec, Smolka, a Mateasik, et al. 2005; Li & Xie 2005; Yong et al. 2006; Skala, Riching, Gendron-Fitzpatrick, et al. 2007a; Skala, Riching, Gendron-Fitzpatrick, et al. 2007b; Butte et al. 2013; Manning et al. 2013; Shah et al. 2014)

There has been increasing focus on the application of optical techniques to further biomedical research itself as well as on the development of potential diagnostic tools for medical applications and clinical diagnosis. (Marcu 2012; Marcu 2010; Lakowicz 2006; Schneckenburger 1992) The motivation for such instruments is the potential to provide immediate biochemical, morphological or physiological information to detect early alterations in tissue in disease states without the introduction of exogenous probes and, ideally, to conduct a 'virtual biopsy' of the tissue without the delays or risks that surgical biopsy necessitates.

There are multiple sources of autofluorescence within a cardiac specimen, both within the cell, e.g. NAD(P)H or FAD, or outside within the extracellular matrix of the tissue (e.g. collagen and elastin). As such the autofluorescence emission spectrum of cardiac tissue is complex. The multiple fluorophores that may be present are discussed below.

1.7.1 Amino acid autofluorescence

Three aromatic amino acids can contribute to the intrinsic autofluorescence of proteins in which they are present: tyrosine, tryptophan and phenylalanine.(Teale & Weber 1957) Phenylalanine has the lowest quantum yield of approximately 3 % (Lakowicz 2006) and absorbs and emits at the shortest wavelengths and so it has a negligible contribution to the total signal in the range typically used for excitation (between 280 and 300 nm). Tryptophan and tyrosine are sensitive to their environment, particularly in terms of their anisotropy and fluorescence lifetime, therefore these properties are harnessed to study protein structure and dynamics, e.g. NADH conformation upon binding to malate dehydrogenase in solution. (Torikata et al. 1979) However the short wavelengths necessary to excite these molecules means that their use *in vivo* might be limited practically owing to concerns regarding malignancy with short wavelength excitation light.

1.7.2 Nicotinamide adenine dinucleotide – NAD(P)H

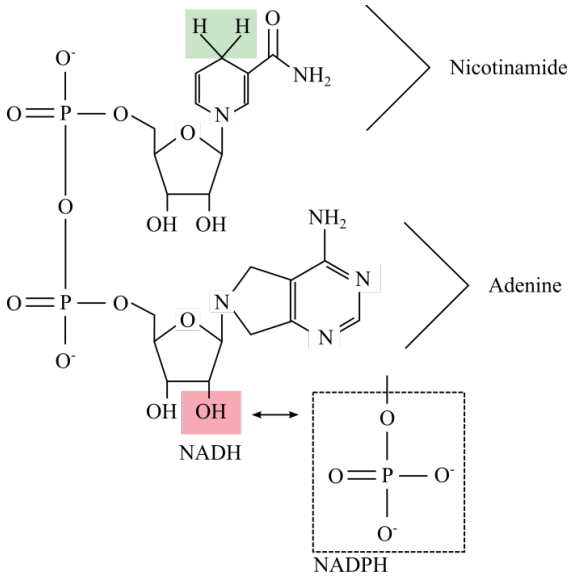


Figure 1.3 Chemical structure of NADH. In the oxidized form NAD+, the two protons shown in green are lost. In NADP+/NADPH the hydroxyl group shown in red is replaced by the phosphate group shown in the dashed box. After (Lakowicz 2006)

The structure of reduced nicotinamide adenine dinucleotide (NADH) is shown in figure 1.3. NADH and its analogue NADPH are both carrier molecules for high-energy electrons and in the absence of the electrons the compounds are in an oxidised state (NAD+ and NAPD+ respectively). At the wavelengths used in biomedical research (i.e. excitation > 340 nm) it is only in their reduced form that they demonstrate fluorescence. When free in solution they are considered to be identical in terms of their photo-physical properties as their fluorescence comes from the nicotinamide ring present in both NADH and NADPH and therefore they have the same spectra, lifetime and anisotropy and therefore it is common to use the term NAD(P)H.

NADH, as explained above, has an essential anabolic role in the generation of ATP in the cell. NADPH is involved catabolic processes including reduction of hydrogen peroxide, processes in the cytochrome p450 monooxygenase system, leucocyte phagocytosis and synthesis of nitric oxide.(Babior 1999) 95% of ATP generation for cardiomyocyte contraction comes from dehydrogenation of NADH from Complex I(Chorvat & Chorvatova 2009) therefore NADH fluorescence represents an important signal in following the metabolic state of the heart.

Owing to these different roles as oxidizing agent/electron acceptor and reducing agent/electron donor respectively, the intracellular ratio of NAD+/NADH is kept high (i.e. higher levels of NAD+), whereas that of NADP+/NAPDH is kept low (i.e. higher levels of NADPH).(Alberts et al. 2008) The concentration of NAPDH in the cells is 5 times lower than that of NADH, and it has been shown to have a lower quantum yield, and therefore fluorescence intensity (in mitochondria at least) is

therefore considered to represent only a small fraction of the cell's total NAD(P)H fluorescence.(Chorvat & Chorvatova 2009)

There are two peaks in the light absorption spectrum of NADH at ~270nm and ~350nm (in the ultraviolet spectrum) and the emission fluorescence is in the range of 410-490nm, with a peak at 450nm. The fluorescence decay of NADH in solution displays a bi-exponential decay. The ratio of shorter: longer component (τ1: τ2) lifetime component is approximately 0.8:0.2 in studies (Vishwasrao et al. 2005; Visser & van Hoek 1981; Kierdaszuk et al. 1996)). The shorter lifetime component $\tau 1$ has a lifetime of approximately 0.3ns (0.25 – 0.35ns in studies(Kierdaszuk et al. 1996; Vishwasrao et al. 2005; Visser & van Hoek 1981)) and the longer component $\tau 2$ has a lifetime of approximately 0.7ns (0.69 – 0.82ns in studies(Kierdaszuk et al. 1996; Vishwasrao et al. 2005; Visser & van Hoek 1981)). Because reduced nicotinamide mononucleotide (NMNH) has a single exponential decay similar to the short component τ1 of NADH (τ 0.29ns at 2°C) – it is inferred that the bi-exponential decay NADH is as a result of two single exponential decays of a folded and unfolded conformation of the molecule with the shorter component due to the unfolded form and the longer component due to the folded form. To complicate matters further, when NADH is bound to a protein, its photo-physical properties change. NADH interacts with a vast number of proteins. For example, upon binding to lactate dehydrogenase complex (which converts pyruvate to lactate in anaerobic metabolism, and lactate to pyruvate in the liver(Alberts et al. 2008)) there is a shift of the fluorescence towards UV (shorter wavelength) and increase in the intensity of fluorescence.(Vellick 1958) Whereas, interaction with glyceraldehyde-3-phosphate dehydrogenase (which catalyses the sixth step of glycolysis (Alberts et al. 2008)) causes a shift to longer wavelength and a decrease in the intensity of the fluorescence. The lifetimes of NADH bound to proteins are longer than unbound, and the lifetimes are different for each given protein – within a range of 0.8 ns – 6 ns. This means that in practice the NADH autofluorescence signal from cardiac tissue consists of contributions from multiple NADH-protein interactions, each with their own specific lifetime. Only a limited number of exponential decay parameters can be resolved from data acquired *in vivo* and typically the cellular signal is approximated to a bi-exponential model, where the interpretation is made that the shorter component ($\tau 1$) represents the unbound or 'free' NADH, whereas the longer component represents the protein-'bound' NADH.

1.7.3 Flavin adenine dinucleotide – FAD

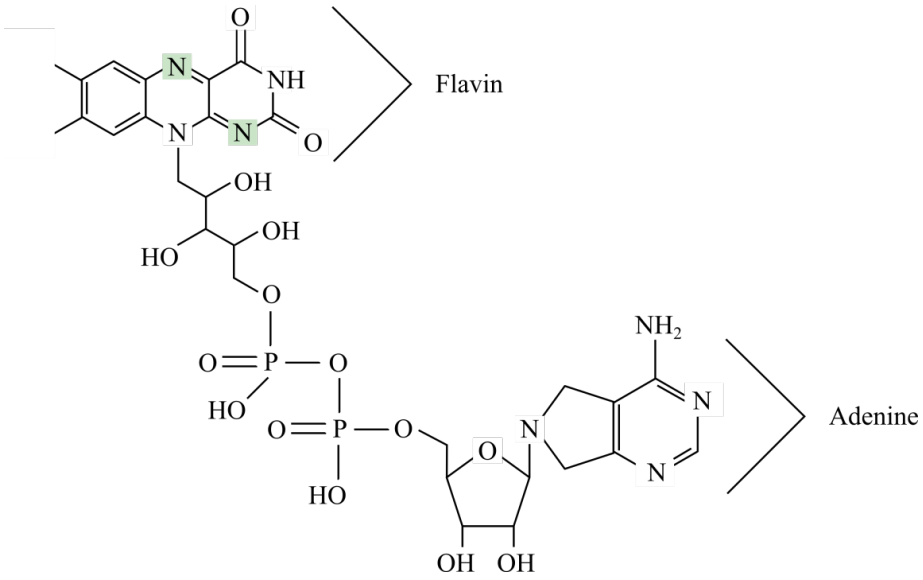


Figure 1.4 Chemical structure of FAD. The reduced form, $FADH_2$ has a proton couple to the nitrogen atoms shown in green. After (Lakowicz 2006)

The structure of flavin adenine dinucleotide (FAD+) is shown in figure 1.4. FAD+ plays an important role in oxidative phosphorylation as an electron-carrier. The reduced form is generated in the Krebs (citric acid) cycle as well as by beta-oxidation of fatty acids (which is an alternative mechanism to generate substrate for the citric acid cycle (Alberts et al. 2008)). It is the oxidized FAD+ form, which is considered the 'fluorescent' form, as the reduced form, while technically displaying fluorescence, has a considerably lower quantum yield. FAD+ has a wide absorption spectrum between 200-500nm and a narrower emission spectrum around a peak at 520nm. The fluorescence decay of FAD+ is generally believed to be bi-exponential with a shorter component $\tau 1$ of 0.3ns (28%) and a longer component $\tau 2$ of 2.8ns (72%). FAD+ lifetimes are reduced upon interaction with proteins thought to be due to photoelectron transfer.

FAD in aqueous solution has two conformational states: a folded conformation; and a more fluorescent open conformation. The difference in fluorescence properties results from whether the isoalloxazine and adenine aromatic rings are in close proximity as the adenine ring quenches the fluorescence. The two conformations have different fluorescent lifetimes – several picoseconds for the folded conformation and 2-3 ns for the open conformation.(Islam et al. 2013a)

The origin of fluorescence of FAD is not directly related to FAD's total concentration in that compartment in the cell. FAD is principally found bound to other enzymes in the mitochondrial matrix (as so called 'flavoproteins') however for the majority of these compounds, such as succinate dehydrogenase, the fluorescence is quenched by the binding partner.(Georgakoudi & Quinn 2012) It is thought that 50% of the fluorescence comes from LipDH-containing complexes

that reduce FAD and a further 25% is produced by electron transfer flavoprotein which serves as an intermediate electron carrier during the β-oxidation of fatty acids.(Cicchi & Pavone 2011) FAD lifetime in buffer solution did not change with changes in pH (range 5-9) (Islam et al., 2013a) however HeLa cells measured with different intracellular pH (range 5-9) showed, that although the shape of the spectrum remained the same, the average fluorescence lifetime shortened as the intracellular pH increased, suggesting that that change is caused by changed interaction between FAD and the surrounding functional groups in a protein. (Islam et al. 2013a) In contrast to NADH, FAD's fluorescence lifetime decreases upon protein binding such that when the autofluorescence lifetime is fitted to a double exponential decay, the shorter lifetime is attributed to the protein-bound form, whilst the longer lifetime is associated with free FAD.

1.7.4 Extracellular matrix autofluorescence – collagens and elastins

Collagen is a structural protein found throughout the body, with 28 types of collagen identified in vertebrates, although predominantly it is fibrillar collagen (types I, II, III, V) that makes up 80-90% of the collagen in the body.

Collagen molecules consist of three polypeptide chains arranged into a helix (α-chains), the composition of which varies by anatomical location and can change during disease progression, healing and aging. The fluorescence of collagen arises from the aromatic amino acids (tryptophan, tyrosine and phenylalanine) in the α-chains and from the fluorescent chemical bonds that crosslink the simple molecules into superstructures.(Eyre et al. 1984) Fibrils are strengthened by cross-links catalysed by enzymes such as lysyl oxidase (LOX) which can be overexpressed in states of myocardial injury.(White et al. 2012) Cross-link formation can also occur due to glycation. Collagen fluorescence is highly attributable to aromatic amino acids and crosslinks, such as lysyl pyridinoline (an enzymatic crosslink), which has an excitation spectrum peak at 325nm and emission spectrum peak at 400nm. Other crosslinks include vesperlysine and crossline. Previous work within our group (Manning 2006) and by others (Marcu et al. 2000) has demonstrated a great heterogeneity in excitation and emission spectra of collagens from different sources, presumably because of the great difference in crosslinking in a given situation.

The cardiac interstitium is a complex space in which cardiac cells, vessels, nerves are embedded in an extracellular matrix. The normal cardiac extracellular matrix is composed primarily of collagen scaffolding, which in humans is approximately 80% type 1 and 10% type 3, and ground substance of proteoglycans and glycosaminoglycan as well as immune cells and fibroblasts.(White et al. 2012) One of the hallmarks of cardiac pathology is expansion of the interstitium - usually through development of fibrosis, which is mediated through a number of processes including an increase in collagen abundance with relatively larger diameter higher-tensile type I collagen and increased fibre cross-linking.(Querejeta et al. 2004)

Elastin is another structural protein that functions to achieve elasticity of tissues such as arteries and is therefore found in the heart. Similarly, to collagen the fluorescence is predominately attributable to the crosslinks between molecules. (Richards-Kortum & Sevick-Muraca 1996) The tricarboxylic triamino pyridium derivative is thought to be a major contributor to the fluorescence, as well as the tyrosine and phenylalanine at shorter UV excitation wavelengths. (Gray et al. 1973)

1.8 Diffuse reflectance of cardiac tissue

The diffuse reflectance spectrum of a given tissue is dependent on the absorption spectra of the individual chromophores present in that tissue and the scattering properties of the tissue. In the heart, as a muscle, the dominant chromophores are myoglobin in the myocytes, and haemoglobin present in the blood circulating in the vessels, and within the cavity of the atria and ventricles. Other chromophores expected to contribute include the mitochondrial cytochromes such as cytochrome c. The absorption spectra of these three chromophores are shown in figure 1.5. Oxygenated myoglobin has a double peak profile with a local maxima at ~544 nm and ~578 nm and minimum at ~560 nm. In contrast, in the absence of oxygen, deoxygenated myoglobin exhibits a broader spectral profile with a single maximum at ~558 nm.(Schenkman et al. 1997) Haemoglobin has a very similar double peak profile in the oxygenated form and a broader profile in the deoxygenated form but at slighter shorter wavelengths. Reduced cytochrome c has a very well defined peak at 550 nm, whereas a much broader profile in the oxygenated state. (Arai et al. 1999)

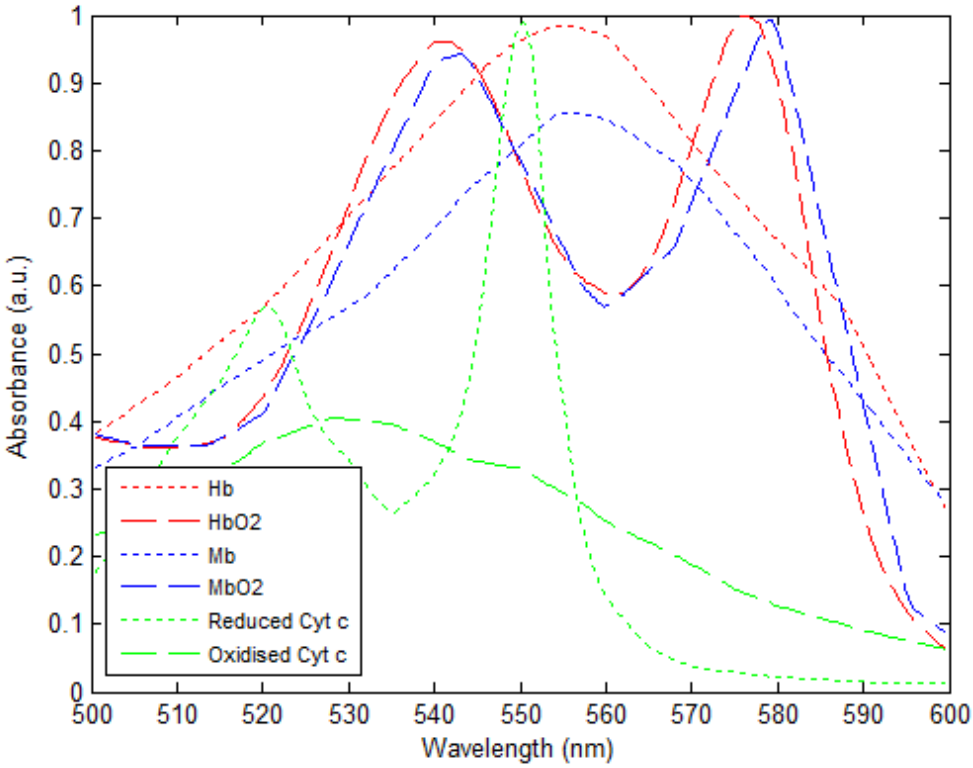


Figure 1.5 Absorbance spectra of key chromophores in cardiac tissue – haemoglobin (Hb), myoglobin (Mb) and cytochrome c in their oxidized and reduced states. Paired oxidized and reduced state of each molecule scaled by normalization of the larger of each curve to 1. Absorption curves obtained from literature: Human Hb and HBO2(Prahl 1999)**, horse cytochrome c** (Arai et al. 1999)**, horse Mb and Mb02** (Margoliash & Frohwirt 1959)**.**

1.9 Structure, physiology and energetics of the heart in health

The heart is a muscle pump, working continuously to circulate blood around the body in two circulations – the high-pressure systemic circulation; and the low-pressure pulmonary circulation. It consists of four chambers: two atria and two ventricles. The venous return of deoxygenated blood from the body is via the superior and inferior venae cavae and the coronary sinus to the right atrium; the blood flows from the right atrium through the tricuspid valve into the right ventricle, from where it is pumped to the lungs at low pressure through the pulmonary arteries. The blood is oxygenated in the lungs and is returned to the left atrium via the pulmonary veins. This oxygenated blood flows through the mitral valve to the left ventricle to be pumped at higher pressure via the aorta and onwards to perfuse the whole body through the systemic circulation. In the normal heart in the absence of shunts or pulmonary hypertension, the left ventricle has a considerably greater wall thickness compared to the right ventricle (~10 mm compared to ~2 mm) to generate the higher pressures required for the systemic circulation. (Camm et al. 2009)

The wall of the heart consists of three layers, the outer epicardium, the mid-myocardium and the inner endocardium, representing 3 different planes from embryological development. The myocardium consists of the individual contractile cells myocytes, which are central to the contractile function and viability of the heart, embedded in an extracellular matrix (ECM) consisting of collagen types I and III responsible for supporting the muscle cells and vessels in a framework as well as providing tensile strength (Weber 1989). Alterations in the ECM collagen network are important features of myocardial disease. In a healthy heart, there is a fine balance between collagen synthesis and re-uptake in the ECM that maintain the proper functioning of the heart. Impairment of this process leads to changes in the concentration of collagen in the tissue, which can affect the mechanical properties of the heart (Cleutjens et al. 1995).

The continuous contractile function of the heart is a process with an extraordinarily high energy demand. The contractile apparatus utilises approximately 70% of the ATP produced by the heart, while the remaining 30% is used in regulating cellular processes such as ion pumps (Gibbs 1978). The mechanism by which the heart converts an electrical impulse into a mechanical contraction is termed excitation-contraction coupling. During a cardiac action potential, Ca^{2+} enters the cell via L-type Ca^{2+} channels and activates the ryanodine receptors (RyRs). This triggers an even greater Ca^{2+} release from the sarcoplasmic reticulum (SR) – so called calcium-induced calcium release. This Ca^{2+} is therefore available for contraction at the myofilaments. In diastole, the SR takes back up the Ca^{2+}, and an amount of Ca^{2+} equal to that which entered the cell via the L-type Ca^{2+} channels is eliminated by Na+/Ca2+ exchangers to maintain equilibrium. There is some interspecies variation in the proportion of Ca^{2+} from these two sources (release from the SR versus entry via L-type Ca^{2+} channels) from around 70/30 % in humans to around 90/10 % in rats. (Bers 2006; Bers 2002) Ca2+ interacts with the myofilament contractile apparatus and ATP to induce contraction of the cardiomyocyte. Excitation-contraction coupling consumes large amounts of free energy in the form of ATP. A single heartbeat consumes ~2 % of the available cellular ATP, and the entire ATP pool within a cardiomyocyte is turned over on a minute-by-minute basis. (Balaban 2002)

Mitochondria participate in a huge number of metabolic reactions in the cell including generation of reactive oxygen species, but their primary function is to generate the energy supply for the processes of the cell through the phosphorylation of ATP. ATP is regenerated from ADP by oxidative phosphorylation at the electron transport chain in the inner mitochondrial membrane. The electron carriers, NADH and $FADH_2$, the main products of the Krebs (citric acid) cycle as well as other metabolic pathways, deliver electrons to the electron transport chain which, via sequential red-ox reactions through the electron transport chain, leads to proton translocation across the inner mitochondrial membrane to generate a proton gradient. The established proton gradient is the driving energy force for ATP production in ATP synthase as summarized in figure 1.9. (Bers 2002)

The heart can produce ATP from a number of different substrates including fatty acids, glucose, amino acids or lactate (William C Stanley et al. 2005; Huss & Kelly 2005). The preferred metabolic pathway to produce ATP is dependent on the availability of the substrates in the blood and in the cells, on coronary flow, and on inotropic state. (William C Stanley et al. 2005) Generally in the human heart in the presence of sufficient oxygen, the Krebs cycle is fuelled by energetic intermediates generated by utilizing fatty acids as substrates, which represents around 70% of the energy source. To a lesser extent glucose, lactate and amino acids can be used. While fatty acids provide the highest energy yield per molecule of substrate metabolized through β-oxidation, they are less efficient than glucose with regard to ATP production per molecule oxygen (O_2) consumed, requiring 15 % more O2 per mole of ATP generated from fatty acids compared to glucose. (Rosano et al. 2008)

Fatty acids cross the cardiomyocyte cell membrane by specific transporters to undergo fatty acid oxidation (FAO) to utilize the energy they contain. Key enzymes include fatty-acyl-CoA synthetase and carnitine palmitoyltransferase I (CPT-1), which together add a coenzyme A moiety to the fatty acids and convert them to a long-chain acylcarnitine to be transported across the inner mitochondrial membrane. The remaining fatty acids not used are stored in lipid droplets in the cytosol for use latter. Carnitine palmitoyltransferase I (CPT-1) is the rate-limiting step in fatty acid oxidation and the process is regulated by inhibitory feedback responses to acetyl-CoA, $FADH_2$, and NADH.(Nickel et al. 2013) Other inputs, e.g. β-adrenergic stimulation, can increase FAO to match energy supply and demand. (Zhou et al. 2008)

A decrease in FAO is associated with an increase in glucose uptake facilitated by diffusion via the glucose transporters GLUT1 and GLUT4, in part regulated by insulin. Inside the cell, glucose is phosphorylated to glucose-6-phosphate to enter glycolysis. Pyruvate, the end product of glycolysis, is taken up into mitochondria via the mitochondrial pyruvate carrier (Herzig et al. 2012) and is converted to acetyl-CoA by pyruvate dehydrogenase (PDH) to enter the Krebs cycle. Glucose oxidation is primarily regulated by the activity of pyruvate dehydrogenase (PDH) which itself is dependent on feedback loops dependent on its products and substrates (Sugden & Holness 2003) and importantly Ca^{2+} concentration.

The balance between glucose- and fatty acid oxidation pathways are thus in balance via feedback loops as initially described by Randle in 1963, subsequently called the “Randle cycle”. Simplistically, FAO inhibits glucose uptake, the presence of glucose and insulin inhibits FAO and the presence of acetyl-CoA has common negative feedback of both FAO and glucose utilization.(Nickel et al. 2013)

The heart needs to have the ability to match energy supply and demand as the demand for ATP consumption changes constantly depending on the stresses placed upon the heart. Ca^{2+} and ADP concentration are two major factors regulating oxidative phosphorylation. (Cortassa et al. 2009) Higher ADP concentration means more ATP production at ATP synthase, increasing electron

transfer chain activity and therefore oxidation of NADH and FADH2. Increased Ca^{2+} stimulates PDH and the rate-limiting dehydrogenases in the Krebs cycle to increase the rate of NADH and $FADH_2$ reduction. Together these factors maintain a constant redox state of $NADH/NAD^+$ and $FADH_2/FAD^+$ in the physiological state.

The heart is essentially an aerobic organ, with very little capacity to work sustainably under anaerobic conditions, and thus an adequate supply of oxygen and energy supply is essential to maintain function of the cardiomyocytes (William C Stanley et al. 2005). Indeed, impairment in the energy production-uptake regulation is thought to be associated with progressive loss of myocardial function that is seen in heart failure disease states. (Neubauer 2007) In addition, the heart muscle is damaged extremely quickly by ischaemia during a myocardial infarction when the blood supply to the heart is interrupted.

As mentioned previously in the healthy adult human heart, if the oxygen supply is sufficient, the dominant source of energy is fatty acids, oxidised in the mitochondria via the beta-oxidation pathway generating the acetyl coenzyme A. This corresponds to approximately 70% of the total ATP production in the myocardium (Doenst, Nguyen & E Dale Abel 2013). The remaining energy is mainly produced by oxidation of glucose by means of glycolysis in the cytosol and further breakdown of its by-product pyruvate in the pyruvate-dehydrogenase complex (PDC), which occurs in the inner mitochondrial membrane. The product of beta-oxidation and glycolysis (and PDC) is acetyl Coenzyme A (acetyl-CoA), which enters the Krebs (citric acid) cycle. In the Krebs cycle, FAD and NAD^+ are reduced to produce $FADH_2$ and NADH, which will serve as electron donors in the electron transport chain (ETC). The movement of electrons through the protein complexes of the ETC promotes the movement of protons (H^+) from the mitochondrial matrix into the intermembrane space. As a result, a differential electrical charge is established across the inner mitochondrial membrane, which drives ATP synthesis in oxidative phosphorylation.

If the oxygen supply is not adequate, e.g. during maximally-intense physical activity, a small amount of ATP can be created from the glycolysis of glucose into pyruvate, which in turn is converted into lactate by lactate dehydrogenase (LDH). The lactate accumulates and can be converted back to pyruvate subsequently by the liver in a process that consumes energy. The anaerobic generation of ATP produces energy at a faster rate than through the oxidative pathway and it allows the cell to temporarily transfer high-energy substrates in the absence of oxygen, albeit by creating an oxygen debt that requires repayment subsequently.

Cellular metabolism can be divided in three phases:

1) production of acetyl-CoA
2) citric acid (Krebs) cycle
3) respiratory chain, electron transport chain and oxidative phosphorylation.

In aerobic metabolism the production of acetyl-CoA is the first step in the pathways leading to the production of ATP in the mitochondria. Acetyl-CoA is derived primarily from the breakdown of fatty acids by beta-oxidation or the breakdown of glucose by glycolysis.(Lodish et al. 2008; Alberts et al. 2008)

Beta-oxidation is the process by which long fatty acid chains are broken down to generate acetyl-CoA to feed into the Krebs cycle. Initially, 2 ATP molecules are required to convert the fatty acid to a fatty acyl within the cytosol of the cell. The fatty acyl is then transported into the mitochondria to be further oxidised within the mitochondrial matrix by a series of sequential reactions that ultimately produce a two-carbon fragment in the form of an acetyl-CoA. The remaining fatty acid chain, two carbons shorter, will go through the beta-oxidation pathways again and the process continues until all carbons are converted into acetyl-CoA. Hence the number of acetyl-CoA molecules generated per mole of fatty acid depends on the number of carbon atoms in the fatty acid undergoing oxidation. Additionally, for each beta-oxidation cycle, one molecule of NADH and another of $FADH_2$ are formed that can be utilised in the electron transport chain as electron donors to produce ATP. The beta-oxidation pathway is summarised in figure 1.6.

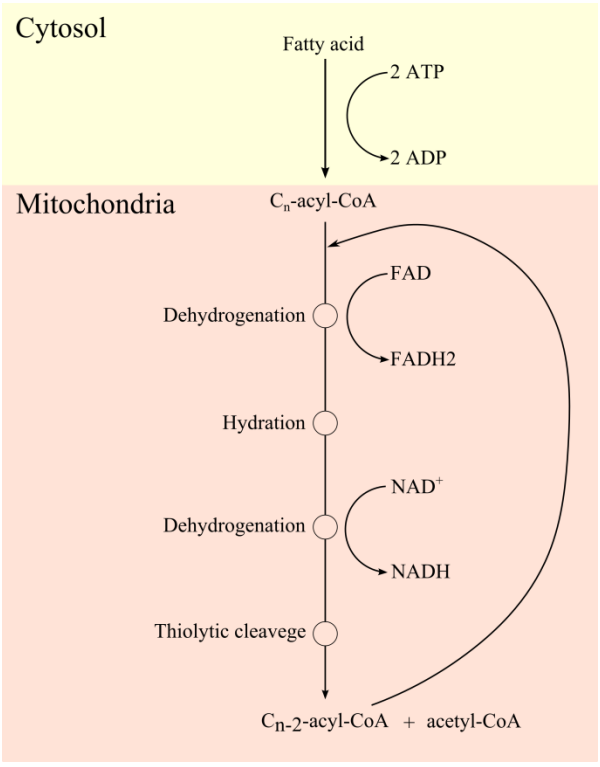


Figure 1.6 Simplified schematic beta-oxidation pathways of a fatty acid, where *n* represents the number of carbon atoms in the fatty acid. The cycle ends when all carbons are converted into acetyl-CoA, i.e. with n = 2. For each cycle, one molecule of NADH and $FADH_2$ are produced. Reproduced with permission from Dr João Lagarto.

Glycolysis is the metabolic pathway by which one mole of glucose is converted to two moles of pyruvate, with the temporary net production of 2 moles of ATP. Unlike beta-oxidation, glycolysis

occurs exclusively in the cytosol and does not require the presence of oxygen. Conversion of glucose to pyruvate occurs in two distinct phases: firstly, a glucose molecule ($C_6H_{12}O_6$) is phosphorylated at the expense of two molecules of ATP and cleaved to form two three-carbon molecules (glyceraldehyde-3-phosphate, $C_3H_7O_6P$), and secondly these two molecules undergo a series of reactions to generate energy-rich compounds, which then transfer the high-energy phosphate to ADP, yielding ATP. The by-product of these reactions is pyruvate. Overall, the net yield of glycolysis per molecule of glucose degraded is two molecules of ATP and two molecules of pyruvate. In addition, two molecules of NADH are generated during the energy gain phase, which can be used in the electron transport chain in the presence of oxygen. In aerobic conditions, the pyruvate derived from glycolysis is transported into the mitochondria where a series of oxidative decarboxylation reactions, catalysed by pyruvate dehydrogenase, generate acetyl-CoA, which can be fed into the citric acid cycle. This is summarised in figure 1.7.

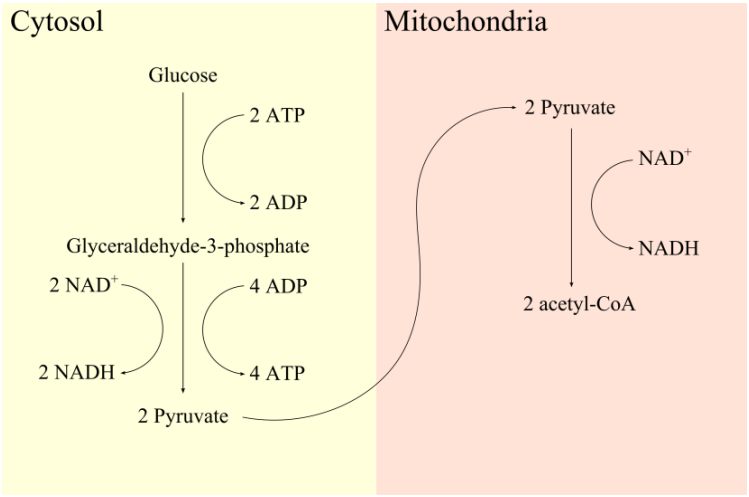


Figure 1.7 Simplified schematic of the aerobic glucose metabolic pathway to generate acetyl-CoA. Glycolysis occurs in the cytosol of the cells (left) and pyruvate is oxidised to acetyl-CoA in mitochondria (right). Reproduced with permission from Dr João Lagarto.

The Krebs cycle is the second stage of the metabolic pathways that lead to production of ATP and it occurs in the mitochondrial matrix. It consists of a number of decarboxylation, oxidation and hydration reactions taking a six-carbon complex, formed from acetyl-CoA and oxaloacetate, and converting it to a four-carbon molecule, resulting in the release of CO_2, as well as three molecules of NADH and one molecule of $FADH_2$ to be used as electron donors in the electron transport system of the respiratory chain.

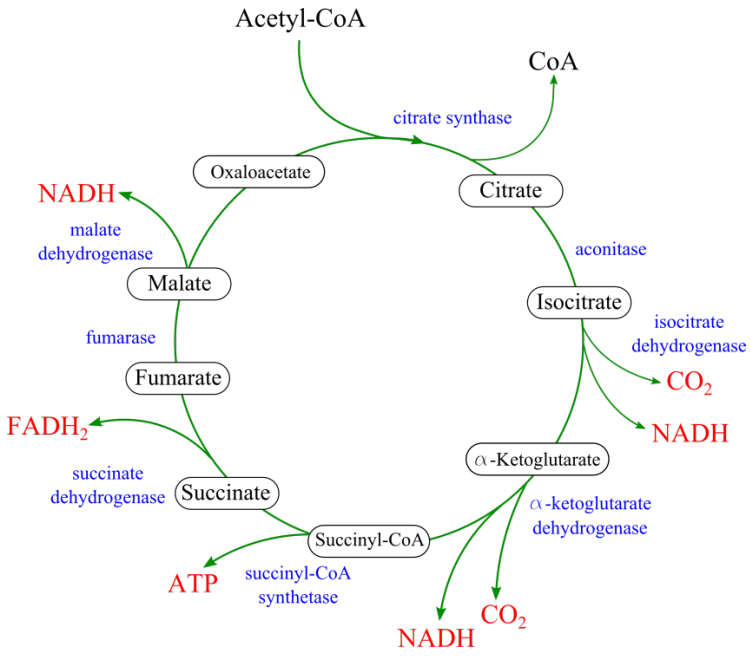


Figure 1.8 A schematic representation of the Krebs (citric acid) cycle, including by-products of electron carriers and CO2 (in red) and enzyme complexes that catalyse each reaction (in blue). Reproduced with permission from Dr João Lagarto.

The initial reaction is between acetyl-CoA and oxaloacetate to form a six-carbon complex, catalysed by citrate synthase. The resultant molecule has an unstable CoA group that is spontaneously hydrolysed, leaving citrate. The second reaction is catalysed by aconitase with isomerisation of citrate, by successive dehydration and hydration. This results in the delocalisation of a hydroxyl (OH) group to generate isocitrate. The third reaction is catalysed by isocitrate dehydrogenase and corresponds to the first oxidative decarboxylation in the cycle. This reaction involves oxidation of isocitrate to an intermediate compound (oxalosuccinate) and formation of NADH from NAD^+. This intermediate is immediately decarboxylated to generate α-ketoglutarate, which is accompanied by the release of a CO_2 molecule. The fourth reaction is the decarboxylation of α-ketoglutarate, with the removal of a CO_2 molecule and a replacement by a CoA complex to give succinyl-CoA, with NADH generated from NAD^+ in the process. The fifth reaction is the phosphorylation of succinyl-CoA, which loses the CoA complex to generate succinate. In this reaction, a molecule of guanine triphosphate (GTP) is synthesised from phosphorylation of guanine diphosphate (GDP). In turn, ATP is synthesised from dephosphorylation of GTP. The sixth reaction of the cycle is the oxidation of succinate to fumarate catalysed by succinate dehydrogenase and reduction of FAD to generate $FADH_2$. FAD is covalently bound to succinate dehydrogenase, which in turn is bound to the mitochondrial inner membrane. The importance of this binding is related to the re-oxidation of $FADH_2$ in the mitochondrial electron transport chain, which is required for the enzyme to act again. The seventh reaction is catalysed by catalysed by fumarase hydratase and converts fumarate to malate. The final reaction regenerates oxaloacetate by dehydrogenation of malate, catalysed by malate dehydrogenase and involves the reduction of NAD^+ to generate NADH. Overall, for a mole

of glucose, two moles of acetyl-CoA are generated which corresponds to two cycles of the Krebs cycle, giving six moles of NADH, two moles of $FADH_2$ and two moles of ATP.

The final stage of cellular respiration generates the bulk of the ATP required by the cell. This is summarised in figure 1.9. The production of acetyl-CoA by glycolysis or beta-oxidation and the Krebs cycle, whilst they generate a small amount of ATP, can be considered as preparatory steps in generating the reduced electron carriers required by the electron transport chain (ETC). Here re-oxidation of NADH and $FADH_2$ will generate most of the energy necessary to create the proton gradient required to drive the ATP synthase that regenerates ATP.

The electron transport chain (ETC) is a metabolic pathway consisting of sequential redox reactions that drive ATP synthesis via oxidative phosphorylation. NADH and $FADH_2$ are oxidised by four enzyme complexes that are bound to the inner membrane of the mitochondria and the resulting electrons are passed along these complexes by electron carriers. Complex I receives electrons from oxidation of NADH to NAD^+ and Complex II carries out a similar reaction from oxidation of $FADH_2$ to FAD^+. This process is related to the oxidation of succinate and consequent reduction of FAD to $FADH_2$ in the Krebs (citric acid) cycle as mentioned earlier. The electrons transferred to the electron transport chain from these reduction reactions are passed onto coenzyme Q, which can move freely through the inner mitochondrial membrane. Coenzyme Q is oxidised by Complex III, which subsequently reduces cytochrome c. Finally, cytochrome c is oxidised by Complex IV and the final acceptor of the reducing equivalents is oxygen, producing water. The movement of electrons along the electron transport chain in the inner membrane causes protons (H^+) to be pumped out of the mitochondrial matrix to the intermembrane space, which generates a net negative charge in the matrix, while a net positive charge and proton gradient is established in the intermembrane space. This resultant electrochemical gradient favours the flow of protons back into the mitochondrial matrix via a specific channel, known as Complex V or ATP synthase. This energy drives the phosphorylation of ADP to ATP in a process known as oxidative phosphorylation. For each mole of NADH that is oxidised, 3 moles of ATP are synthesised; similarly, for each mole of $FADH_2$ oxidised, 2 moles of ATP are synthesised.

Tables 1.1 – 1.3 summarise the number of NADH, $FADH_2$ and ATP molecules generated for aerobic cellular respiration of glucose, aerobic cellular respiration through beta-oxidation of an example fatty acid, and anaerobic metabolism respectively. There is a difference in the energetic yield in terms of moles of ATP /carbon atom, which is higher for beta-oxidation than for glycolysis. It is additionally worth noting that there is a difference in terms of proportion of NADH and $FADH_2$ generated for a given number of carbon atoms, because of the fact that beta-oxidation yields both NADH and $FADH_2$ whereas glycolysis yields only NADH.

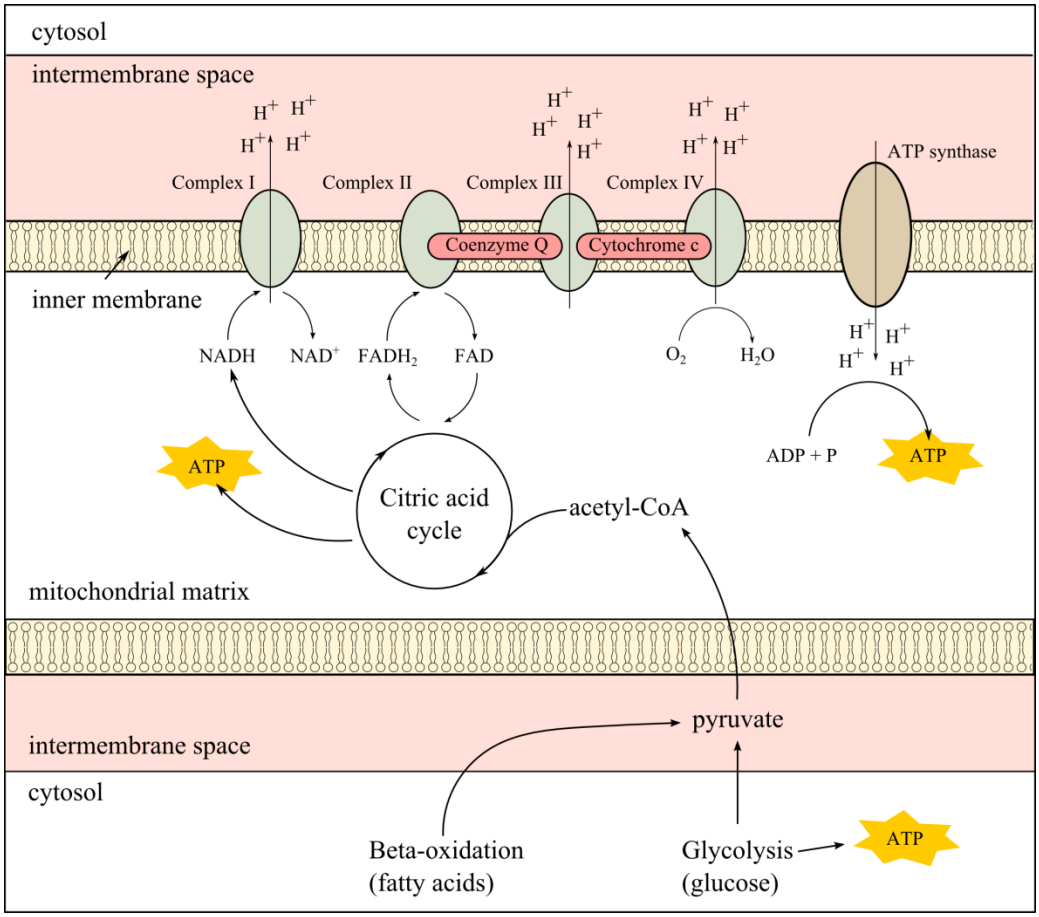


Figure 1.9 Summary of aerobic metabolic pathways for production of ATP. Reproduced with permission from Dr João Lagarto.

	NADH	$FADH_2$	ATP	Total ATP synthesised
Glycolysis	2	0	2	2 × 3 + 2 = 8
Pyruvate dehydrogenase complex	2	0	0	2 × 3 = 6
Krebs cycle	6	2	2	6 × 3 + 2 × 2 + 2 = 24
Total ATP synthesised	10 × 3 = 30	2 × 2 = 4	4	38 (6.3 ATP/carbon)

Table 1.1 Energetic yield of aerobic cellular respiration through glucose ($C_6H_{12}O_6$) metabolism (in moles)

	NADH	$FADH_2$	ATP	Total ATP synthesised
Beta-oxidation	7	7	-2	7 × 3 + 7 × 2 - 2 = 33
Krebs cycle	24	8	8	24 × 3 + 8 × 2 + 8 = 96
Total ATP synthesised	31 × 3 = 93	15 × 2 = 30	6	129 (8.1 ATP/carbon)

Table 1.2 Energetic yield of aerobic cellular respiration through beta-oxidation of an example fatty acid, e.g.16-C fatty acid (palmitate) (in moles)

	NADH	$FADH_2$	ATP	Total ATP synthesised
Glycolysis	0	0	2	2
Total ATP synthesised	-	-	2	2 (0.33 ATP/carbon)

Table 1.3 Energetic yield of anaerobic metabolism of glucose (in moles)

1.10 Structure, physiology and energetics of the heart in disease

As briefly discussed above, the heart in the healthy state is maintained in equilibrium by a great number of homeostasis mechanisms acting at both an organ and at a cellular level to maintain the proper functioning of the heart. Heart failure (HF) is a pathophysiological state in which an abnormality of cardiac function is responsible for the failure of the heart to pump blood at a rate commensurate with the requirements of the metabolising tissues. Heart failure is defined clinically as a syndrome in which patients have typical symptoms (e.g. breathlessness, ankle swelling, and fatigue) and signs (e.g. elevated jugular venous pressure, pulmonary crackles, and displaced apex beat) resulting from an abnormality of cardiac structure or function.(Camm et al. 2009; Wijns et al. 2012; Ponikowski et al. 2016) The definition of heart failure is based upon the presence of symptoms, however it is clear that prior to the development of symptoms there is an asymptomatic period during which a structural and functional cardiac abnormality is present and the homeostatic mechanisms are impaired or acting in a fashion which is detrimental in longer term. The underlying aetiology can be a disease of the myocardium (ischaemic heart disease, toxic damage such as anthracycline chemotherapy, inflammatory conditions, infiltrative conditions or metabolic derangements), abnormal loading conditions placed on the heart (hypertension, valve disease, pericardial or endocardial disease, and high output disease states) or arrhythmias. The clinical syndrome of heart failure represents an advanced stage of a pathophysiological process, which is initiated by an injury or deleterious change in structure and/or function of the heart, and manifests either acutely or develops over time through adverse remodelling or progression of a disease process. Chapter 4 looks at a model of post-myocardial infarction heart failure and Chapter 5 looks at a model of chemotherapy cardiomyopathy heart failure and the specific features of these conditions are discussed in the introductions of the relevant chapters.

Heart failure is characterized by alteration in the extracellular matrix and by changes in the energetic state and, as such, the motivation for the creation of the custom-built single-point fibre-optic probe based instrument is the potential to provide immediate biochemical, morphological or physiological information to detect alterations in the heart in disease states *in vivo* without the introduction of exogenous probes. If the autofluorescence lifetime signatures associated with known pathological diagnoses were obtained, such a technique could be used for rapid confirmation of heart failure diagnosis or to conduct a 'virtual biopsy' in presence of symptoms to aid diagnosis. Identification of those autofluorescence lifetime signatures in the asymptomatic period known to be associated with progression toward heart failure would be particularly powerful as it would permit prevention of progression where it was possible to reverse the cause, or early instigation of prognostic heart failure treatment where this were not possible.

1.11 Summary, hypothesis and aims

In summary, autofluorescence provides opportunities to study biological systems without the introduction of exogenous compounds that can introduce issues of toxicity or affect the biological system under investigation. Interest in this readout is growing rapidly in many branches of medicine and it has already been applied successfully to the study of other human diseases. A number of molecules in the heart demonstrate autofluorescence, including those involved in the energetics of the heart, such as NADH and flavins, as well as structural molecules, such as collagen. A novel autofluorescence lifetime probe system developed at Imperial College London gives the ability to investigate and evaluate the autofluorescence metrology of the heart and thereby characterize the autofluorescence 'signature' that accompanies the histological, morphological, metabolic and functional changes found in myocardial tissue in health and disease states. By understanding the changes in the autofluorescence signature that accompany disease, it could offer a potential diagnostic tool, and this technology would be readily translatable into clinical practice.

The primary hypothesis addressed in this thesis is that measurement of myocardial autofluorescence lifetime and spectral properties by use of a custom-built single-point fibre-optic probe based instrument will identify specific alterations in the autofluorescence 'signature' that accompany the histological, morphological, metabolic and functional changes in the heart in health and disease states.

In order to address this, there were a number of specific aims in this thesis:

1. Application of the custom-built, single-point, fibre-optic probe based instrument to an *ex-vivo* Langendorff perfused heart to characterise the myocardial-specific fluorescence lifetime signature and changes upon altering physiological parameters

2. Application of the custom-built, single-point, fibre-optic probe based instrument *in vivo* to a model of post-myocardial infarction heart failure to characterise the autofluorescence lifetime signature at different time points after the myocardial infarction
3. Development of a model of doxorubicin chemotherapy cardiomyopathy
4. Application of the custom-built, single-point, fibre-optic probe based instrument *in vivo* to a model of doxorubicin chemotherapy cardiomyopathy to characterise the autofluorescence lifetime signature accompanying the disease state
5. Collaboration with colleagues in the Photonics Group to work towards developing a user-friendly, point-of-care fluorescence lifetime system for practical application in the clinical setting

2 Methods and Materials

This chapter explains in detail the materials and methods used in the experimental work detailed within this thesis. It includes details of the materials used (e.g. animal species, surgical protocols) and a detailed description of the custom-built single-point fibre-optic probe based instrument to study the application of autofluorescence lifetime measurements and diffuse reflectance spectroscopy to the study of heart disease.

2.1 Autofluorescence lifetime and diffuse reflectance spectroscopy custom-built single-point fibre-optic probe based instrument

2.1.1 Optical setup and fibre optic probe

All measurements were made using a custom designed instrument that was designed to discriminate and maximise the speed of acquisition of signal for the study of the energetic and structural properties of cardiac tissue via endogenous fluorescent molecules such as the important electron donors involved in mitochondrial metabolism i.e. NADH and FAD, and structural molecules, such as collagen, in the extracellular structure of the heart.

The configuration of the device is shown in figure 2.1.

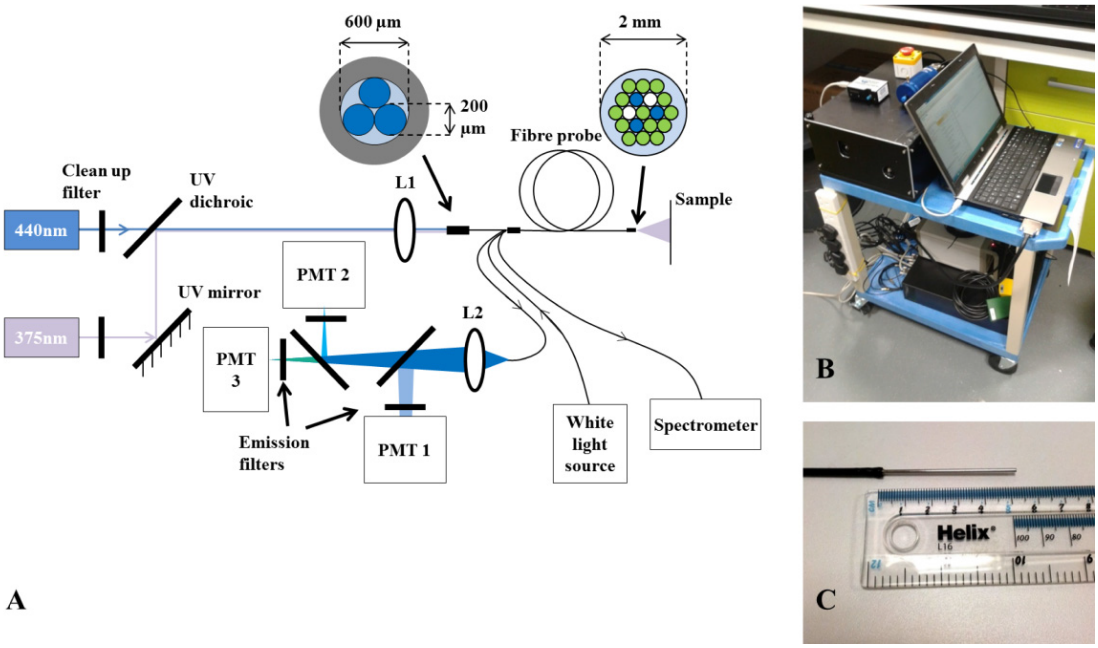


Figure 2.1 (A) Experimental layout of the autofluorescence lifetime & diffuse reflectance spectroscopy custom-built single-point fibre-optic probe based instrument and its optical fibre configuration at the excitation (proximal) and sample (distal) ends. Optical fibre cores are coloured blue for excitation fibres, white for fibres delivering white light and collecting the diffuse reflected light and green for fibres collecting returned fluorescence. (B) Portable trolley mounting of the system allows ease of deployment in clinical settings. (C) Distal end of the fibre-optic probe with ruler for scale.

Two compact lasers provide the excitation light sources: a laser diode (LDH-P-C-375B, PicoQuant GmbH, Germany) providing 70 ps pulses at 375 ± 5 nm with an average output power of 3.3 mW; and a second laser diode (LDH-P-C-440B, PicoQuant GmbH, Germany) generating 90 ps pulses at 440 ± 5 nm, with 3.5 mW of average power. These are controlled with a single laser driver, (Sepia II, PicoQuant GmbH, Germany) allowing both power control and adjustment of the repetition rate up to 80 MHz. Experimental data was acquired at 20MHz. A dichroic mirror combines the two laser beams (Di01-R405, Semrock, USA) and they are subsequently coupled into a custom-made optical fibre bundle (FiberTech Optica, Canada) consisting of three excitation fibres and fourteen detection fibres arranged in a hexagonal structure around the excitation fibres, see Figure 2.2. There are two additional fibres within the bundle that are used for white light delivery and diffuse reflectance detection.

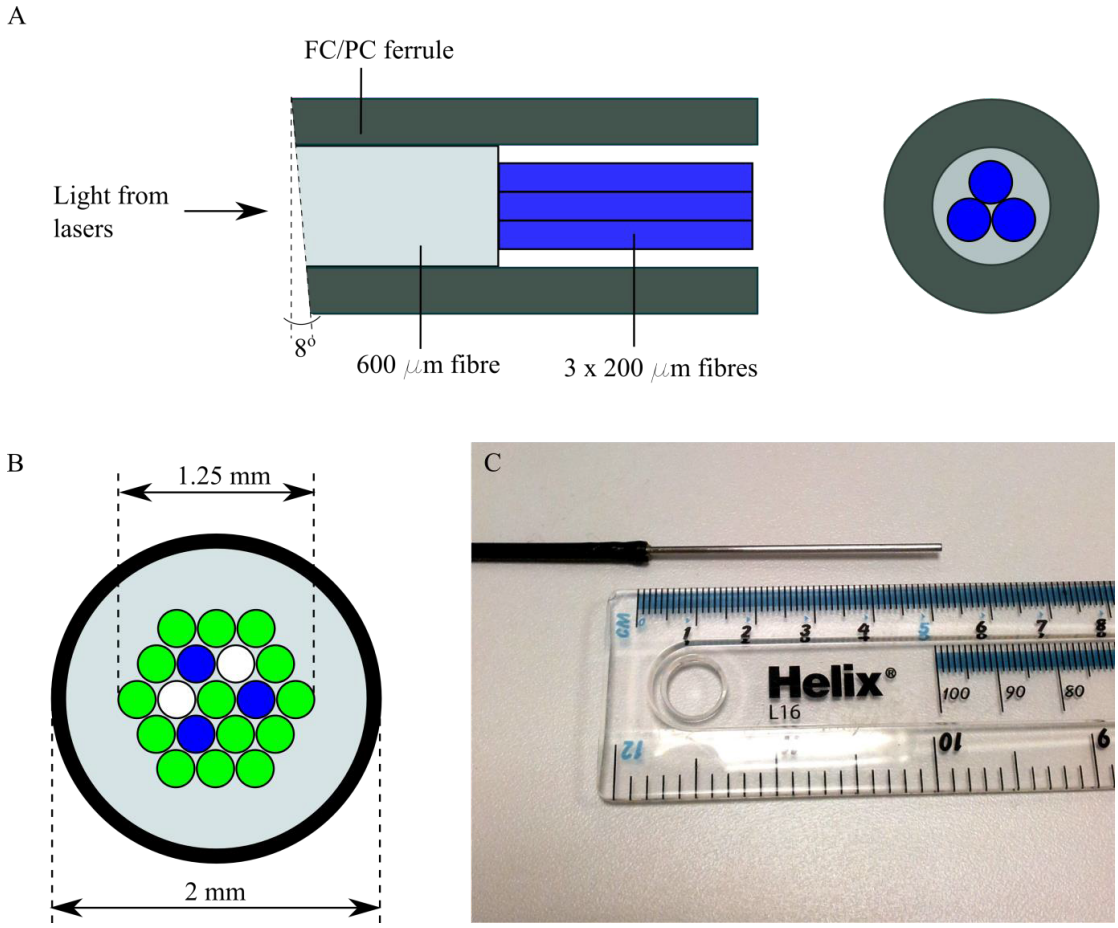


Figure 2.2 Detail of the fibre optic bundle with (A) detail of the cross-section (left) and en-face (right) views of the proximal end of the fibre-bundle, at the fluorescence excitation branch where it is coupled to the lasers (B) Colour-coded cross-section en-face view showing arrangement of delivery and collection fibres at the distal end of the probe: blue - fluorescence excitation fibres; green - fluorescence collection fibres; and white - light delivery and collection fibres. (C) Photograph of the distal end of the fibre bundle with ruler for scale.

The custom-made fibre-optic bundle consists of 19 multimode optical fibres, each one having 200 μm diameter core with a further 20 μm cladding and numerical aperture (NA) 0.22, with four individual branches (excitation, detection, white light, spectrometer) at the proximal end and a common distal end, as illustrated in Figure 2.2. Of the 19 optical fibres: 3 are used for fluorescence excitation; 14 are used for fluorescence collection; and the remaining 2 used for white light delivery and detection. At the proximal end of the fluorescence excitation branch, the excitation light is coupled into a short length of 600 μm fibre, which is in turn coupled with three 200 μm closely packed excitation fibres that deliver the light into the sample, as illustrated in Figure 2.2(A). The input of the 600 μm fibre is cleaved at 8° to minimise back-reflection. The hexagonal configuration of the fibre with the excitation fibres at the centre and the collection fibres surrounding them was arrived at to maximize signal-to-noise ratio and to achieve precise target interrogation (T. Papaioannou, N. Preyer, Q. Fang, H. Kurt, M. Carnohan, R. Ross, A. Brightwell, G. Cottone, L. Jones 2003; T. J. Pfefer, K. T. Schomacker, M. N. Ediger 2002) and this arrangement has proven to be a popular configuration within our group (De Beule et al. 2007; Thompson et al. 2012). The fibres are fixed with epoxy glue inside a 2mm diameter medical

grade stainless steel ferrule approximately 5cm long which is the tip handled by the operator to take measurements from the sample.

Detection fibres collect the fluorescence from the sample and direct it to three spectrally resolved detection channels by means of a set of dichroic mirrors and band-pass filters. With the 375 nm excitation light, all three PMTs are used to collect fluorescence: the first PMT collects 400 – 420 nm and this combination is hereafter called channel 1 (CH1); the second PMT collects 430 – 480 nm (CH2); and the third PMT collects 500 – 550nm (CH3). With the 440 nm excitation light, only the third PMT collects 500 – 550 nm and this combination is referred to as channel 4 (CH4). The emission spectra of the principal fluorophores of interest NADH, FAD and collagen I with 375nm excitation in relation to the spectral range of the detection channels (CH1, CH2, CH3) of the custom designed instrument are shown in figure 2.3. Each detection channel consists of a photon-counting photomultiplier (PMC-100-1, Becker-Hickl GmbH, Germany), controlled by DCC-100 modules (Becker-Hickl GmbH, Germany). A router (HRT-41, Becker-Hickl GmbH, Germany) serializes these inputs for the time-correlated single photon counting (TCSPC) acquisition card (SPC-830, Becker-Hickl GmbH, Germany), which in turn records the temporal fluorescence decay profile for each of the spectral channels (CH1, CH2, CH3, CH4). To permit diffuse reflectance measurements the instrument also comprises a white light source (HL-2000, Ocean Optics, USA) and a compact spectrometer (USB-2000+, Ocean Optics, USA). The optical setup is assembled on a 30 × 45 cm^2 breadboard (Thorlabs, USA), which is enclosed and mounted on a portable trolley for safe use and ease of deployment.

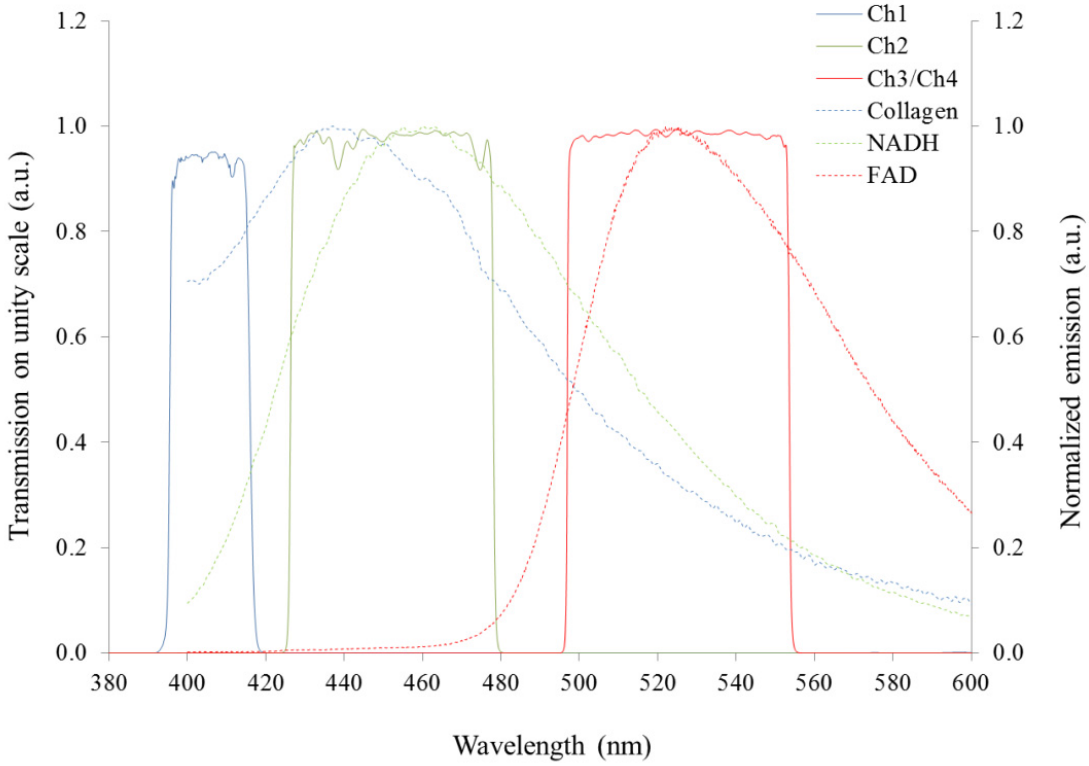


Figure 2.3 Emission spectra of endogenous fluorophores of interest excited at 375 nm and plotted to show their relation to the spectral range of the detection channels of the fluorescence lifetime point probe system. Curves are normalized to their maximum amplitude. Solutions of β-NADH (N1161, Sigma-Aldrich, Germany) and FAD (F6625, Sigma-Aldrich, Germany) were prepared by diluting the respective powder in phosphate buffered saline (PBS) solution. Collagen type-I from rat tail was from Sigma (C8897, Sigma-Aldrich, Germany) and was used directly without further preparation. Measurements of the fluorescence emission spectra is carried out on a spectrofluorophotometer (RF-5301PC, Shimadzu, Japan) using 375 nm excitation. Emission spectra were recorded from 400 to 700 nm. A 390 nm long-pass filter was placed at the entrance slit of the monochromator to prevent contamination of the fluorescence signal by the excitation light.

The system is fully controlled via a custom application written in LabVIEW (LabVIEW, National Instruments, USA, which took previously developed code from our laboratory and was build upon to allow:

- control of lasers (on/off/power level);
- control of white light source (on/off);
- interface with SPC-830 TCSPC acquisition card to allow real-time readout of photon counts and data acquisition;
- interface with spectrometer;
- and configuration of SPC-830 TCSPC card and DCC-100 photon-counting photomultipliers.

Figure 2.4 shows the graphical user interface (GUI).

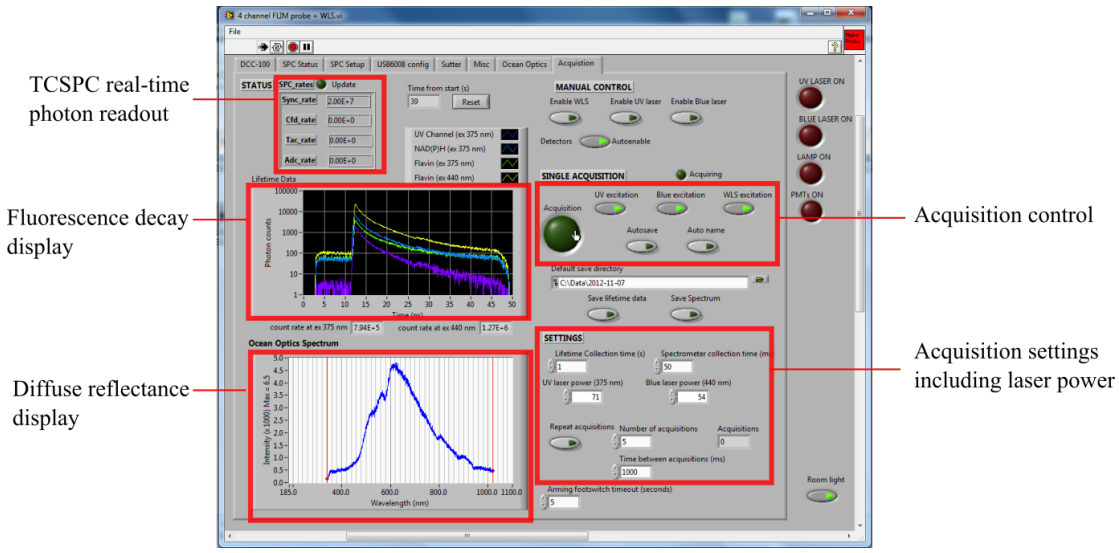


Figure 2.4 LabVIEW graphical user interface (GUI) – an update of the code, previously developed in our laboratory, by Dr João Lagarto

Safety features employed to protect both user and equipment include:

- limiting the laser power to below the maximal permissible energy (MPE) for accidental exposure for up to 100 seconds;
- a laser interlock controlled by the software to turn off the laser if the software is not loaded;
- automatically disabling the laser and detection in the even of any of the PMTs being overloaded with light

The instrument and fibre optic probe was extensively characterised and calibrated and the instrument response function for autofluorescence lifetime and diffuse reflectance was determined through extensive work by Dr João Lagarto.

2.1.2 Data acquisition

Due to the natural movement of the heart, the distance from the heart or pressure of the probe tip on the surface of heart can vary slightly during each measurement and between consecutive measurements. We therefore ensured that the fluorescence data acquisition protocol would cover multiple heart beats (typically 3-6 at heart rates of 200 to 400 beats per minute) so that any artefacts due to the heart motion during a measurement are averaged. The integration time used in a single acquisition was 1 second for UV excitation, 1 second for blue excitation and 50 milliseconds for diffuse reflectance measurements with white light illumination. The specific details of data acquisition in terms of location, repeat measurements etc., for each protocol with will be detailed in the relevant chapter.

2.1.3 Data analysis

2.1.3.1 Fluorescence decay analysis

As discussed in chapter 1 autofluorescence of biological tissue usually exhibits a complex profile due to the presence of multiple fluorophores with spectra that overlap (Lakowicz 2006; Marcu 2012) Such complex decay profiles are commonly described by a multi-exponential decay model

Equation 2.1

$$I(t)^n = \sum_{i=1}^{N} a_i e^{-\frac{t}{\tau}} + C$$

where τ_i is the decay time a_i is the pre-exponential factor of each component in the decay and C is background light. Due to the limited number of photons in each spectral channel, we chose to fit a single exponential decay model to channel 1 data and a double exponential decay model to the remaining channels. Using the decay parameters from equation 2.1 applied to a double exponential decay model, the mean lifetime can be calculated as defined in equation 2.2:

Equation 2. 2

$$\tau_{mean} = \beta\tau_1 + (1-\beta)\tau_2$$

where β refers to the contribution of the first component to the overall decay and is calculated as shown in equation 2.3.

Equation 2.3

$$\beta = \frac{\alpha_1\tau_1}{\alpha_1\tau_1 + \alpha_2\tau_2}$$

To accurately fit a complex decay model to the data, it is necessary to measure the temporal instrument response function (IRF) of our custom-built instrument. The measurement of the IRF includes the temporal broadening of the excitation pulse during transmission through the excitation fibre and the broadening of the collected fluorescence returning through detection fibres of the instrument. The IRF was measured with reference to commercially available fluorophores with known decay characteristics. 4′,6-Diamidino-2-phenylindole dihydrochloride (DAPI) (Sigma-Aldrich, USA) with 372 nm excitation in all detection channels (CH1, CH2, CH3 as detailed before) and Erythrosin B (Sigma-Aldrich, USA) with 438 nm excitation and collection at 500 – 550 nm (CH4 as detailed before). These reference dyes have lifetimes of approximately 200 ps and 90 ps, respectively, which are comparable to the pulse lengths of the lasers in the instrument. Analysis of the autofluorescence lifetime data from each detection channel employs the non-linear least squares fitting routine from MATLAB (lsqnonlin function, R2011b, The Mathworks Inc., USA) to minimize the goodness-of-fit chi-square value χ^2, expressed as equation

2.4

Equation 2.4

$$\chi^2 = \sum_{k=1}^{n} \left(\frac{(I(t_k) - I_{model}(t_k))^2}{I(t_k)} \right)$$

where n represents the number of bins in the decay, I represents the measured decay at each time delay and I_{model} represents the model decay function convolved with the instrument response function. The fitting model included the measured background offset and the measured after-pulsing probability of the detectors. To account for the minor temporal shift of the IRF with respect to the data caused by the distance between the tip of the probe and the reference dye solution, a temporal offset fit parameter was included in the fluorescence decay analysis. For all detection channels but channel 1, 4 lifetime parameters are extracted: β, τ_1, τ_2, and τ_{mean}. For channel 1, as data is fitted with a single exponential decay model, the lifetime parameter is τ.

2.1.3.2 Spectral analysis of fluorescence measurements

The fractional photon count in each spectral channel of the total autofluorescence signal collected under UV excitation and the ratio of the autofluorescence signal between each of these channels is calculated as CH1 R, CH2 R, and CH3 R as summarized in table 2.1. CH4 was excluded from ratio calculations as this is sensitive to any small day-to-day changes in fibre optic coupling efficiency and laser power differences between the 372 and 438 nm lasers. Because of the aim to have photon counts in each channel to be approximately 1% of the laser repetition rate, this sometimes requires output power to be adjusted. The ratios derived from channels 1-3 are inherently ratiometric as they are excited by the same laser. For each acquisition, we can derive up to 19 lifetime and spectral parameters:

Channel	Index	Description
Channel 1	τ	Fluorescence lifetime
Channel 2	τ_{mean}	Weighted mean fluorescence lifetime
	τ_1	Short lifetime component
	τ_2	Long lifetime component
	β	Contribution of the first component
Channel 3	τ_{mean}	Weighted mean fluorescence lifetime
	τ_1	Short lifetime component
	τ_2	Long lifetime component
	β	Contribution of the first component
Channel 4	τ_{mean}	Weighted mean fluorescence lifetime
	τ_1	Short lifetime component
	τ_2	Long lifetime component
	β	Contribution of the first component
	CH1 R	Relative fluorescence in channel 1
	CH2 R	Relative fluorescence in channel 2
	CH3 R	Relative fluorescence in channel 3
	CH1 I/CH2 I	Fluorescence intensity in CH 1 / Fluorescence intensity in CH2
	CH2 I/CH3 I	Fluorescence intensity in CH 2 / Fluorescence intensity in CH3
	CH1 I/CH3 I	Fluorescence intensity in CH 1 / Fluorescence intensity in CH3

Table 2.1 List of spectroscopic parameters that are extracted from an acquisition

2.1.3.3 Diffuse reflectance measurements

Diffuse reflectance spectroscopy is a well-established technique that has previously been used to characterize tissue optical properties such as absorption coefficient, reduced scattering coefficient, haemoglobin and myoglobin concentrations and total blood oxygenation (Arai et al. 1999; Zonios & Dimou 2006; Lindbergh et al. 2011) as has been discussed in chapter 1. Acquired spectra are normalized to the signal of the diffuse reflectance from a white reference target (WS-1-SL, Labsphere, USA). All diffuse reflectance values are reported in units of absorbance, calculated as shown in equation 2.5, where A is the tissue absorbance, I is the measured spectrum, and I_0 is the calibrated spectrum of the white light source.

Equation 2.5

$$A(\lambda) = -\log_{10}\left(\frac{I(\lambda)}{I_0(\lambda)}\right)$$

2.2 Surgery protocols

All studies involving animals were carried out under protocols approved and regulated under the Animals (Scientific Procedures) Act 1986 (Project Licenses PPL 70/7399 and 70/7419). All animal surgical procedures and perioperative management were carried out in accordance with

the United Kingdom Home Office Guide on the Operation of the Animals (Scientific Procedures) Act 1986, which conforms to the Guide for the Care and Use of Laboratory Animals published by the US National Institutes of Health.

The myocardial infarction induction surgeries were performed by Dr Markus Sikkel and Dr Adam Mills. All in-vivo myocardial fluorescence measurements were performed by myself.

2.2.1 Animals

All studies were performed using Sprague-Dawley male rats procured from Harlan Laboratories. Animals weighing 250-350g (9-12 weeks old) were used. The Sprague-Dawley rat is an albino outbred strain of *Ratus norvegicus* (Norway rat or brown rat). Though several generations of inbreeding, the strain was developed by the R. Dawley of Sprague-Dawley Company, Madison, Wisconsin in 1925. The rats are maintained as outbred closed colonies and all current colonies arise from this original stock. Outbreeding results in some genetic variability, however this is very limited owing to the original inbreeding to develop the colony. It is widely used in cardiovascular research as it is well established as a reliable strain for cardiovascular physiological experiments and it is calm, easy to handle and relatively inexpensive.

Sprague-Dawley rats have a typical lifespan of 2.5-3 years. The normal heart rate is 250-400 beats per minute. The normal respiratory rate is 75-115 respirations per minute. There is a fold of tissue at the junction of the oesophagus and stomach, which prevents vomiting and therefore removes the need for fasting prior to anaesthesia and intubation.

The animals are housed in a highly controlled environment in the animal facilities at Imperial College London with a 12 hour on- / 12 hour off- light-dark cycle and free access to food and water. The average consumption is 5g food/100g body weight/day and 10-12ml water/100g body weight/day.

2.2.2 Anaesthesia, endotracheal intubation and pre-operative management for surgery protocols

Adult male Sprague-Dawley Rats are used. Induction of anaesthesia is achieved with a mixture of 5% isoflurane/95% oxygen in the induction chamber, and the rat is then rapidly transferred to a Bain coaxial circuit and anaesthesia is maintained with 2% isoflurane/98% oxygen prior to intubation. Once anaesthetized, 0.015-0.03mg buprenorphine (0.05-0.1mg/kg), 1.25-1.5mg enrofloxacin (5mg/kg), and 2ml of warmed 0.9% saline are administered subcutaneously (sc).

The left anterior chest wall is shaved, and the rat is positioned on the anaesthetic board to permit use of the “hanging teeth” method of endotracheal intubation. The endotracheal tube, fashioned

from a 16G intravenous cannula (1.7Å ~45mm Venflon™, Becton Dickinson, UK) with a blunted stylet, is advanced across the vocal cords under direct vision assisted by transillumination of the trachea with an external light source. The rat is connected via the endotracheal cannula to a Harvard Ventilator (Harvard Apparatus, Massachusetts), and ventilated using volume-controlled ventilation with a minute volume of 180-250 ml/min (cycle rate 100/min; tidal volume 1.8-2.5ml). The maintenance of anaesthesia is with 2% isoflurane/98% oxygen unless stated otherwise.

Upon completion of recovery cardiac surgery for myocardial infarction, a 22G Abbocath®-T catheter (Hospira Venisystems TM, Ireland) with added side-holes is inserted as a chest drain to prevent pneumothorax, and continuous positive airways pressure (CPAP) is delivered by temporary occlusion of the ventilator exhaust for 2-3 respiratory cycles to facilitate lung re-expansion. The thoracotomy and skin are closed using a 4.0 105 Ethicon polyester non-absorbable suture (Johnson and Johnson Medical Ltd, UK) and the wound is cleaned with 1% Chlorhexidine (Hibiscrub™, Astra Zeneca, UK), and 2mls of warmed 0.9% saline is injected subcutaneously.

2.2.3 Myocardial infarction induction surgery

Adult Male Sprague-Dawley Rats (250-350g) are anaesthetised and prepared as outlined as per section 2.2.2. A left parasternal incision is followed by division of the tissue planes, with retraction of pectoralis major and minor, to expose the intercostal muscles. A left thoracotomy is fashioned via the 4th intercostal space, and the pericardial sac is divided. Anterior mobilization of the thymus gland is used to stabilize the heart and elevate the anterolateral aspect of the left ventricle into the centre of the surgical field to facilitate the surgery.

The left anterior descending coronary artery (LAD) becomes intramyocardial shortly after the origin, and is rarely seen on the epicardial surface (Haplen 1957). The course of the LAD is relatively preserved, and therefore its location can be predicted relative to other anatomical landmarks, namely the left atrial appendage, the anterior interventricular groove and the pulmonary artery conus. The artery is ligated proximal to the first diagonal using a 7.0 Prolene suture at a point 1-2mm distal to the left atrium inferior border along an axis parallel to the atrioventricular groove. Around 0.5-1.5mm of myocardium is ensnared by the suture. Effective ligation-induced myocardial ischaemia is confirmed by observing blanching and cyanosis of a significant sized ischaemia zone in the LAD territory. If this is not observed, further ligations lateral and/or medial to the initial point are performed until a significant ischaemia zone is induced. After successful coronary ligation, maintenance isoflurane is reduced to 1.0% during chest closure. Any instances of myocardial bleeding from the needle puncture are treated with gentle swab pressure, and a further subcutaneous fluid bolus is administered as necessary for fluid resuscitation. Immediate ischaemia-related ventricular fibrillation is treated by either a

short phase of CPAP delivered for 2-3 ventilatory cycles, or by mechanical blow to the fibrillating heart by means of flicking with a finger, or by compression between two tweezers' handles.

Animals are weaned off the ventilator using 100% oxygen, and transferred after spontaneous breathing is returning to the Bain coaxial circuit and the fraction of inspired oxygen is weaned down. The chest drain and endotracheal cannula are only removed after the animal has regained consciousness, and after suctioning of the chest drain to remove any air or blood that may be present in the hemithorax. In the event of failure to regain consciousness then the animal is re-anaesthetized, reconnected to the ventilator for ventilation plus CPAP. The chest drain is repositioned if there was no successful air/blood draining after the initial siting. Rats are then housed in single cages and in a stable environment with the standard facility 12/12 light-dark cycle, maintained on standard rat chow and water ad libitum, analgesia and are checked daily for any signs of distress.

This method has been extensively validated and is a well-established model within our institution. (Lyon et al. 2009)

2.2.4 *In vivo* autofluorescence lifetime measurements

In vivo fluorescence lifetime measurements were always performed as a terminal procedure. Adult Male Sprague-Dawley Rats are anaesthetized and prepared as outlined as per section 2.2.2. Once anaesthetized, 0.015-0.03mg buprenorphine (0.05-0.1mg/kg) and 2ml of warmed 0.9% saline are administered subcutaneously (sc), however antibiotics are not given as the procedure is non-recovery. The anterior chest wall and abdominal wall are shaved. Diathermy is available to deal with minor bleeding. A midline incision is made to permit division of the linea alba and to avoid the rectus abdominal muscles on either side to prevent bleeding. The peritoneum is punctured with forceps and the absence of adhesions is confirmed prior to extending the incision cephalically with scissors. The diaphragm is punctured with forceps and carefully dissected to avoid bleeding. Two clamps are applied to the ribs either side of the sternum to clamp the intercostal arteries and the sternum is divided with scissors. This permits exposure of the heart. Following the in vivo fluorescence measurements and at the end of the study, blood can be sampled by venepuncture of the inferior vena cava using a heparinized syringe. This is rapidly followed by explanation of the heart, which is either formalin-fixed for histology or flash-frozen with liquid nitrogen and stored at -80°C in a biobank for future analysis. As this is a non-recovery procedure, the animal undergoes an appropriate schedule 1 procedure at the end of a procedure.

2.3 Echocardiography

Echocardiography measurements are performed as a recovery procedure. Adult male Sprague-Dawley Rats undergo induction of anaesthesia. This is achieved with placing 5 % isoflurane/95

% oxygen in the induction chamber, and the animal is then rapidly transferred to a Bain coaxial circuit and anaesthesia is maintained with 1.5% isoflurane/98.5% oxygen during the procedure. The left thorax is depilated using an electric shaver and commercially available hair removal cream. Anaesthesia is maintained using with 98.5% O_2 / 1.5% isoflurane with the animal on a heat mat with ECG electrodes to concurrently record an electrocardiogram. Echocardiographic analysis was performed using a Visualsonics Vevo 770 echo machine with 7-24MHz transducer (both Visualsonics B.V., Netherlands) A left ventricular M-mode tracing was obtained using 2D parasternal long axis imaging as a guide from which the following standard echocardiographic measurements were recorded: end-diastolic and systolic interventricular septum dimensions (IVSd and IVSs), left ventricular internal diameter (LVIDd and LVIDs), and end-diastolic and systolic left ventricular posterior wall dimensions (LVPWd and LVPWs), as well as M-mode velocity of the posterior wall and heart rate. See figure 2.5. Animals were recovered following the procedure.

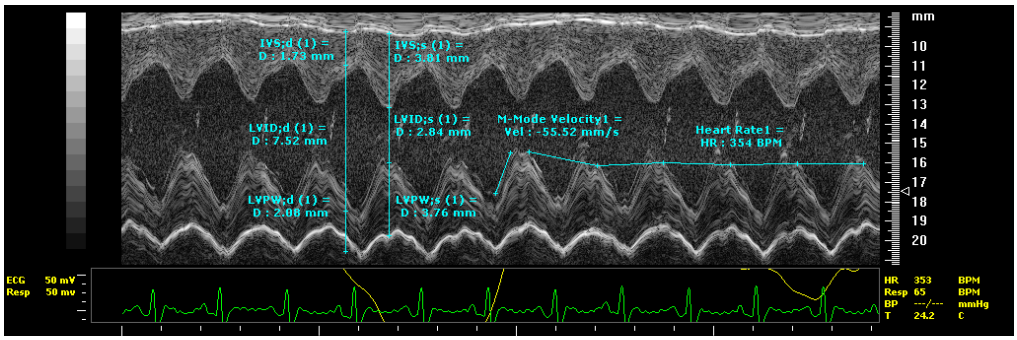


Figure 2.5 Example left ventricular M-mode tracing from a control animal, from which can be calculated end-diastolic and systolic interventricular septum dimensions (IVSd and IVSs), left ventricular internal diameter (LVIDd and LVIDs), and end-diastolic and systolic left ventricular posterior wall dimensions (LVPWd and LVPWs), M-mode velocity and heart rate.

2.4 *Ex vivo* isolated perfused heart

2.4.1 Background

A number of scientists in the 19th century worked on the ability to keep beating an isolated heart outside of the body: Wild and Ludwig in 1846 demonstrated that an empty heart could continue beating when connected to a donor living animal.(Wild & Ludwig 1846) Cyon and Ludwig demonstrated that the completely isolated frog heart continued to beat if perfused with warmed rabbit serum. (Zimmer 1998) Henry Martin visited Ludwig and extended this idea to attempt the first mammalian heart 'isolation', in which the systemic circulation (except for the coronary circulation) was excluded. Blood was perfused into the right atrium and was ejected by the right ventricle into an intact pulmonary circulation to be oxygenated by the lungs (of the animal anaesthetized and ventilated), and then ejected by the left ventricle into the ascending aorta and only into the coronary arteries and from there emptied into the right atrium again.

Oscar Langendorff was the first to isolate the mammalian heart completely and maintain cardiac contraction by continuous perfusion for several hours. (Bell et al. 2011) This was performed on isolated feline or canine hearts, and perfusion was with defibrinated blood from the same species. The major innovation was the use of an aortic cannula connected to a reservoir of blood, warmed indirectly via a water bath. He reported that the arrested heart could be resuscitated and continues to beat for hours with blood perfusion even with an empty ventricle, thereby observing that the presence of blood in the ventricle was not required for cardiac contraction. He and his contemporaries used this technique to make a number of important advances in heart biology including the successful substitution of blood for a physiological (glucose-rich) solution, the ability to measure myocardial oxygen consumption and therefore the beginning of the detailed study of cardiac metabolism, the discovery of the Frank-Starling relationship between stroke volume and end diastolic volume (Patterson et al. 1914).

These principles are still widely used today with the heart perfused in a retrograde fashion with either serum or physiological solution (e.g. Krebs-Henseleit buffer). Retrograde perfusion meets a closed aortic valve and therefore the entire perfusate is circulated in the coronary arteries via the ostia and then via the coronary sinus to drain into the right atria. The original, pressure-based method of coronary perfusion was refined to a constant-flow system by Katz in 1939 which allowed the complete regulation of coronary perfusion pressure and the ability precisely determine the drug concentration perfused.

The isolated rat heart was comprehensively characterized by Neely (J. R. Neely, H Liebermeister, E. J. Battersby 1967) and he observed that an isolated rat heart preparation can be stable for over three hours when perfused with physiological buffer. The isolated rat heart preparation has become a key tool in the study of cardiac biology and is widely used in physiological, pharmacological and metabolic studies (R. M. Bell, M. M. Mocanu 2011) owing to its reproducibility, ease of setup, cost, and ability to address specific hypotheses.

2.4.2 Langendorff perfusion apparatus

The Langendorff perfusion apparatus is detailed in figure 2.6. This is a constant flow apparatus in which the perfusates can be placed into two water-jacketed 2L reservoirs (Radnoti, USA) and in which can be bubbled via gas tubing a scintillator in contact with the perfusate a gas of choice, e.g. mixture of 5% CO_2 & 95% O_2 (Carbogen, BOC, UK). The use of a three-way tap permits 'switching' between the two different reservoirs as required. The perfusate is warmed by a circulating-water heating system and a series of thermally-insulated tubes to maintain the perfusate at a temperature of 36.5-37.5°C.

The warmed and bubbled perfusate is passed through a 5-micron filter and then taken to the aortic cannula by a series of thermally insulated flexible Tygon tubes and two bubble traps

(Radnoti, USA) conducted by a peristaltic pump (Radnoti, USA). The flow rate of the pump can be controlled between 1.0-100ml/min (typical flow rate used is 16-18ml/minute). The constant flow apparatus has an in-line pressure transducer, mounted proximal to the aortic cannula which allows measurement and titration of the perfusion pressure to maintain it at 90-100 mmHg.

2.4.3 Isolated heart protocol

For all *ex vivo* Langendorff preparations the following protocol is used. Hearts are explanted from male Sprague-Dawley rats via a 'Home Office Schedule 1' method of cervical dislocation under terminal anaesthesia (5% Isoflurane, 95% Oxygen mix) and following rapid excision of the aorta, heart, lungs and thymus they are placed into an ice-cold dish of heparinized, buffered Krebs-Henseleit solution (KHB).

The ascending aorta is identified following careful but rapid dissection away of the thymus, lungs and other mediastinal vessels taking care to minimize air intake into the aorta. The ascending aorta is cannulated onto a 1.2 mm diameter metal cannula (Radnoti, USA) at the distal end of the perfusion apparatus and is held in place with a small artery clip prior to it being secured in place with a 3-0 silk suture (Ethicon, UK). The pulmonary trunk is identified and a small incision made to allow for free drainage of effluent.

Buffered Krebs-Henseleit solution (as described by Krebs and Henseleit in 1932) is the base perfusate (with details of the modifications for specific protocols in the relevant chapter) used for all studies owing to its ease of synthesis from stock chemicals, low cost and well established use within our group and others.

In mmol/L Krebs-Henseleit solutions contains:

- Na^+ 118
- K^+ 4.5
- Mg^{2+} 2.4
- Ca^{2+} 1.85
- Glucose 11.1
- CO_2^{3-} 25
- PO_2^{3-} 1.38

with a pH between 7.35-7.45 when bubbled with 5% CO_2, 95% O_2 (Carbogen, BOC, UK).

Once the heart is secured onto the cannula and attached to the perfusion system the flow and pressure is increased until desired pressure (90-100mmHg) reached at which point the heart is allowed to stabilize for 10 minutes. The mean time from explant to the start of stabilization was under three minutes. A silver electrode is lightly placed on the epicardial surface away from the

area of interest for study and a reference electrode is connected to the metal cannula to create a whole-heart unipolar electrode input via a BioAmplifier (ADInstruments, USA) to a data acquisition system (Powerlab 8/35, AD Instruments, USA) and displayed in real time using LabChart 7 (ADInstruments, USA) at a sampling rate of 1KHz and with input band pass filtered between 0.3-30Hz. Hearts were only studied further if after the end of stabilization the heart rate (HR) is in the range 200 – 400 beats per minute (bpm) and there have been no sustained arrhythmias during the last 8 minutes of stabilization. Following stabilization, studies are continued as described in chapter 3.

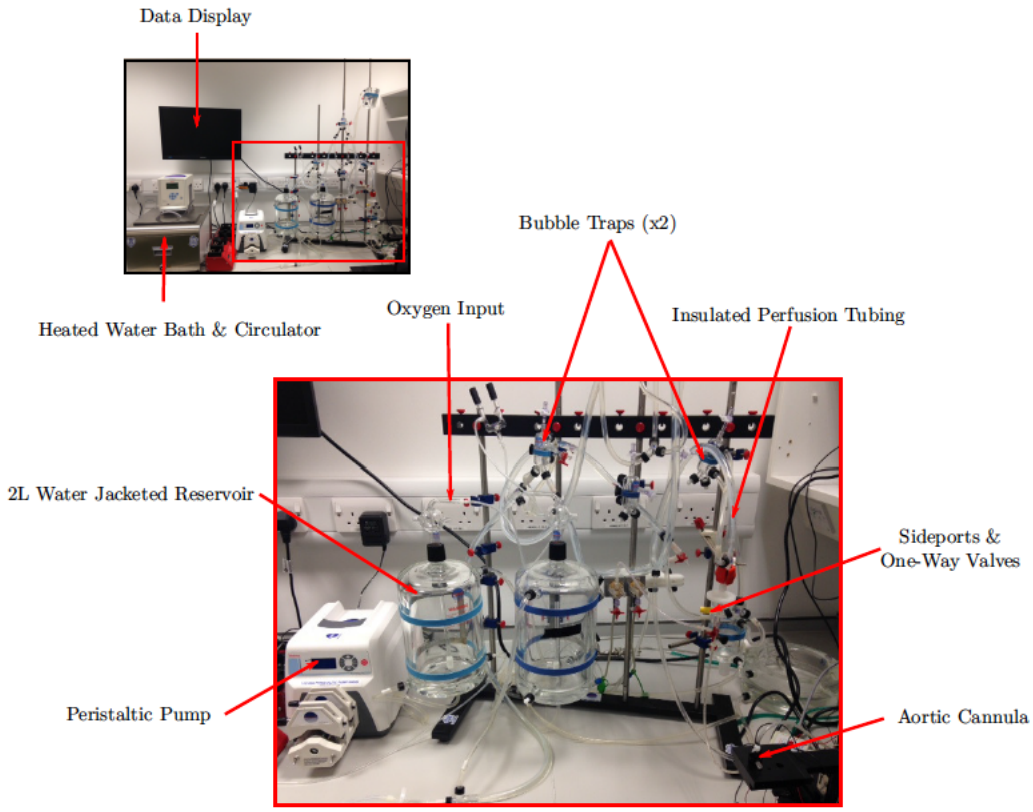


Figure 2.4: Langendorff Perfusion Apparatus

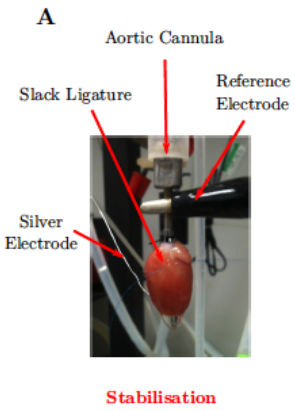


Figure 2.6 Langendorff perfusion apparatus (figure reproduced with permission from Dr M Debney)

2.5 Myocardial histology: PSR staining

Cardiac tissue sampled for histology was washed in sterile PBS, fixed in 10% paraformaldehyde for 48 hours and then processed for paraffin embedding. 6 µm thick sections were stained with picosirius red (PSR) to demonstrate interstitial collagen content (Lyon et al. 2009). Whole sections were imaged using a 10x objective on a Zeiss Axio Observer inverted microscope with a fully motorized stage. Percentage interstitial fibrosis in each anatomical area of interest was

quantified using Fiji image analysis software (Whittaker et al. 1994) by colour thresholding to calculate the area of tissue positively stained with PSR.

2.6 Statistical analysis

All statistical analysis was performed using GraphPad Prism (v5.0, GraphPad Software Inc., CA, USA). Data that were normally distributed were displayed as mean with standard error of the mean (SEM) and analysed using two-tailed students t-test, or, for three groups or more, one-way ANOVA. Data that were not normally distributed were displayed as median with interquartile range (25%-75%) and analysed using Mann-Whitney test, or, for three groups or more, Kruskal-Wallis. For all statistical analyses, $p<0.05$ was considered statistically significant. Specific statistical methods used are covered in the relevant chapters.

3 Autofluorescence in an *ex vivo* Langendorff heart model

The study in this chapter describe the application of time resolved fluorescence spectroscopy and diffuse reflectance measurements to characterise the pattern of changes in autofluorescence parameters accompanying hypoxia and glucose deprivation in an *ex vivo* Langendorff heart model.

3.1 Introduction

The Langendorff heart preparation is a convenient method to study biochemical or physiological responses of the heart in response to a specific alteration in conditions to address a specific hypothesis in a way that might be challenging or not possible *in vivo*. The history of the development of this technique and further technical details were outlined in the Materials and Methods, chapter 2.

The common endogenous fluorophores of the heart (NADH, FAD, collagen and other extracellular molecules) and details of cardiac metabolism and extracellular structure of the heart and changes in the range of health and cardiac disease states are discussed in the Introduction, chapter 1.

In the Langendorff heart preparation, the heart is perfused in a retrograde fashion with either serum or more usually physiological solution (e.g. Krebs-Henseleit buffer, 'Krebs'). The retrograde perfusion meets a closed aortic valve and therefore the entire perfusate is circulated in the coronary arteries via the ostia and then via the coronary sinus to drain into the right atria. The constant-flow system allows the complete regulation of coronary perfusion pressure. The advantages of this technique are the reproducibility, ease of setup, and low cost compared to *in vivo* work. The disadvantages are the fact that the heart is isolated and is perfused with the a physiological Krebs solution rather than the haemoglobin-containing blood, which aside from potential physiological differences of not having circulating blood, haemoglobin itself has a specific optical absorption and fluorescence profile.

The reproducibility of the Langendorff technique provides an opportunity to establish the baseline autofluorescence signature using the fibre-optic probe system of male Sprague-Dawley rat myocardium with the removal of any signal from blood in normal physiological conditions on a beating heart. Changes in metabolism with insults such as hypoxia, ischaemia or loss of energy substrate happen in the timescale of seconds. For the probe system to be useful clinically, it is important to demonstrate that the probe system can measure autofluorescence lifetimes reliably on a second-by-second basis from the surface of a beating heart, and furthermore confirm that

the system has the sensitivity to detect changes in the autofluorescence signature upon such physiological changes.

Additionally, the ability to obtain reproducible physiological insults of hypoxia and glucose deprivation provides an opportunity to determine the pattern of changes in the autofluorescence signature with these known physiological changes. The establishment of a guide to the changes in autofluorescence signature would then further inform the results of the *in vivo* studies of myocardial infarction-heart failure model (MI-HF) and doxorubicin chemotherapy cardiomyopathy-heart failure model (DOX-HF).

3.2 Methods

3.2.1 Animals

All studies were performed using Sprague-Dawley male rats (250 – 350g) as detailed in chapter 2. All studies involving animals were carried out under protocols approved and regulated under the Animals (Scientific Procedures) Act 1986 (Project Licenses PPL 70/7399 and 70/7419). All animal surgical procedures and perioperative management were carried out in accordance with the United Kingdom Home Office Guide on the Operation of the Animals (Scientific Procedures) Act 1986, which conforms to the Guide for the Care and Use of Laboratory Animals published by the US National Institutes of Health.

3.2.2 Langendorff apparatus

Full details of the Langendorff apparatus is described in chapter 2 and a photograph of the set-up are shown in figure 2.6. A schematic of the Langendorff system is shown in figure 3.1, which has a three-way tap to permit the switching between two reservoirs each containing a perfusate solution bubbled with a gas mixture. The flow is maintained at 18 ml/min by a peristaltic pump (which can be turned on and off) and there are bubble traps within the circuit to ensure that no air bubbles enter the coronary circulation of the perfused heart. Temperature control and monitoring were used to ensure that a constant temperature of the perfused heart was maintained at 37.5 ± 1°C.

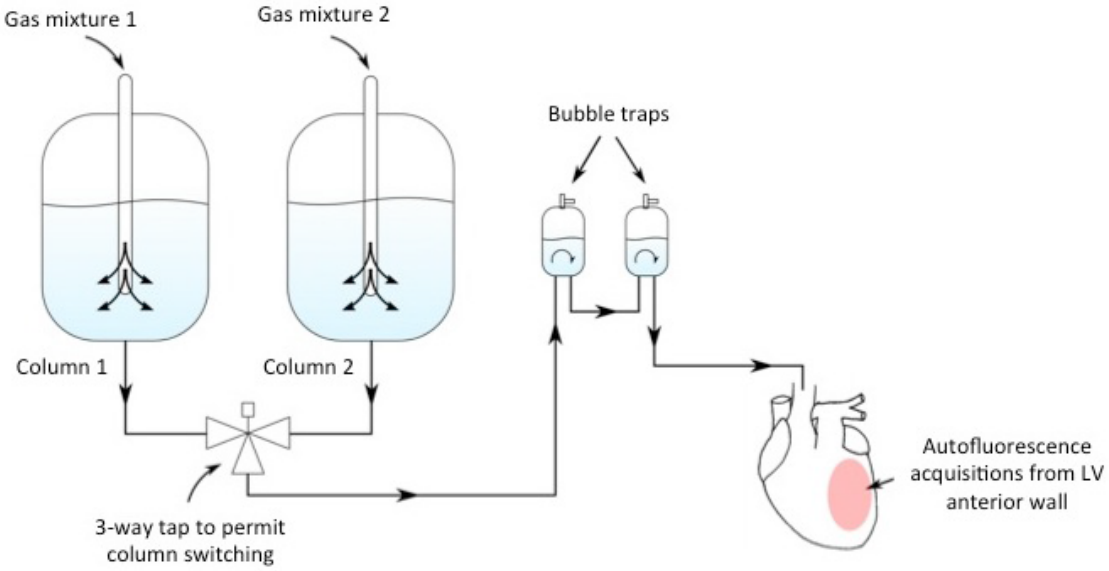


Figure 3.1 Schematic representation of the Langendorff system with three-way tap to permit switching between two different perfusate solutions and / or gas mixtures

3.2.3 *Ex vivo* heart protocol

The Langendorff perfusion apparatus is detailed in figure 3.1. This is a constant flow apparatus in which the perfusates can be placed into two water-jacketed 2L reservoirs (Radnoti, USA) and in which can be bubbled via gas tubing to a sintered glass gas distributor in contact with the perfusate, a gas of choice e.g. mixture of 5% CO_2 & 95% O_2 (Carbogen, BOC, UK). The use of a three-way tap permits 'switching' between the two different reservoirs as required. The perfusate is warmed by a circulating water heating system and a series of insulated tubes to maintain the perfusate at a temperature of 36.5-37.5°C.

The warmed and bubbled perfusate is passed through a 5-micron filter and then taken to the aortic cannula by a series of thermally-insulated flexible Tygon tubes and two bubble traps (Radnoti, USA) conducted by a peristaltic pump (Radnoti, USA). The flow rate of the pump can be controlled between 1.0-100ml/min (typical flow rate used is 16-18ml/minute). The constant flow apparatus has an in-line pressure transducer, mounted proximal to the aortic cannula which allows measurement and titration of the perfusion pressure to maintain it at 90-100 mmHg, which was achieved in all of our experiments using a flow rate of 18ml/min.

The isolated heart protocol is described in full in chapter 2. Hearts are explanted from male Sprague-Dawley rats via a 'Home Office Schedule 1' method of cervical dislocation under terminal anaesthesia (5% Isoflurane, 95% Oxygen mix) and following rapid excision of the aorta, heart, lungs and thymus they are placed into an ice-cold dish of heparinised, buffered Krebs-Henseleit solution (KHB).

The ascending aorta is identified following careful but rapid dissection and is cannulated onto a 1.2 mm diameter metal cannula (Radnoti, USA) at the distal end of the perfusion apparatus and secured in place with a 3-0 silk suture (Ethicon, UK). The pulmonary trunk is identified and a small incision made to allow for free drainage of effluent perfusate. Buffered Krebs-Henseleit ('Krebs') solution (as described by Krebs and Henseleit in 1932) is the base perfusate and has a pH of 7.35 – 7.45 when bubbled with a gas mixture containing 5% CO_2.

Once the heart is secured onto the cannula and attached to the perfusion system the flow is set at 18 ml/min, giving a perfusion pressure of 90-100mmHg. The heart is permitted to stabilize for 10 minutes. The mean time from explant to start of stabilisation was under three minutes with the explanted heart in heparinized ice cold Krebs. Hearts were only studied further with the following protocol if, after the end of stabilization, the heart rate (HR) was in the range 200 – 400 beats per minute (bpm) and there had been no sustained arrhythmias during the last 8 minutes of stabilisation.

Preliminary work with this experimental set-up used a model of 'no-flow ischaemia', where ischaemia of the coronary arteries is achieved by stopping the peristaltic pump, which has been widely reported before in studies in the literature. However, it was clear that in a 'no-flow ischaemia' model there is a significant drop in heart temperature, which is known itself to be a modifier of autofluorescence lifetime. Therefore a column-switching approach was used to permit modification of only one physiological factor in each protocol.

As shown in the figure 3.1, there are two columns. Column 1 contained oxygenated Krebs solution, which was bubbled with gas mixture (95% O_2 / 5% CO_2), and column 2 contained either a 'hypoxia' perfusate (deoxygenated Krebs solution bubbled with a 95% N_2 / 5% CO_2 gas mixture) or a glucose-depleted oxygenated (95% O_2 / 5% CO_2) 'mannitol' perfusate, where the glucose in the Krebs solution was replaced by mannitol (a sugar alcohol with similar molecular weight and osmotic properties but metabolically inert in mammalian cells (Nasrallah & Iber, 1969; Saunders & Wiggins, 1981)).

Autofluorescence and diffuse reflectance data were collected from the anterior wall of the left ventricle. The tip of the probe was positioned in gentle contact with the epicardial surface of the beating heart and held in place by a clamp stand during the protocol. Owing to the movement of the beating heart, acquisition times were chose to cover multiple heartbeats so that the integration times used were 1 s for UV excitation, 1 s for blue excitation and 50 ms for white light illumination for diffuse reflectance measurements. Acquisitions were made every 5 seconds during the protocol. The following protocol was used:

1. Stabilization period (10 minutes) with inclusion criteria for intrinsic heart rate and absence of sustained arrhythmia in the last 8 minutes of the stabilization period with heart perfused from column 1 (oxygenated (95% O_2 / 5% CO_2) Krebs solution)

2. Baseline measurements (3 minutes) with heart perfused from column 1 (oxygenated (95% O_2 / 5% CO_2) Krebs solution)

3. Physiological insult measurements (7.5 minutes) with heart perfused with from column 2 – either:

    a. CONTROL - oxygenated (95% O_2 / 5% CO_2) Krebs solution

    b. HYPOXIA – hypoxic (95% N_2 / 5% CO_2) Krebs solution

    c. MANNITOL – oxygenated (95% O_2 / 5% CO_2) modified - Krebs solution (where glucose is replaced with metabolically inert mannitol)

4. 'Reperfusion' (15 minutes) with column 1 (oxygenated (95% O_2 / 5% CO_2) Krebs solution)

3.2.4 Data analysis: spectral analysis, fluorescence lifetime data analysis and diffuse reflectance data analysis

Spectral analysis of autofluorescence data was performed as described previously in chapter 2. Autofluorescence intensity data was normalised to the average of the first minute of baseline measurement. Ratios of autofluorescence channel intensity were calculated for UV 375nm excitation channels 1, 2 and 3 only, with blue 440nm excitation channel 4 excluded. This is because it would be potentially be affected by day-to-day minor variation in coupling efficiency or laser power differences between the two lasers of the instrument.

Fluorescence lifetime data was analysed as described previously in chapter 2. Channel 1 analysed using by fitting a single exponential decay model giving a lifetime τ. Channels 2, 3 and 4 were analysed by fitting a double exponential decay model giving the following lifetime parameters β, τ_1, τ_2, τ_{mean}. The system response was measured using reference fluorophores: 4',6-Diamidino-2-phenylindole dihydrochloride (DAPI) (Sigma-Aldrich, USA) for 375nm excitation in all detection channels, and Erythrosin B (Sigma-Aldrich, USA) for 440nm excitation.

Diffuse reflectance data was analysed as described previously in chapter 2 and results are reported in units of absorbance, normalised to a white reference target (WS-1-SL, Labsphere, USA).

3.3 Results

3.3.1 Preliminary 'no-flow ischaemia' experiments

Preliminary work with a 'no-flow ischaemia' model showed a significant change in autofluorescence upon 'no flow ischaemia' as shown in figure 3.2. There was a significant increase in mean autofluorescence lifetime τ_{mean} of channel 2 (NADH) on no-flow ischaemia. In the majority of hearts there was an increase in τ_{mean} of channel 4 (FAD) on no-flow ischaemia. There was a significant rise in the redox ratio – (CH2 I / CH3 I) – on no-flow ischaemia. However there was noted to be a significant temperature drop of the heart with no-flow ischaemia, which is predictable as the warmed perfusate is the heat source for the heart in the Langendorff setup. Figure 3.3 highlights the change in NADH lifetime and the change in temperature of the heart. The correlation between these curves is very high, r = 0.905. Figure 3.4 shows the change in the autofluorescence lifetime of a solution of NADH with temperature measured using a cuvette system and this shows that with a decrease in temperature, there is an increase in the fluorescence lifetime of NADH potentially confusing interpretation of the results of 'ischaemia'. Therefore the decision was made that experiments would be conducted using a column switch protocol between oxygenated (95% O_2 / 5% CO_2) and hypoxic (95% N_2 / 5% CO_2) Krebs solution, which would do everything possible to abrogate temperature as a confounding factor in the results.

3.3.2 Diffuse reflectance measurements

Figure 3.5 shows tissue absorption curves from the diffuse reflectance measurements from the Langendorff preparation from the oxygenated 'baseline' state and deoxygenated 'hypoxic' state. In the baseline oxygenated curve (in blue) a double peak profile is seen as expected with local maxima calculated by the first order derivative (FOD) at 543.9 nm and 578.3 nm. The deoxygenated 'hypoxic' state shows a complex spectrum and shows a pronounced peak at 550 nm and a shoulder at 520 nm, attributable to reduced cytochrome c. There is a shoulder at approximately 560 nm, which is attributable to deoxygenated myoglobin. The difference between the curves for oxygenated and deoxygenated tissue is greatest at 578.3 nm and 600.4 nm as calculated by first order differential (FOD).

The ratio of absorbance at the wavelengths where the difference is maximal, i.e. A(578.3 nm) / A(600.4 nm) can be used as a readout of the oxygenation state of the tissue. Figure 3.6 shows the variation of tissue oxygenation derived from tissue absorbance [A(578 nm)/A(600 nm) a.u.] in control (blue, n=4), hypoxia (red, n=5) and mannitol (green, n=4) protocols. This shows that in

the hypoxia protocol (red curve) there was a decrease in tissue oxygenation upon column switching from oxygenated to hypoxic Krebs solution, returning to baseline levels upon column switch back to oxygenated Krebs solution. The curves for the control and mannitol protocols confirm that tissue oxygenation did not change during the protocol.

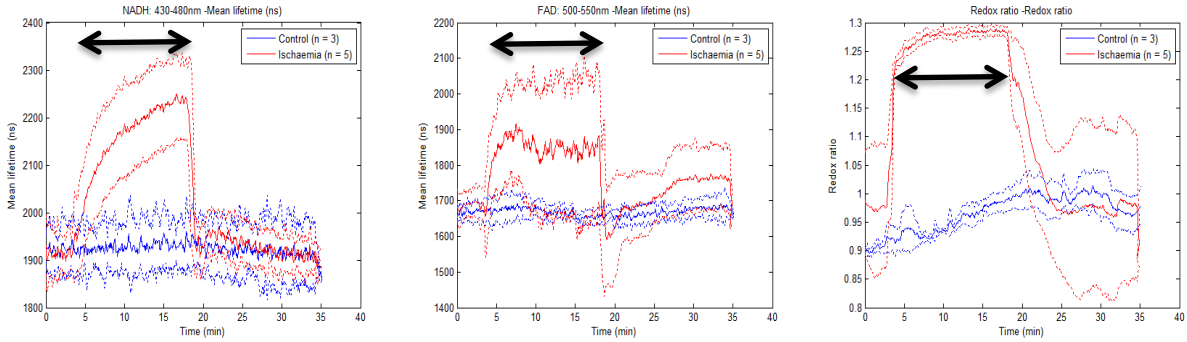


Figure 3.2 From left to right: initial results of 'No-flow ischaemia' method. Mean fluorescence lifetime for channel 2 (NADH), mean fluorescence lifetime for channel 4 (FAD), and redox ratio (Ch2 I / Ch2 + Ch3 I = [NADH]/(*a*[NADH] + *b*[FAD])). Black arrows show the duration of 'no flow ischaemia'. Blue indicates control, red indicates ischaemia, solid lines indicate mean, and pale dashed lines indicate ± 1 s.d.

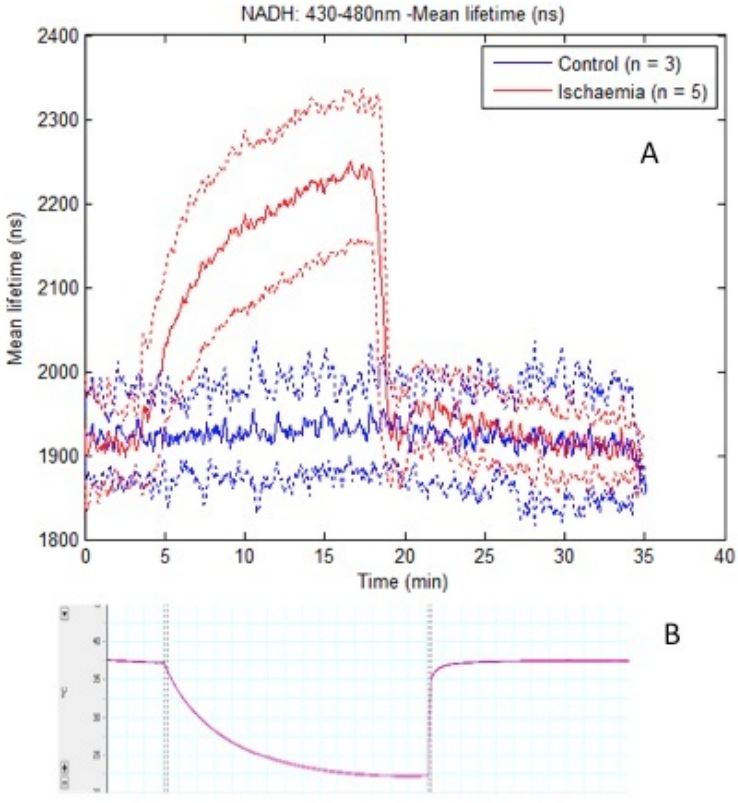


Figure 3.3 Mean fluorescence lifetime for channel 2 (NADH) on 'no-flow ischaemia' (A) against time, and temperature measurement just proximal to the aortic cannula against time (B) showing a high degree of correlation (r = 0.905). In (A) blue indicates control, red indicates ischaemia, solid lines indicate mean, and pale dashed line indicate ± 1 s.d.

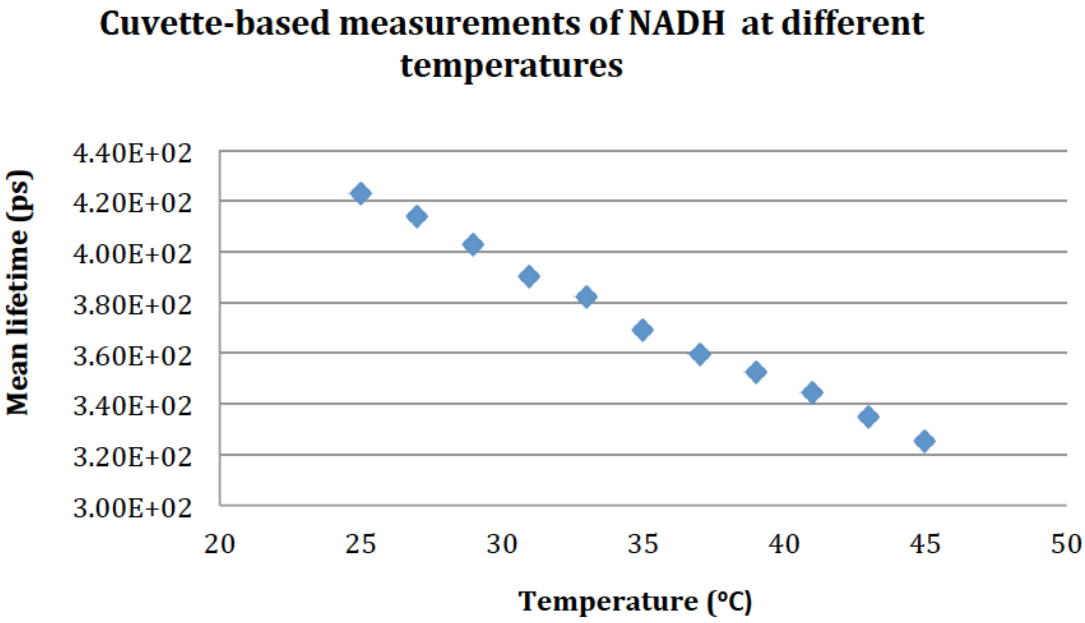


Figure 3.4 Variation of NADH in solution mean lifetime with temperature measured in cuvette system

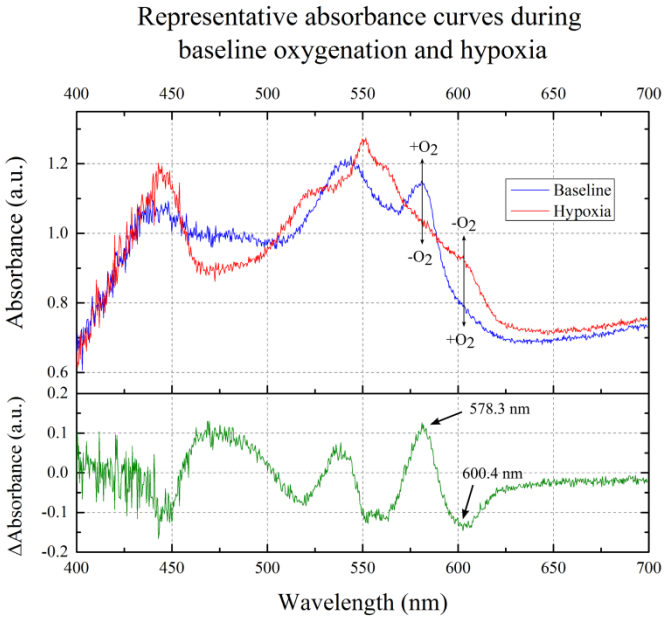


Figure 3.5 Absorbance spectra at baseline (blue) and on hypoxia (red) obtained from the Langendorff hypoxia model. Difference between the two states is summarised as Δabsorbance (green). Black arrows are positioned at position of maximum difference in absorbance in oxygenated and deoxygenated states - 578nm and 600nm

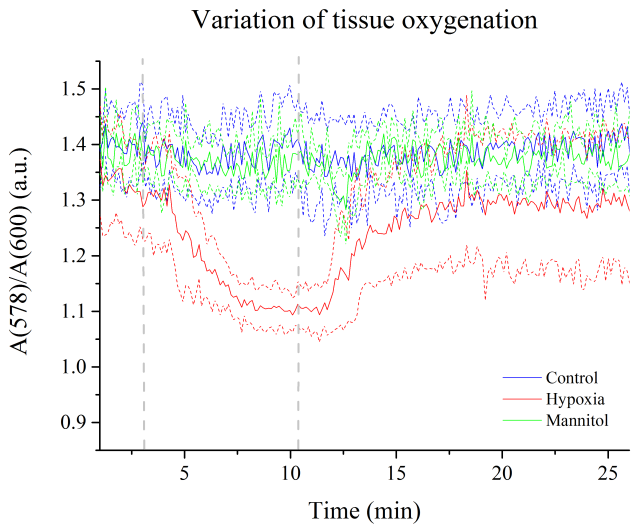


Figure 3.6 Variation of tissue oxygenation derived from tissue absorbance [A(578 nm)/A(600 nm) a.u.] in control (blue, n=4), hypoxia (red, n=5) and mannitol (green, n=4) protocols (solid line = mean, dashed lines = 1 .s.d.). Column switches shown by vertical dashed lines.

3.3.3 Autofluorescence spectral measurements

Figure 3.7 shows the autofluorescence intensity during protocols normalised to the first minute of measurements for control, hypoxia and mannitol protocols. In the control protocol there was noted to be a very slight increase in fluorescence intensity over time in channels 1,2 & 3 and a short temporary increase in fluorescence intensity on switching from column 2 to column 1.

On hypoxia, an increase of autofluorescence intensity is seen in channels 1, 2, & 3 and a decrease of autofluorescence intensity is seen in channel 4. Figure 3.8 shows that there is a shift towards shorter wavelengths with an increase in the relative intensity of fluorescence in channel 1 (400 – 420 nm) and channel 2 (430 – 480 nm) and a relative decrease intensity of fluorescence in channel 3 (500 – 550nm) under UV excitation. Figure 3.9 shows the redox ratio, which is the relative intensity of channels 2 and 3 [NADH]/(α[NADH] + β[FAD]), where α and β are the contribution of NADH and FAD respectively to channel 3 with UV excitation. This figure shows that there is an increase in the redox ratio with hypoxia. During hypoxia there is a change to a new plateau at a higher fluorescence intensity for channels 1, 2, 3 and also for redox ratio, and a lower plateau for channel 4 intensity. Upon reperfusion there is a decrease in autofluorescence intensity for channels 1, 2, 3 and redox ratio to values below the original baseline and furthermore the rate of change in fluorescence intensity (Δfluorescence intensity) on reperfusion (taking approximately 5 minutes to change from 10% - 90% intensity) is slower than on initial hypoxia (taking approximately 2 minutes to change from 90% to 10% intensity). Additionally on reperfusion there is an increase in channel 4 autofluorescence intensity although there is not an overshoot compared to original baseline, as is seen in channels 1, 2 and 3.

During glucose deprivation in the mannitol protocol there is a decrease in autofluorescence intensity in channels 1, 2 and 3 as shown in figure 3.7, and there is a decrease in redox ratio as shown in figure 3.9. There is a shift towards longer wavelengths as shown in figure 3.8 with a decrease in the relative fluorescence intensity from channels 1 and 2, and an increase in the relative intensity of channel 3 upon glucose deprivation. There is a decrease in redox ratio, which continues to fall even after the switch back to glucose-containing perfusate. There was some variation in the channel 4 autofluorescence intensity changes upon glucose deprivation, with 1 out of 4 specimens showing an increase in autofluorescence whilst for the remainder the autofluorescence intensity remained essentially unchanged, which is shown in the flat mean autofluorescence curve for channel 4.

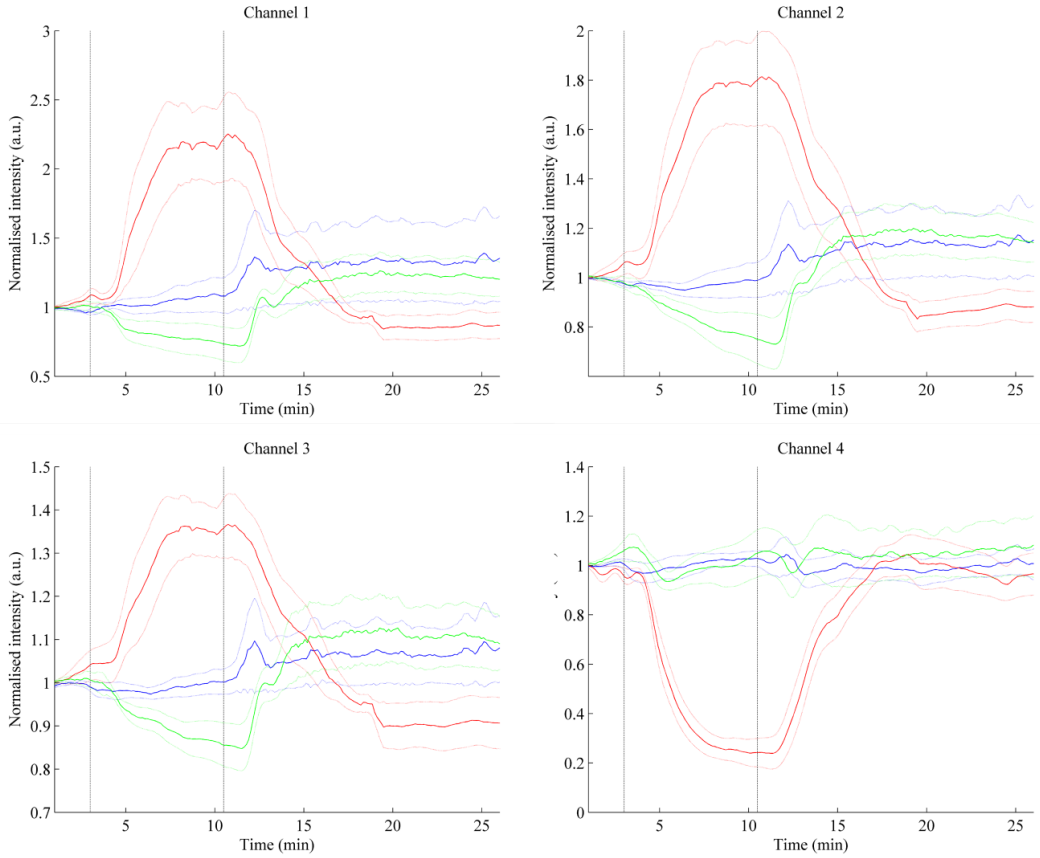


Figure 3.7 Normalised fluorescence intensity during protocols: control (blue, n=4), hypoxia (red, n=5) and mannitol (green, n=4) (solid line = mean, pale dashed lines = 1 .s.d.) Switch of perfusate shown by grey vertical dashed line

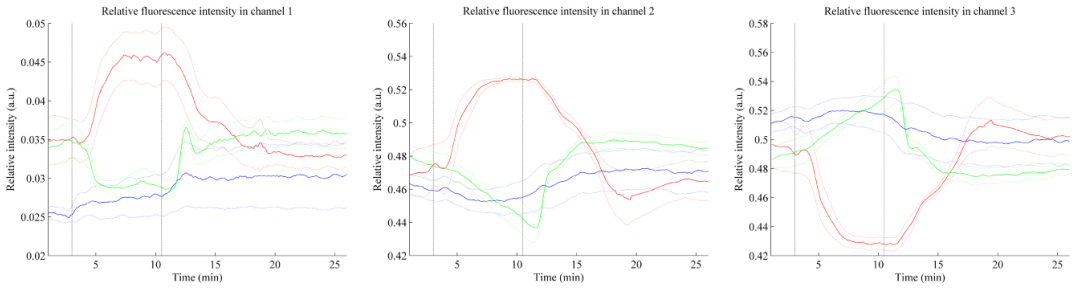


Figure 3.8 Relative fluorescence intensity in each detection channel using UV excitation – (Ch X / (CH1+CH2+CH3)): control (blue, n=4), hypoxia (red, n=5) and mannitol (green, n=4) (solid line = mean, pale dashed lines = 1 .s.d.) Switch of perfusate shown by grey vertical dashed line

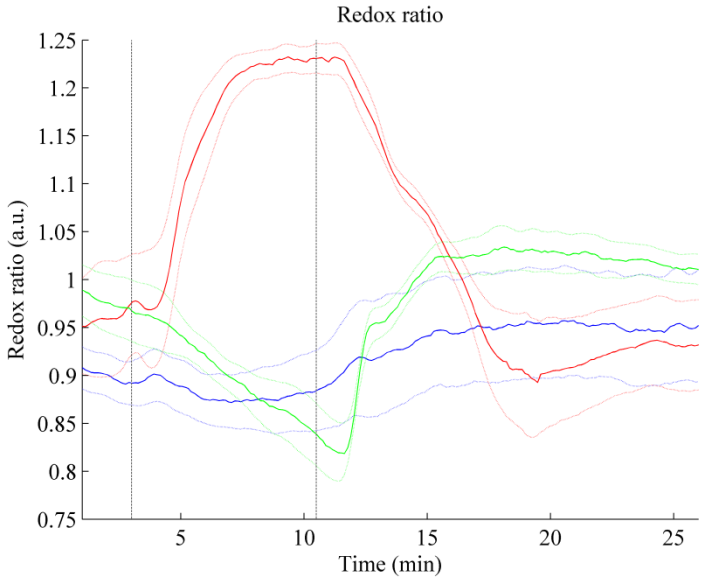


Figure 3.9 Redox ratio (ratio CH2 : CH3 fluorescence : control (blue, n=4), hypoxia (red, n=5) and mannitol (green, n=4) (solid line = mean, pale dashed lines = 1 .s.d.) Switch of perfusate shown by grey vertical dashed line

3.3.4 Autofluorescence lifetime measurements

Figure 3.10 shows the autofluorescence lifetime measured in channel 1 for the control, hypoxia and mannitol protocols. As discussed in chapter 2, channel 1 data were fitted using a single exponential decay model because of the low number of photons detected in this channel during baseline measurements (~5000 photons). In all cases the noise level is high. The mean fluorescence lifetime using acquisitions from all data gave a fluorescence lifetime of 1.75 ± 0.13 ns (n = 4). During hypoxia, there is little obvious change during hypoxia but there is an increase in the autofluorescence lifetime seen upon reperfusion with oxygenated KH solution, followed by a decrease until stabilization is reached. This is a similar pattern to that observed in mean autofluorescence lifetime of channel 2 (see figure 3.11) although in this case changes during hypoxia are well pronounced. During glucose deprivation with the mannitol protocol we observe

an apparent decrease in autofluorescence lifetime in channel 1 which, returning to baseline values upon reperfusion with normal glucose-containing Krebs solution.

Figure 3.11 shows the autofluorescence lifetime parameters in channel 2, calculated with a double exponential fitting model. Utilizing all data points from control hearts (n = 4) we obtained a mean lifetime (τ_{mean}) of 1.85 ± 0.04 ns, a short lifetime (τ_1) of 0.82 ± 0.02 ns, a long lifetime (τ_2) of 3.47 ± 0.16 ns and a fraction of the short lifetime component (β) of 0.61 ± 0.01 (n = 4). During hypoxia we observe a decrease in the mean autofluorescence lifetime, a decrease in the short lifetime (τ_1), an increase in the long lifetime (τ_2) and an increase in the fraction of the short lifetime component (β). Glucose deprivation causes changes in autofluorescence decay characteristics in channel 2 that are less pronounced than those seen with hypoxia. Indeed, overall there is no change in overall mean autofluorescence lifetime of NADH at this detection wavelength. Clear changes are only observed in the long lifetime, which shows a slight decrease upon perfusion with mannitol, returning to the baseline upon reperfusion with glucose. We also note a slight increase in the contribution of the short lifetime component after reperfusion with glucose-containing Krebs solution.

Figure 3.12 shows the autofluorescence lifetime data for channel 3, calculated with a double exponential fitting model. Utilizing all data points from control hearts (n = 4) obtained mean lifetime (τ_{mean}) of 1.59 ± 0.01 ns, a short lifetime (τ_1) of 0.77 ± 0.02 ns, a long lifetime (τ_2) of 3.08 ± 0.15 ns and a fraction of the short lifetime component (β) of 0.65 ± 0.02 (n = 4). The pattern of changes is similar to channel 2 as this channel contains predominately NADH, with some contribution of FAD. The mean autofluorescence lifetime extracted for this channel is shorter than channel 2 mean lifetime (τ_2) for control data, which can be attributed to a shorter long lifetime component and a greater fraction of short lifetime component (β) and may represent the contribution FAD in this channel. During hypoxia, there is a clear decrease in the mean autofluorescence lifetime, a decrease in the short lifetime (τ_1), an increase in the long lifetime (τ_2) and an increase in the fraction of the short lifetime component (β). On glucose deprivation there is an increase in the long lifetime (τ_2) and there is a decrease in the contribution of short lifetime component (β), which slowly returns to the baseline value on return of glucose.

Figure 3.13 shows the autofluorescence lifetime data for channel 4, calculated with a double exponential fitting model. The changes in the channel are more complex than in the other channels and there was a slightly greater degree of variation of approximately 50 ps during the control protocol. Utilizing all data points from control hearts (n = 4) obtained mean lifetime (τ_{mean}) of 1.524 ± 0.048 ns, a short lifetime (τ_1) of 0.83 ± 0.022 ns, a long lifetime (τ_2) of 3.047 ± 0.114 ns and a fraction of the short lifetime component (β) of 0.685 ± 0.036 (n = 4). During hypoxia there is a biphasic response. Initially there is an increase in mean autofluorescence lifetime due to a decrease in the fraction of the short component β, despite a fall in the short lifetime (τ_1) followed by a rapid decrease in mean lifetime upon reperfusion with oxygenated

Krebs solution which undershoots beyond the baseline, which then increases again and then overshoots beyond the initial baseline during the period measured in the protocol. The changes on reperfusion with oxygenated Krebs solution are caused by a rapid increase in the long lifetime (τ_2), a rapid rise of the short lifetime (τ_1) to return to baseline followed by a rapid increase in and overshoot compared to baseline in the fraction of the short lifetime component (β). It is challenging to explain these changes, particularly because we do not observe a similar pattern in any other autofluorescence parameter. Indeed, we have previously demonstrated that changes in the steady-state autofluorescence signal occur at a slower rate in reperfusion relative to the initial oxygen depletion and a similar pattern can be observed for the time-resolved properties of channels 2 and 3. It is possible that FAD autofluorescence decay properties are more sensitive to metabolic alterations in the myocardium than NADH autofluorescence, which would explain the differences observed. Moreover, in contrast with NADH, FAD autofluorescence derives from mitochondria only. Therefore, these alterations may also indicate a rapid reestablishment of the oxidative pathway. This would not be observed in the NADH autofluorescence properties since NADH is present in both the aerobic and anaerobic pathways. However, this still requires validation. On glucose deprivation there doesn't appear to be any significant changes in channel 4 lifetime parameters, other than a possible decrease in the fraction of the short lifetime component.

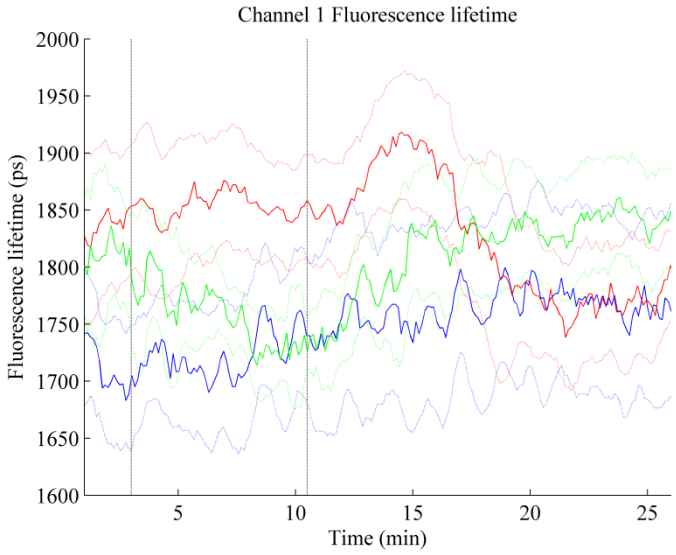


Figure 3.10 Channel 1 autofluorescence lifetime (single exponential decay model) during protocols: control (blue, n=4), hypoxia (red, n=5) and mannitol (green, n=4) (solid line = mean, pale dashed lines = 1 .s.d.) Switch of perfusate shown by grey vertical dashed line

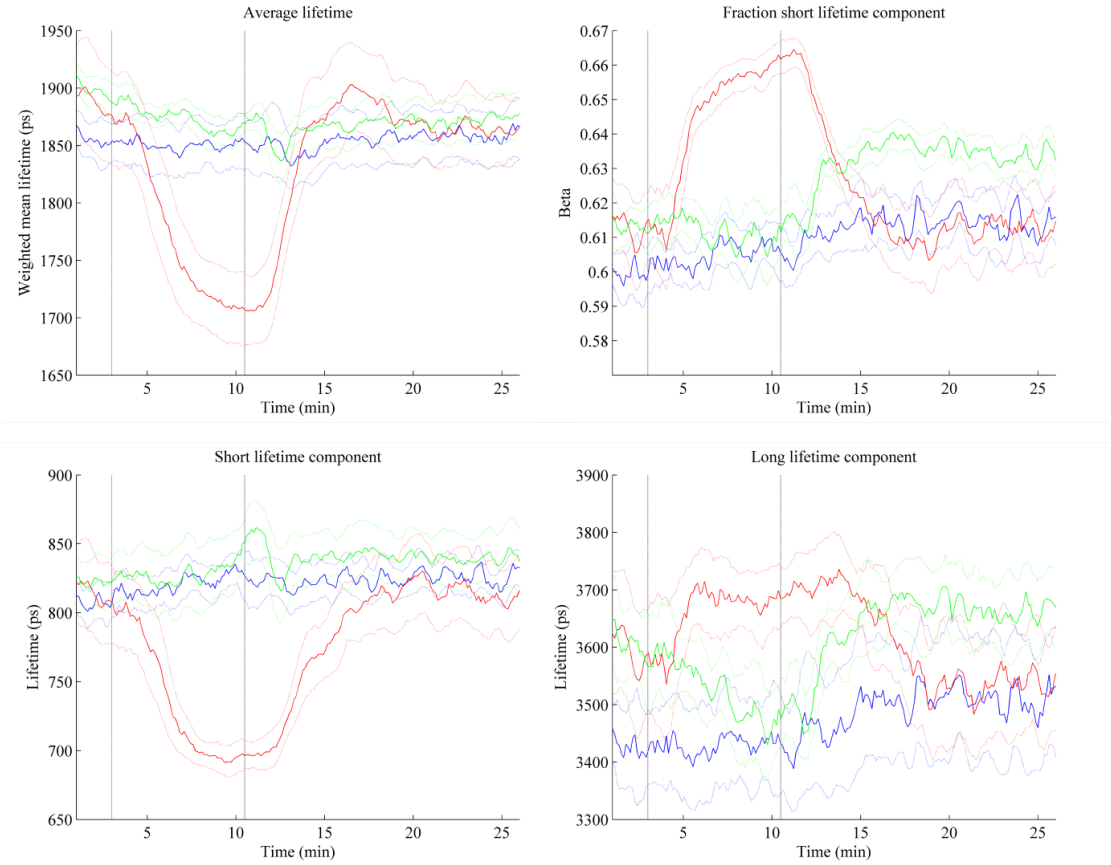


Figure 3.11 Channel 2 ('NADH' - 375nm excitation, 430nm – 480nm emission) autofluorescence lifetime parameters (double exponential model) during protocols: control (blue, n=4), hypoxia (red, n=5) and mannitol (green, n=4) (solid line = mean, pale dashed lines = 1 s.d.) Switch of perfusate shown by grey vertical dashed line

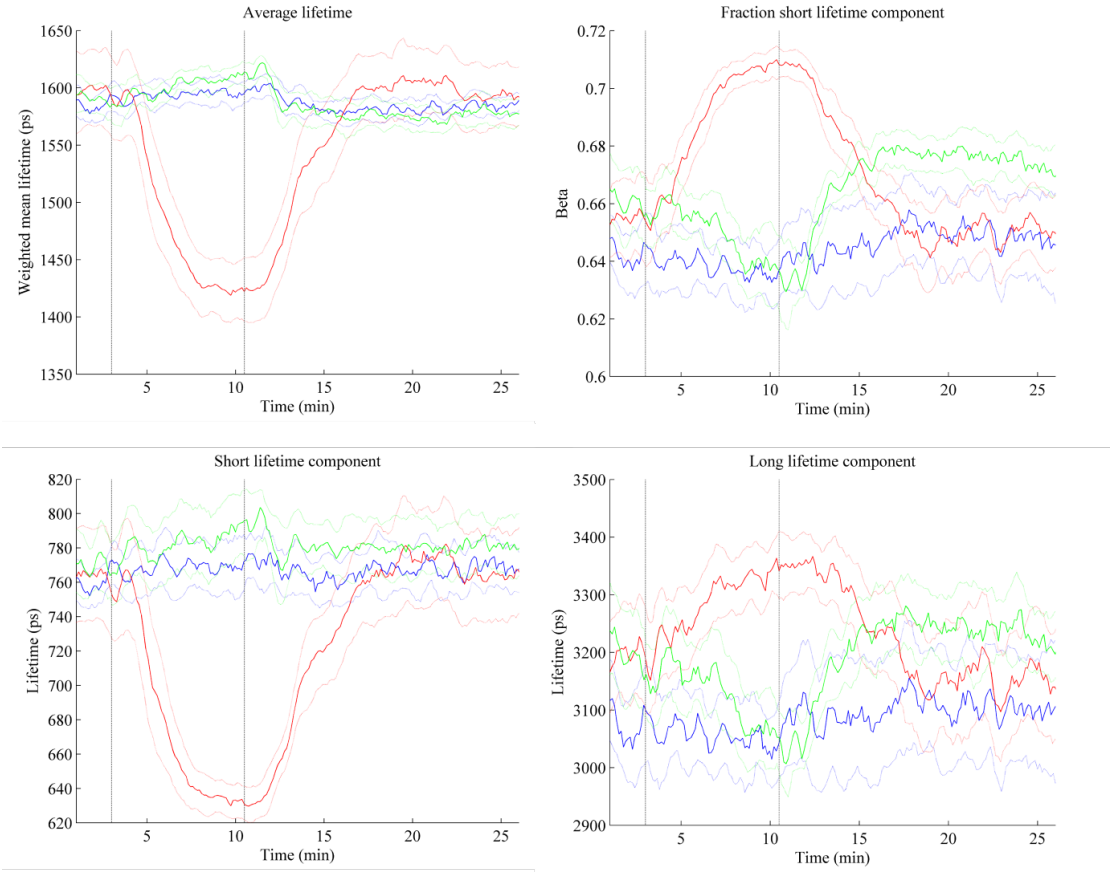


Figure 3.12 Channel 3 ('NADH' & 'FAD' - 4375nm excitation, 500nm – 550nm emission) autofluorescence lifetime parameters (double exponential model) during protocols: control (blue, n=4), hypoxia (red, n=5) and mannitol (green, n=4) (solid line = mean, pale dashed lines = 1 s.d.) Switch of perfusate shown by grey vertical dashed line.

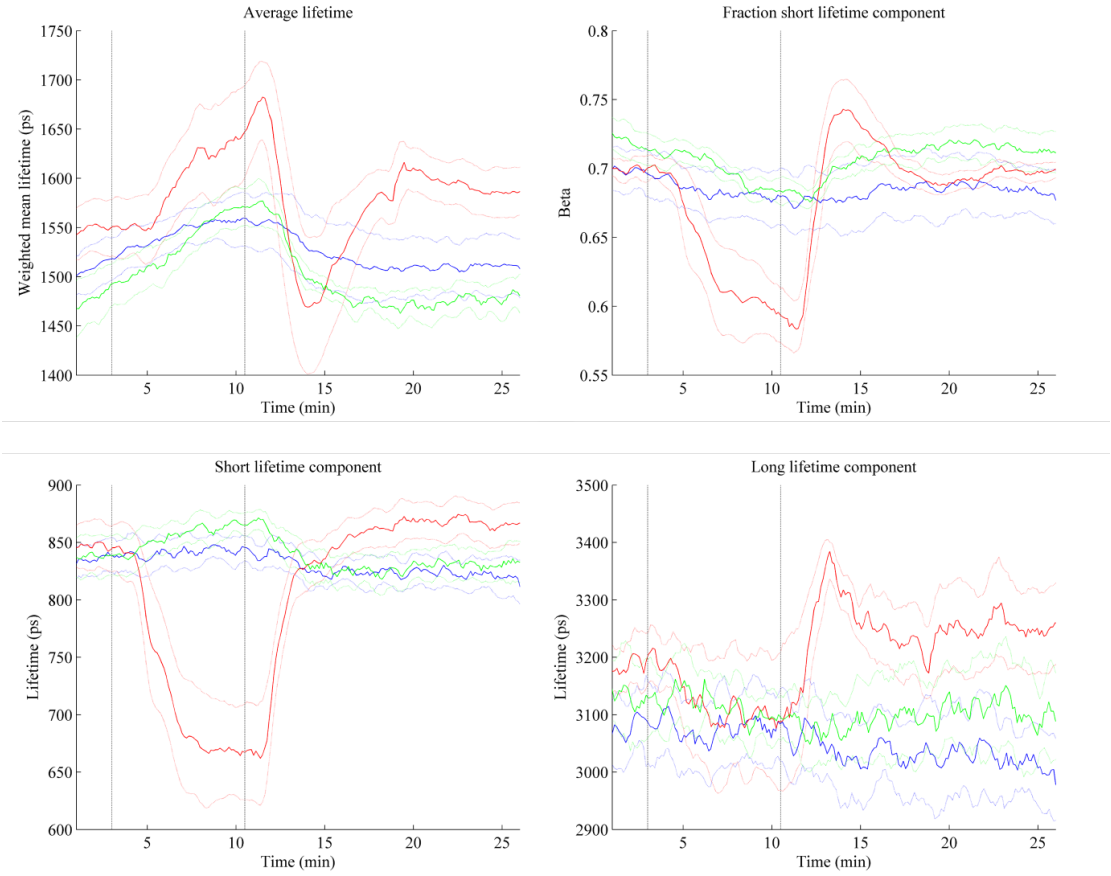


Figure 3.13 Channel 4 ('FAD' - 440nm excitation, 500nm – 550nm emission) autofluorescence lifetime parameters (double exponential model) during protocols: control (blue, n=4), hypoxia (red, n=5) and mannitol (green, n=4) (solid line = mean, pale dashed lines = 1 s.d.) Switch of perfusate shown by grey vertical dashed line.

3.4 Discussion

3.4.1 Diffuse reflectance measurements

The absorbance spectra of the key cardiac tissue chromophores are shown in chapter 1. In a Langendorff preparation the predominant chromophore in the cardiac tissue is myoglobin as the preparation is blood-free and therefore there are no haemoglobin-containing red blood cells. As discussed in chapter 1, myoglobin has a double peak absorption spectrum profile with maxima at approximately 544 nm and 578 nm, with a minimum at approximately 560 nm (Schenkman, Marble, Burns, & Feigl, 1997). Mitochondrial cytochromes also contribute significantly to the absorption spectrum of cardiac tissue, in particular cytochrome c, discussed in chapter 1, which in its reduced form has a well-defined peak at approximately 550 nm. Figure 3.5 shows tissue absorption curves from the diffuse reflectance measurements from the Langendorff preparation from the oxygenated 'baseline' state and deoxygenated 'hypoxic' state. In the baseline oxygenated curve (in blue) a double peak profile is seen as expected with local maxima calculated by the first order derivative (FOD) at 543.9 nm and 578.3 nm. This is in agreement with previously reported

values in the literature. (Schenkman et al., 1997) The FOD-derived minimum was calculated as 568 nm, which is considerably red-shifted compared to the expected value of 560nm. The deoxygenated 'hypoxic' state shows a complex spectrum, which doesn't match simply the deoxygenated myoglobin curve shown in figure 1. The deoxygenated 'hypoxic' state shows a pronounced peak at 550 nm and a shoulder at 520 nm, attributable to reduced cytochrome c. There is a shoulder at approximately 560 nm, which is attributable to deoxygenated myoglobin. The maximum difference by FOD between the curves for oxygenated and deoxygenated tissue is at 578.3 nm and 600.4 nm.

Diffuse reflectance measurements can be used to quantify myoglobin and haemoglobin concentrations as well as oxygen saturations. Oxygen pulse oximetry quantification such as is used clinically requires careful calibration and most devices typically use absorption at key wavelengths in the infrared spectrum (e.g. 660 nm and 950 nm). With the probe system, only the visible spectrum is recorded, but the variation of tissue oxygen 'state' can be calculated from the ratio of absorbance at the wavelengths where the difference is maximal, i.e. A(578.3 nm) / A(600.4 nm). Figure 3.6 shows the variation of tissue oxygenation derived from tissue absorbance [A(578 nm)/A(600 nm) a.u.] in control (blue, n=4), hypoxia (red, n=5) and mannitol (green, n=4) protocols. This shows that in the hypoxia protocol (red curve) there was a decrease in tissue oxygenation upon column switching from oxygenated to hypoxic Krebs solution, returning to baseline levels upon column switch back to oxygenated Krebs solution. The curves for the control and mannitol protocols show that tissue oxygenation did not change during the protocol and therefore variations in the autofluorescence readout in control or mannitol experiments cannot be attributed to variation in tissue oxygenation.

3.4.2 Autofluorescence spectral measurements

In control protocols there was noted to be a very slight increase in fluorescence intensity over time in channels 1, 2 and 3, which is possibly explained by a small increase in NADH concentration over time. The transient short temporary increase in fluorescence intensity on switching from column 2 to column 1 possibly represents a slight transient variation in temperature. Although all components of the Langendorff setup are surrounded in water-jacketing it is plumbed in series and therefore there may be a small difference in temperature between columns 1 and 2 given that there is a relationship between NADH quantum yield and temperature.

With hypoxia there is an increase of autofluorescence intensity seen in channels 1, 2 (NADH), & 3 and a decrease of autofluorescence intensity in channel 4 (FAD) with a shift towards shorter wavelengths in terms of the intensities seen in each channel under UV excitation. These results suggest a decrease in aerobic metabolism and a switch from oxidative phosphorylation to glycolysis. The absence of oxygen prevents the oxidation of NADH and $FADH_2$, which would

normally use oxygen as the final electron acceptor in the electron transport chain. As a result, NADH and $FADH_2$ accumulate which explains the increase in the NADH fluorescence signal and a decrease in FAD fluorescence signal. The same applies to the changes in the optical redox ratio which is given by the relative intensity of channels 2 and 3 [NADH]/(α[NADH] + β[FAD]), where α and β are the contribution of NADH and FAD to channel 3 with UV excitation. On hypoxia there is an increase in the redox ratio on hypoxia to a new plateau, which is possibly the point at which the oxidative pathway is inhibited and energy is entirely from glycolysis in anaerobic conditions. The heart rate falls during ischaemia (data not shown). Maintenance of this pathway for a longer period would result in irreversible cell damage and cell death. In the protocol, upon reperfusion, there is a decrease in autofluorescence intensity for channels 1-3, and redox ratio to values below the original baseline and furthermore the rate of change in fluorescence intensity on reperfusion (taking approximately 5 minutes to change from 10% - 90% intensity) is slower than on initial hypoxia (taking approximately 2 minutes to change from 90% to 10% intensity). It is well known that myocardial ischaemia has profound effects on the energetics and contractile performance of the myocardium. Furthermore there is a concept that in ischaemia without cell death, there may be adaptive process called preconditioning that potentially can protect the heart from subsequent insults. It is therefore not surprising that there are differences in the temporal changes in and subsequent levels of energetic molecules detected on induction of ischaemia, during ischaemia and subsequent reperfusion and in the period immediately post-insult.

The changes with glucose deprivation are more complicated to interpret. As discussed in the introduction the main source of energy to the normal heart is from fatty acid metabolism (Doenst, Nguyen & E. Dale Abel 2013; W C Stanley et al. 2005). It is thought that the heart has limited scope to store nutrients and therefore in a Langendorff heart model the substrate for energy is glucose within the Krebs solution as the perfusate doesn't contain any fatty acids. With permanent loss of energy substrate it would be expected that there would be a fall in tissue levels of ATP, and increase in reactive oxidative species (ROS), with impaired contractile function and then progressive cell death. An increase in oxidative state has been shown in glucose deprivation studies in the cardiomyocyte cell lines. (Marambio et al. 2010) During glucose deprivation with the mannitol protocol the results show a decrease in autofluorescence from NADH channels, and there is a decrease in redox ratio suggesting a more oxidative state. The rate of change in autofluorescence parameters is slower with glucose deprivation than with hypoxia, and at the point of switch back to glucose there is still continuing fall in the redox ratio. This suggests a progressive rather than abrupt change in metabolism or that there is some level of stored substrate within the myocardium such as intracellular glucose.

3.4.3 Autofluorescence lifetime measurements

With respect to time-resolved autofluorescence measurements the intention was to characterize

the signal during hypoxia and glucose deprivation states so that these measurements could potentially inform *in vivo* models such as myocardial infarction-heart failure or doxorubicin chemotherapy cardiomyopathy-heart failure.

As discussed in chapter 2, channel 1 data were fitted using a single exponential decay model because of the low number of photons detected in this channel during baseline measurements (~5000 photons). In normal healthy myocardium such as in the Langendorff heart, the presence of collagen is relatively small compared to NADH. The channel 1 signal therefore may be dominated by shorter wavelength NADH giving the overall shorter fluorescence lifetime seen of 1.75 ± 0.13 ns (n = 4) in this channel than might be expected from collagen measurements seen in the literature. The changes characterized in the results section for channel 1 show a similar pattern to those in channel 2. It is probable that having a single exponential decay to characterize channel 1 is not sufficient to read out alterations in cardiac tissue metabolism as by its nature cannot describe the contribution of collagen (which would be a longer component) and NADH (which would be a shorter component) in this channel.

Channel 2 is centred on the emission spectrum of NADH and in normal myocardium this will be the predominant fluorophore in this channel. The decay characteristics are calculated from a double exponential model. During hypoxia we observe a decrease in the mean autofluorescence lifetime, a decrease in the short lifetime (τ_1), an increase in the long lifetime (τ_2) and an increase in the fraction of the short lifetime component (β). As discussed in the introduction, NADH in tissue can exist in free form or bound to proteins. In its free form it can exist in two conformations – extended and folded – that have decay components at approximately 300 ps and 700 ps respectively. NADH can bind a very large number of enzymes in the metabolic pathway, and each of these will yield longer lifetimes in the range of 1 to 6 ns (Lakowicz & Masters 2008). Therefore an accurate description of such a complex autofluorescence signal would require fitting four, six, or potentially more exponentially components to describe the folded and extended form of free-NADH, and the bound forms with the possible enzyme-binding partners in a tissue. This would be difficult in terms of number of photons required within acceptable acquisition times. Therefore NADH fluorescence in the literature is usually presented in a simpler double exponential format where the short component is loosely associated with the free NADH and the long component is loosely associated with the protein-bound NADH. In hypoxia, we see an increase in the fraction of the short lifetime component (β) suggesting an increase in the contribution of free NADH to the decay. The decrease in the short lifetime (τ_1) suggests an increase in the proportion of the free NADH in the extended conformation of the molecule, which is associated with a shorter lifetime than the folded conformation. The long component lifetime (τ_2) increases with hypoxia and it is possible that this represents changes in the relative proportion of NADH bound to the different enzymes involved in the metabolic pathways. A change to anaerobic respiration on hypoxia would mean that glycolysis becomes the predominant pathway and therefore lactate dehydrogenase (LDH) would become the

predominant enzyme partner. The change in long lifetime could represent the switch away from other binding partners from the aerobic pathways, such as malate dehydrogenase (MDH), when there is a state of hypoxia. An alternative explanation could be that there is an alteration in the relative ratio of NADPH to NADH. NADP governs lipid, amino acid and nucleotide biosynthetic pathways and the defence against reactive oxygen species by glutathione (GSH) and a recently published paper (Blacker et al. 2014) suggests that changes in long lifetime component may reflect an alteration in the ratio of NADPH and NADH autofluorescence. Channel 3 shows similar patterns of changes as in channel 2, which is expected, as the predominant signal in this channel is NADH with some contribution of FAD.

Changes in the lifetime signature of glucose deprivation in both channels 2 and 3 are less clear-cut than those seen with hypoxia. There appears to be a decrease in long lifetime (τ_2) upon glucose deprivation seen in both channels 2 and 3. There is a slow decrease during the glucose deprivation period which slowly returns to baseline on reperfusion with glucose-containing Krebs solution. There is a decrease in the fraction of the short component (β) along with an overall decrease in the autofluorescence signal would suggest an overall decrease in NADH concentration and, perhaps, an increase in free FAD, given the decrease in the long lifetime, since both free and protein bound forms of the molecule have shorter lifetimes – however further investigation would be needed to validate this.

Channel 4 in normal cardiac tissue is thought to contain autofluorescence signal from FAD, which is optimally excited at 440nm with peak emission between 500 to 550nm. The results showed a complex pattern on hypoxia with a biphasic response with an initial increase in mean autofluorescence lifetime due to a decrease in the fraction of the short component β, despite a fall in the short lifetime (τ_1) followed by a rapid decrease in mean lifetime upon reperfusion with oxygenated Krebs solution which undershoots beyond the baseline, then increases again and then overshoots beyond the initial baseline during the period measured in the protocol. The changes on reperfusion with oxygenated Krebs solution are caused by rapid increases in the long lifetime ($\tau 2$), rapid rise of the short lifetime ($\tau 1$) to return to baseline followed and an rapid increase in and overshoot compared to baseline in the fraction of the short lifetime component (β). It is possible that FAD fluorescence is more immediately sensitive to the metabolic alterations in the cell i.e. redox state or other biochemical alteration of FAD's biochemical and electro physical environment. FAD autofluorescence derives from mitochondria only compared to NADH, which is present both in the cytosol and mitochondria and involved with both anaerobic and aerobic metabolism. It is possible that these changes in the lifetime signature on hypoxia and reperfusion with oxygenated Krebs represent the rapid reestablishment of the oxidative pathways in which FAD fluorescence is involved.

There appears to be little change in the lifetime parameters in channel 4 on glucose deprivation except possibly a decrease in the fraction of short lifetime (β) suggesting that FAD

autofluorescence is less sensitive to changes upon glucose deprivation, suggesting that possibly stored substrate or alternative pathways feeding into the Krebs/citric acid cycle causing therefore less effect upon the reactions in which FAD is involved.

The overall trends in autofluorescence lifetime parameters in this *ex vivo* Langendorff model in terms of increase (+), decrease (-), or no variation (0), are summarized in table 3.1.

		Hypoxia	Glucose deprivation
Redox ratio		**+**	**-**
CH1	**Intensity**	**+**	**-**
	τ	**0**	**0**
CH2	**Intensity**	**+**	**-**
	τ_{mean}	**-**	**0**
	τ_1	**-**	**0**
	τ_2	**+**	**-**
	β_1	**+**	**-**
CH3	**Intensity**	**+**	**-**
	τ_{mean}	**-**	**0**
	τ_1	**-**	**0**
	τ_2	**+**	**-**
	β_1	**+**	**-**
CH4	**Intensity**	**-**	**0**
	τ_{mean}	**+**	**0**
	τ_1	**-**	**0**
	τ_2	**-**	**0**
	β_1	**-**	**?-/0**

Table 3.1 Summary of trend in autofluorescence lifetime parameters during hypoxia and glucose deprivation (mannitol) protocols compared to control: increase (+), decrease (-) or no change observed (0)

3.5 Summary

In summary, the results in the chapter demonstrate the successful application of time resolved fluorescence spectroscopy and diffuse reflectance measurements to characterise the pattern of changes in autofluorescence parameters accompanying hypoxia and glucose deprivation in an *ex vivo* Langendorff heart model. As far as we are aware, this is the first report of autofluorescence reproducibly and reliably recorded from the surface of the beating heart in a Langendorff preparation on a second-by-second basis. Furthermore, the sensitivity of the probe system to detect the changes in the autofluorescence signature upon hypoxia and glucose deprivation was demonstrated. These results gave the reassurance that embarking on *in vivo* studies of myocardial infarction-heart failure (MI-HF) and doxorubicin chemotherapy cardiomyopathy-heart failure (DOX-HF) would be a worthwhile endeavour.

4 Autofluorescence in a myocardial infarction-heart failure model

The study in this chapter describe the application of time resolved fluorescence spectroscopy and diffuse reflectance measurements to measure structural and metabolic changes in a post-myocardial infarction heart failure model at 1, 2, 4 and 16 weeks post myocardial infarction surgery.

4.1 Introduction

Heart failure is defined as the inability of the heart, resulting from an abnormality of heart structure or function, to deliver oxygen to the metabolizing tissues at the rate matching the requirement of those tissues thereby causing a clinical syndrome with typical symptoms and signs, such as breathlessness and fluid overload. (Wijns et al. 2012) In the developed world 1-2 % of the population has heart failure, rising to greater than 10 % of those aged 70 years or older. Despite huge advances in therapy, the annualized mortality can still approach 10 %. The abnormality in function can be of systolic function, resulting in a heart failure with reduced ejection fraction (HF-REF), or of diastolic function, resulting in a heart failure with preserved ejection fraction (HF-PEF). In systolic heart failure, there is a myocardial injury causing a loss of myocytes, and maladaptive changes in the surviving myocytes and extracellular matrix in a process called 'pathological remodelling' with heart dilatation and reduction in contractility (Shah & Mann 2011). In the developing world, around two-thirds of systolic heart failure is attributable to myocardial infarction (MI) from coronary artery disease (CAD).

Myocardial infarction (MI) is characterized by cardiomyocyte death due to an impairment in the energy supply and demand, typically caused by rupture of an atherosclerotic plaque and consequent interruption of blood supply to the heart, i.e. a type-1 MI. (Thygesen et al. 2012) Following an MI, a number of repair mechanisms try to maintain the structural integrity and viability of the infarcted myocardium, including replacement of injured tissue by a fibrotic scar and remodelling of the remaining ventricle. These structural changes may initially be compensatory or adaptive, however on-going remodelling becomes maladaptive and causes changes leading towards a heart failure syndrome. (W M Blankesteijn et al. 2001; Cohn et al. 2000) Adverse ventricular remodelling is generally accepted as a determinant precursor of heart failure following MI, although it can also be developed as consequence of other causes of myocardial injury (e.g. myocarditis, chemotherapeutics) (Stefanon et al. 2013).

The progression of the injured myocardium from compensatory hypertrophy to decompensated failure is a field of huge research interest, as elucidation and modification of these pathways will

yield future targets for heart failure therapies. What is clear is that remodelling after a myocardial infarction involves complex and dynamic functional, morphological and biochemical changes both in the region of infarction itself, but also in the 'remote' non-infarcted myocardium. (Opie et al. 2006) Reported changes include hypertrophy of individual cardiomyocytes, remodelling of the blood supply with collateralisation of vasculature, and an increase of interstitial collagen in remote sites to the MI. Maladaptive structural changes impair tissue compliance, contraction and relaxation, (Lyon et al. 2009; Caorsi et al. 2013) as well as alteration of the neurohumoral receptor and electrical properties of the tissue (Kumarswamy et al. 2012; Lyon et al. 2012) leading to further functional impairment and progression toward the heart failure syndrome. This is compounded by impairment of mitochondrial function and energy utilisation within the failing cardiomyocytes, so called "metabolic remodelling" of the failing heart. (Doenst, Nguyen & E Dale Abel 2013)

The common endogenous fluorophores of the heart (NADH, FAD, collagen and other extracellular molecules) and details of cardiac metabolism and extracellular structure of the heart and changes in the structure and postulate changes in metabolism in the range of health and cardiac disease states are discussed in chapter 1.

A number of structural alterations occur in the heart failure that develops following a large myocardial infarction (MI). After an acute myocardial injury such as myocardial infarction of the left ventricle, the wound-healing process is rapidly initiated, typically within a few hours after the injury occurs, and is initially localized to the area of infarction. The initial remodelling phase consists of the repair of the wounded area via deposition of collagen and rearrangement of the collagenous matrix to form a non-contractile and potentially expanding scar. This process is induced by the proliferation and up-regulation of myofibroblasts. (W M Blankesteijn et al. 2001; Cleutjens et al. 1995) The deposition of collagen increases the tensile strength of the muscle, which helps to try to maintain the cardiac output. Collagen deposition is seen within two days of infarction but continues and is still seen after three months and this process is observed throughout the heart, including in areas remote to the infarction. However, this interstitial fibrosis also contributes to increased ventricular stiffness and reduced compliance. In response to the reduced contraction function there can be significant resultant dilation of the left ventricular chamber, with thinning and elongation of the infarction area. This dilation causes an increased volume load in the ventricle, which may initially help to maintain the stroke volume according to the Starling mechanism to try to maintain cardiac output, but this is at the expense of a greater pressure load on the already poorly contractile ventricle. Sympathetic activation, activation of the neurohumoral systems (e.g. renin-angiotensin-aldosterone system) and changes in wall stress affect areas of the heart remote to the infarction. This results in a 'compensatory' hypertrophy in these areas. Therefore it can be appreciated that the early remodelling changes may be beneficial for immediate survival after a myocardial infarction, but their continued activation in the long term may have deleterious consequences. (Opie et al. 2006) Long-term

pathological remodelling is seen after large myocardial infarctions with myocyte hypertrophy, further myocyte loss through apoptosis and further injury events to the heart (such as further myocardial infarctions), and subsequent further ventricular dilatation such that LV volume stands out amongst other surrogate markers for a poorer outcome in heart failure. (Tuunanen & Knuuti 2011; Ingwall 2009)

The concept of the heart as an "engine running out of fuel" was first postulated in 1939 by Hermann and Dechard. (Herrmann & Decherd 1939) In addition to the structural changes that the heart undergoes following a large myocardial infarction leading to maladaptive remodelling, there are a number of changes in cardiac energetics in heart failure. This is often referred to as 'metabolic remodelling'. (Tuunanen & Knuuti 2011) There are three components to the metabolic machinery: substrate utilization – with cellular uptake of free fatty acids principally and glucose, and subsequent production of intermediate metabolites for the citric acid cycle by beta-oxidation and glycolysis respectively; oxidative phosphorylation – the production of ATP by the mitochondrial respiratory chain; and ATP transfer and utilization – transferring the energy store ATP from the mitochondria to the contractile myofibrils. (Neubauer 2007)

Substrate utilization can become the rate-limiting step for cardiac metabolism in heart failure due to reduced uptake, reduced oxidation or reduction of both. Studies have shown a switch away from the favoured beta oxidation of fatty acids to the increased use of glucose in late heart failure, associated with the down regulation of enzymes involved in the oxidation of fatty acids. (W C Stanley et al. 2005) There is an impairment of oxidative phosphorylation reducing the available supply of ATP to cardiomyocytes. The activity of electron transport–chain complexes and ATP synthase capacity are reduced, the regulation of oxidative phosphorylation by the phosphate acceptors ADP, AMP, and creatine is impaired, and the levels of uncoupling proteins reduced. The overall result is a reduction in oxygen consumption and ATP production in the failing myocardium. There are profound changes in creatine levels and in the creatine kinase system, reduced to as little as 20% of normal activity, with a resultant reduction in energy flux within the cell and reduced delivery of energy to the contractile myofibrils with resultant poor contractility and loss of inotropic reserve. (Neubauer 2007) Another important abnormality is associated with excessive formation of reactive oxygen species (ROS). ROS are by-products of aerobic metabolism whose production is normally tightly regulated by the cell, but these regulatory mechanisms can become impaired in heart failure. ROS damage lipids and proteins within the cell ultimately leading to reduced activity of enzyme complexes and ATP synthase in oxidative phosphorylation and other enzymes involved in the citric acid cycle. Reactive oxygen species can also induce myocyte hypertrophy, apoptosis, and the development of interstitial fibrosis by activating matrix metalloproteinases. Overall these cellular events play an important role in the development and continued progression of maladaptive myocardial remodelling and failure. (Tsutsui et al. 2009)

The goal of heart failure therapies is to prevent the deleterious cycle of remodelling, or ideally to "reverse remodel" failing myocardium. The effectiveness of these therapies is increased the earlier they are instigated. To facilitate this, the ability to identify such patients at an early stage by identifying early alterations in properties of the failing heart would represent an enormous diagnostic advance. A label-free method for *in vivo* characterisation of cardiac tissue and would therefore be highly desirable. The aim of this experiment was to explore the application of the custom-built single point fibre-optic probe-based time resolved spectrofluorometer to see if the autofluorescence signature changes with the structural and metabolic remodelling in a post-myocardial infarction heart failure (MI-HF) model that has been previously well characterised in our laboratory (Nikolaev et al. 2010; Lyon et al. 2012; Lyon et al. 2009; Kumarswamy et al. 2012)

4.2 Experimental methods

4.2.1 Myocardial infarction induction surgery, *in vivo* autofluorescence lifetime measurements and histology

Adult male Sprague-Dawley rats (Charles Rivers UK, Ltd.) weighing 250g-300g underwent proximal left anterior descending (LAD) coronary artery ligation to induce myocardial infarction as described in 2.2.3. Myocardial infarction heart failure (MI-HF) animals and their age-matched controls were studied *in vivo* for epicardial fluorescence and diffuse reflectance characteristics, as described in 2.2.4, during a terminal procedure at 1, 2, 4, and 16-weeks post-surgery. At the end of the procedure the heart was taken for histology, as described in 2.2.4 and 2.5, and stained with picosirius red to permit quantification of the degree of positively-stained fibrosis (%) in each anatomical area using Fiji image analysis.

The number of animals studied at each time point is summarised in table 4.1

Timepoint	Myocardial-infarction heart failure (MI-HF)	Age-matched controls (AMC)
1 week	3	3
2 weeks	3	4
4 weeks	3	4
16 weeks	6	6

Table 4.1 Summary of numbers of myocardial-infarction heart failure (MI-HF) and age-matched control (AMC) animals studied by timepoint

4.2.2 Data collection

Autofluorescence and diffuse reflectance were collected from four regions of interest (ROI) from the epicardial surface of the heart during *in vivo* measurements: left ventricle anterior ('scar'); interventricular septum ('border zone'); right ventricle; and left ventricle posterior, as shown in figure 4.1. In the MI-HF hearts, the border-zone was defined as the non-infarcted myocardium at the boundary of the scar and in the control hearts the anatomical equivalent area of the septum was studied. From each ROI, 3 repeat acquisition measurements at each of three positions within in ROI were measured. Each acquisition used integration times of 1 second for UV excitation and 1 second for blue excitation for autofluorescence lifetime measurements and 50 ms white light illumination for diffuse reflectance measurements.

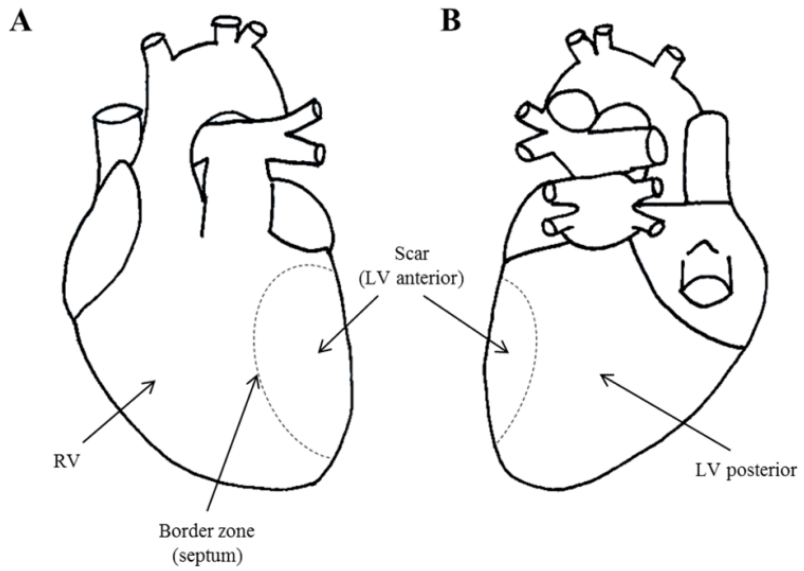


Figure 4.1 Figurative diagram of regions of interests (ROI) for *in vivo* epicardial measurements in the MI-HF model studies. (A) anterior view; (B) posterior view; left ventricle (LV) anterior ('scar'); interventricular septum ('border zone'); right ventricle; LV posterior

4.2.3 Spectral analysis, fluorescence lifetime data analysis and diffuse reflectance data analysis

Spectral analysis of fluorescence data was performed as described previously in section 2.1.3.2. Fluorescence lifetime data was analysed as described in section 2.1.3.1. Diffuse reflectance data was analysed as described in 2.1.3.3 and results are reported in units of absorbance, normalised to a white reference target. (WS-1-SL, Labsphere, USA)

4.2.4 Principal component analysis and linear discriminant analysis

To quantify the differences between MI-HF and AMC hearts within a region of interest (ROI), a classification algorithm was performed similar to those described in the following references. (Thompson et al. 2012; Talbot et al. 2011; Pu et al. 2013). Principal component analysis (PCA) is employed for selection of the 5 most significant principal components. Linear discriminant analysis is then performed on these using a 'leave-one-out' cross-validation approach that allows each measurement to be classified as either MI-HF or AMC. Of note, the region of the heart is known, but not the condition of the heart. This is because in a diagnostic application, e.g. a fluoroscopically-guided cardiac catheter study, the position of the probe within the heart would be known but not the disease condition. Each individual point measurement was used in the analysis. Receiver operator characteristic (ROC) curves were generated and the performance of algorithm was measured by area under the ROC curve (AUC)

4.2.5 Statistical analysis

Results are expressed as mean ± standard deviation (SD). Statistical analysis was performed using a two-tailed Student t-test, with a p value < 0.05 considered to be statistically significant. The following notation is used to identify statistical significance between two sets of data: * $p < 0.05$; ** $p < 0.01$; *** $p < 0.001$; **** $p < 0.0001$.

The Cohen's *d* coefficient was used calculate the power of discrimination of each parameter as it indicates the standardised difference between two means and expresses this difference in standardised units. The Cohen's *d* coefficient can be defined in terms of population means μ and standard deviations *s* by the following equation:

Equation 4.1

$$d = \frac{|\mu_1 - \mu_2|}{\sqrt{\frac{{s_1}^2 + {s_2}^2}{2}}}$$

Cohen's *d* acts as a measure of effect size where a larger Cohen's *d* represents a greater differentiation between two groups. It is traditionally presented as complementary to the results of statistical significance test to report on the magnitude of the difference.

4.3 Results

4.3.1 1 week-post myocardial infarction induction

At 1 week post-surgery, the scar tissue is only subtly visualised macroscopically. Heart weight to body weight ratio appeared increased but not statistically significantly at MI-HF (3.75 ± 0.22 g/kg (n=3)) compared to AMC animals (3.36 ± 0.17 g/kg (n=3)).

4.3.1.1 Diffuse reflectance measurements

Figure 4.2 shows the tissue absorbance between 400 – 700 nm calculated from the diffuse reflectance spectra at the 1 week timepoint for MI-HF (in red) & AMC (in blue) hearts for the 4 ROIs. There is an overall decrease in tissue absorbance in MI-HF hearts compared to the AMC hearts, most marked in the LV anterior wall / 'scar'. A double peak profile corresponding to the oxygenated haemoglobin / myoglobin with its maxima at approximately 540nm and 580nm is seen in all AMC ROIs. This profile is also observed in the RV and LV anterior wall 'scar' region of MI-HF hearts. In the LV posterior and border zone regions there is a shift in the peak identified at 540nm in AMC hearts to 550nm in the MI-HF hearts, which could suggest the presence of reduced cytochrome c or deoxygenated haemoglobin or myoglobin.

4.3.1.2 Autofluorescence spectral measurements

At the 1 week timepoint, there is a significant increase in the autofluorescence signal contribution from channel 1 (400 - 420 nm) in all regions of interest in MI-HF except RV, which itself shows a trend but this is not statistically significant (see figure 4.3). Figure 4.4 shows that this is due to a shift in fluorescence emission to shorter wavelengths. There is also a significant increase in the autofluorescence signal contribution from channel 2 (430 – 480 nm) in the LV posterior, interventricular septum / 'border zone', and LV anterior / 'scar' ROIs.

4.3.1.3 Autofluorescence lifetime measurements

Figure 4.5 summarises the autofluorescence lifetime results by region of interest for each spectral channel. There is a significant increase in mean lifetime (τ_{mean}) in LV anterior wall 'scar' compared to healthy tissue for channels 1 and 4, and in channel 1 LV posterior. There is a significant increase in the long decay component (τ_2) in channels 2, 3, and 4 in the MI-HF LV anterior wall 'scar', and in the areas remote to the site of the infarction - the interventricular septum / 'border zone' and the LV posterior wall in channels 2 and 3. Additionally in the LV posterior wall, remote from the infarction, a statistically significant decrease in the short lifetime component (τ_1) is seen in channels 2, 3, and 4 together with an increase to contribution to the overall decay (β) in channels 2 and 3 and a decrease in channel 4. There is a trend for τ_1 being

reduced in all regions of MI-HF hearts, relative to AMC, most apparent in channel 4, although statistical significance is only reached in the LV posterior wall.

4.3.1.4 Discriminant analysis

The application of the classification algorithm to all the fluorescence parameters, both lifetime and intensity, to establish the discriminative ability of the instrument to separate MI-HF and AMC hearts is described in 4.2.4. Figure 4.6 shows the separation achieved by the first two principal components (PCs) by the classification algorithm and the decision line shown in black. Table 4.2 shows that the instrument can discriminate between MI-HF and AMC hearts at this time-point, not only in the infarcted LV anterior wall, but in all ROIs with a diagnostic accuracy of 100%.

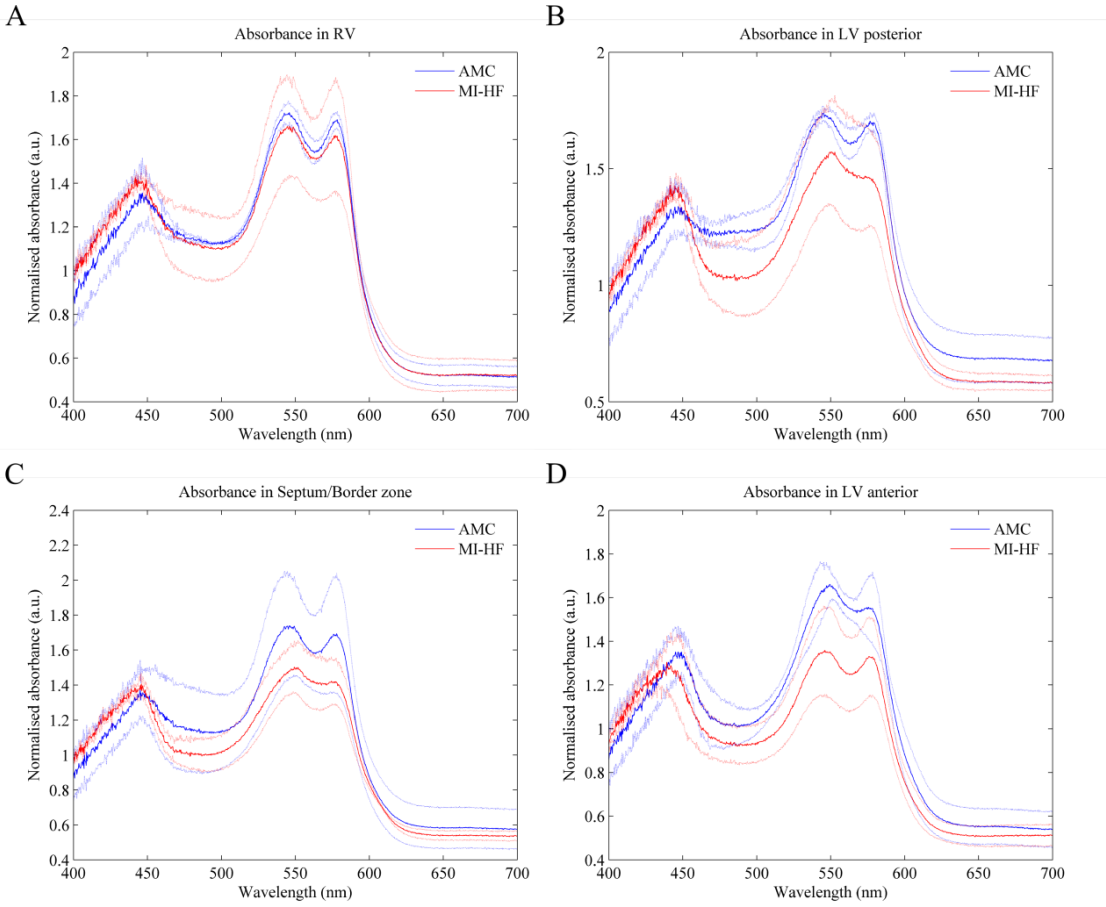


Figure 4.2 1 week timepoint diffuse reflectance data for MI-HF model in MI-HF and AMC, displayed by region of interest (ROI): A – RV; B – LV posterior; C – Interventricular septum / 'border zone'; D – LV anterior / 'scar'. Pale dashed lines indicate ± 1 SD.

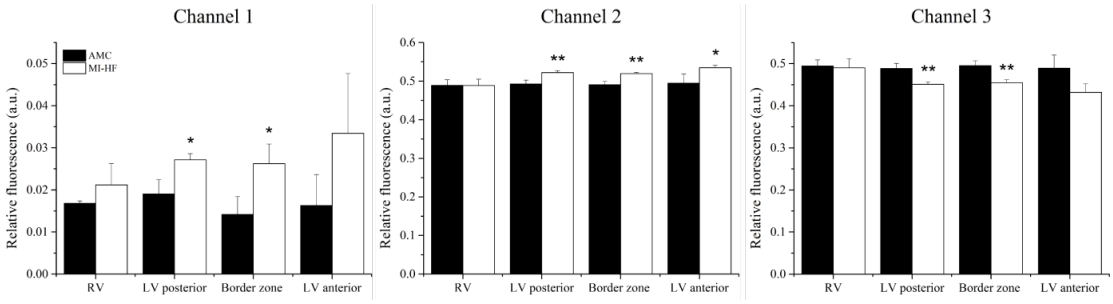


Figure 4.3 1 week timepoint relative contribution of each spectral channel to total autofluorescence from UV excitation in MI-HF and AMC, displayed by ROI. * p < 0.05; ** p < 0.01

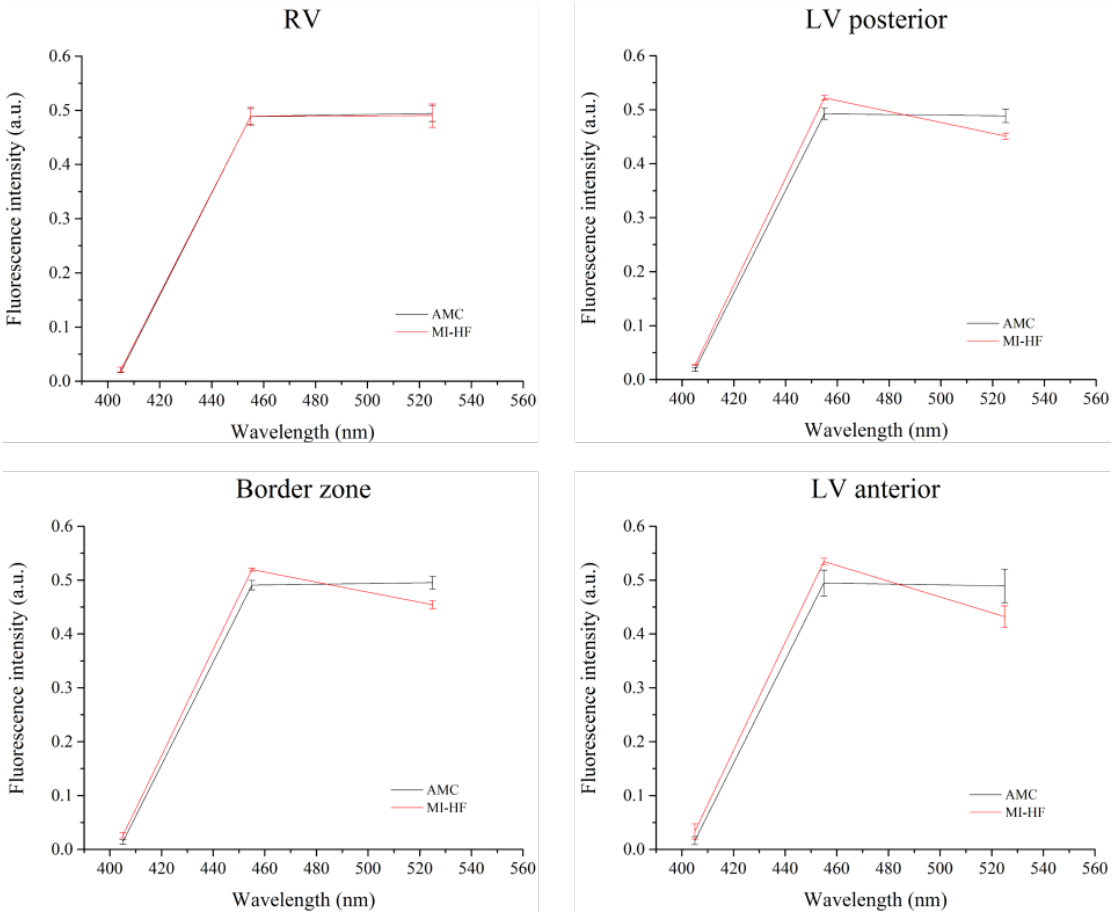


Figure 4.4 1 week timepoint relative autofluorescence in each ROI in MI-HF and AMC

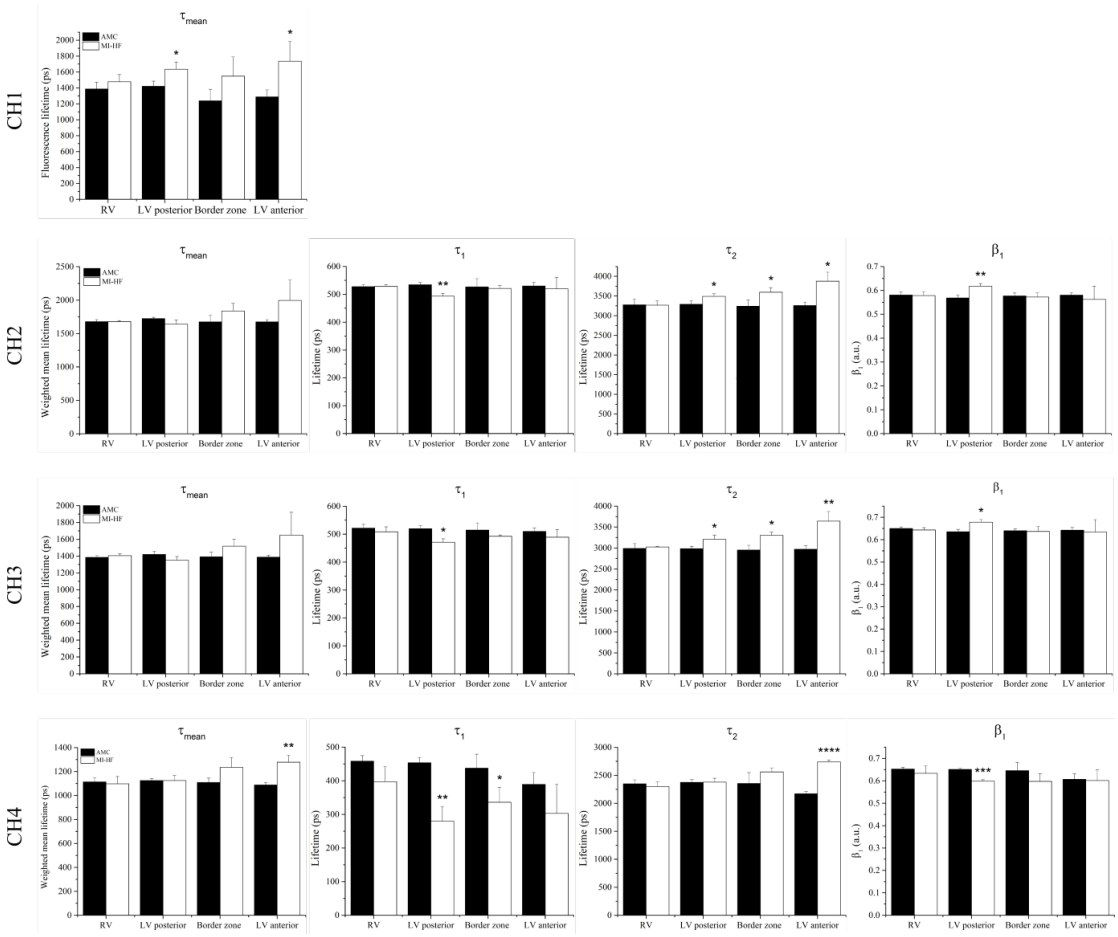


Figure 4.5 1 week timepoint autofluorescence lifetime parameters for each spectral channel for MI-HF and AMC, displayed by ROI. * p < 0.05; ** p < 0.01; *** p < 0.001; **** p < 0.0001

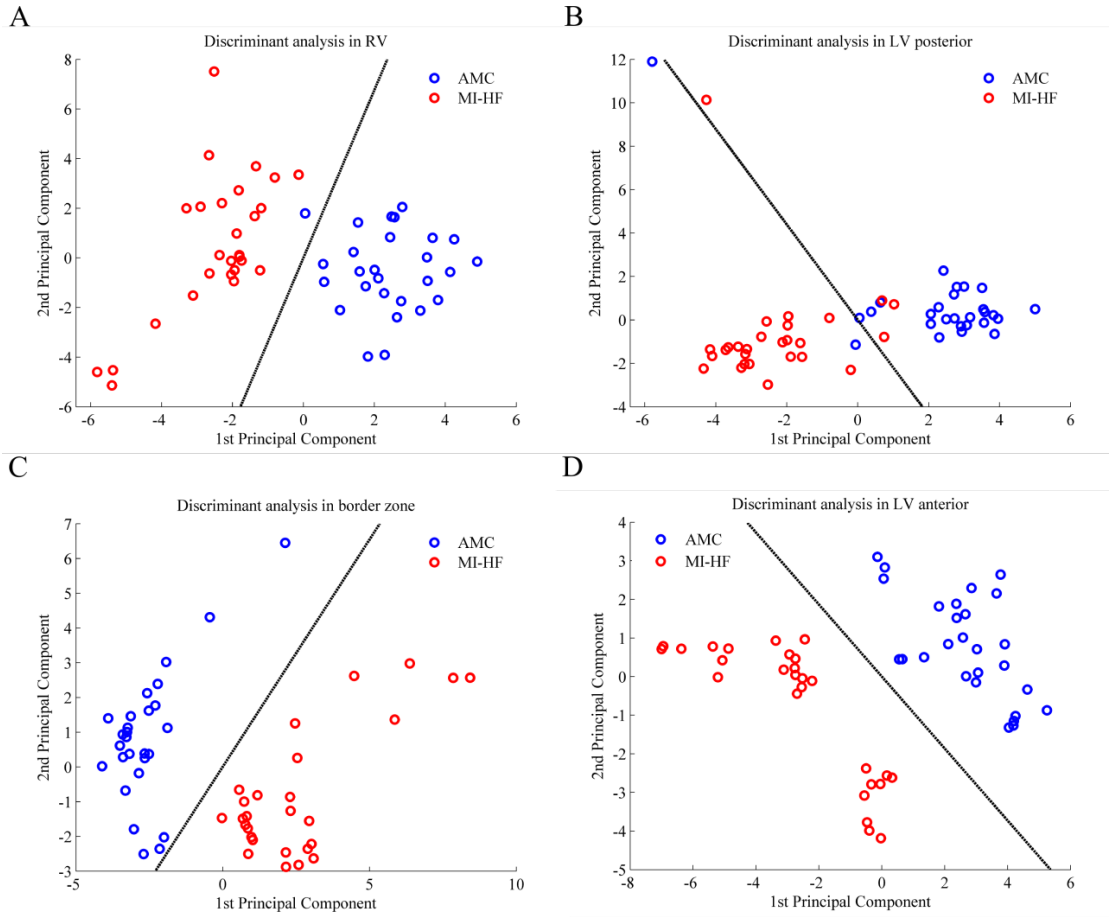


Figure 4.6 1 week timepoint scores of first 2 principal components from classification algorithm for MI-HF and AMC, displayed by ROI: A – RV; B – LV posterior; C – Interventricular septum / 'border zone'; D – LV anterior / 'scar'. Decision line shown as black line.

1 week timepoint	RV	LV posterior	IVS 'Border' zone	LV anterior
Variance	95.53	94.07	92.51	94.94
Sensitivity (%)	100.00	100.00	100.00	100.00
Specificity (%)	100.00	100.00	100.00	100.00
Diagnostic accuracy (%)	100.00	100.00	100.00	100.00
AUC	1.0000	1.0000	1.0000	1.0000

Table 4.2 1 week timepoint LDA-PCA algorithm classification results (using 5 most significant principal components)

4.3.2 2 weeks-post myocardial infarction induction

At the 2 weeks timepoint, identification of the scar becomes easier macroscopically in the anterior wall of left ventricle owing to its change to whiter colouration, with the beginnings of formation of well-defined scar. Heart weight to body weight ratio appeared increased, but did not reach statistical significance, at MI-HF (4.07 ± 0.80 g/kg (n=3)) compared to AMC animals (3.11 ± 0.47 g/kg (n=3)).

4.3.2.1 Diffuse reflectance measurements

Figure 4.7 shows the tissue absorbance between 400 - 700 nm calculated from the diffuse reflectance spectra at the 2-weeks timepoint for MI-HF (in red) and AMC (in blue) hearts for the four regions of interest (ROI). Similarly to the 1-week timepoint there is a decrease in tissue absorbance in MI-HF hearts compared to AMC hearts in all ROIs. As discussed above the double peak profile corresponding to oxygenated haemoglobin/myoglobin with its maxima at approximately 540 nm and 580 nm is seen in all AMC ROIs. This profile is also clearly observed in the RV and LV anterior wall / 'scar' region of MI-HF hearts. In the LV posterior and border zone regions this pattern is not present and appears changed to more of a single peak at around 550nm with a shoulder at 590nm.

4.3.2.2 Autofluorescence spectral measurements

At the 2 weeks timepoint, there is a significant increase in the autofluorescence signal contribution from channel 1 (400 - 420 nm) in all regions of interest in MI-HF except RV, which itself shows a trend but it is not statistically significant (see figure 4.8). There is also a significant increase in the autofluorescence signal contribution from channel 2 (430 – 480 nm) in the LV posterior, interventricular septum / 'border zone', and LV anterior / 'scar' ROIs. Figure 4.9 shows that this is due to a shift in fluorescence emission to shorter wavelengths.

4.3.2.3 Autofluorescence lifetime measurements

Figure 4.10 summarises the autofluorescence lifetime results by region of interest for each spectral channel. There is a very significant increase in mean lifetime (τ_{mean}) in LV anterior wall 'scar' compared to healthy tissue that is seen in all channels. This increase is more prominent than at the 1-week time point. As at the 1-week time point, it would appear that this overall increase in mean lifetime (τ_{mean}) is as a result of an increase in the long decay component (τ_2) and an increase to its contribution to the overall decay (β). The trend seen at the 1-week timepoint of τ_1 being globally reduced in MI-HF hearts in all channels and all ROIs, relative to AMC, is not present at the 2 weeks time point. The short component τ_1 has a trend to being reduced in channel 4, with statistical significance reached in the LV anterior 'scar'.

4.3.2.4 Discriminant analysis

Figure 4.11 shows the separation achieved by the first two principal components (PCs) by the classification algorithm and the decision line shown in black using the data from the 2 weeks time point. Table 4.3 shows that the instrument can discriminate between MI-HF and AMC hearts at this time-point in the LV anterior 'scar' with a diagnostic accuracy of 100%. In the interventricular septum / 'border zone' region, diagnostic accuracy was 87.50%. In regions remote to the MI, where changes are subtler, sensitivity was 93% in the LV posterior wall, and 70% in the RV with diagnostic accuracy of 88% and 78% respectively.

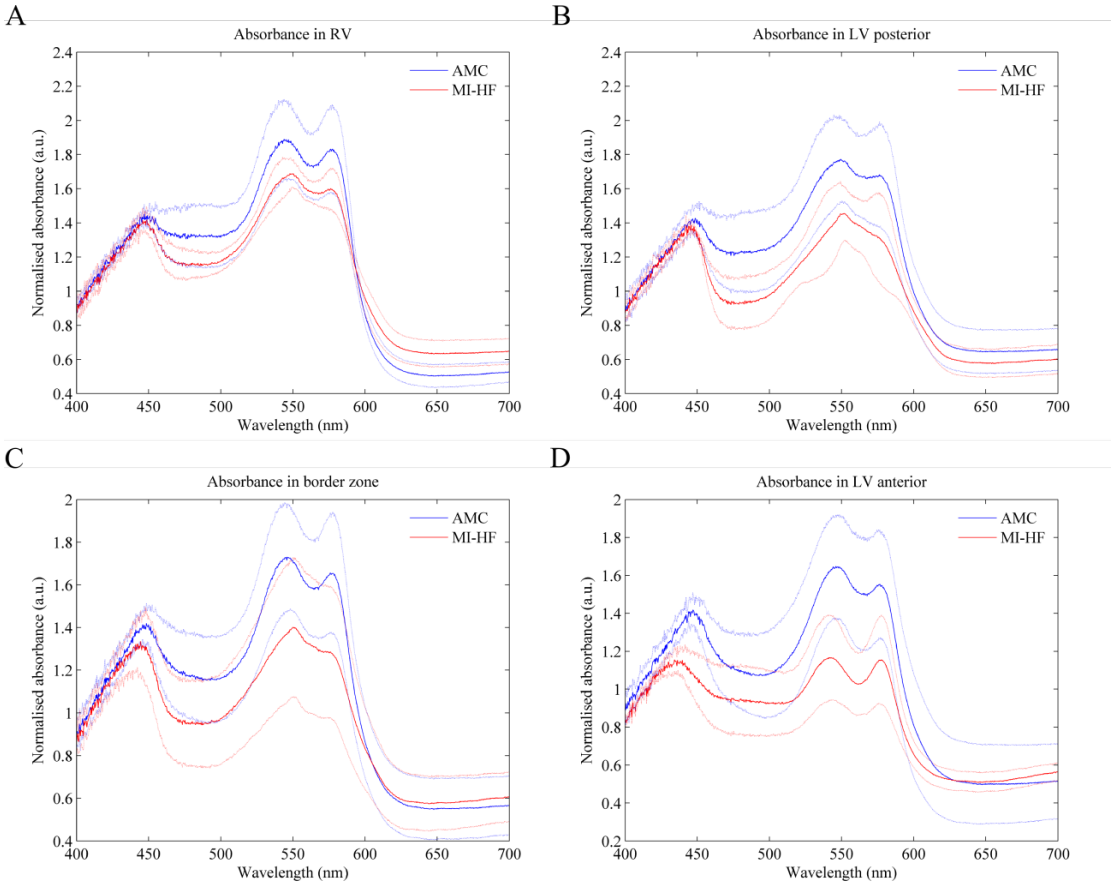


Figure 4.7 2 weeks timepoint diffuse reflectance data for MI-HF model in MI-HF and AMC, displayed by region of interest (ROI): A – RV; B – LV posterior; C – Interventricular septum / 'border zone'; D – LV anterior / 'scar'. Pale dashed lines indicate ± 1 SD.

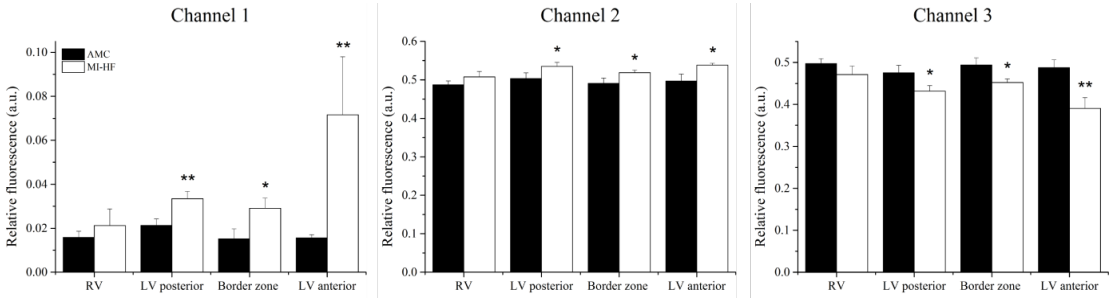


Figure 4.8 2 weeks timepoint relative contribution of each spectral channel to total autofluorescence from UV excitation in MI-HF and AMC, displayed by ROI. * p < 0.05; ** p < 0.01

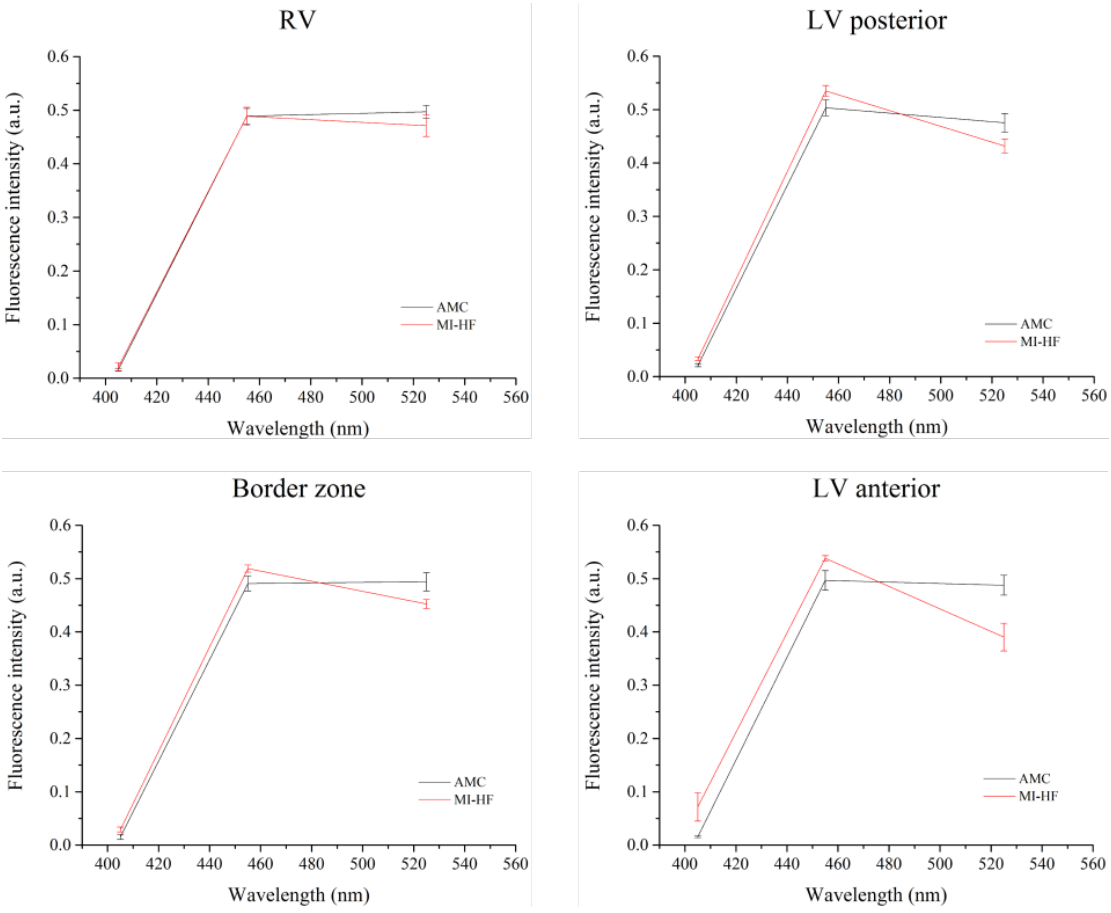


Figure 4.9 2 weeks timepoint relative autofluorescence in each ROI in MI-HF and AMC

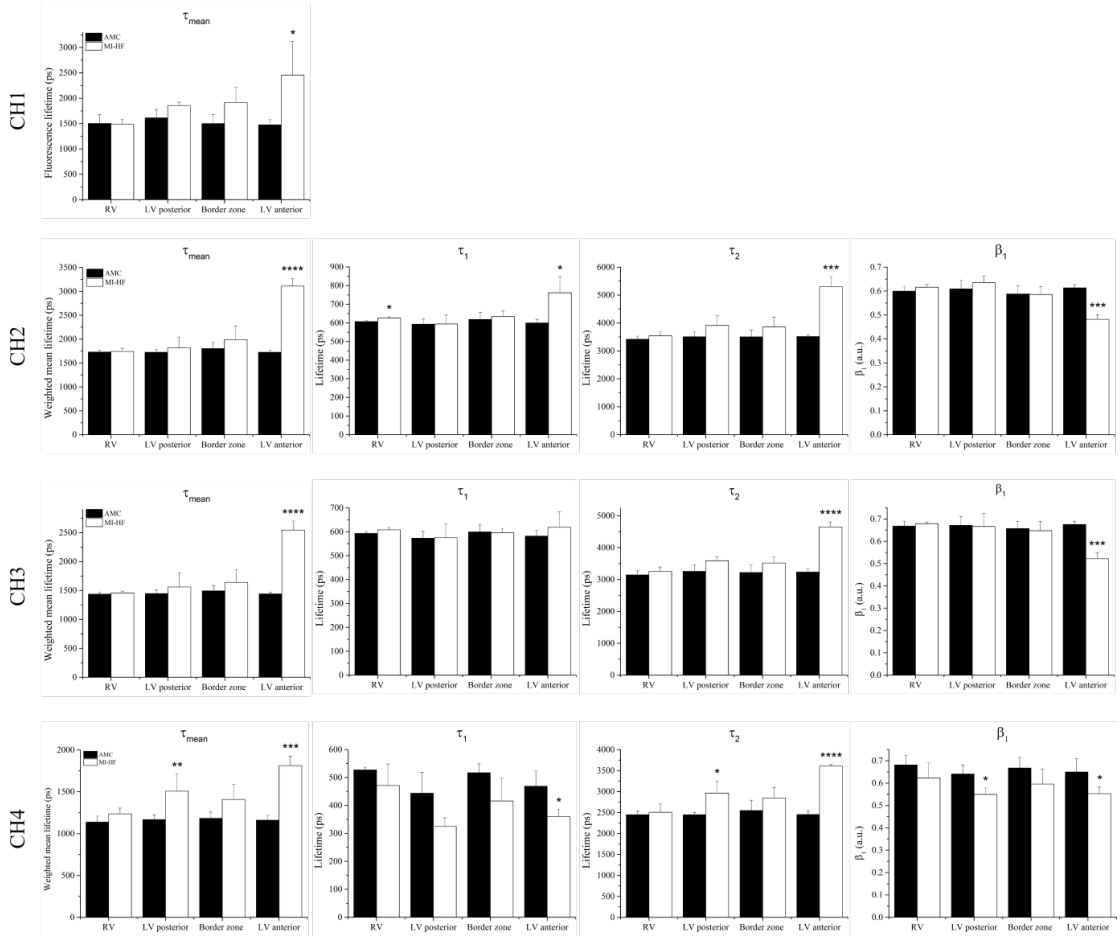


Figure 4.10 2 weeks timepoint autofluorescence lifetime parameters for each spectral channel for MI-HF and AMC, displayed by ROI. * p < 0.05; ** p < 0.01; *** p < 0.001; **** p < 0.0001

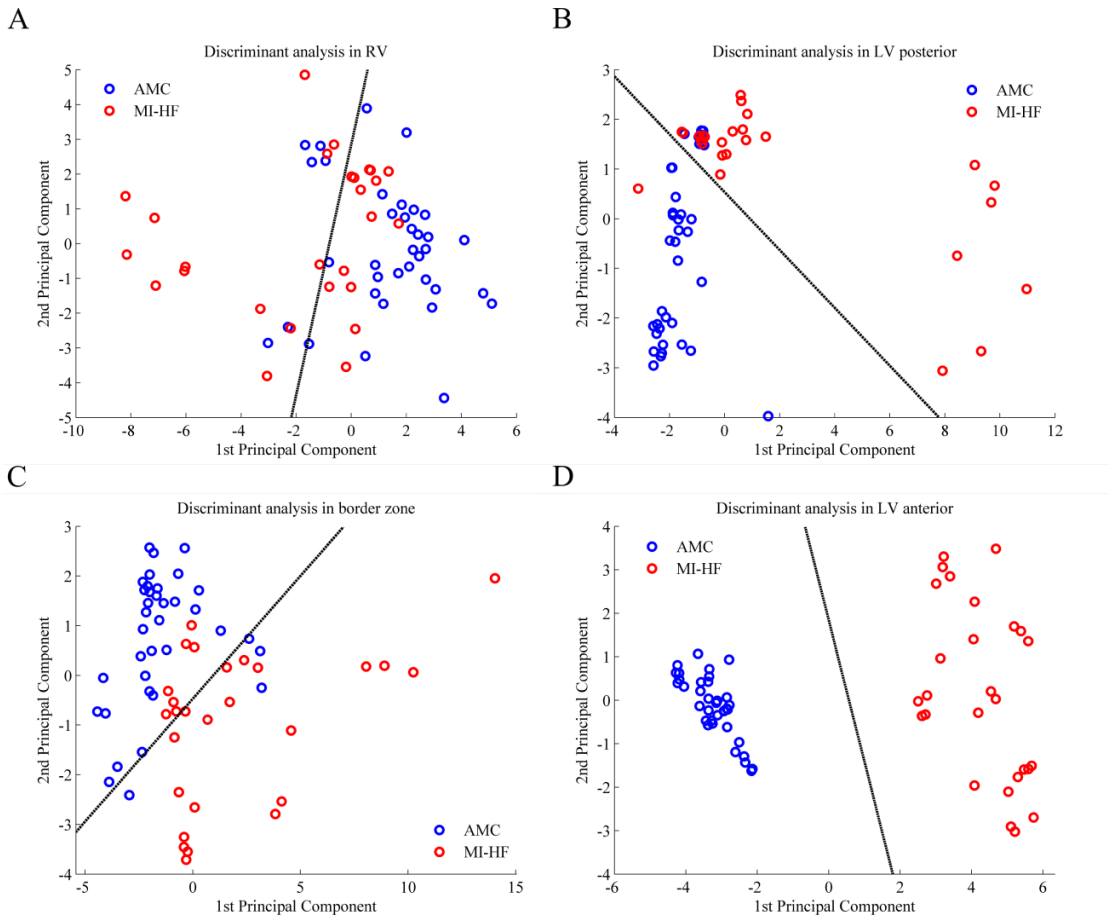


Figure 4.11 2 weeks timepoint scores of first 2 principal components from classification algorithm for MI-HF and AMC, displayed by ROI: A – RV; B – LV posterior; C – Interventricular septum / 'border zone'; D – LV anterior / 'scar'. Decision line shown as black line.

2 weeks timepoint	RV	LV posterior	IVS 'Border' zone	LV anterior
Variance	90.73	94.92	94.36	98.00
Sensitivity (%)	70.37	92.59	77.78	100.00
Specificity (%)	86.11	83.33	97.22	100.00
Diagnostic accuracy (%)	78.24	87.96	87.50	100.00
AUC	0.9095	0.8951	0.9444	1.0000

Table 4.3 2 weeks timepoint LDA-PCA algorithm classification results (using 5 most significant principal components)

4.3.3 4 weeks-post myocardial infarction induction

At the 4 weeks timepoint, the scar tissue is clearly visible macroscopically but the edge of the scar's 'border zone' in the interventricular septum remains relatively diffuse. There was a statistically increased heart weight to body weight ratio of MI-HF animals (3.89 ± 0.38 g/kg (n=3)) compared to AMC animals (2.33 ± 0.17 g/kg (n=3)).

4.3.3.1 Diffuse reflectance measurements

Figure 4.12 shows the tissue absorbance between 400 - 700 nm calculated from the diffuse reflectance spectra at the 4-weeks timepoint for MI-HF (in red) and AMC (in blue) hearts for the four regions of interest (ROI). There is a decrease in tissue absorbance in MI-HF hearts in the LV anterior and LV posterior ROIs, but unlike at earlier timepoints this is no longer observed in the RV and interventricular septum / 'border zone' ROIs. As at earlier 1- and 2-week timepoints, the characteristic double peak corresponding to oxygenated haemoglobin/myoglobin with its maxima at approximately 540 nm and 580 nm is seen in all AMC hearts. In MI-HF hearts the pattern becomes more complicated. In the LV anterior / 'scar' of MI-HF we see the similar double peak but with a lower tissue absorbance than control. In the LV posterior, within the curve there is a shoulder at 520nm and a peak at 550nm and a smooth shoulder at 550-560nm. In RV and border zone regions a single peak with maximum at approximately 550nm is seen, although in both there is a clear shoulder at 580nm.

4.3.3.2 Autofluorescence spectral measurements

At the 4 weeks timepoint, there is a significant increase in the autofluorescence signal contribution from channels 1 (400 - 420 nm) and 2 (430 – 480 nm) and a decrease in the autofluorescence contribution from channel 3 (500 – 550 nm) in all regions of interest in MI-HF animals with the exception of RV channel 1 where significance is not reached. (See figure 4.13) This is due to a shift towards longer wavelengths with UV excitation (see figure 4.14).

4.3.3.3 Autofluorescence lifetime measurements

Figure 4.15 summarises the autofluorescence lifetime results by region of interest for each spectral channel. There is a further significant increase in mean lifetime (τ_{mean}) in LV anterior wall 'scar' compared to healthy tissue and this is seen in all channels. As at the 1 week and 2 weeks time points – the overall increase in mean lifetime (τ_{mean}) appears to result from an increase in the long decay component (τ_2) and an increase to its contribution to the overall decay (β). The trend seen at the earlier timepoints of τ_1 being globally reduced in MI-HF hearts in all channels and all ROIs, relative to AMC, is more localized at 4 weeks. The short component τ_1 is

seen to be reduced in channel 4, with statistical significance reached in the LV anterior 'scar', and additionally in LV posterior ROI in channel 3.

4.3.3.4 Discriminant analysis

Figure 4.16 shows the separation achieved by the first two principal components (PCs) by the classification algorithm and the decision line shown in black. Table 4.4 shows that the instrument can discriminate between MI-HF and AMC hearts at this time-point in the LV anterior 'scar' with a diagnostic accuracy of 100% (specificity = 100%, sensitivity = 100%, AUC = 1). This accuracy was also seen in the LV posterior region, remote to the infarction. In the RV, also remote to the area of infarction, sensitivity was 81.4% and specificity was 86.11% giving an overall diagnostic accuracy of 83.4%. Classification performance was poorest in the interventricular septum / 'border zone' region, where diagnostic accuracy was 78.70% due to poor sensitivity (62.96%) despite very high specificity (94.44%).

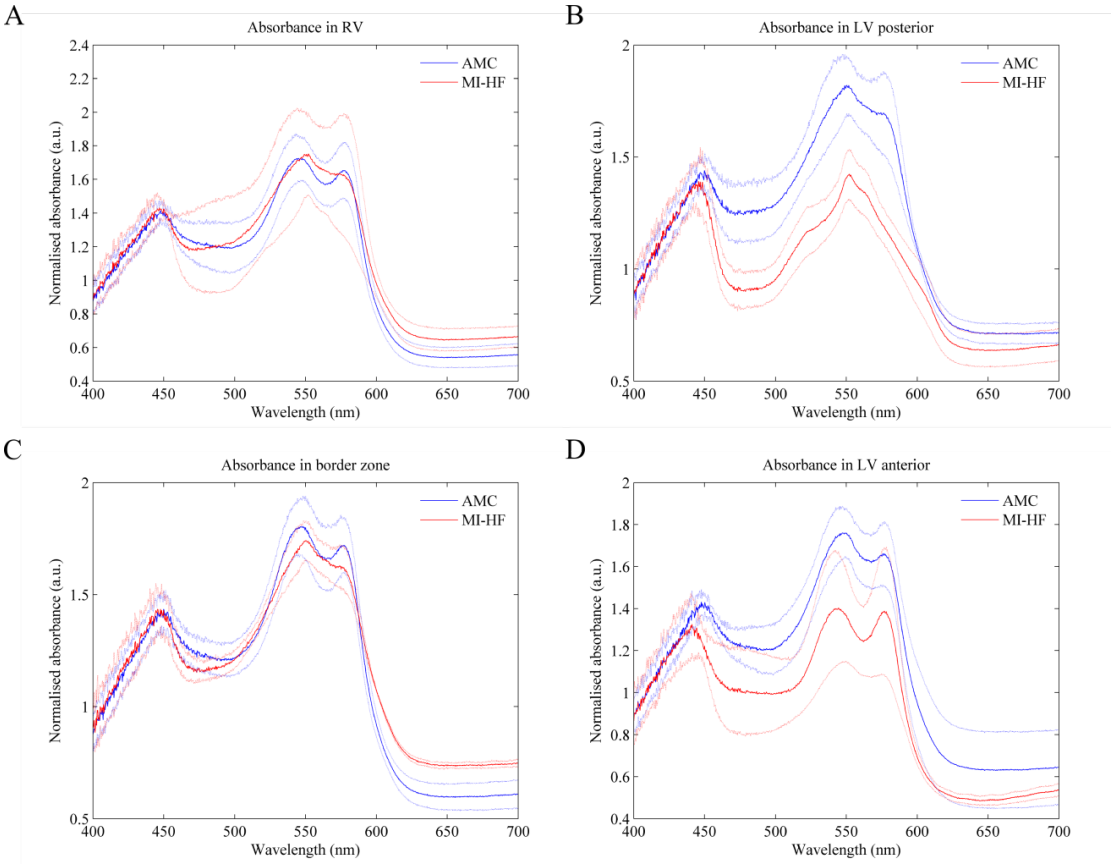


Figure 4.12 4 weeks timepoint diffuse reflectance data for MI-HF model in MI-HF and AMC, displayed by region of interest (ROI): A – RV; B – LV posterior; C – Interventricular septum / 'border zone'; D – LV anterior / 'scar'. Pale dashed lines indicate ± 1 SD.

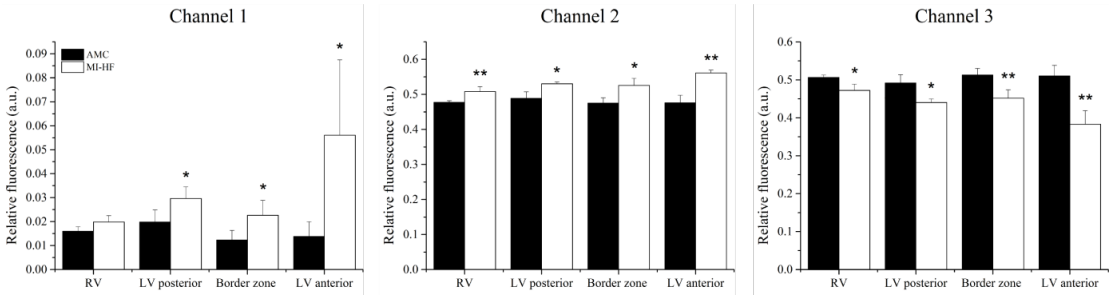


Figure 4.13 4 weeks timepoint relative contribution of each spectral channel to total autofluorescence from UV excitation in MI-HF and AMC, displayed by ROI. * p < 0.05; ** p < 0.01

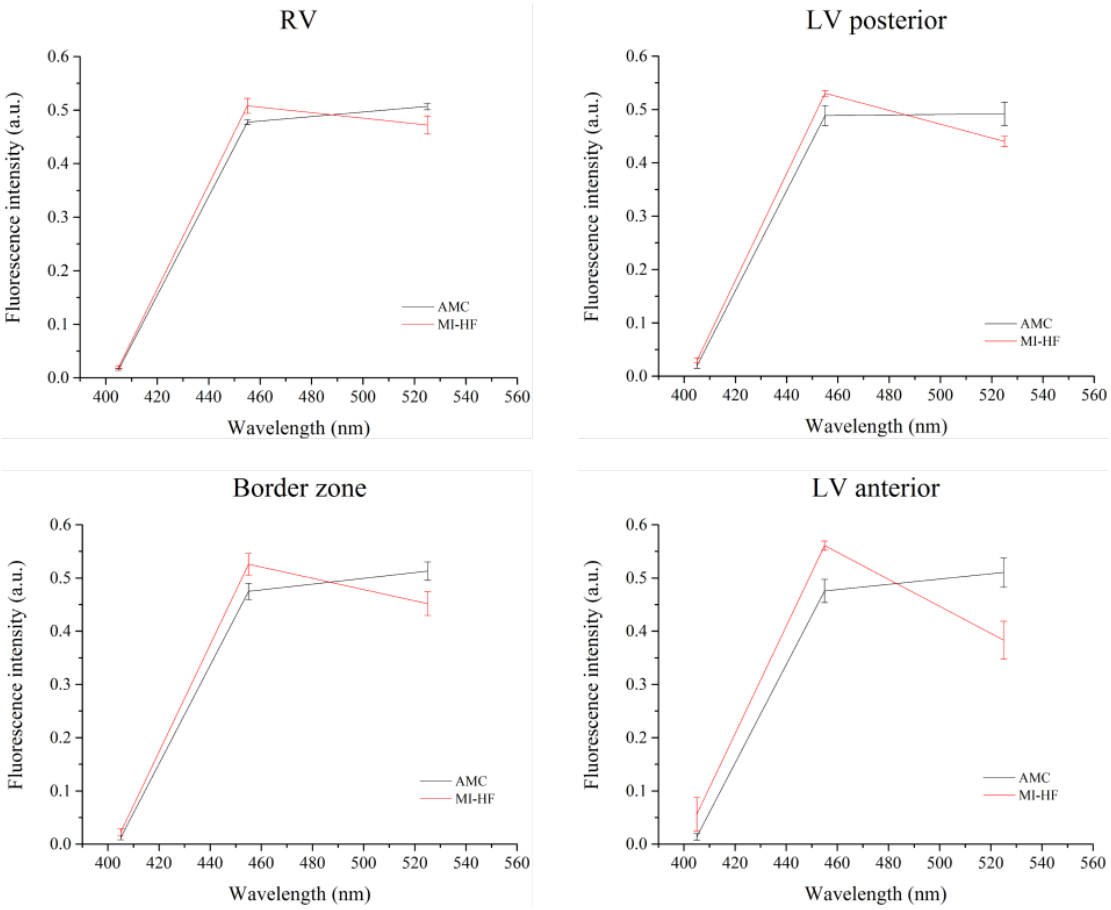


Figure 4.14 4 weeks timepoint relative autofluorescence in each ROI in MI-HF and AMC

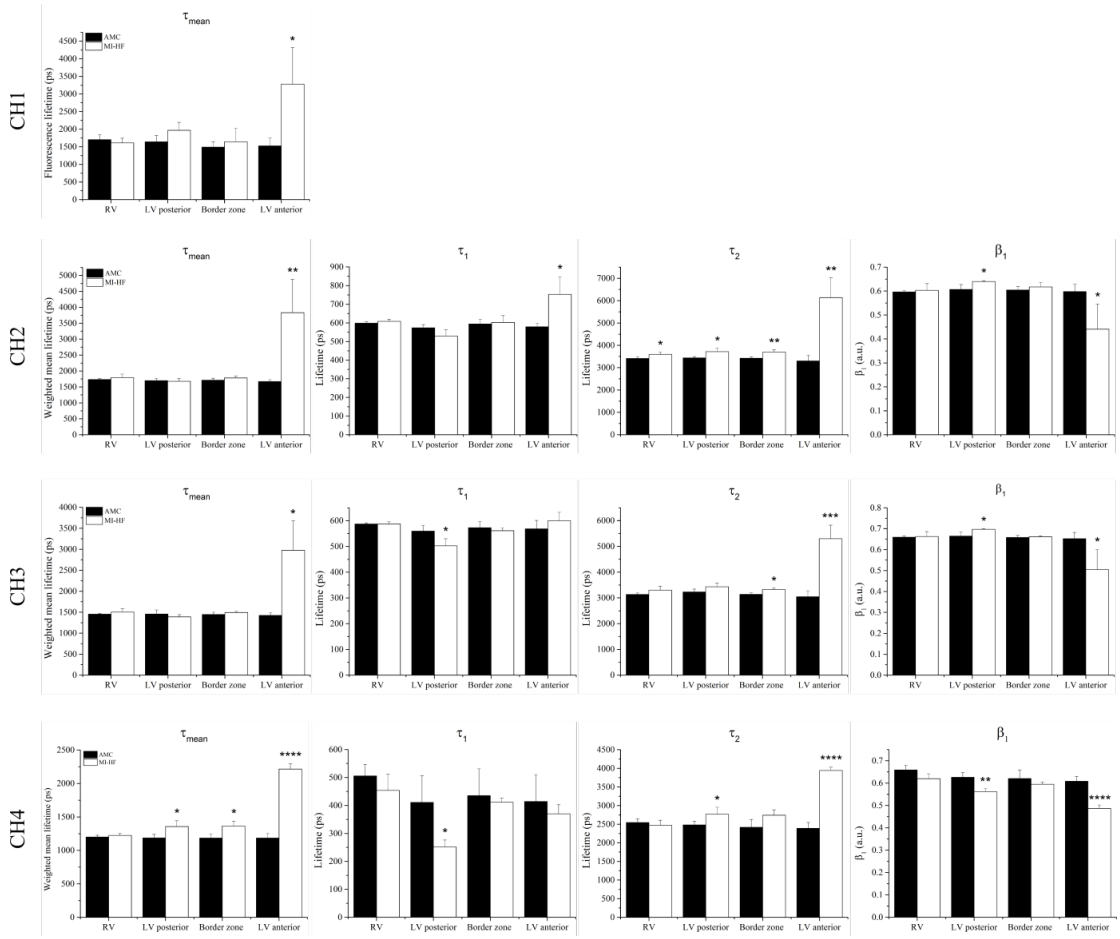


Figure 4.15 4 weeks timepoint autofluorescence lifetime parameters for each spectral channel for MI-HF and AMC, displayed by ROI. * p < 0.05; ** p < 0.01; *** p < 0.001; **** p < 0.0001

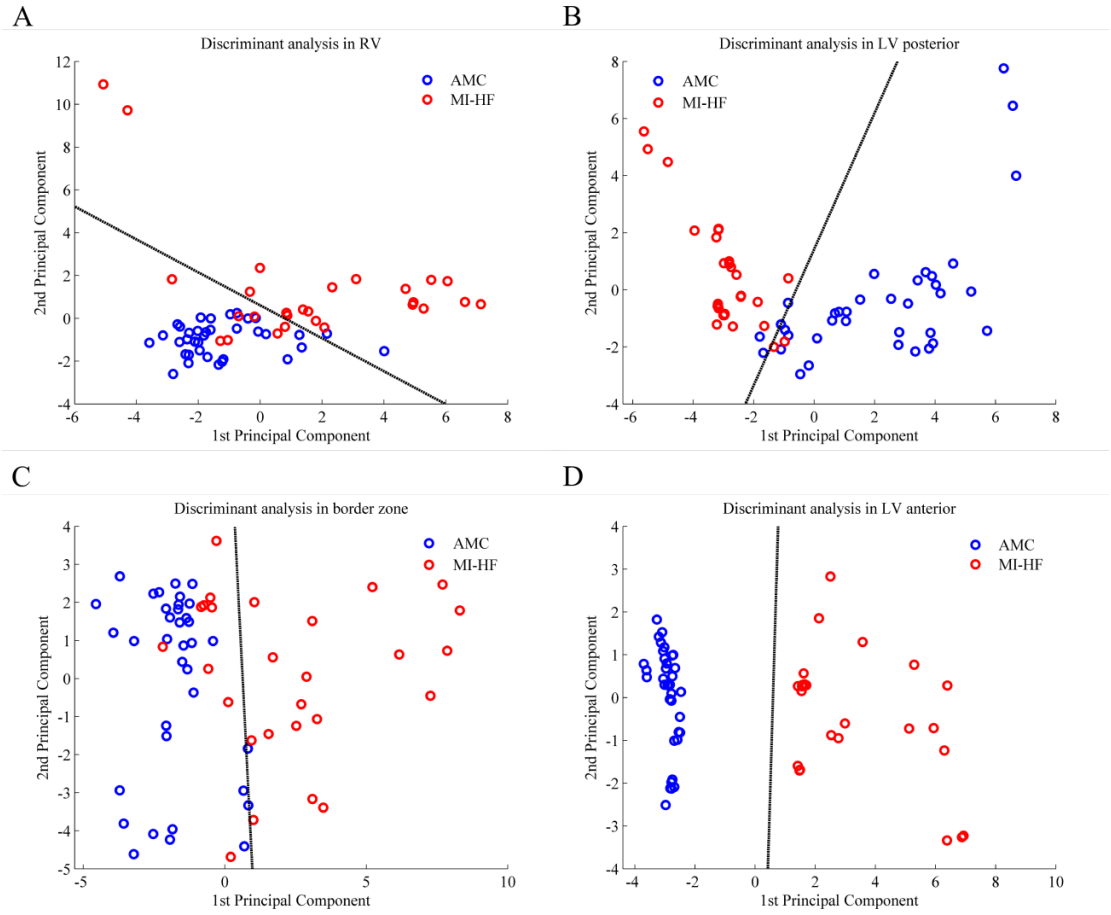


Figure 4.16 4 weeks timepoint scores of first 2 principal components from classification algorithm for MI-HF and AMC, displayed by ROI: A – RV; B – LV posterior; C – Interventricular septum / 'border zone'; D – LV anterior / 'scar'. Decision line shown as black line.

4 weeks timepoint	RV	LV posterior	IVS 'Border' zone	LV anterior
Variance	91.4	93.99	93.79	98.18
Sensitivity (%)	81.48	100	62.96	100.00
Specificity (%)	86.11	100	94.44	100.00
Diagnostic accuracy (%)	83.80	100.00	78.70	100.00
AUC	0.9475	1.0000	0.9156	1.0000

Table 4.4 4 weeks timepoint LDA-PCA algorithm classification results (using 5 most significant principal components)

4.3.4 16 weeks-post myocardial infarction induction

At the 16 weeks timepoint, ligation of the LAD has produced a large transmural MI with a well-defined scar in the anterior wall of the LV seen in all specimens. (See figure 4.22) There was a statistically significant increased heart weight to body weight ratio of MI-HF animals (3.40 ± 0.60 g/kg (n=6)) compared to AMC animals (2.84 ± 0.45 g/kg (n=6)). Histological confirmation of the collagen content of the heart demonstrated that it was significantly increased in MI-HF animals in all ROI, compared to AMC. See figure 4.22 and table 4.7.

4.3.4.1 Diffuse reflectance measurements

Figure 4.18 shows the tissue absorbance between 400 - 700 nm calculated from the diffuse reflectance spectra at the 16-weeks timepoint for MI-HF (in red) and AMC (in blue) hearts for the four regions of interest (ROI). In AMC hearts, there are some changes compared to at earlier timepoints, which is likely a function of age with the ventricular wall thickness being greater at 16 weeks than at earlier timepoints. The maximum peak at approximately 550nm is seen in all regions apart from the RV and is likely attributable to a greater quantity of cytochrome c, present in mitochondria and reduced penetration of white light into the blood volume. There is a shoulder at 580nm, attributable to oxygenated haemoglobin/myoglobin as expected in healthy AMC hearts, which is most visible in the RV ROI curve likely due to penetration of white light into the blood volume through the thinner RV wall. In MI-HF hearts in the LV anterior / 'scar', there is loss of the peak at 550nm, which likely represents the loss of mitochondria-containing myocytes and replacement with scar tissue and penetration of white light into the blood volume. In the regions remote from the scar there is a single peak at around 550nm and a variable smooth shoulder at approximately 580nm.

4.3.4.2 Autofluorescence spectral measurements

Figures 4.19 and 4.20 summarise the relative autofluorescence signal in each spectral channel for UV excitation by ROI (figure 4.19) and by wavelength (figure 4.20). They show increased contribution of channel 1 to the total fluorescence signal in MI-HF hearts in all regions of interest, most significantly in the LV anterior / 'scar' of MI-HF hearts. Histological confirmation (figure 4.22 and table 4.7) agreed with previous histology of this model [(Lyon et al. 2009)] which demonstrated an increase in type I collagen within the scar. Type I collagen has a fluorescence emission spectrum consistent with the increase in this channel. The increase in channel 1 contributions in sites remote the MI, such as the RV and LV posterior site, also suggests an increase in collagen in these sites, which is confirmed by the histology. The increase in the relative contribution of channel 2 in all ROIs is consistent with collagen type I, and its relatively broad emission spectrum, which would also be detected in the 430 – 480 nm range of channel 2. Figure 4.20 confirms the shift toward the dominance of shorter wavelengths (from the increased

collagen level within the tissue) in the total signal, in all ROIs, but is most apparent in the LV anterior / 'scar'. Figure 4.23 summarises the increase in relative channel 1 (400 – 420 nm) autofluorescence in MI-HF to AMC hearts in each ROI against time point after MI induction surgery.

4.3.4.3 Autofluorescence lifetime measurements

Figure 4.21 summarises the autofluorescence lifetime results by region of interest for each spectral channel. There is a significant increase in mean lifetime (τ_{mean}) in MI-HF LV anterior wall / 'scar' compared to AMC in all channels. It appears that this overall increase in mean lifetime (τ_{mean}) is resultant of an increase in both the short component (τ_1) and the long component (τ_2) and a decrease in the contribution of the short component to the overall decay (β). This is consistent with an increase in collagen type-1 content. Changes to NADH or FAD fluorescence could also be contributing to the overall changes in mean autofluorescence lifetime in the infarcted zone, however given the huge change in collagen and therefore its autofluorescence signal (see figure 4.22 and table 4.7) it may not be possible to observe this. In the interventricular septum / 'border zone' the same pattern of a statistically significant increase in mean autofluorescence lifetime is also seen, likely attributable to the increase in collagen type-I content in this region. In areas remote from the scar tissue, i.e. RV and LV posterior, statistically significant differences in decay profile in channels 3 and 4 are observed with a decrease in the short decay component (τ_1) as seen more globally in earlier time points. This cannot be explained by increases in collagen type-I but could be explained by alteration in tissue metabolism. Figure 4.24 shows the variation of the short lifetime component $\tau 1$ of detection channel 4 (500 – 550 nm) in MI-HF to AMC hearts in each ROI against each time point after MI induction surgery to highlight this.

4.3.4.4 Discriminant analysis

The differences between AMC and MI-HF hearts are the most pronounced at the 16-week time point, due to a significant change in collagen content, not only in the area of the infarction, but in areas remote from it and establishment of the heart failure phenotype in the model. Therefore the potential of all the spectroscopic data that the instrument records were evaluated to establish the discriminative ability between MI-HF and AMC hearts in each ROI. To establish which combination of spectroscopic parameters yielded the best results, the classification algorithm was applied to the following sets of data: diffuse reflectance only; fluorescence intensity only; all fluorescence data (both lifetime and intensity); diffuse reflectance and fluorescence intensity only; diffuse reflectance and all fluorescence data. Figure 4.22 shows the scatter plots of the scores from the first two principle components (PCs) for each ROI using all fluorescence data. Classification results for the algorithm using the 5 different methods are summarized in table 4.6. This shows that all methods are suitable for discrimination between healthy and diseased tissue

in LV anterior / 'scar' region, where the AUC values from the ROC curves are close to 1 for all methods and the sensitivity ranges from 91 – 96% and the specificity ranges from 96 – 100% for the various methods. In remote regions, i.e. LV posterior wall and RV, the best classification performance was seen with use of the combined diffuse reflectance and fluorescence intensity parameters, which gave AUC of 0.8375 and 0.9886 respectively and in the RV sensitivity and specificity of 93% and 100% respectively. Of note the LV posterior had poorer classification performance by the algorithm compared to other regions. In the interventricular septum / 'border zone', the most accurate classification was achieved through use of all fluorescence parameters (i.e. intensity and lifetime) – either in combination with diffuse reflectance (diagnostic accuracy = 94.44%) or alone (diagnostic accuracy = 93.52%) compared to the use of steady-state methods alone.

Table 4.7 shows the autofluorescence parameters for each ROI ranked by their Cohen's d coefficient. This shows which parameters offer the best discrimination. In the LV anterior wall / 'scar' and the interventricular septum / 'border zone', the best discrimination is achieved with autofluorescence decay parameters, primarily channel 2 long component (CH2 τ_2) and channel 3 long component (CH3 τ_2). In areas remote from the infarction, i.e. LV posterior and RV, intensity-based parameters provide better discrimination. Of note, the most discriminatory parameter in the LV posterior zone is the channel 4 short component (CH4 τ_1), seemingly independent to changes in tissue collagen content and possibly relating to changes in tissue energetics.

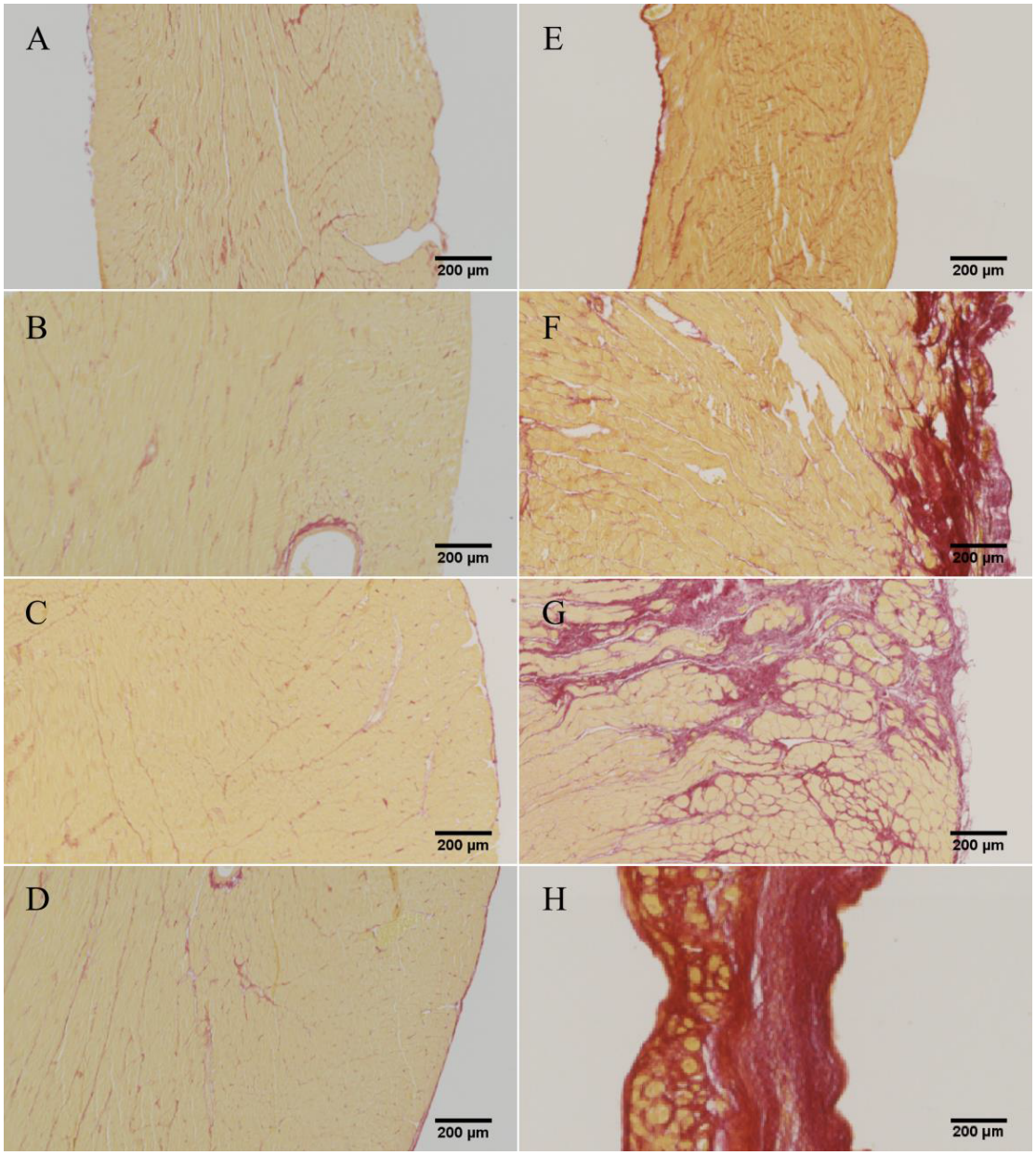


Figure 4.17 Representative histology images from AMC (left column) and MI-HF (right column) hearts. (A, E) RV; (B, F) LV posterior; (C, G) Interventricular septum / Border zone; (D, H) LV anterior / 'scar'

Collagen content assessed by PSR staining (%)	AMC	MI	P value
RV	4.50 ± 1.69	22.87 ± 4.17	0.0021
LV posterior	6.53 ± 1.98	35.49 ± 9.09	0.0057
IVS / Border zone	4.65 ± 0.73	28.30 ± 1.30	< 0.0001
LV anterior / 'scar'	2.64 ± 0.17	74.19 ± 5.02	< 0.0001

Table 4.5 Collagen content calculated from representative histology images in MI-HF hearts and AMC hearts. (two-tailed Student t-test, n=3)

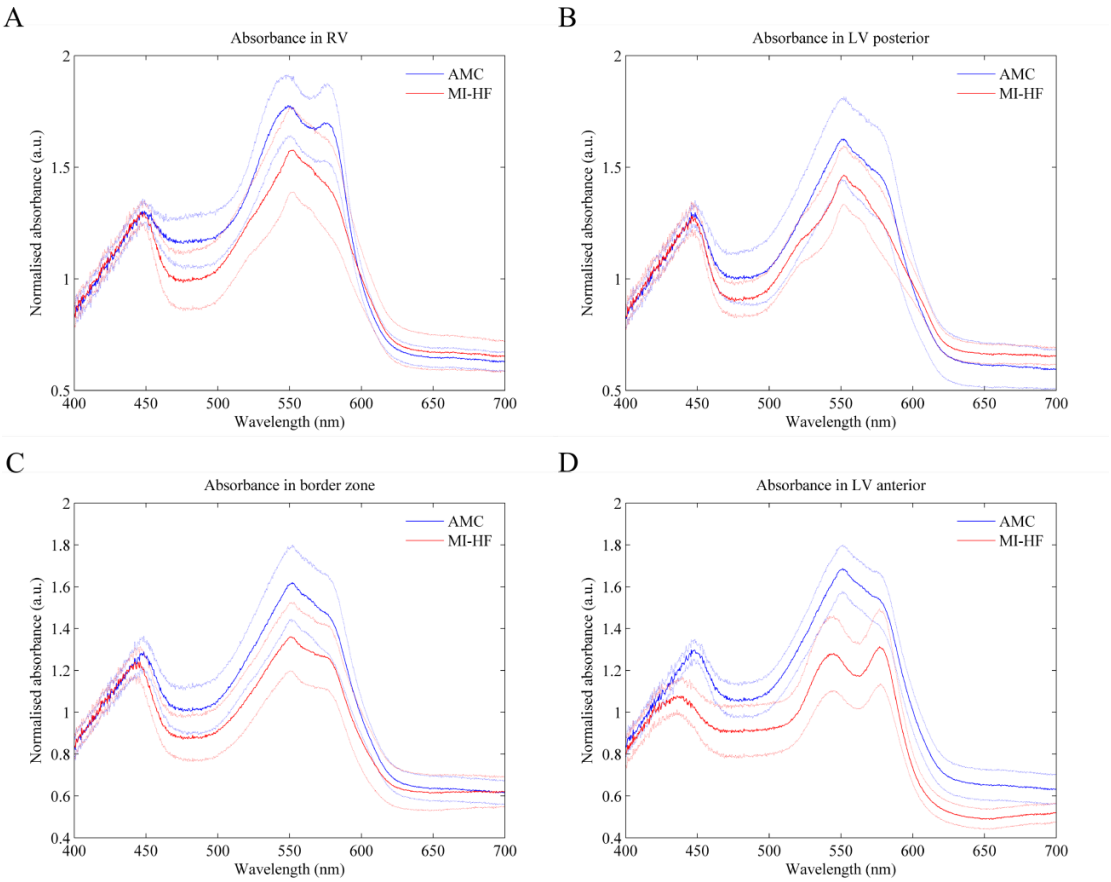


Figure 4.18 16 weeks timepoint diffuse reflectance data for MI-HF model in MI-HF and AMC, displayed by region of interest (ROI): A – RV; B – LV posterior; C – Interventricular septum / 'border zone'; D – LV anterior / 'scar'. Pale dashed lines indicate ± 1 SD.

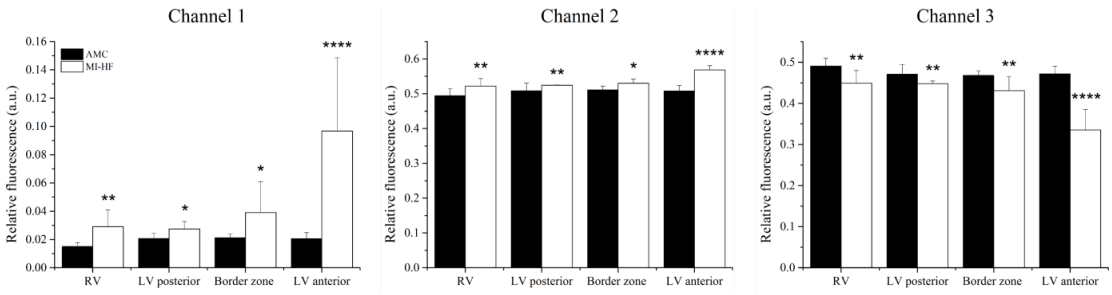


Figure 4.19 16 weeks timepoint relative contribution of each spectral channel to total autofluorescence from UV excitation in MI-HF and AMC, displayed by ROI * p < 0.05; ** p < 0.01; *** p < 0.001; **** p < 0.0001

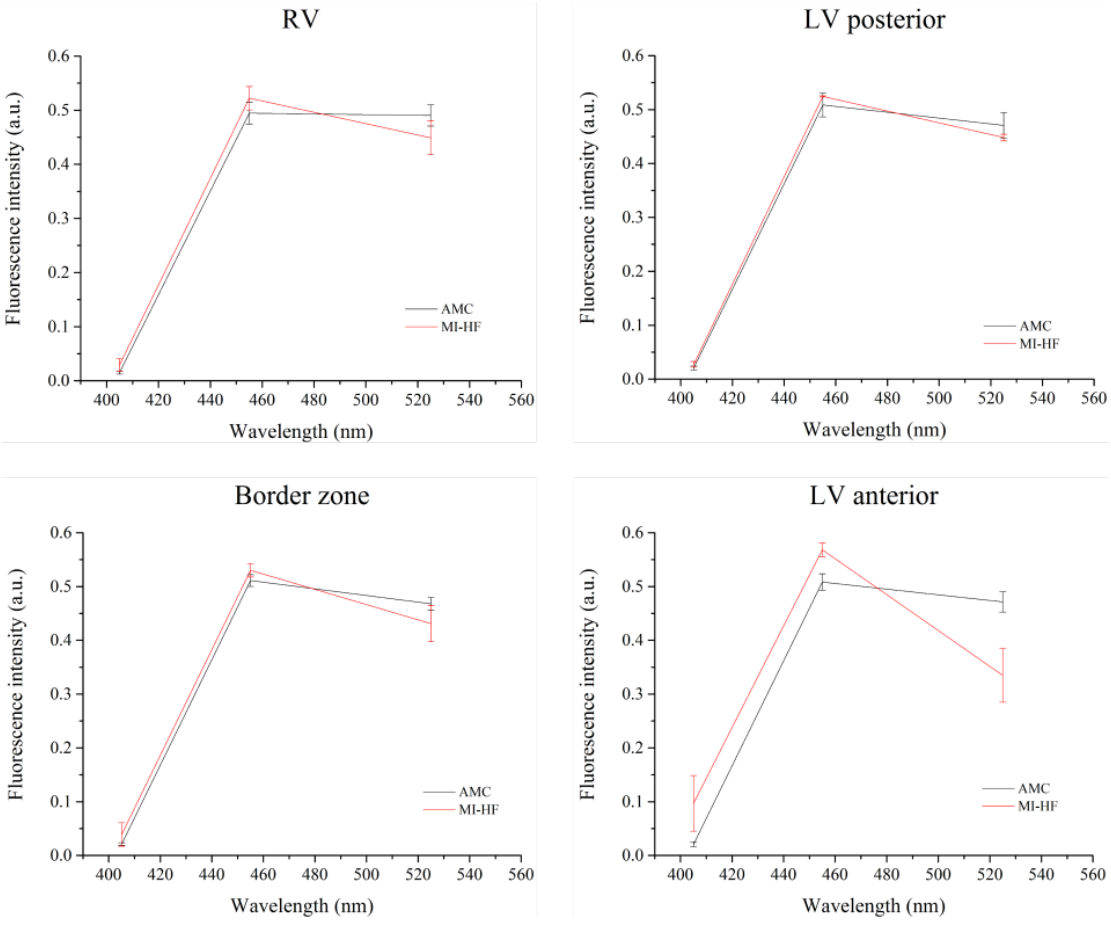


Figure 4.20 16 weeks timepoint relative autofluorescence in each ROI in MI-HF and AMC

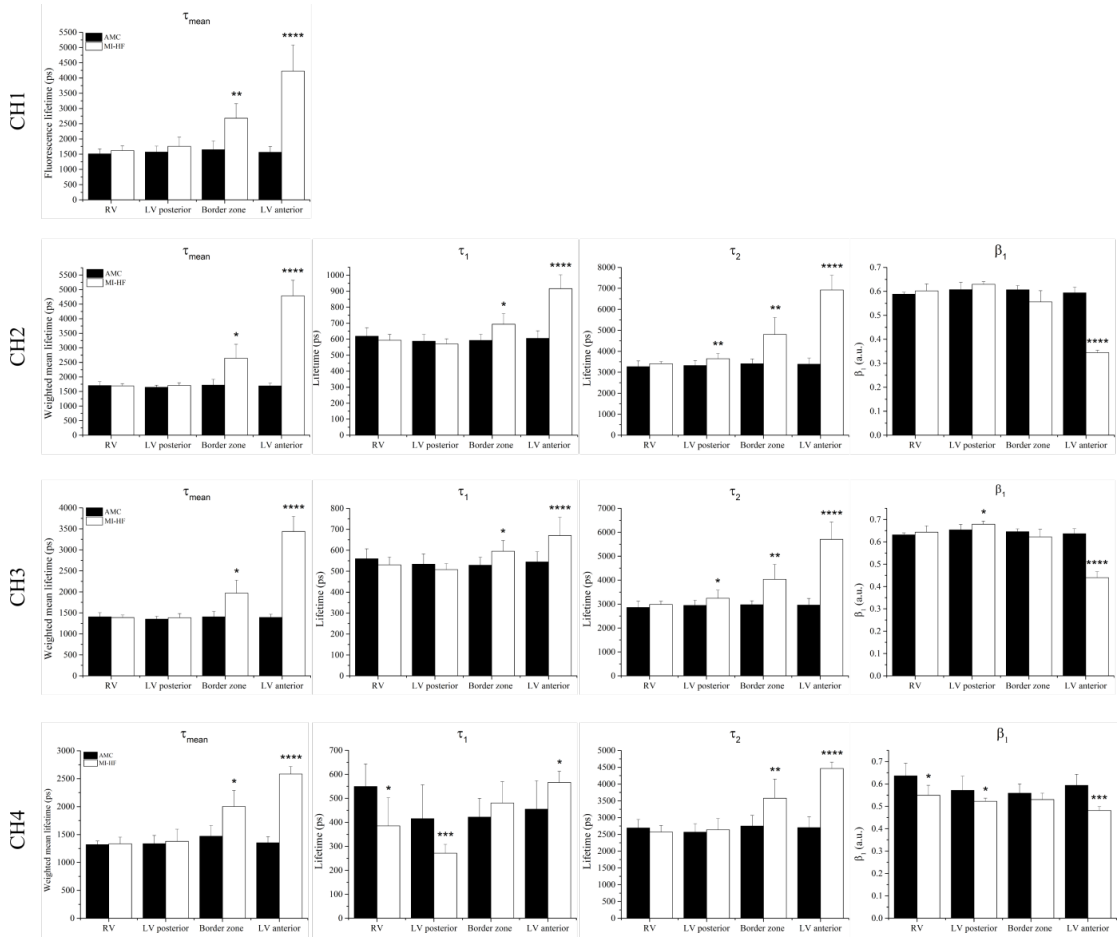


Figure 4.21 16 weeks timepoint autofluorescence lifetime parameters for each spectral channel for MI-HF and AMC, displayed by ROI. * p < 0.05; ** p < 0.01; *** p < 0.001; **** p < 0.0001

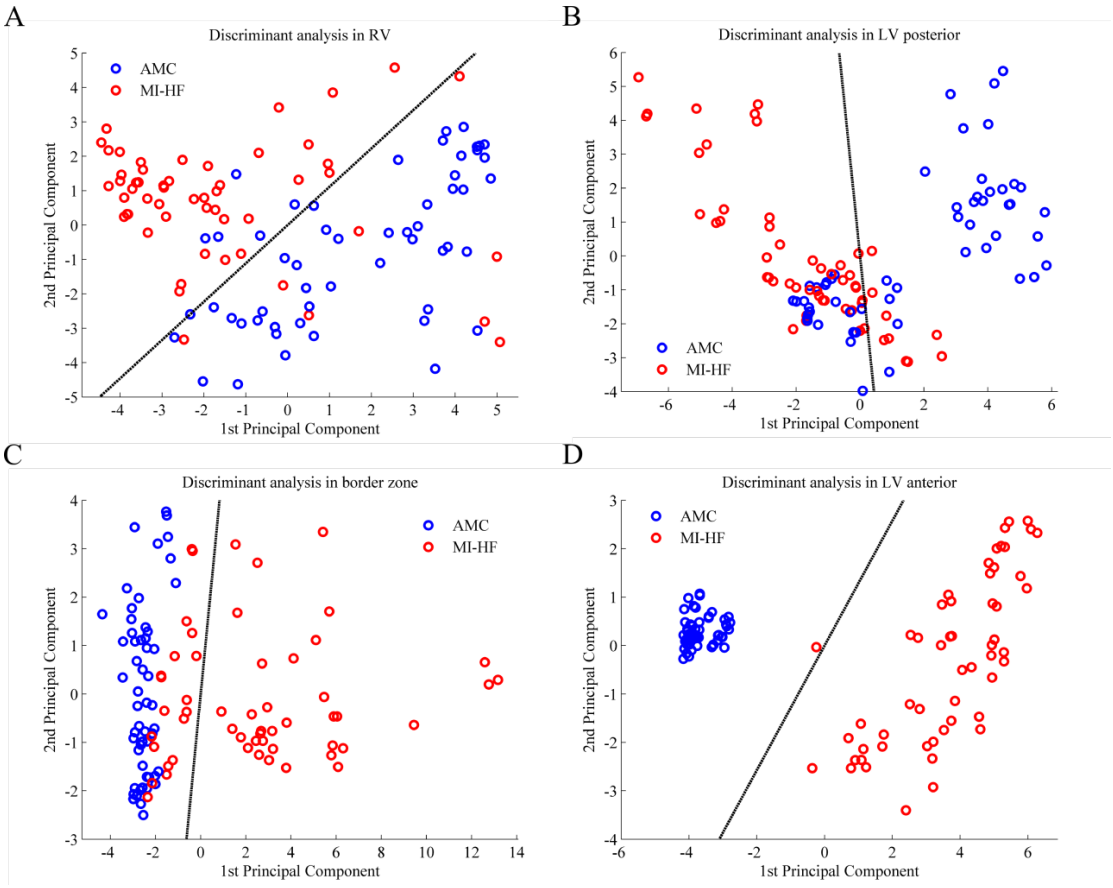


Figure 4.22 16 weeks timepoint scores of first 2 principal components from classification algorithm for MI-HF and AMC, displayed by ROI: A – RV; B – LV posterior; C – Interventricular septum / 'border zone'; D – LV anterior / 'scar'. Decision line shown as black line.

		RV	LV posterior	IVS / 'Border zone'	LV anterior / 'scar'
Diffuse reflectance	**Variance in data (%)**	97.58	98.33	98.81	98.76
	Sensitivity (%)	86.67	80.00	82.22	100.00
	Specificity (%)	75.56	64.44	80.00	97.78
	Diagnostic accuracy (%)	81.11	72.22	81.11	98.89
	AUC	0.8993	0.8247	0.8978	0.9995
Fluorescence intensity	**Variance in data (%)**	100.00	100.00	100.00	100.00
	Sensitivity (%)	88.89	87.04	75.93	90.74
	Specificity (%)	92.59	61.11	100.00	100.00
	Diagnostic accuracy (%)	90.74	74.07	87.96	95.37
	AUC	0.9556	0.8169	0.9009	0.9966
Fluorescence data (lifetime + intensity)	**Variance in data (%)**	89.31	89.77	95.57	97.47
	Sensitivity (%)	92.59	75.93	87.04	98.15
	Specificity (%)	92.59	66.67	100.00	100.00
	Diagnostic accuracy (%)	92.59	71.30	93.52	99.08
	AUC	0.9722	0.8261	0.9599	1.0000

Diffuse reflectance	**Variance in data (%)**	90.80	91.50	92.74	95.32
+					
Fluorescence intensity	**Sensitivity (%)**	93.33	84.44	88.89	100.00
	Specificity (%)	100.00	68.89	82.22	95.56
	Diagnostic accuracy (%)	96.67	76.67	85.56	97.78
	AUC	0.9886	0.8375	0.9235	1.0000
Diffuse reflectance	**Variance in data (%)**	90.07	90.90	92.27	95.12
+					
Fluorescence data	**Sensitivity (%)**	88.89	84.44	91.11	100.00
(lifetime + intensity)					
	Specificity (%)	95.56	71.11	97.78	100.00
	Diagnostic accuracy (%)	92.22	77.78	94.44	100.00
	AUC	0.9768	0.8351	0.9610	1.0000

Table 4.6 16 weeks timepoint LDA-PCA algorithm classification results by ROI using autofluorescence intensity and/or lifetime and diffuse reflectance parameters, and a combination of both autofluorescence intensity and/or lifetime and diffuse reflectance parameters

RV		LV posterior		Border zone		LV anterior	
Parameter	**Cohen's d**	**Parameter**	**Cohen's d**	**Parameter**	**Cohen's d**	**Parameter**	**Cohen's d**
CH1/CH2	3.6194	**CH4 τ_1**	4.1481	**CH2 τ_2**	2.7878	**CH2 τ_2**	17.4190
CH3 R	3.1850	**CH2/CH3**	3.2969	**CH1/CH2**	2.7672	**CH3 τ_2**	14.5197
CH1 R	3.0655	**CH3 R**	2.9840	**CH3 τ_2**	2.6609	**CH2 τ**	14.1334
CH2/CH3	2.8421	**CH2 R**	2.7562	**CH2/CH3**	2.5063	**CH4 τ**	12.6139
CH2 R	2.6249	**CH2 τ_2**	2.6377	**CH3 R**	2.5026	**CH3 τ**	12.3597
CH1/CH3	2.5775	**CH4 β**	2.1054	**CH1 τ**	2.4691	**CH4 τ_2**	11.823
CH4 β	2.2724	**CH3 τ_2**	2.0933	**CH4 τ_2**	2.3660	**CH2 β**	11.4449
CH4 τ_1	2.0679	**CH1/CH2**	2.0349	**CH4 τ**	2.3323	**CH3 R**	9.9226
CH3 τ_1	1.1111	**CH1/CH3**	1.8427	**CH2 τ**	2.3001	**CH1 τ**	9.5940
CH2 τ_2	0.9962	**CH3 β**	1.7171	**CH2 R**	2.1521	**CH2/CH3**	8.8942
CH2 τ_1	0.9591	**CH1 R**	1.7059	**CH3 τ**	2.1376	**CH3 β**	7.8543
CH3 τ_2	0.8610	**CH2 β**	1.4943	**CH1 R**	2.1263	**CH1 R**	7.5021
CH1 τ	0.7456	**CH1 τ**	1.4824	**CH2 τ_1**	2.0304	**CH2 R**	7.1382
CH4 τ_2	0.6885	**CH3 τ_1**	1.4791	**CH1/CH3**	1.9282	**CH1/CH2**	7.0825
CH2 β	0.6270	**CH2 τ**	1.2145	**CH3 τ_1**	1.8181	**CH1/CH3**	6.1895
CH3 β	0.5323	**CH2 τ_1**	0.7917	**CH2 β**	1.5082	**CH2 τ_1**	5.3901
CH3 τ	0.3719	**CH3 τ**	0.6608	**CH3 β**	0.8523	**CH3 τ_1**	4.0100
CH4 τ	0.2552	**CH4 τ**	0.5169	**CH4 β**	0.8157	**CH4 β**	3.8476
CH2 τ	0.2258	**CH4 τ_2**	0.4723	**CH4 τ_1**	0.6735	**CH4 τ_1**	1.8502

Table 4.7 16 weeks timepoint autofluorescence parameters calculated for LDA-PCA algorithm classification method ranked by Cohen's d coefficient.

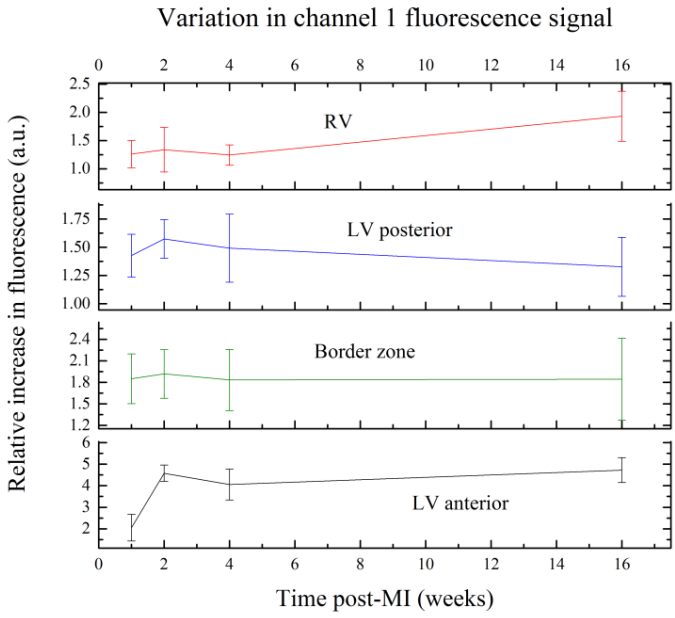


Figure 4.23 Relative channel 1 (400 – 420 nm) autofluorescence in MI-HF to AMC hearts in each ROI against time point after MI induction surgery

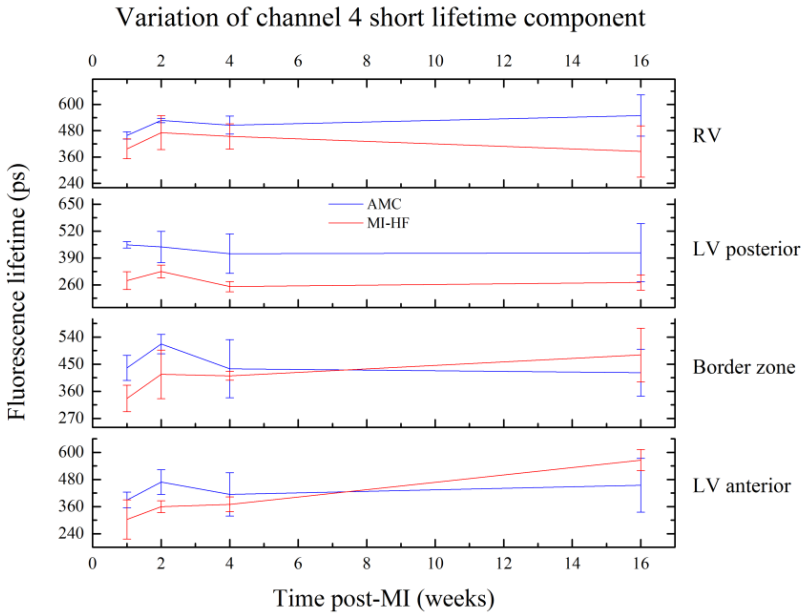


Figure 4.24 Variation of short lifetime component $\tau 1$ of detection channel 4 (500 – 550 nm) in MI-HF to AMC hearts in each ROI against time point after MI induction surgery

4.4 Discussion

This chapter describes the application of a compact instrument combining time-resolved spectrofluorometry and diffuse reflectance spectroscopy to explore the potential of these label-free optical readouts to detect the structural and metabolic changes in an established myocardial infarction heart failure model. Owing to absorption and scattering of both the excitation light and emitted fluorescence, our instrument is most sensitive to autofluorescence signal emitted from the epicardial surface of the myocardium. This could be disadvantageous in disease processes that vary with depth within the myocardium. As myocardial infarction causes both localized and global remodelling, measurements from the epicardial surface represent an initial window to probe the metabolic and structural state. In the future, incorporation of the fibre-optics into a cardiac catheter could facilitate endocardial *in vivo* measurements in a minimally-invasive procedure. One concern regarding autofluorescence intensity and diffuse reflectance spectroscopy measurements from the beating heart is related to the effect of movement artefact in terms of variation in intensity of steady state parameters from changes in distance affecting optical absorption. Additionally, variable pressure applied by the probe to the epicardial surface could theoretically affect blood content in the tissue on contact, again affecting optical absorption. This would influence the measured fluorescence intensity and diffuse reflectance spectrum most strongly. An acquisition time of 1 second was chosen for each excitation as this spans several cardiac cycles in the rat – with typically 6 heart beats per acquisition - in order to average these effects. In addition, three repeat measurements at each spatial location within a region of interest were performed to achieve an average over multiple applications of the probe tip to the tissue surface. Whilst the distance from surface and the pressure on contact of the probe may influence the mean depth that is probed, it should not greatly influence the fluorescence decay recorded given the inherent ratiometric nature of fluorescence lifetime. Overall, relatively small standard deviations of fluorescence lifetime parameters obtained from AMC hearts indicate that any variation in lifetime caused by variations in probe-heart surface distance or pressure is minimal.

Myoglobin and haemoglobin are the most abundant chromophores present in cardiac tissue in cardiomyocytes and blood cells respectively. The absorption spectra of these key chromophores are highly dependent upon their oxygenation and are very similar in profile, as shown in chapter 1. Oxygenated haemoglobin has a double peak profile, with local maxima at ~540 nm and ~576 nm. In contrast, deoxygenated haemoglobin has a broader curve profile with a single maximum peak at ~555 nm. Oxygenated and deoxygenated myoglobin present very similar spectra to oxygenated and deoxygenated haemoglobin, although are very slightly red-shifted to longer wavelengths. Cytochrome c is an electron carrier of the electron transport chain located in the mitochondrial membrane. It is another chromophore that contributes to the absorption spectra of cardiac tissue. The absorbance spectrum of reduced cytochrome c exhibits a pronounced peak at ~550 nm, as discussed in chapter 1.

Absorption was reduced in MI-HF relative to AMC hearts, which we attribute to reduced blood content and, as consequence, a decrease in haemoglobin present in the tissue. The presence of the double peak profile in the LV anterior wall / 'scar' in MI-HF hearts from the 2 week timepoint onwards is suggestive of 'high levels of oxygenation'. The finding of this double peak pattern of diffuse reflectance was noted in a heart 2 weeks post MI by others, (Ti et al. 2010) although they attributed it to some recovery of tissue oxygenation. In our MI-HF model, the LV anterior wall scar by two weeks becomes very thinned (approximately 700 μm) and the excitation light travelling through oxygenated blood in the LV cavity lumen could alternatively explain this finding. A similar effect appears to be occurring for measurements of the RV in AMC hearts where the double peak profile is also observed. The normal RV is a thin-walled cardiac chamber. In the case of the RV in AMC region however, the signal also reflects the contribution of mitochondrial cytochromes, in particular cytochrome c, of which the reduced form has a strong absorption peak at 550 nm. Interestingly this pattern is lost in the RV in MI-HF after 4 week timepoint, which is consistent with the previously described (Voelkel et al. 2006) hypertrophy of the RV wall in MI, as consequence of the structural remodelling. A single peak profile was seen in AMC LV posterior and interventricular septum / 'border zone' ROIs consistent with the presence of reduced cytochrome c with a single peak at 550 nm, accompanied with a shoulder at approximately 580nm owing to the contribution of oxygenated myoglobin/haemoglobin. In MI-HF this shoulder is less evident in the LV posterior in MI hearts, which may be the result of decreased tissue oxygenation as a consequence of reduced tissue oxygenation or blood content in this area following myocardial infarction. Diffuse reflectance spectrum seems to be most sensitive to the thickness of the myocardium.

Our instrument recorded the autofluorescence emission into three spectral emission channels – channel 1 (400 – 420 nm), channel 2 (430 – 480 nm) and channel 3 (500 – 550 nm). For UV 372nm excitation, the relative signal in these three channels is in agreement with the fluorescence emission spectra acquired by others. Ti et al. measured the autofluorescence spectra of infarcted and non-infarcted regions of rat hearts 1, 2 and 4 weeks after MI induction surgery. In these experiments a 337 nm excitation laser was used. (Ti et al. 2010) They reported a general increase in autofluorescence intensity at week 1. They only reported a rise in fluorescence, which they attributed to collagen, 2 weeks after MI with a pronounced emission peak at ~400 nm, which was also present at 4 weeks. In our experiments however an increase in the relative fluorescence from channel 1 is seen from week 1, which suggests collagen proliferation immediately after infarction, particularly in the infarcted area (LV anterior), but also to a lesser extent in sites remote to the MI, reflecting interstitial fibrosis. If we assume that the fluorescence signal in detection channel 1 arises predominantly from collagen and other ECM molecules, we can use the relative contribution of this channel to the total fluorescence signal as a quantitative measure of collagen content in all regions and at different time points after MI. The results, plotted in Figure 4.23, indicate a sharp increase in collagen content in the region of infarction (LV anterior) between weeks 1 and 2, in agreement with previously published results

of Ti et al. Interestingly, the significant change in the channel 1 fluorescence signal occurred at the 1 week and 2 weeks time points, suggesting that bulk of collagen deposition proportionately in the scar region occurs predominantly in the early stages of remodelling. In contrast, these results suggest that collagen proliferation in RV occurs predominantly at a later stage of disease progression, in agreement with previous observations, (Cleutjens et al. 1995; Stefanon et al. 2013) resultant from the consequent structural remodelling of the remote non-infarcted myocardium. There is highly significant positive correlation between mean increase in relative channel 1 'collagen' autofluorescence (RV 93%, LV posterior 32.7%, interventricular septum / 'border zone' 84.5%, LV anterior / 'scar' 372%) and the histology data increase in collagen content ($r = 0.98$, $p < 0.05$). These results demonstrate the sensitivity of the instrument to report structural changes in remodelling, both in infarcted and remote regions.

The mean autofluorescence lifetime in scar tissue was significantly increased in all spectral channels, which we attribute to an increase in autofluorescence from collagen type I, given its broad emission spectrum and its previously reported longer fluorescence lifetime. Previous studies of collagen fluorescence lifetime (Marcu et al. 2000; Ashjian et al. 2004) have demonstrated that collagen's autofluorescence lifetime properties are highly dependent, not only on the wavelength of excitation and emission, but also of the source of collagen itself. We previously demonstrated that commercially available rat tail collagen type-I powder, yields a long and complex autofluorescence decay of approximately 6 ns in a cuvette spectrofluorometer that has been previously been described in the literature.(Manning et al. 2008) Using emission wavelengths of 410 nm, 455 nm and 525 nm that correspond to the centre of the instrument's detection channels 1, 2, and 3 respectively, mean lifetimes of 6.1 ns, 5.8 ns and 5.9 ns were obtained. These results are in agreement with the range of lifetimes reported in the literature (Li et al. 1997; Marcu et al. 2000). This confirms that myocardium extracellular matrix yields a longer autofluorescence lifetime compared to free and protein-bound NADH (0.4-0.5 ns and 1.0-3.0 ns respectively (Lakowicz et al. 1992; Vishwasrao et al. 2005; Skala, Riching, Bird, et al. 2007) and free and protein-bound FAD (3.0 ns to 0.3 ns) respectively. (Islam et al. 2013a; Skala, Riching, Gendron-Fitzpatrick, et al. 2007b) The relatively smaller increase in mean fluorescence lifetime in the MI-HF interventricular septum / 'border zone' region is consistent with the smaller rise in collagen seen in this region compared to the LV anterior wall / 'scar'.

We aimed to measure changes in the fluorescence lifetimes of NADH and FAD for all regions of the heart in the expectation that we would observe changes consistent with metabolic remodelling in the heart failure state. Owing to the spectral overlap of the broad emission spectrum of collagen type-I into detection channels 2 and 3, which are centred on the emission peaks of NADH and FAD respectively, it is difficult to identify and quantify changes in NADH and FAD lifetime due to an overwhelmingly large increase in the contribution of collagen type-I to the signal. As demonstrated in the *ex vivo* Langendorff perfused heart experiments described in chapter 4, NADH lifetime would be expected to decrease in poorly oxygenated tissue such as scar.

However it is likely given the considerable increase in collagen type I in MI-HF (372% increase in the LV anterior / 'scar' at 16 weeks time point confirmed histologically) along with myocyte loss, thinning of the ventricle wall and therefore potential detection of the oxygenated blood within the LV cavity, that any changes in NADH and FAD lifetimes in these regions are being masked.

In remote regions, where increase in collagen content is subtler, e.g. LV posterior and RV, it is reasonable to attribute the changes in fluorescence lifetime to changes in energetics and metabolic status as part of the metabolic remodelling of heart failure. These changes are most clearly visible at the earliest time point studied, when collagen deposition is not yet as extensive. At the 1-week time point, a statistically significant decrease in the short component (τ_1) of channels 2, 3 and 4 was seen in the LV posterior myocardium in MI-HF compared to AMC ($p < 0.01$, $p < 0.05$ and $p < 0.01$, respectively). Similar changes are also visible at 4 and 16 weeks post-MI but are less pronounced, which is likely due to overlap of the much increased collagen signal as discussed above. These changes are most visible in detection channel 4 (500 – 550nm, using 440nm excitation), which is the least affected from overlap as it detects the longest wavelengths and uses a different excitation wavelength. It is expected that FAD autofluorescence would dominate channel 4, and the short lifetime component is thought to represent the protein-bound form of FAD.(Skala, Riching, Bird, et al. 2007). Despite collagen proliferation in these areas of remote remodelling, a statistically significant decrease in the short lifetime component τ_1 at 16 weeks is still seen in both RV and LV posterior myocardium in MI-HF compared to AMC hearts ($p < 0.05$ and $p < 0.001$, respectively). Given that the effect of collagen 'noise' into channel 4 would be to increase fluorescence lifetime, these changes appear to be independent of the structural remodelling, and we therefore attribute them to changes in energetic state due to metabolic remodelling.

Changes in the metabolic state of tissue are also known to affect the 'optical redox ratio' of NADH to FAD fluorescence in biological tissues. (Skala, Riching, Gendron-Fitzpatrick, et al. 2007b; Yager et al. 1991; Duchen & Biscoe 1992; Palero et al. 2011) This was studied in the *ex vivo* Langendorff perfused heart experiments in chapter 4. The redox ratio in our instrument can be estimated from the ratio of the fluorescence intensities in channels 2 and 3, which in healthy tissue is equivalent to the ratio of [NADH]/(α[NADH] + β[FAD]), where α and β represent the relative contributions of NADH and FAD in channel 3 with 372nm excitation. This was clearly demonstrated in the rapid changes in autofluorescence signal that were clearly related to changes in metabolic state in the studies in the *ex vivo* Langendorff perfused heart. In the MI-HF model however, owing to the very large changes in collagen type I autofluorescence whose broad emission spectrum 'contaminates' the intensities of channel 2 and 3, it is not possible to determine the changes seen in the optical redox ratio, which could be due to structural or metabolic changes in the tissue.

To investigate the potential of our instrument as a diagnostic tool to differentiate healthy from

MI-HF myocardium, a discrimination algorithm based on a leave-one-out cross validation approach was performed. This used principal component analysis to identify the five parameters offering the best separation followed by linear discriminant analysis to determine the position of the decision surface. Excellent discriminative ability was demonstrated in the LV anterior wall and diagnostic accuracy was always around 100% at all time points. This would be expected in this MI-HF model, in which there is a full thickness infarction and development of a scar, which at least at later time points can readily be appreciated macroscopically due to its change in colour. What was particularly interesting was the almost-100% discriminative ability of the instrument at the 1-week time point in all regions of interest, including when some of the distal remodelling changes are subtler than at later time points.

The results in table 4.6 showed the results of the LDA-PCA algorithm classification by ROI at the 16 week timepoint using different combinations of the data collected: autofluorescence intensity and/or lifetime and diffuse reflectance parameters, and a combination of both autofluorescence intensity and/or lifetime and diffuse reflectance parameters. This showed that overall the best classification was achieved using a combination of all available autofluorescence intensity and lifetime parameter with diffuse reflectance parameters. There was however a marked difference in which parameters were the most discriminative in a given ROI as summarised in table 4.7, which ranks the parameters by their Cohen's d value by ROI.

The most discriminative parameters in the LV anterior / 'scar' region are all lifetime based – CH2 τ_2, CH3 τ_3, CH2 τ_1, CH4 τ_1, CH3 τ_1 – and all have very high Cohen's d values, which is confirmed by the higher diagnostic accuracy using a method that utilizes lifetime parameters. In the interventricular septum / 'border zone', the accuracy of the classification is lower than in the LV anterior / 'scar' although in the comparison of methods, again the use of lifetime parameters markedly improved the classification performance of the algorithm. Overall this suggests that the lifetime parameters are most sensitive to the increase in collagen content and therefore identify the structural remodelling that occurs in this model.

In areas remote to the infarction, intensity-based parameters dominated the Cohen's d value ranking. This is particularly true in the RV, where the best classification performance was obtained using diffuse reflectance and fluorescence intensity measurements. This might be due in part to changes in wall thickness and therefore optical properties of the normally thin-walled RV in post-MI remodelling with increased fibrosis and compensatory hypertrophy. In the LV posterior ROI, the best discriminative parameter was CH4 τ_1. Of note this region saw the smallest relative increase in collagen. As discussed above, the reduction in lifetime of the short component of CH4 cannot be attributed to an increase in collagen but may represent the altered metabolic milieu of post-MI heart failure as it this parameter is often attributed to the protein-bound form of FAD. The next most discriminative parameters in LV posterior ROI are CH2 I / CH3 I, CH3 R, CH2 R, CH2 τ_2. These channels include the emission wavelengths of NADH and FAD suggesting

that despite the collagen proliferation, the autofluorescence signature collected in this region is likely to be a result of both structural and metabolic alterations as part of the post-myocardial infarction remodelling.

4.5 Summary

In this chapter we described the application of time resolved fluorescence spectroscopy and diffuse reflectance measurements to characterise the autofluorescence and diffuse reflectance signatures that accompany the structural and metabolic changes in a post-myocardial infarction heart failure model at 1, 2, 4 and 16 weeks post myocardial infarction surgery. Changes in the autofluorescence signatures were seen not only in the area of infarction but also in the remodelled remote myocardium. This is the first report of a change in the autofluorescence signal that can be attributable to metabolic alterations in the myocardium. The overwhelming increase in collagen content observed from the earliest timepoints post MI is likely to mask some of the changes in NADH and FAD caused by metabolic remodelling. However changes are still observed in the short lifetimes attributable to NADH and FAD, especially at the earlier timepoints post myocardial infarction. Overall the results demonstrate the ability of the instrument to characterise structural and metabolic changes *in vivo* without the use of exogenous labels, and its potential as a diagnostic tool given its high discriminative ability to distinguish diseased and healthy myocardium.

5 Autofluorescence in a preclinical doxorubicin chemotherapy cardiomyopathy heart failure model

The study in this chapter describes the development of a intravenous doxorubicin chemotherapy cardiomyopathy heart failure model (DOX-HF) within our institution followed by the application of time resolved fluorescence spectroscopy to characterise the pattern of changes in autofluorescence parameters seen *in vivo* in this heart failure model.

5.1 Introduction

Tremendous advances have been made in the treatment of many cancers, such as breast cancer. The development of improved surgical techniques, combination chemotherapies, adjuvant and neo-adjuvant strategies and most recently molecular targeted therapies have improved outcomes, with breast cancer mortality in the UK falling by ~40% between 1989 and 2006. (Cancer Research UK n.d.) Owing to the cardiotoxicity of some therapies, the increasing population of surviving patients is experiencing a growing burden of cardiovascular sequelae, and in particular heart failure due to 'chemotherapy cardiomyopathy'. Anthracyclines are the leading cause of cardiomyopathy in cancer survivors, but remain highly efficacious drugs with a valuable role in the treatment of breast cancer and haematological malignancies.

Doxorubicin was the first anthracycline to be extracted from *Streptomyces peucetius* during the 1960s. Its cardiovascular toxicity was quickly apparent, but it has remained in widespread clinical use owing to its high potency against many cancers.(Minotti et al. 2004) The mechanisms of doxorubicin-induced cardiotoxicity are multiple and complex. Oxidative stress is a key-mediator, as cardiomyocytes are densely packed with mitochondria, which reduce doxorubicin into a free radical semiquinone-form generating high concentrations of reactive oxygen species (ROS).(Minotti et al. 2004) Lower levels of antioxidant enzymes in the heart compared to other tissues, and the high basal metabolic activity, may explain the heart-specific sensitivity.(Roca-Alonso et al. 2012) Increased ROS generation disrupts cardiomyocyte calcium cycling, leading to acute depression of myocardial contraction and relaxation. Increased ROS generation and direct mitochondrial toxicity (e.g. mitochondrial DNA fragmentation) initiate cardiomyocyte apoptosis, and this cell loss, combined with contractile depression of the remaining cells, leads to generation of heart failure.(Monsuez et al. 2010)

Doxorubicin-related cardiotoxicity manifests clinically in three time-courses: acutely with either acute pericarditis or rarely acute cardiac depression and heart failure; a sub acute heart failure

syndrome manifest by early changes in relaxation and subsequently a left ventricular ejection fraction (LVEF) decline over days to weeks; or chronic heart failure presenting several years after treatment. Emerging data suggest that these represent a spectrum of disease, and their detection depends upon the rigor of cardiac assessment during chemotherapy and follow up period, versus waiting for the later presentation of clinical symptoms. Acute cardiac injury can be seen histologically within hours. Damage is progressive with subsequent dosing causing myofibril disarray, vacuolisation, mitochondrial oedema and distorted sarcoplasmic reticulum. The interstitial perimyocytic matrix is replaced with areas of collagen-rich fibrosis.(Singal & Iliskovic 1998) Overall there is cardiomyocyte loss by necrosis and apoptosis and reduced contractile function due to altered calcium cycling and impaired energetics.

The most important factor is the total cumulative dose, with an incidence of clinical heart failure of 5% at 400 mg/m^2, 16% at 500 mg/m^2, 26% at 550 mg/m^2, and 48% at 700mg/m^2 received.(Swain et al. 2003) However, even when restricting total doses to within the perceived safer range e.g. <400mg/m^2, other factors can greatly increase the risk, compatible with a 'multiple hit' hypothesis, such as age, hypertension, previous cardiac disease, as well as exposure to other cardiotoxic chemotherapeutic agents. (Monsuez et al. 2010)

In most human trial data LVEF is established by echocardiography or MUGA (multi-gated acquisition scan) scans. However owing to functional reserve, decline in LVEF at rest is a late phenomenon. Cardiac MRI is a useful modality for establishing LV volumes and LVEF and offers potential for tissue characterisation. Presence of late gadolinium enhancement, a potential marker of myocardial fibrosis, portends a poorer prognosis in a general 'dilated cardiomyopathy' population, and signals that this translates to chemotherapy cardiomyopathy are emerging.(Fallah-Rad et al. 2011) Diagnosing cardiotoxicity and prompt commencement of treatment is essential. Treatment is currently similar to other forms of heart failure with the aim long term to prevent remodelling and progression. In patients with reduced LVEF after anthracycline therapy, commencement of enalapril and where possible, carvedilol as a 'rescue' strategy yielded complete LVEF recovery in 42% or patients, and partial recovery in 13%. All responders had commenced heart failure treatment within 6 months of chemotherapy, whereas intervening greater than 6 months after chemotherapy was significantly less effective (Cardinale et al. 2010).

The initial aim of the work in this chapter was to develop and establish a reproducible sub acute/chronic model of doxorubicin chemotherapy cardiomyopathy heart failure model within our institution. Establishment of a reliable model would permit further elucidation of the gaps in our current understanding of doxorubicin-induced cardiomyopathy as well as the investigation of preventative and treatment strategies.

Once the model was established, the second aim was to explore the application of time resolved fluorescence spectroscopy *in vivo* to see if the autofluorescence signature changes with the

structural and metabolic remodelling expected with the doxorubicin chemotherapy cardiomyopathy heart failure phenotype. The common endogenous fluorophores of the heart (NADH, FAD, collagen and other extracellular molecules) and details of cardiac metabolism and extracellular structure of the heart and changes in the heart failure states were discussed extensively in chapters 1 and 4.

The ability to appropriately instigate heart failure treatment in those patients undergoing cancer treatment by identifying early alterations in properties of the heart and therefore prevent progression before the clinical heart failure syndrome is manifest by symptoms or reduced LVEF would represent an enormous advance. A label-free method for *in vivo* characterisation of the heart would be highly desirable and could help facilitate this aim as a potential diagnostic technique.

5.2 Methods

5.2.1 Animals

All studies were performed using Sprague-Dawley male rats of approximately 250g as detailed in section 2.2. All studies involving animals were carried out under protocols approved and regulated under the Animals (Scientific Procedures) Act 1986 (Project Licenses PPL 70/7399 and 70/7419). All animal surgical procedures and perioperative management were carried out in accordance with the United Kingdom Home Office Guide on the Operation of the Animals (Scientific Procedures) Act 1986, which conforms to the Guide for the Care and Use of Laboratory Animals published by the US National Institutes of Health.

5.2.2 Doxorubicin heart failure model

The aim of the work was to develop a doxorubicin chemotherapy heart failure model in our institution. Initial work used intraperitoneal injections as the mode of administration, which has been previously well described in the literature. (Tang et al. 2013; Kharin et al. 2013; Alsaad et al. 2012; Spivak et al. 2013; Ivanová et al. 2012; Gu et al. 2012; Swamy et al. 2011; Demirkaya et al. 2009; Bugger et al. 2011; Alshabanah et al. 2010; Sayed-Ahmed et al. 2010)

In the first protocol male Sprague-Dawley rats (Charles River) of approximately 250g received a total dose of 10mg/kg doxorubicin (Teva UK Ltd, UK) or saline control via a series of five intraperitoneal (i.p.) injections of 2mg/kg over a 9-day period. Animals were observed for the severity limits in the project license (PPL 70/7399): signs of severe toxicity including blood-stained diarrhoea, abnormal secretions from the mouth, weight loss >20% baseline body weight, abdominal swelling and ascites, reduced interaction with the environment which would

necessitate culling under schedule 1. In the initial studies, at either 2 weeks or 4 weeks after the last injection animals were studied with echocardiogram (Vevo system, Visualsonics BV, Netherlands).

The second protocol that followed aimed to expand upon this initial pilot and additionally to study the protective effect of angiotensin-converting enzyme inhibition (ACEi) and beta-blockade upon the development of chemotherapy cardiomyopathy. Male Sprague-Dawley rats (Charles River) received a total dose of 10mg/kg doxorubicin treatment (n=25) (Teva UK Ltd, UK) or saline control (n=5) via a series of five intraperitoneal (i.p.) injections of 2mg/kg over a 9-day period, and received treated drinking water containing low-dose or high-dose enalapril 50mg/L or 200mg/L (TEVA UK Ltd, UK), and/or carvedilol 50mg/L (Teva UK Ltd, UK) such that there were 6 groups:

1) Control i.p. injection + Control drinking water (n=5);
2) Doxorubicin 10mg/kg i.p. + control drinking water (n=5);
3) Doxorubicin 10mg/kg i.p. + enalapril 50mg/kg drinking water (n=5);
4) Doxorubicin 10mg/kg i.p. + carvedilol 50mg/kg drinking water (n=5);
5) Doxorubicin 10mg/kg i.p. + enalapril 50mg/kg + carvedilol 50mg/kg drinking water (n=5);
6) Doxorubicin 10mg/kg i.p. + enalapril 200mg/kg drinking water (n=5).

Animals were observed for the severity limits in the project license (PPL 70/7399). Four weeks after the last injection animals were studied with echocardiogram (Vevo system, Visualsonics BV, Netherlands) and then had *in vivo* epicardial autofluorescence and diffuse reflectance measurements recorded from the LV anterior wall as a terminal procedure.

Owing to concerns regarding the severity and reproducibility of the cardiac injury a completely new approach was required. During the course of our own experiments there was publication of paper characterizing an intravenous (IV) doxorubicin model by Cove-Smith *et al* (Cove-Smith et al. 2014). Subsequent correspondence with the authors regarding their practical experience allowed the methodology to be refined and the protocol was changed to an IV administration model. This is better tolerated and furthermore better replicates doxorubicin treatment as it is given in the treatment of human patients.

In the finalized protocol, male Sprague-Dawley rats (Charles River) of approximately 250g received a total dose of 10 mg/kg of doxorubicin (Teva UK Ltd, UK) in 8 divided doses of 1.25 mg/kg via tail vein injection through a 26G Abbocath cannula (Hospira, Ireland). The tail was prepared with Hibiscrub 1:100 dilution pre and post injection and the cannula was flushed pre- and post-procedure with 0.6 ml and 1.2 ml normal saline respectively. The animals had echocardiographic assessment of cardiac function at baseline, 4, 8 and 11 weeks. In the 12th week

in vivo autofluorescence data was collected from the epicardial surface of the heart during a terminal procedure.

5.2.3 Echocardiography

Echocardiographic assessment of cardiac function at all the time points in the protocol was performed as described previously in chapter 2.

5.2.4 *In vivo* autofluorescence lifetime measurements

In vivo autofluorescence lifetime measurements were performed as described previously in chapter 2.

5.2.5 Data collection

Autofluorescence measurements were collected from three anatomical regions of interest (ROIs) of the epicardial surface of the heart during *in vivo* measurements: left ventricle; right ventricle; and posterior wall similarly to as shown in figure 4.1. From each ROI, 3 repeat acquisition measurements were measured. Each acquisition used integration times of 1 second for UV excitation and 1 second for blue excitation for autofluorescence lifetime measurements.

5.2.6 Spectral analysis and fluorescence lifetime data analysis

Spectral analysis of fluorescence data was performed as described previously in chapter 2. Fluorescence lifetime data was analysed as described in chapter 2.

5.2.7 Principal component analysis and linear discriminant analysis

To quantify the differences between DOX-HF and control hearts within a region of interest (ROI), a classification algorithm was performed similar to those described in references and as described in chapter 4. (Thompson et al. 2012; Talbot et al. 2011; Pu et al. 2013). Principal component analysis (PCA) is employed for selection of the 5 most significant principal components. Linear discriminant analysis is then performed on these using a 'leave-one-out' cross-validation approach that allows each measurement to be classified as either DOX-HF or control. Each individual point measurement was used in the analysis. Receiver operator characteristic (ROC) curves were generated and the performance of algorithm was measured by are under the ROC curve (AUC)

5.3 Results

5.3.1 Intraperitoneal doxorubicin treatment models

In the initial cohort with intraperitoneal doxorubicin administration, there was a significantly lower body weight in doxorubicin treated animals compared to control (n = 4) at both the 2 weeks' timepoint (2 week DOX (n = 2) 381.5 g ± 13.5 g vs. 479.5g ± 17.5 g, * p = 0.02) and at the 4 weeks' timepoint (4 week DOX (n = 5) 393.8 g ± 16.71 g vs. 479.5g ± 17.5 g, ** p = 0.0093) as shown in figure 5.1. There was a significant reduction in ejection fraction assessed by echocardiogram in the doxorubicin treated animals compared to controls (n = 4) at the 4 weeks' timepoint (n = 5) (59.82 % ± 4.872 % vs. 85.46 % ± 2.45 %, ** p = 0.0033) as shown in figure 5.2. There was one death in the doxorubicin-treated group at approximately 3 weeks after administration of doxorubicin (1 out of 6 (16.66 %) of the 4 weeks' group). Two of the doxorubicin-treated animals had fluid in the peritoneal cavity, and this observation was noted during the examination of the sudden death animal post-mortem.

In the subsequent protocol an intraperitoneal mode of doxorubicin administration was used with treated drinking water looking to observe the protective effect of ACEi or beta blocker given concurrently with the doxorubicin. There was a significantly higher than expected mortality seen overall in the study with the following sudden deaths observed within each group: Control i.p. injection + Control drinking water (0/5); Doxorubicin 10mg/kg i.p. + control drinking water (4/5); Doxorubicin 10mg/kg i.p. + enalapril 50mg/kg drinking water (1/5); Doxorubicin 10mg/kg i.p. + carvedilol 50mg/kg drinking water (2/5); Doxorubicin 10mg/kg i.p. + enalapril 50mg/kg + carvedilol 50mg/kg drinking water (1/5); Doxorubicin 10mg/kg i.p. + enalapril 200mg/kg drinking water (1/5). This is summarised in figure 5.3. There was a significantly reduced mortality rate in those animals that were given ACEi and / or beta-blocker in the drinking water concomitantly with the intraperitoneal doxorubicin (Treated, n = 20) compared to those that received control drinking water (DOX, n = 5) (DOX mortality 20% vs. Treated 80%, χ^2 = 6.6176, 1.d.f. * p = 0.01) as shown in figure 5.4. Figure 5.5 shows the mean lifetime (τ) of channels 1 – 4 for each of the treatment groups however there was only n = 1 in the doxorubicin treatment arm. There was no statistical significance between the mean lifetime amongst the other treatment groups, although there did appear to be a longer lifetime especially in channel 1, in the single doxorubicin + control drinking water treated animal.

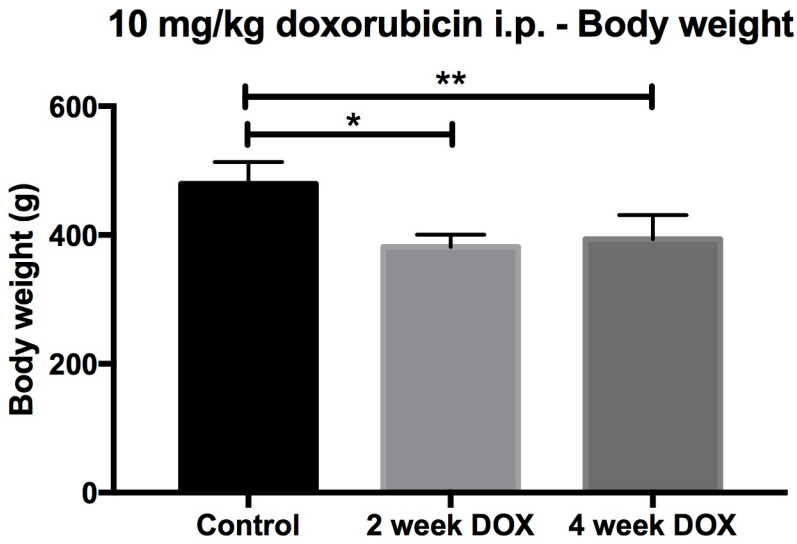


Figure 5.1 Body weight (g) in animals treated with 10 mg / kg intraperitoneal doxorubicin or intraperitoneal saline control at 2 weeks and 4 weeks post last injection. * p < 0.05; ** p < 0.01.

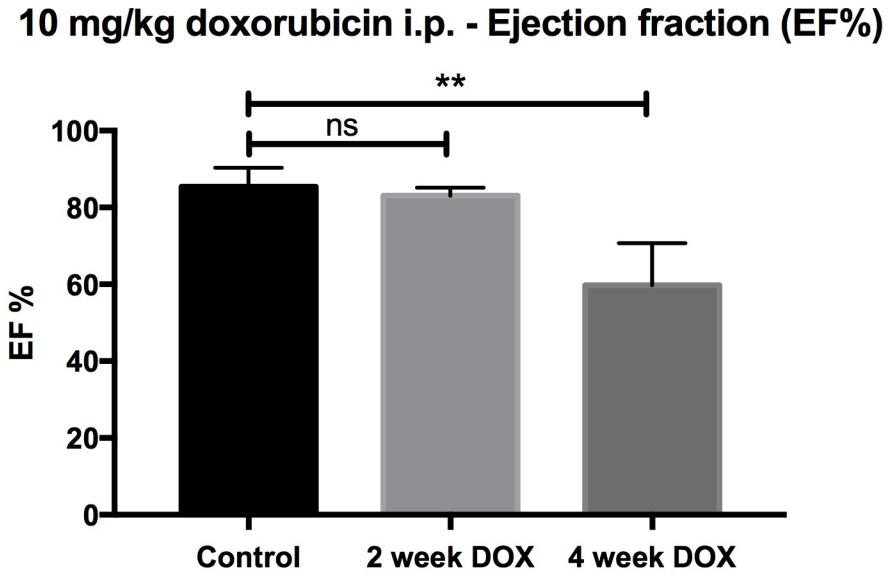


Figure 5.2 Ejection fraction (%) assessed by echocardiography in animals treated with 10 mg / kg intraperitoneal doxorubicin or intraperitoneal saline control at 2 weeks and 4 weeks post last injection. ** p < 0.01.

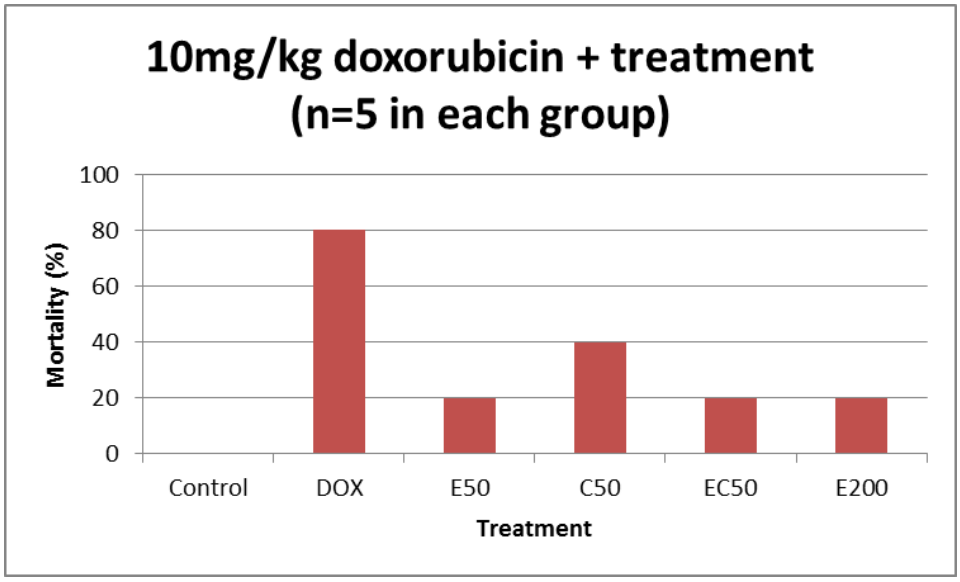


Figure 5.3 Mortality (%) in animals treated with 10 mg / kg intraperitoneal doxorubicin or intraperitoneal saline control and treated or control drinking water: Control - control i.p. injection + control drinking water (n = 5); DOX - doxorubicin 10mg/kg i.p. + control drinking water (n = 5); E50 - doxorubicin 10mg/kg i.p. + enalapril 50mg/kg drinking water (n = 5); C50 - doxorubicin 10mg/kg i.p. + carvedilol 50mg/kg drinking water (n = 5); EC50 - doxorubicin 10mg/kg i.p. + enalapril 50mg/kg + carvedilol 50mg/kg drinking water (n = 5); E200 – doxorubicin 10mg/kg i.p. + enalapril 200mg/kg drinking water (n = 5).

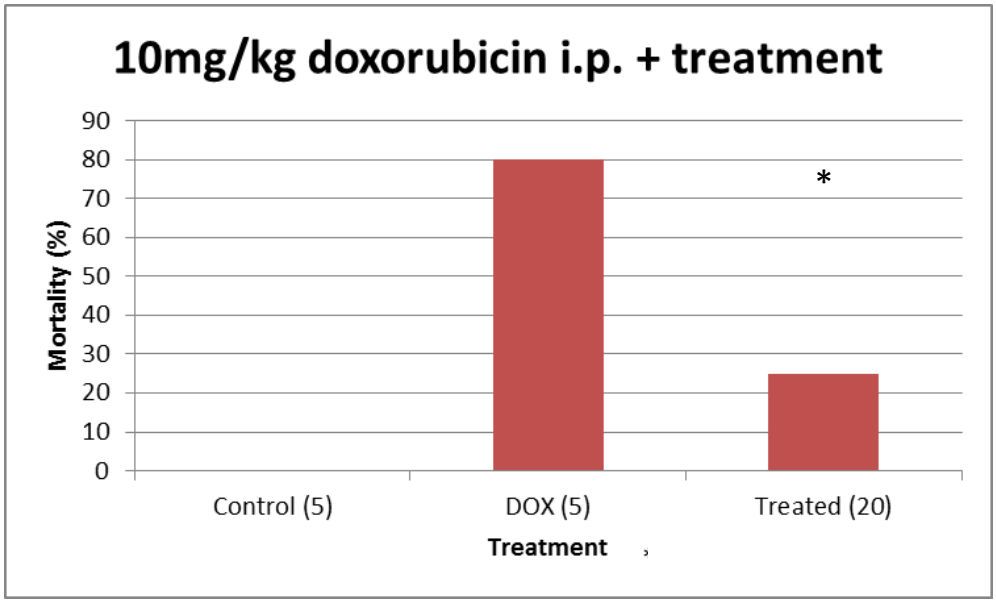


Figure 5.4 Mortality (%) in animals treated with 10 mg / kg intraperitoneal doxorubicin (DOX) or intraperitoneal saline control (Control) and treated drinking water (Treated) or control drinking water (control) (* p = 0.01)

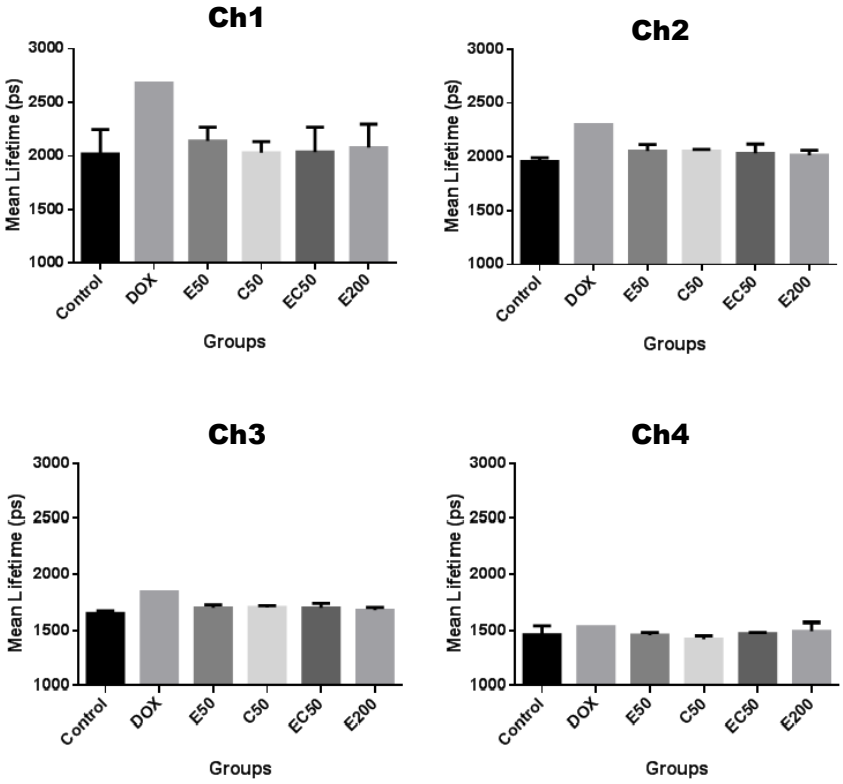


Figure 5.5 Mean lifetime (τ) of LV anterior wall (LV) by channel in animals treated with 10 mg / kg intraperitoneal doxorubicin or intraperitoneal saline control and treated or control drinking water: Control - control i.p. injection + control drinking water (n = 5); DOX - doxorubicin 10mg/kg i.p. + control drinking water (n = 1); E50 - doxorubicin 10mg/kg i.p. + enalapril 50mg/kg drinking water (n = 4); C50 - doxorubicin 10mg/kg i.p. + carvedilol 50mg/kg drinking water (n = 3); EC50 - doxorubicin 10mg/kg i.p. + enalapril 50mg/kg + carvedilol 50mg/kg drinking water (n = 4); E200 – doxorubicin 10mg/kg i.p. + enalapril 200mg/kg drinking water (n = 4).

5.3.2 Intravenous doxorubicin treatment model

Figure 5.6 shows body weight vs. timepoint during the protocol of 8 weekly injections of IV doxorubicin 1.25mg/kg (total cumulative dose of 10 mg/kg) and the post-dosing period in the IV doxorubicin treated animals (DOX-HF) compared to the controls. There was no significant difference using a Bonferroni-adjusted alpha level of .0042 per test (0.05/12) in body weight between DOX-HF animals (n = 9) and control animals (n = 4) at baseline and at the week 1, 2 and 3 timepoints (Week 0: DOX-HF 253.00 ± 1.68 g vs. control 248.00 ± 3.29 g, ns p=0.115; Week 1: DOX-HF 293.2 ± 13.22 g vs. control 301.8 ± 13.22 g, ns p=0.115; Week 2: DOX-HF 300.6 ± 14.24 g vs. control 313.3 ± 12.61 g, ns p=0.1413; Week 3: DOX-HF body weight 338.56 ± 6.88 g vs. control 376.25 ± 6.88 g, p = 0.0168) but from the 4 weeks timepoint onwards there is a significantly

reduced body weight in DOX-HF animals (n = 7-9) compared to control animals (n = 4) at all later timepoints (Week 4: DOX-HF body weight 342.22 ± 6.62 g vs. control 397.50 ± 8.75 g, * p = 0.0028; Week 5: DOX-HF body weight 342.26 ± 19.49 g vs. control 408.80 ± 14.36 g, * p = 0.0028; Week 6: DOX-HF body weight 352.50 ± 24.35 g vs. control 430.00 ± 14.72 g, * p = 0.0040; Week 7: DOX-HF body weight 349.4 ± 31.33 g vs. control 450.00 ± 17.8 g, * p = 0.0040; Week 8: DOX-HF body weight 343.80 ± 27.48 g vs. control 476.30 ± 14.93 g, * p = 0.0040; Week 9: DOX-HF body weight 352.50 ± 28.28 g vs. control 486.3 ± 17.02 g, * p = 0.0040; Week 10: DOX-HF body weight 342.9 ± 29.28 g vs. control 500.00 ± 15.81 g, * p = 0.0006; Week 11: DOX-HF body weight 339.57 ± 14.19 g vs. 523.5 ± 8.75 g, * p = 0.0006)

Figure 6.7 shows the ejection fraction (EF%) calculated from M-mode echocardiography in IV doxorubicin (total cumulative dose of 10 mg/kg) treated animals (DOX-HF) compared to the controls at the timepoints baseline, 4 weeks, 6 weeks, 8 weeks, and 11 weeks. There was no significant difference in EF% at baseline between doxorubicin-treated DOX-HF animals (n = 9) compared to controls (n = 4) (Week 0: DOX-HF EF% 83.78 ± 1.59 % vs. 80.83 ± 1.91 %, ns p = 0.28). At all later timepoints there was a significantly reduced EF% using a Bonferroni-adjusted alpha level of 0.01 per test (0.05/5) in DOX-HF animals (n = 7-9) compared to control animals (n = 4). (Week 4: DOX-HF EF% 64.49 ± 1.18 % vs. 79.26 ± 0.42%, * p = 0.003; Week 6: DOX-HF EF% 61.38 ± 2.703 % vs. 83.94 ± 2.86 %, * p = 0.004; Week 8: DOX-HF EF% 58.16 ± 3.08 % vs. 84.10 ± 0.69 %, * p = 0.004; Week 11: DOX-HF EF% 49.60 ± 3.81 % vs. 80.45 ± 3.12 %, * p = 0.006).

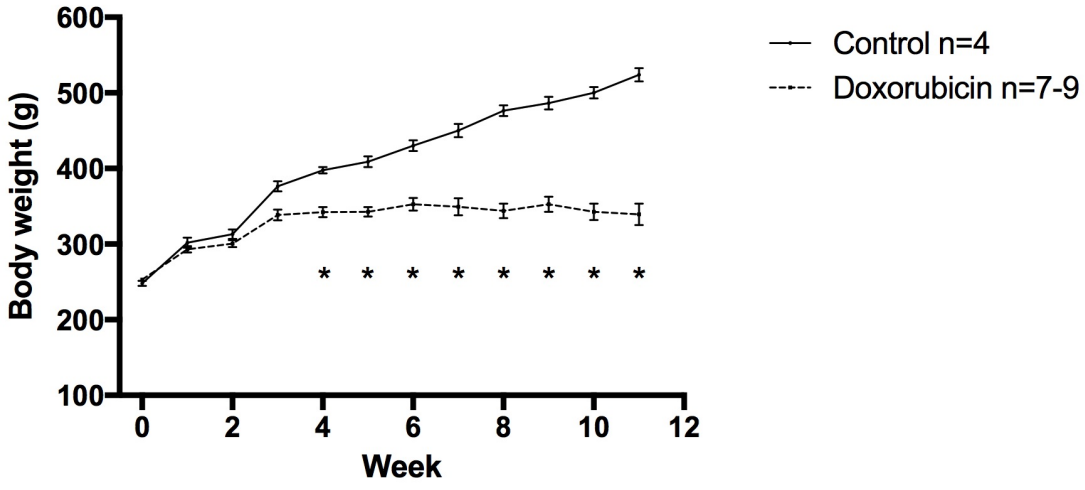


Figure 5.6 Body weight (g) in control (solid line, n=4) and 10 mg/kg IV doxorubicin treated (dashed line, n = 7-9) * p < 0.0042 Bonferroni-adjusted alpha level (0.05/12)

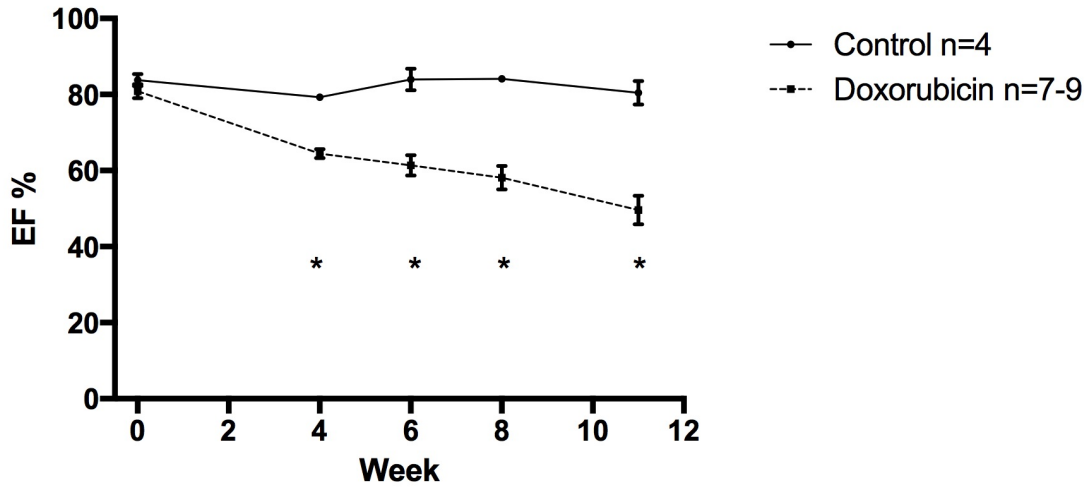


Figure 5.7 Ejection fraction calculated from M-mode echocardiography in control (solid line, n = 4) and 10 mg/kg IV doxorubicin treated (dashed line, n = 7-9) * p < 0.01 Bonferroni-adjusted alpha level (0.05/5)

5.3.2.1 Autofluorescence spectral measurements

Figures 5.8 – 5.19 show the autofluorescence parameters for each of the spectral channels measured from the LV, RV, and 'Posterior' LV. The spectral measurements can be considered from the 'Ch X' ratio from each of the Ch 1-3 results for the regions of interest where the 'Ch X' represents the proportion of the total autofluorescence from the UV excitation collected within that spectral channel 'X'. In the results from the RV region of interest shown in figures 5.12, 5.13 and 5.14, doxorubicin-treated DOX-HF animals (n = 6) showed a statistically significant increase in channel 1 ratio (**, p=0.0064) and channel 2 ratio (*, p = 0.0108) and decrease in channel 3 ratio (**, p = 0.0075) compared to controls (n = 3). Similarly in the 'Posterior' LV, as shown in figures 6.16, 6.17, and 6.18, the same pattern was observed with a statistically significant increase in channel 1 ratio (*, p=0.0138) and channel 2 ratio (*, p = 0.0196) and decrease in channel 3 ratio (**, p = 0.0121) in DOX-HF (n = 6) compared to controls (n = 3). In the results from the LV anterior wall, shown in figures 5.8, 5.9, and 5.10, the same trend is observed as in the other areas with an increased channel 1 ratio and channel 2 ratio and a decreased channel 3 ratio, however it does not reach statistical significance in this region of interest. Overall these changes represent a shift in fluorescence emission towards shorter wavelengths with a greater proportion of the signal falling in channels 1 (400 – 420 nm) and channel 2 (430 – 480 nm) than in channel 3 (500 – 550 nm).

5.3.2.2 Autofluorescence lifetime measurements

Figures 5.8, 5.9, 5.10 and 5.11 summarise the autofluorescence lifetime results for the left ventricle anterior wall 'LV' region of interest for channels 1 – 4 respectively for IV doxorubicin DOX-HF animals (n = 6) vs. control (n = 3). In channel 1 (400 – 420 nm) there appears to be a

trends towards an increase in channel 1 mean tau (τ) (ns, p = 0.07) in DOX-HF hearts. In channel 2 (430 – 480 nm) there appears to be a trend towards an increase in the long component lifetime (τ_2) (ns, p = 0.0929), an increase in mean tau (τ) in DOX-HF hearts. In channel 3 (500 – 500 nm with 375 nm excitation) there again appears to be a trend towards an increase in the long component lifetime (τ_2) (ns, p = 0.0589), an increase in mean tau (τ) (ns, p = 0.0546) in DOX-HF hearts, not quite reaching the threshold for statistical significance at $p < 0.05$. In channel 4 (500 – 550 nm with 435nm excitation) there was a statistically significant increase in the long component lifetime (τ_2) (*, p = 0.0235), however the mean tau (τ) changes are less clear-cut in this region of interest.

Figures 5.12, 5.13, 5.14 and 5.15 summarise the autofluorescence lifetime results for the right ventricle 'RV' region of interest for channels 1 – 4 respectively for IV doxorubicin DOX-HF animals (n = 6) vs. control (n = 3). In channel 1 (400 – 420 nm) there appears to be a trend towards an increase in channel 1 mean tau (τ) in DOX-HF hearts. In channel 2 (430 – 480 nm) there is a significant increase in the long component lifetime (τ_2) (*, p = 0.0308) in DOX-HF hearts and there also appears to be a trend towards an increase in mean lifetime in channel 2, which didn't reach statistical significance. In channel 3 (500 – 500 nm with 375 nm excitation) the same pattern is seen with a significant increase in the long component lifetime (τ_2) (*, p = 0.0193) and a trend towards an increase in mean lifetime (τ) in DOX-HF hearts. In channel 4 (500 – 550 nm with 435nm excitation) there is a statistically significant increase in long component lifetime (τ_2) (**, p = 0.0082) and the mean lifetime (τ) (*, p = 0.0232) in DOX-HF hearts.

Figures 5.16, 5.17, 5.18 and 5.19 summarise the autofluorescence lifetime results for the posterior wall of the left ventricle 'Posterior' region of interest for channels 1 – 4 respectively for IV doxorubicin DOX-HF animals (n = 6) vs. control (n = 3). In channel 1 (400 – 420 nm) there is no significant change in mean tau (τ) in DOX-HF hearts and the possible trend towards an increase suggested in the LV and RV is not seen. In channel 2 (430 – 480 nm) there is a significant increase in the long component lifetime (τ_2) (*, p = 0.0326) and the mean lifetime (τ) (*, p = 0.0415) in DOX-HF hearts. In channel 3 (500 – 500 nm with 375 nm excitation) the same pattern is seen with a significant increase in the long component lifetime (τ_2) (*, p = 0.0234) and mean lifetime (τ) (*, p = 0.0400) in DOX-HF hearts. In channel 4 (500 – 550 nm with 435nm excitation) there is a statistically significant increase in long component lifetime (τ_2) (**, p = 0.0082) and the mean lifetime (τ) (*, p = 0.0232) in DOX-HF hearts.

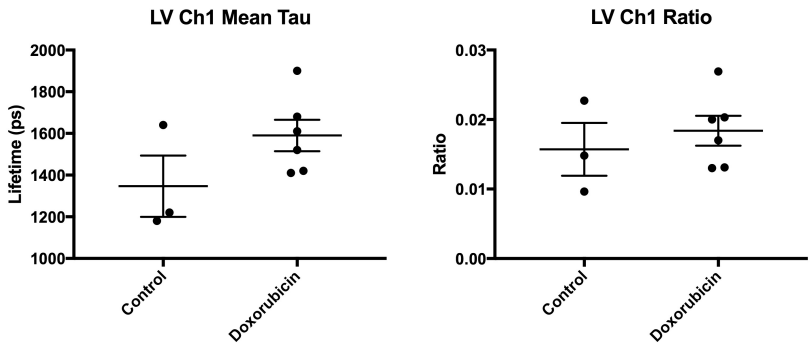


Figure 5.8 - Anterior left ventricle (LV) autofluorescence lifetime parameters for spectral channel 1 (Ch1) in IV doxorubicin (n = 6) and control (n = 3) animals (n.s.)

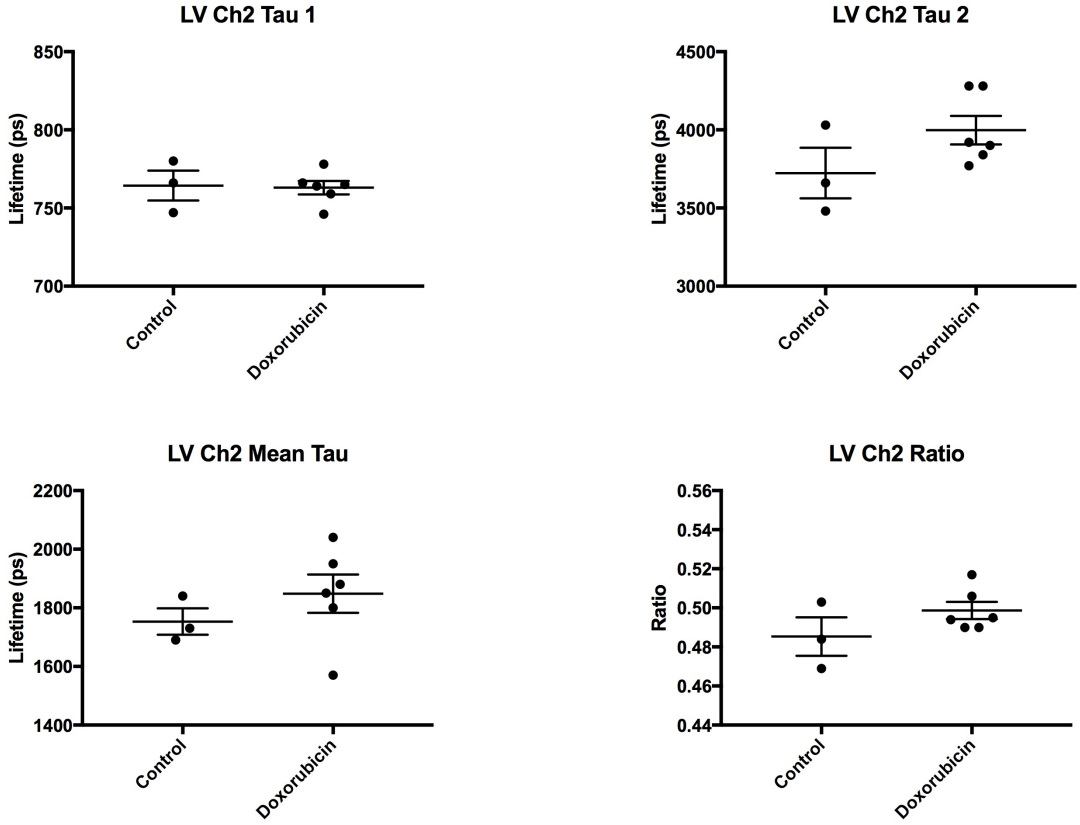


Figure 5.9 - Anterior left ventricle (LV) autofluorescence lifetime parameters for spectral channel 2 (Ch2) in IV doxorubicin (n = 6) and control (n = 3) animals (n.s.)

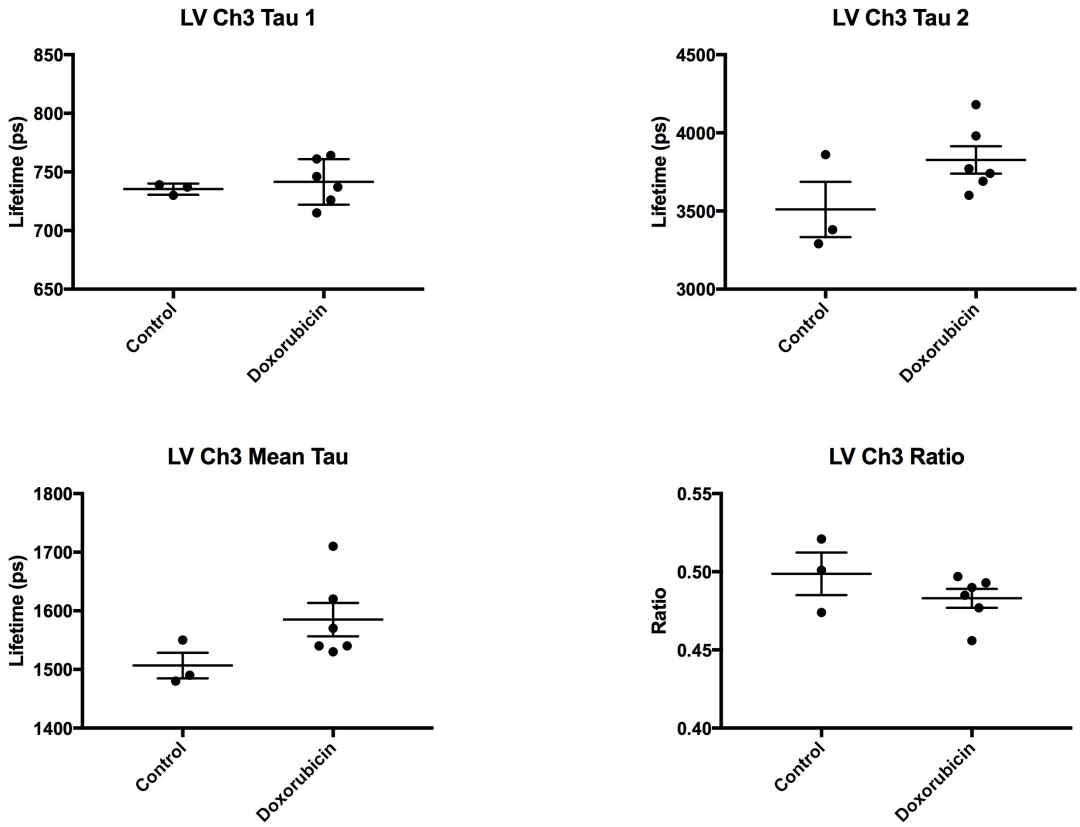


Figure 5.10 Anterior left ventricle (LV) autofluorescence lifetime parameters for spectral channel 3 (Ch3) in IV doxorubicin (n = 6) and control (n = 3) animals (n.s.)

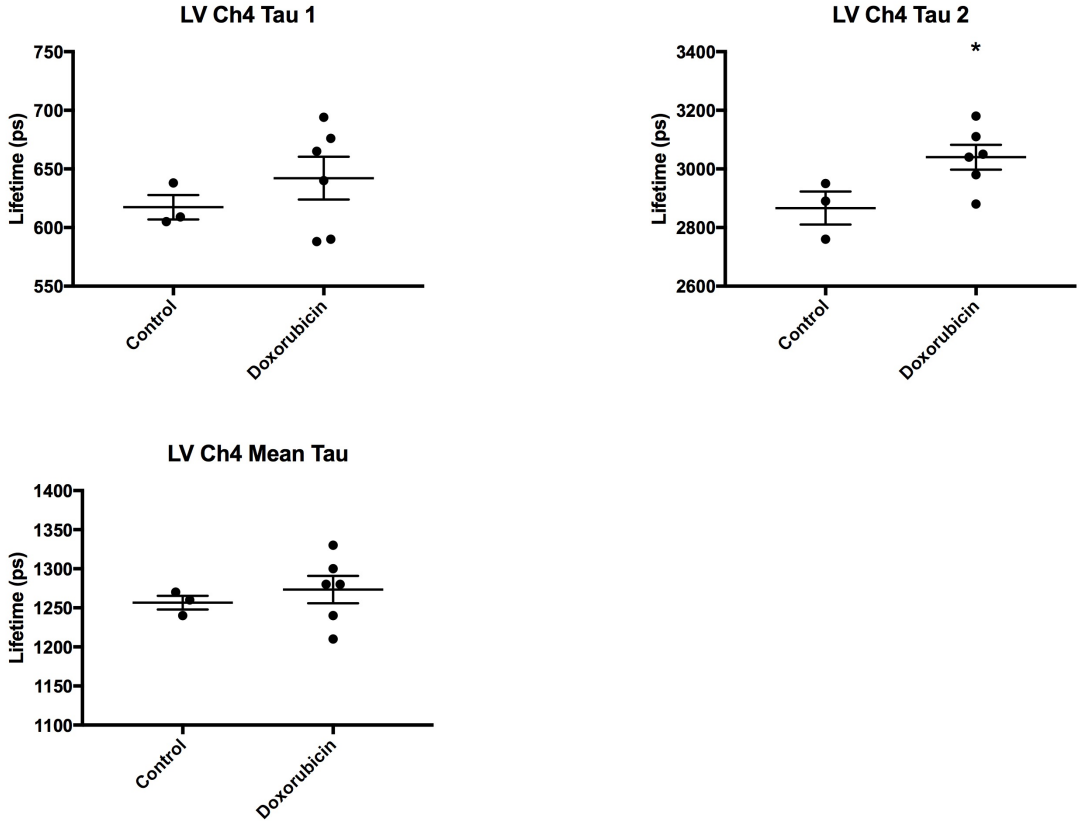


Figure 5.11 Anterior left ventricle (LV) autofluorescence lifetime parameters for spectral channel 4 (Ch4) in IV doxorubicin (n = 6) and control (n = 3) animals (n.s.)

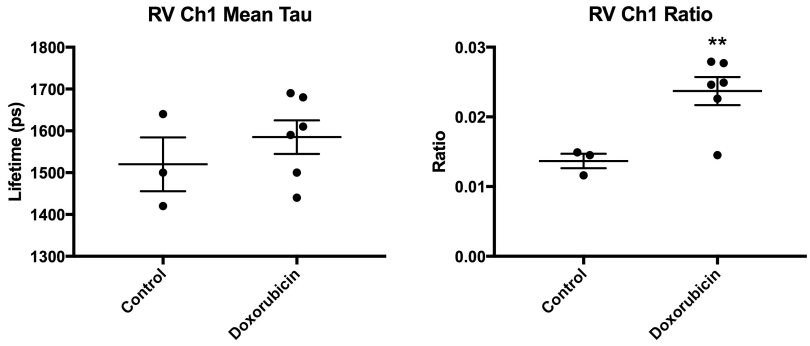


Figure 5.12 Right ventricle (RV) autofluorescence lifetime parameters for spectral channel 1 (Ch1) in IV doxorubicin (n = 6) and control (n = 3) animals ** $p < 0.01$.

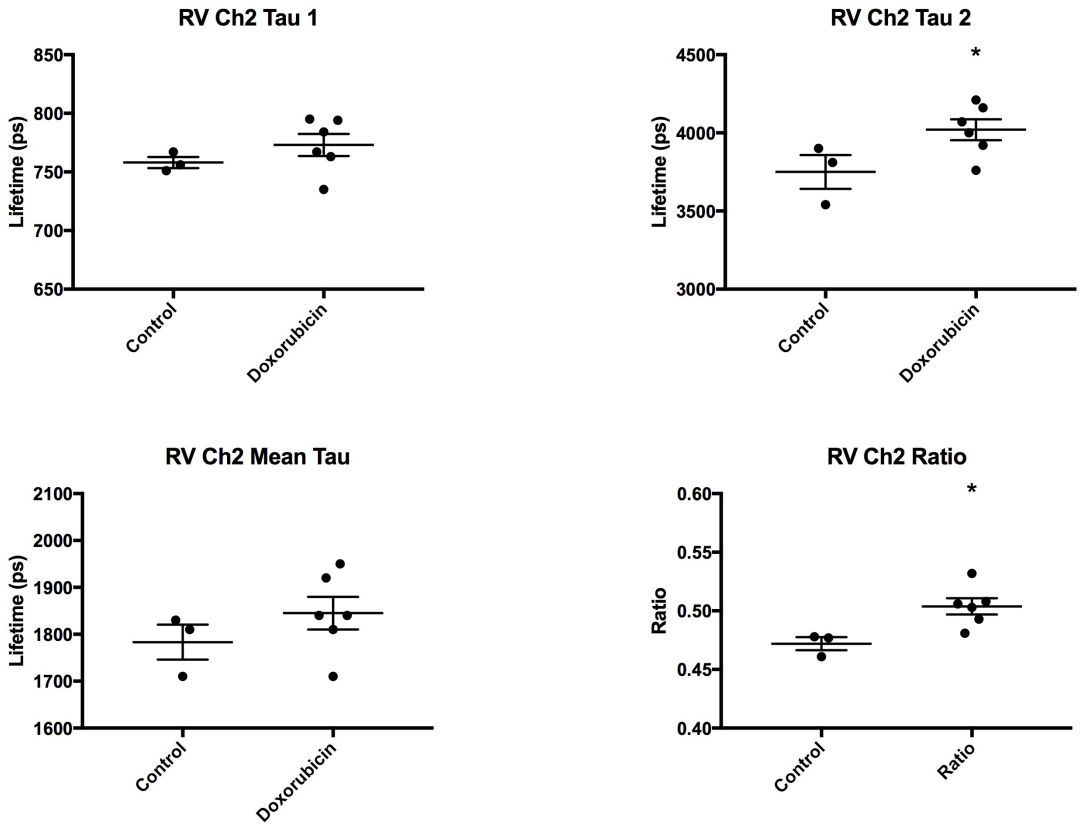


Figure 5.13 Right ventricle (RV) autofluorescence lifetime parameters for spectral channel 2 (Ch2) in IV doxorubicin (n = 6) and control (n = 3) animals. * $p < 0.05$.

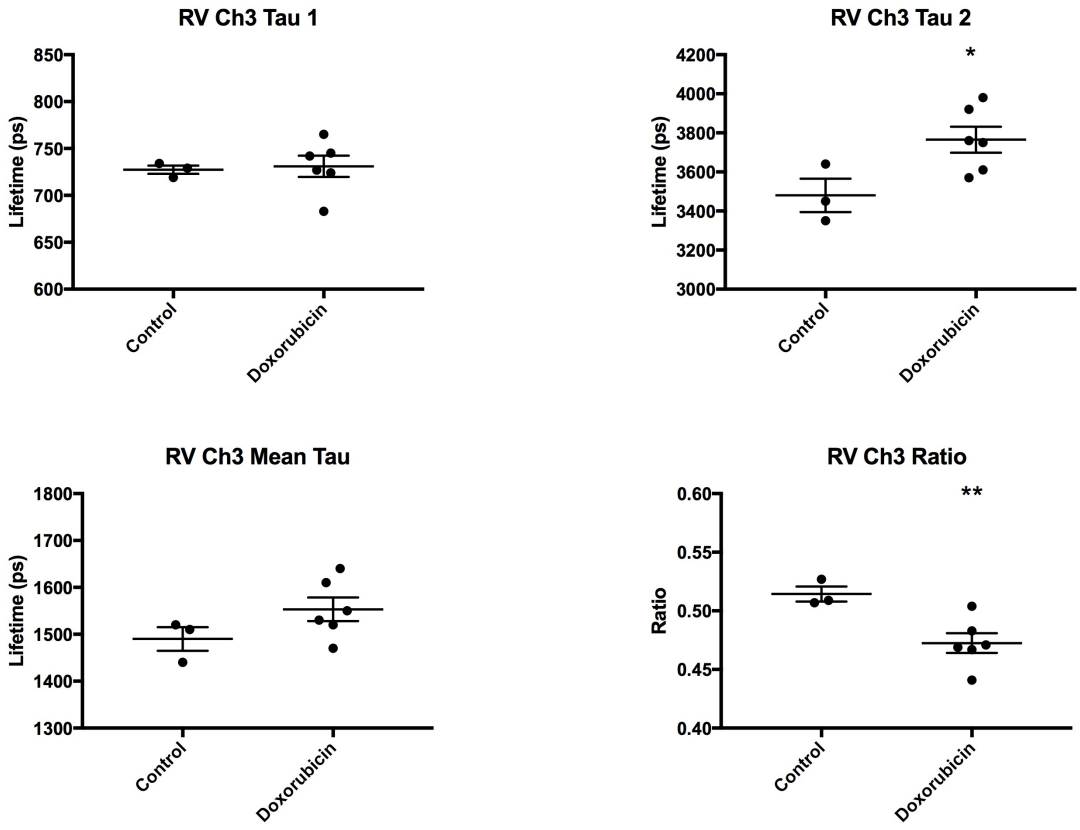


Figure 5.14 Right ventricle (RV) autofluorescence lifetime parameters for spectral channel 3 (Ch3) in IV doxorubicin (n = 6) and control (n = 3) animals. * $p < 0.05$; ** $p < 0.01$.

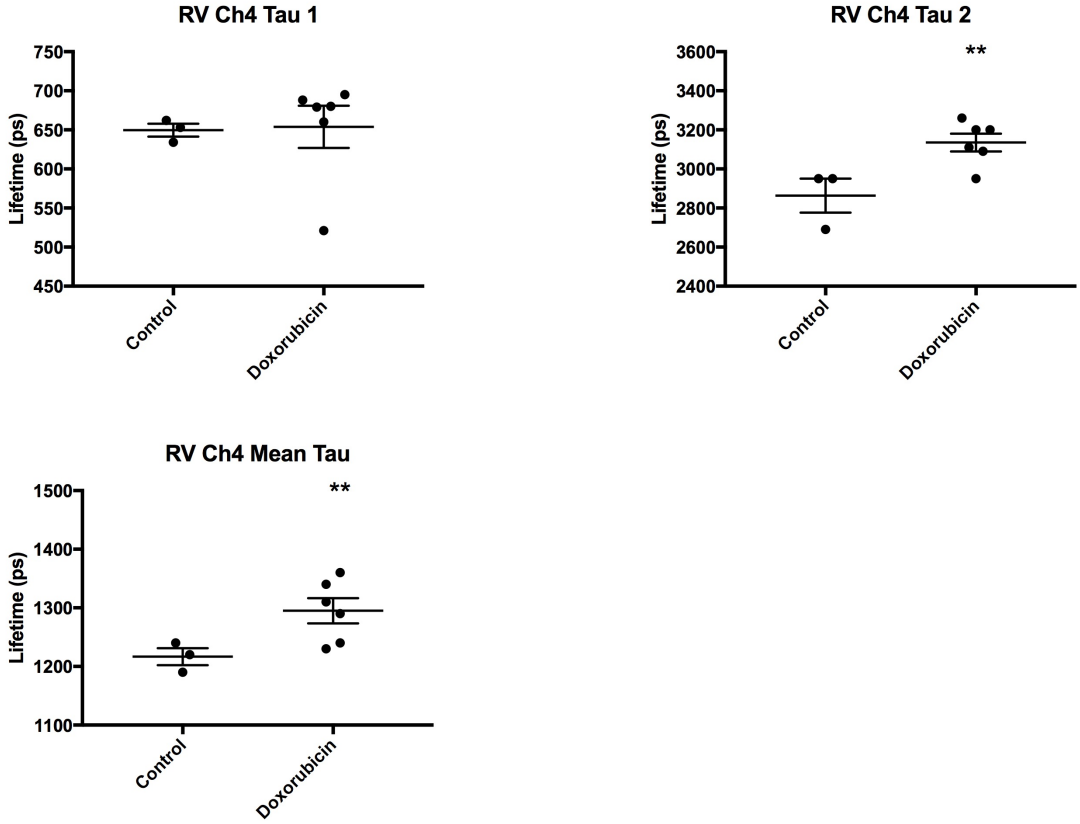


Figure 5.15 Right ventricle autofluorescence lifetime parameters for spectral channel 4 (Ch4) in IV doxorubicin (n = 6) and control (n = 3) animals. ** p < 0.01.

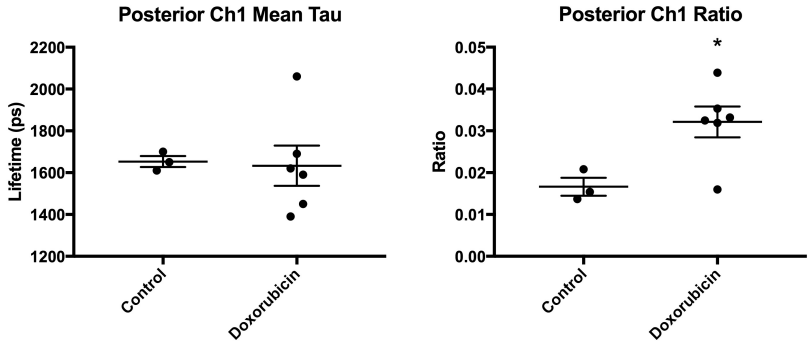


Figure 5.16 Posterior aspect of left ventricle (Posterior) autofluorescence lifetime parameters for spectral channel 1 (Ch1) in IV doxorubicin (n = 6) and control (n = 3) animals. * p < 0.05.

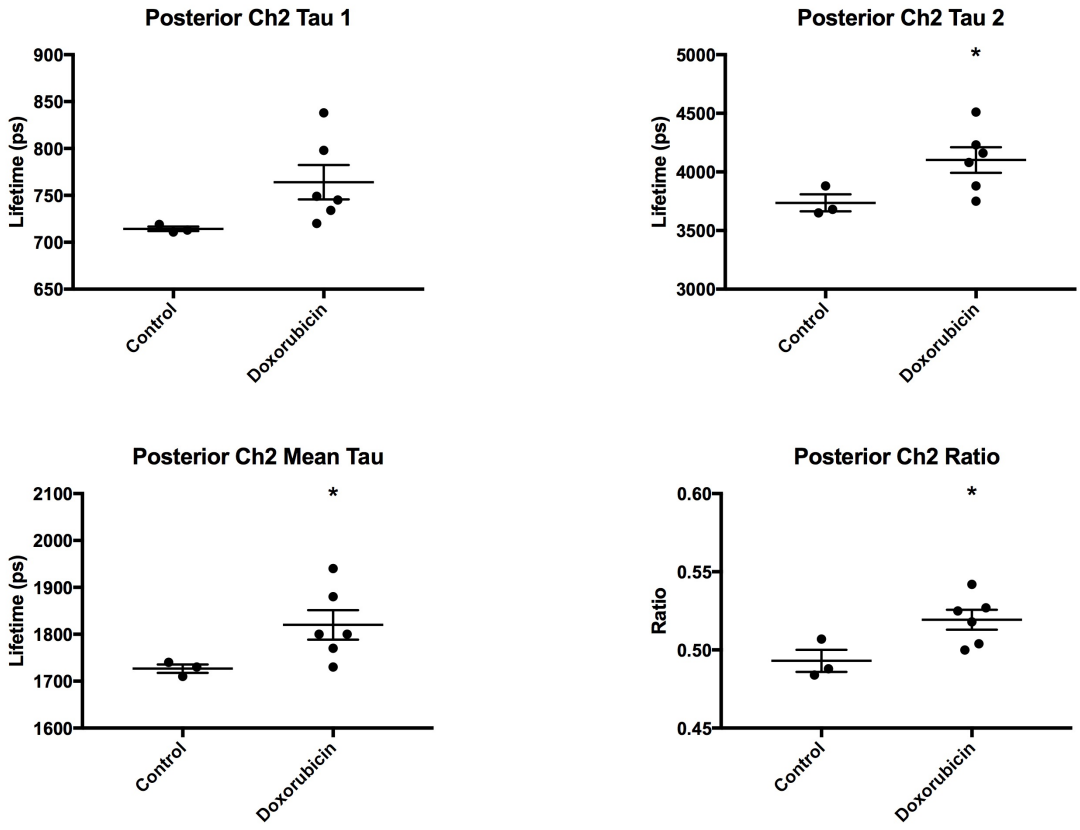


Figure 5.17 Posterior aspect of left ventricle (Posterior) autofluorescence lifetime parameters for spectral channel 2 (Ch2) in IV doxorubicin (n = 6) and control (n = 3) animals. * $p < 0.05$.

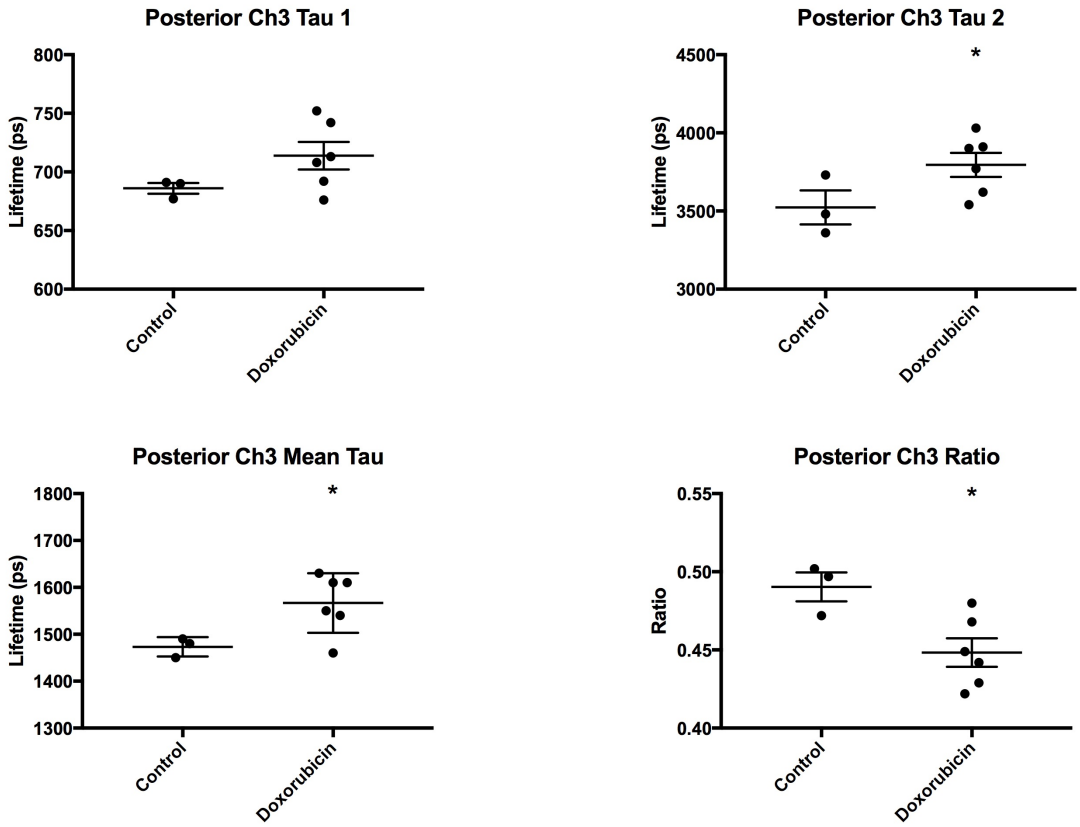


Figure 5.18 Posterior aspect of left ventricle (Posterior) autofluorescence lifetime parameters for spectral channel 3 (Ch3) in IV doxorubicin (n = 6) and control (n = 3) animals. * $p < 0.05$.

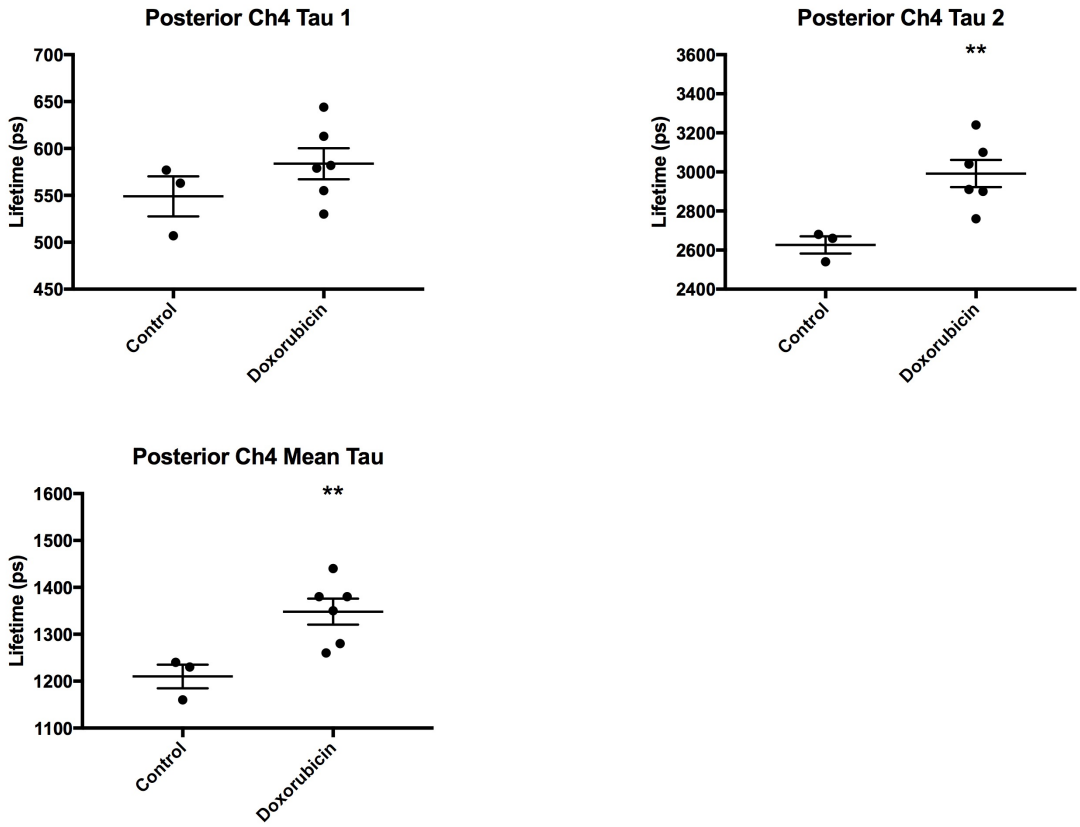


Figure 5.19 Posterior aspect of left ventricle (Posterior) autofluorescence lifetime parameters for spectral channel 4 (Ch4) in IV doxorubicin (n = 6) and control (n = 3) animals. ** p < 0.01.

5.3.2.3 Quantification of collagen content in IV doxorubicin model

Figure 5.20 shows examples of screenshots from the calculation of the percentage of interstitial fibrosis in each anatomical area using Fiji image analysis software by a standardised colour thresholding method to calculate the area of tissue positively stained with picosirius red (PSR) stain in control hearts (A) and DOX-HF hearts (B & C), where PSR positive staining shows as red pixels superimposed on the image where the colour thresholding conditions are met. The greater density of PSR-staining in the doxorubicin-treated (DOX-HF) compared to control hearts can be appreciated in this figure. Figure 5.21 summarises the collagen content by % of tissue positively-stained by PSR for each region of interest for IV doxorubicin treated DOX-HF (n = 9) and control (n = 4) animals. There was significantly higher collagen content in all regions of interest in DOX-HF animals compared to control animals: LV (3.132 ± 0.355 % vs. 1.008 ± 0.071 %, ** p = 0.0025); RV (4.448 ± 0.486 % vs. 1.801 ± 0.099 %, ** p = 0.0047); and Posterior (3.346 ± 0.425 % vs. 1.083 ± 0.152 %, ** p = 0.0056).

5.3.2.4 Linear discriminant analysis in IV doxorubicin model

Figure 6.22 shows the separation achieved by the first two principal components (PCs) by the classification algorithm and the decision line shown in black for the LV anterior wall. Application

of linear discriminant analysis gave sensitivity 70%, specificity of 81% and diagnostic accuracy of 75.5% for detection of the DOX-HF disease state.

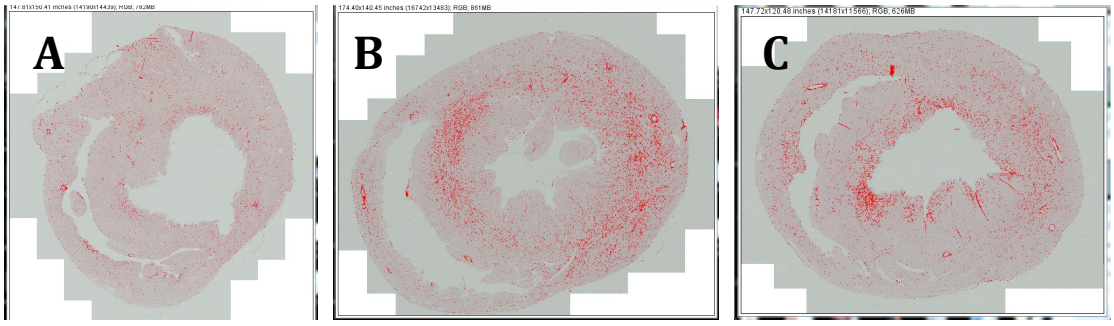


Figure 5.20 Example PSR positive staining to show collagen content of tissue (superimposed on histology image in red) in control (A) compared to IV doxorubicin treated DOX-HF hearts (B & C)

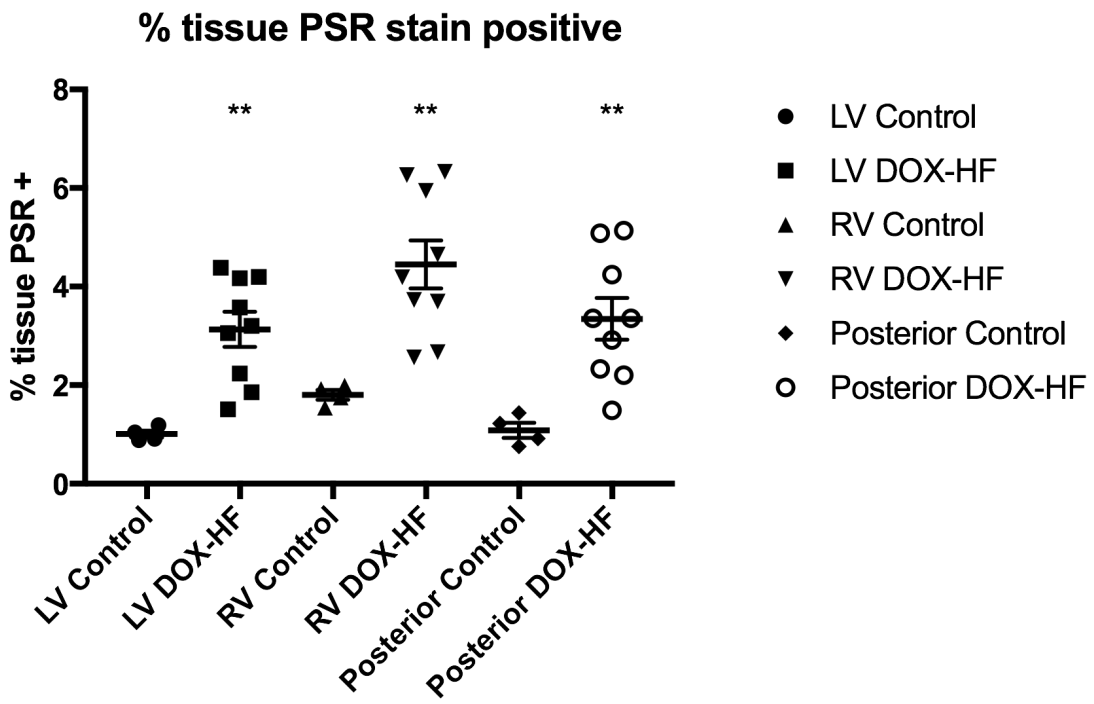


Figure 5.21 Histological quantification of collagen content by % tissue PSR-positive staining by region of interest in IV doxorubicin DOX-HF (n = 9) and control (n = 4) animals. ** $p < 0.01$.

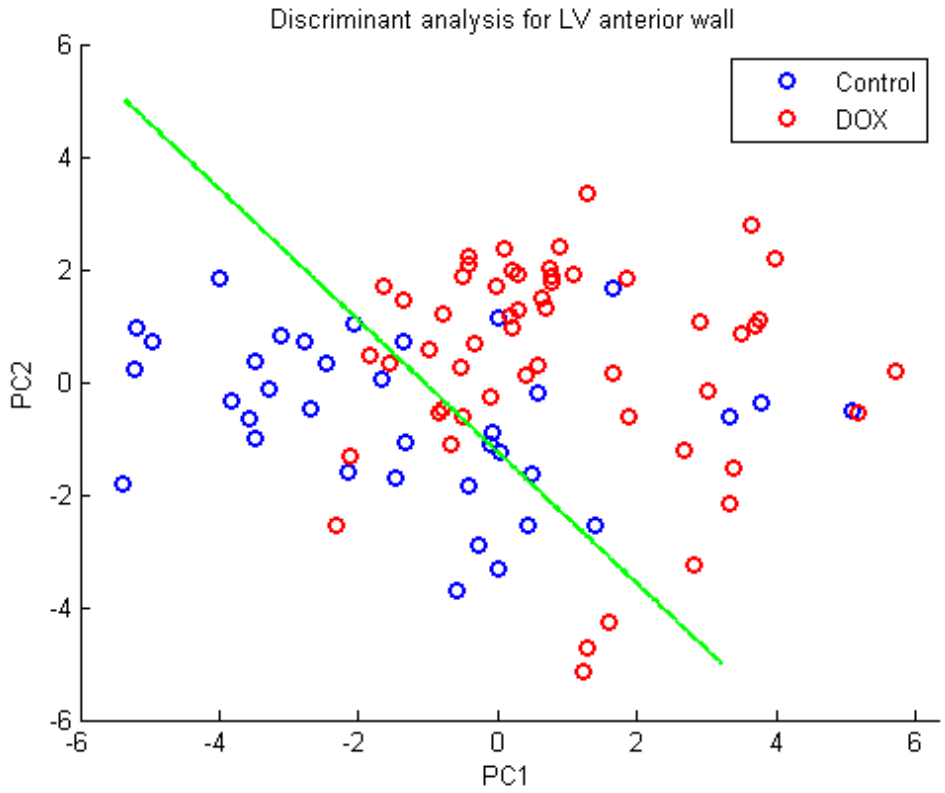


Figure 5.22 Scores of first 2 principal components from classification algorithm for IV doxorubicin (DOX) (blue) and control (red) for the LV region of interest. Decision line shown as green line.

5.4 Discussion

This chapter describes both the development and establishment of a sub acute / chronic IV doxorubicin heart failure model at our institution and thereafter the application of a compact instrument combining time-resolved spectrofluorometry to explore the potential of label-free optical readouts to detect the structural and metabolic changes in the chemotherapy cardiomyopathy doxorubicin heart failure model.

The development of a reliable chronic model of doxorubicin chemotherapy cardiomyopathy is important because there is a growing recognition of the scale of the problem of cardiotoxicity given the large and increasing "survivorship" of patients living long lives after completion of treatment for cancer. Such a model would permit further investigation into the mechanisms underlying this cardiotoxicity. The development of a stable chronic model is the preferred option because it better represents the problem encountered in humans of longer-term sequelae to treatment rather than acute toxicity, which is rarely encountered clinically. Furthermore, there is increasing recognition of the importance of a 'multi-hit' element to chemotherapy cardiotoxicity with synergy of cardiotoxicity mechanisms from other agents, or other disease processes such as hypertension or concomitant coronary artery disease. A reliable chronic model would permit the sequential or co-administration of other chemotherapeutics or other cardiac insults to better model the disease process as it is seen in clinical practice.

In the intraperitoneal doxorubicin models a total dosage of 10 mg/kg doxorubicin was used because earlier work at our institution had showed that higher doses were not well tolerated and would be unacceptable in terms of severity and mortality on animal welfare grounds. Furthermore, a total dose of 10 mg/kg in rats equates to the recommended maximum lifetime dose exposure to doxorubicin for humans, which is considered to be 400 mg/m^2.(Bovelli et al. 2010; Swain et al. 2003) The project license stated that signs of severe toxicity including blood-stained diarrhoea, abnormal secretions from the mouth, weight loss >20% baseline body weight, abdominal swelling and ascites, and reduced interaction with the environment would necessitate culling under schedule 1. Previous studies (Czarnecki 1984; Arola et al. 2000; Takaseya et al. 2004; Takemura & Fujiwara 2007) have involved large single doses or short duration of injections over 1 – 2 weeks giving an acute cardiotoxicity picture. With the use of the intraperitoneal route of administration in the initial protocols, there were problems with weight loss, sudden death and ascites. It seems likely that there are additional effects of doxorubicin in the peritoneal cavity adversely effecting gut function, increasing the risk of gut perforation, as well as causing a localised inflammation of the peritoneum as doxorubicin is a vesicant and is known to lead to severe extravasation injuries in humans. (Schrijvers 2003)

The initial cohort of animals to receive 10 mg/kg intraperitoneal doxorubicin appeared promising and did show a significant reduction in ejection fraction assessed by echocardiogram in the doxorubicin treated animals compared to controls (n = 4) at the 4 weeks' timepoint (n = 5) (59.82 % ± 4.872 % vs. 85.46 % ± 2.45 %, ** p = 0.0033). The mortality in this cohort was (1 of 5) 17% at 4 weeks. In the subsequent protocol, the same intraperitoneal mode of doxorubicin administration was used with treated drinking water looking to observe the protective effect of ACEi or beta-blocker given concurrently. The cohort received 10 mg/kg intraperitoneal doxorubicin or control, with either treated drinking water containing enalapril 50 mg/kg, or carvedilol 50 mg/kg, enalapril 200 mg/kg, or the combination of enalapril 50 mg/kg and carvedilol 50 mg/kg. However there was great concern during this experiment as the number of cases of spontaneous mortality, or cases where welfare endpoints were reached necessitating culling via schedule 1 method, was 80%. Throughout the experiment there was constant liaison with the named veterinary surgeons and the Home Office regarding the situation. There was however a significantly reduced mortality rate in those animals that were given ACEi and / or beta-blocker in the drinking water concomitantly with the intraperitoneal doxorubicin (Treated, n = 20) compared to those that received control drinking water (DOX, n = 5) (DOX mortality 20% vs. Treated 80%, * p = 0.01). This was a particularly interesting finding suggestive of some protection of giving ACEi and/or beta blocker concurrently with the doxorubicin treatment, which would make sense given that Cardinale *et al* (Cardinale et al. 2010) described the complete normalisation of LVEF in 42% of trial participants, and partial improvement in 13% of patients who had been identified as having a cardiomyopathy with LVEF less than 45% after receiving doxorubicin treatment. With 80% mortality in doxorubicin-treated animals without concomitant ACEi and / or beta-blocker however, a complete change of approach was required.

Given the concerns regarding the confounding extra-cardiac problems of the peritoneal route of administration, it was clear that an intravenous mode of administration would be the most appropriate, firstly for reasons of welfare but additionally because this route of administration replicates treatment as given in humans. The experience of problems with the intraperitoneal route of administration may suggest that interpretation of results from experimental work using intraperitoneal injection should be cautious, as it may be confounded by the localised effects of the doxorubicin administration. Additionally they may not be reproducible in the UK, owing to breaching Home Office welfare humane endpoints, which are not observed in all countries around the world.

Establishing the intravenous doxorubicin model used a protocol of 8 weekly injections of IV doxorubicin 1.25mg/kg (total cumulative dose of 10 mg/kg) in the IV doxorubicin treated animals (DOX-HF) compared to the controls, which was the same dose used by the Manchester group with whom we liaised regarding their experiences of the model. In their experience on characterisation of an intravenous doxorubicin model, Cove-Smith *et al* (Cove-Smith et al. 2014) found that doses higher than 10 mg/kg were not tolerated on welfare grounds owing to significant weight loss. They had intended to give a cumulative dose of total 20mg / kg, by means of 2.5 mg/kg/week for 8 weeks followed by a 4 week off-dosing period. However due to intolerance, animals in the 2.5 mg/kg dose group had to be dose-reduced to 1.75 mg/kg during week 4 and the majority of these animals were subsequently terminated for welfare reasons between weeks 5 and 8.

In our experiment, there was no significant difference in body weight between DOX-HF animals at baseline but from the 4 weeks' timepoint onwards there was a significantly reduced body weight in DOX-HF animals compared to control animals at all later timepoints and by week 11 DOX-HF body weight was 339.57 ± 14.19 g vs. 523.5 ± 8.75 g (** p = 0.0061). This represented a failure to gain weight week-by-week compared to controls from around the 3 weeks' timepoint, rather than any significant loss of weight in doxorubicin-treated animals.

The ejection fraction (EF%) in DOX-HF was significantly reduced compared to the controls at all timepoints after baseline and by 11 weeks' was 49.60 ± 3.81 % in DOX-HF compared to 80.45 ± 3.12 % vs. 49.60 ± 3.81 % (* p = 0.0006, using a Bonferroni-adjusted alpha level of .0042 per test (0.05/12)). This was in very good agreement to the LVEF% figure of 49.2%, calculated using cardiac magnetic resonance imaging in the Cove-Smith *et al.* paper.(Cove-Smith et al. 2014)

The time resolved fluorescence spectrometer separates the autofluorescence emission with UV excitation at 375 nm into three spectral emission channels– channel 1 (400 – 420 nm), channel 2 (430 – 480 nm) and channel 3 (500 – 550 nm). The channel ratio for each channel 1 – 3 represents the proportion of the total autofluorescence from the UV excitation that is collected within a given channel. Overall there is a clear shift in fluorescence emission to shorter wavelengths in the DOX-HF animals with an increase in channel 1 ratio, channel 2 ratio and a

decrease in channel 3 ratio compared to controls. This was seen to be statistically significant in the RV and posterior regions of interest, but did not reach statistical significance in the LV anterior wall. The most likely explanation for the change in spectral data is the development of interstitial fibrosis expected as part of the chemotherapy cardiomyopathy with an increase in total collagen content in the tissue causing a greater proportion of the total autofluorescence signal to fall in channel 1 which is centred on the emission spectrum for collagen. The significant increase in collagen was confirmed histologically by quantification using picosirius red staining, which showed an increase in all anatomical areas of the heart of around 250-300% by histological assessment. Cove-Smith *et al.* observed significant increases in collagen content by PSR quantification in the LV of similar magnitude, but they did not measure RV collagen content.

There is general agreement in changes in autofluorescence lifetime parameters throughout all the anatomical regions of interest in DOX-HF hearts compared to control. However the results in the LV showed the same trends as other areas but did not reach statistical significance in most channel parameters, except for the channel 4 long component lifetime (τ_2). In terms of fluorescence intensity, channel 1 (400 – 420 nm with 375 nm excitation, associated with collagen) showed a clear increase in channel 1 ratio as would be expected with an increase in collagen. The changes in mean lifetime (τ) in this channel were less clear-cut with no statistical change noted. However channel 2 (430 – 480nm with 375 nm excitation, associated with NADH) and channel 3 (500 – 550nm with 375 nm excitation, associated with NADH and FAD) showed a clear increase in the long component lifetime (τ_2) and mean lifetime (τ). In channel 4 (500 – 550nm with 440 nm excitation most associated with FAD) there was again a clear increase in the long component lifetime (τ_2) and mean lifetime (τ).

One explanation for these changes in fluorescence lifetime parameters could be the increased collagen content resultant from the interstitial fibrosis, which given its broad emission spectrum which crosses into the other spectral channels as discussed in chapter 1 and its previously reported longer fluorescence lifetime could account for the increased lifetimes observed in all other channels. One of the aims of the experiment was to measure changes in the fluorescence lifetimes of NADH and FAD in the expectation that we would observe changes consistent with metabolic alteration in the heart failure state. Owing to this spectral overlap of the broad emission spectrum of collagen type-I into detection channels 2 and 3, which are centred on the emission spectra of NADH and FAD respectively, it is difficult to identify and quantify changes in NADH and FAD lifetime due to an large increase in the contribution of collagen type-I to the overall signal which makes interpretation of changes more challenging.

Channel 4 (emission 500 – 550nm) is excited with blue light (440 nm) and is the most spectrally removed from collagen's peak emission wavelength and as such it would be thought to have the least crosstalk. In the hypoxia protocol Langendorff experiments described in chapter 3 the autofluorescence lifetime results for FAD showed a complex pattern on hypoxia with a biphasic

response with an initial increase in mean autofluorescence lifetime due to a decrease in the fraction of the short component β, despite a fall in the short lifetime (τ_1) followed by a rapid decrease in mean lifetime upon reperfusion with oxygenated Krebs solution which undershoots below the baseline, increases again and then overshoots beyond the initial baseline during the period measured in the protocol. The changes on reperfusion with oxygenated Krebs solution are caused by rapid increases in the long lifetime (τ_2), rapid rise of the short lifetime (τ_1) to return to baseline followed by a rapid increase and overshoot compared to baseline in the fraction of the short lifetime component (β). The reperfusion state therefore has higher long lifetime component (τ_2) and mean lifetime (τ) and represents an altered metabolic state. Therefore it is possible that the changes in lifetime in channel 4 in DOX-HF with an increase in long lifetime component ($\tau 2$) and mean lifetime (τ) could alternatively be representative of an altered metabolic status compared to control, rather than just reflective of an increased collagen content. Further work is needed to evaluate this further.

To investigate the potential of our instrument as a diagnostic tool to differentiate healthy from DOX-HF hearts, a discrimination algorithm on a leave-one-out cross validation approach was performed. This gave sensitivity 70%, specificity of 81% and diagnostic accuracy of 75.5% for detection of the DOX-HF disease state. This was just marginally inferior than that seen in MI-HF model in the distally remodelled regions (i.e. posterior LV) remote to the area of infarction, (diagnostic accuracy 75.5 % in DOX-HF vs. 77.8 % in the Posterior LV in MI-HF). As discussed in chapter 4, the instrument is most sensitive to autofluorescence signal emitted from the epicardial surface of the myocardium, owing to the nature of absorption and scattering of excitation light and of the emitted fluorescence. In the future, incorporation of the fibre-optics into a cardiac catheter could facilitate endocardial *in vivo* measurements in a minimally-invasive procedure. One concern regarding autofluorescence intensity and diffuse reflectance spectroscopy measurements from the beating heart is movement artefact in terms of variation in intensity of steady state parameters from changes in distance affecting optical absorption. The use of an acquisition time of 1 second, spanning typically 6 heart beats per acquisition, and the use of three repeat measurements at each spatial location should average out these effects. In doxorubicin chemotherapy cardiomyopathy a diffuse interstitial fibrosis is one of the pathological hallmarks. However, studying the histology (see figure 6.20) of the PSR-staining shows that fibrosis is not uniformly spread throughout the heart. In figure 6.20B, for example, there is fibrosis seen throughout the thickness of the ventricle in the endocardium, myocardium and epicardium, whereas in figure 6.20C the fibrosis is predominantly endocardial. An explanation for the lower discriminative ability seen in the DOX-HF model, could be due to the fact that the acquisition is taken from an area where the fibrosis is less pronounced, or is purely endocardial at that anatomical location and is therefore not sampled owing to the optical properties of the instrument's' fibre probe tip and heart tissue.

5.5 Summary

In summary, this chapter described the iterations of development of a sub-acute / chronic doxorubicin chemotherapy cardiomyopathy model, which led to the establishment of a reproducible model of doxorubicin heart failure (DOX-HF) within our institution. The application of a custom time resolved fluorescence spectroscopy instrument characterised the autofluorescence signatures that accompany the chronic doxorubicin heart failure model (DOX-HF) compared to the normal heart. Statistically significant changes in the autofluorescence signatures were seen throughout the heart. Whilst the histologically-confirmed fibrosis is clearly observed in the changes in the autofluorescence profile, it may have also masked changes or confounded the interpretation of changes in NADH and FAD caused by the metabolic remodelling that is thought to occur in the heart failure state. Overall the sensitivity, specificity and diagnostic accuracy are somewhat disappointing compared to those seen in the post myocardial-infarction heart failure model. In the future, it may be include more numerous measurements from one heart from multiple anatomical areas to reduce the risk of not sampling in an area of fibrosis, which would likely improve diagnostic accuracy. The results demonstrate the ability of the instrument to characterise structural changes *in vivo* without the use of exogenous labels. Further work with a focus on improving diagnostic accuracy is required to demonstrate better discriminative ability before it could be said to have potential as a clinical diagnostic tool to distinguish the disease and health states in this histologically-variable phenotype of doxorubicin chemotherapy cardiomyopathy heart failure.

6 Conclusions

6.1 Summary

The aim of this thesis was to test the primary hypothesis that measurement of the myocardial autofluorescence lifetime spectra by use of a custom-built single point fibre-optic probe-based time resolved spectrofluorometer that was described in chapter 2 would be able to identify specific alterations in the autofluorescence 'signature' that accompany the histological, morphological and functional changes in the heart in health and disease states. To investigate this aim, the system was applied to models of heart disease both *ex vivo* and *in vivo*. These models included the established *ex vivo* Langendorff heart model and the *in vivo* myocardial infarction heart failure (MI-HF) model as well as a newly established model of chemotherapy cardiomyopathy. The development and establishment of a tolerated and reproducible model using IV doxorubicin treatment for the first time in our institution represented a significant undertaking and addressed specific thesis aim 3 (see section 1.11). The primary aim of the thesis was met in that the custom-built single point fibre-optic probe-based time resolved spectrofluorometer succeeded in obtaining reproducible recordings and in detecting differences in the control and pathological state of in both *ex vivo* and *in vivo* models from the epicardial surface of the beating heart.

6.2 Background

Heart failure represents a huge burden of disease with a prevalence of 1-2% of the population, rising to 10% of those aged 70 years or older. Heart failure is the end stage of a disease process that starts with an injurious event (e.g. myocardial infarction, chemotherapy treatment) affecting the structure and function of the heart. This may present acutely, or more commonly, presents insidiously and chronically following further insults or adverse remodelling of the heart after the initial injury. The heart failure state is characterized by disturbances in mitochondrial metabolism and energetic dysfunction as well as alterations in extracellular matrix and the development of interstitial fibrosis. There is growing evidence that these structural and functional abnormalities contribute to progression of contractile dysfunction and electrical instability, underpinning the progression to pump failure and malignant ventricular arrhythmias, the two leading causes of morbidity and mortality in patients with left ventricular hypertrophy and heart failure. Although great improvements have been made in heart failure treatment in previous decades, there is no cure, particularly in the latter stages of the disease process when the deleterious changes are manifest. It is therefore well understood that the earlier in the natural history of heart failure that treatment is instigated the better will be the likely outcome for the patient.

The diagnostic tools generally used in the diagnosis of heart failure currently involve a measure of mechanical function. This is primarily echocardiography, which is used to establish ejection fraction, cardiac volumes, wall thickness and movement, chamber dimensions, valvular function, and to characterize the filling parameters of diastole. In terms of the alternative modalities that are able to assess and to evaluate and potentially monitor myocardial fibrosis and metabolism, the most commonly utilised is cardiac magnetic resonance imaging with the use of late gadolinium enhancement (LGE-CMR). LGE-CMR offers the ability to quantify areas of expansion of the extracellular space (i.e. fibrosis or oedema) along with excellent spatial resolution with anatomical images. In the United Kingdom, there is generally good access to CMR, however LGE-CMR doesn't give information regarding metabolism, involves relatively long scan-times, and is contraindicated in patients with significant metal implants including older models of pacemaker and intracranial clips for example, and by definition LGE-CMR requires the administration of the contrast agent gadolinium.

Other modalities that are able to investigate metabolic status include fluorodeoxyglucose positron emission tomography with computerized tomography (^{18}F-FDG-PET CT) and nuclear magnetic resonance spectroscopy (NMR spectroscopy). However these techniques expose the patient to a significant radiation dose, have low sensitivity, suboptimal spatial resolution and a great number of practical barriers including high cost, the use of a radio nucleotide in the case of ^{18}F-FDG-PET CT, limited availability, and limits on the frequency of repeated measures possible in the same individual. Therefore the development of new technologies with greater ability to detect and monitor changes in myocardial metabolism, and to establish the presence and development of fibrosis are needed. Such a tool could aid rapid diagnosis and guide treatment selection and stratification at an earlier stage in the disease process. The ability to cross correlate structural and functional changes could provide new insights into the pathophysiology of myocardial disease.

Chapter 1 discussed an overview of autofluorescence spectroscopy and noted that it is a promising tool for characterization of biological tissues, which has already shown potential for *in vivo* clinical diagnosis of diseased tissues and therefore optimization of therapeutic procedures. It can exploit the photo-physical properties of endogenous fluorophores to probe the structural and functional properties of biological tissue and thus may provide label-free molecular contrast to report biochemical and metabolic information. The most common endogenous fluorophores in healthy cardiac tissue are the enzyme co-factors nicotinamide adenine dinucleotide (NADH) and flavin adenine dinucleotide (FAD), as well as extracellular matrix (ECM) components such as collagen. The custom-built single point fibre-optic probe-based time resolved spectrofluorometer prioritised acceleration of acquisition times of the autofluorescence decays by not using an imaging modality. The motivation for this was that it would be rapidly translatable, either incorporated into current catheter-based cardiovascular techniques e.g. coronary angiography, into the leads of devices such as pacemaker, or used at the time of cardiac surgery, to enable a

label (contrast)-free method for *in vivo* characterization of cardiac tissue. Such a 'virtual biopsy' to identify the early alterations in the failing heart would represent a useful diagnostic advance to target early therapeutic intervention or monitoring.

6.3 *Ex vivo* Langendorff heart model

Chapter 3 described the use of an *ex vivo* Langendorff heart model to investigate the effect of known specific stress conditions on the autofluorescence signal obtained from the heart. The autofluorescence and diffuse reflectance signatures of cardiac tissue were investigated under conditions of known stress conditions, hypoxia and glucose deprivation. The successful application of the instrument to the *ex vivo* Langendorff model demonstrated that it is both possible and feasible to make time-resolved spectroscopy measurements from the surface of the beating heart on a second-by-second basis, giving the confidence to proceed with the planned *in vivo* models. Furthermore, it demonstrated that the device can detect changes in the autofluorescence signature resultant from the altered metabolic state in conditions of hypoxia and of glucose deprivation.

In the initial work using a *no flow* ischaemia model – a protocol commonly used in Langendorff studies of ischaemia-reperfusion injury in the literature – it was interesting to observe a rapid linear change in fluorescence lifetime. Trying to ascertain the cause of this linear change in fluorescence lifetime lead us to closely focus on all variables and through doing this it was established that there was also a linear decrease in the temperature of the heart upon *no flow* ischaemia and that there was significant correlation between these two curves ($r = 0.905$). This temperature drop on *no flow* ischaemia is not always acknowledged as a limitation in some papers using the method but it should be an important consideration in models of ischaemia-reperfusion. If a heart undergoes both a hypoxia event and a simultaneous hypothermia, this is thought to confer protection against the subsequent ischaemia-reperfusion injury. This finding highlighted the new insights that can be made in science from the application of new tools to older experimental models.

6.4 Preclinical doxorubicin chemotherapy cardiomyopathy heart failure model

Chapter 6 described the development and establishment of a sub-acute / chronic preclinical intravenously administered doxorubicin heart failure model (DOX-HF) at our institution and thereafter the application of a custom-built single point fibre-optic probe-based time resolved spectrofluorometer to explore the potential of label-free optical readouts to detect the structural and metabolic changes in the chemotherapy cardiomyopathy doxorubicin heart failure model.

The establishment in our institution of a tolerated and reproducible model of doxorubicin chemotherapy cardiomyopathy is important. Owing to the recognition of the scale of the problem of cardiotoxicity in a large and increasing "survivorship" of treated cancer patients living long lives after successful cancer therapy, the model developed will permit further investigation into the mechanisms underlying this cardiotoxicity by ourselves and other groups. A stable sub acute / chronic preclinical model is the preferred option because it better represents the problem encountered in man of a long-term sequel to treatment rather than acute toxicity, which is now very rarely encountered clinically. The dose of 10 mg/kg in rats equates to the recommended lifetime exposure in humans, which is considered to be 400 mg / m^2. Furthermore, there is increasing recognition of the importance of a 'multi-hit' element to chemotherapy cardiotoxicity with synergy of cardiotoxicity mechanisms from other agents, or other disease processes such as hypertension or concomitant coronary artery disease. A reliable and tolerated model permits the investigation of additional insults, e.g. co-administration of other chemotherapeutics, or other cardiac insults e.g. hypertension, to better model the pathological process as it is thought to occur in human patients.

Despite an extensive literature review of groups who report successful use of intraperitoneal doxorubicin models, it was not possible to reproduce this model at our institution as it proved unacceptable in terms of severity and mortality on animal welfare grounds. This experience of the intraperitoneal route of administration would suggest that caution is required in the interpretation of results from experimental work using intraperitoneal mode of administration as the results in these studies maybe confounded by the localised effects of doxorubicin on the peritoneum and gastrointestinal tract.

An interesting observation was made during the experiments using treated drinking water looking to observe a protective effect of concurrent angiotensin converting enzyme inhibitors (ACEi) or beta blocker at the time of doxorubicin treatment. The unacceptably high mortality rate in the control arms in particular led to great difficulties with this model because of concerns regarding welfare limits. This required constant liaison with the veterinarians and the Home Office and it ultimately led to the abandonment entirely of use the intraperitoneal mode of administration. The high mortality in the control group did however give the opportunity to observe a significant protective effect against a hard mortality endpoint from the concurrent use of ACEi and or beta blocker therapy. There was a significantly reduced mortality rate observed in those animals that were given ACEi and / or beta-blocker in the drinking water concomitantly during intraperitoneal doxorubicin therapy (Treated, n = 20) compared to those that received control drinking water (DOX, n = 5) (DOX mortality 20% vs. Treated 80%, * p = 0.01). Previous work by Cardinale et al. (Cardinale et al. 2010) had demonstrated that in patients identified with LVEF <45% after receiving doxorubicin treatment, treatment with ACEi and beta-blocker led to the complete normalisation of LVEF in 42% of trial participants, and partial improvement in 13% of patients. Many groups are looking at the co-administration of such agents concomitantly with

doxorubicin treatment to see if can protect against and reduce the number of patients developing chemotherapy cardiomyopathy.

Overall the pattern of change in the autofluorescence signature in DOX-HF is consistent with an increase in collagen content of the myocardium owing to fibrosis, in agreement with the literature, and confirmed by histological analysis with an increase in picosirius red staining of around 250-300% by histological assessment in all areas of the heart. There were no changes observed in the fluorescence parameters that could be considered with any certainty to reflect changes in the metabolic state of the heart, as the alternative explanation for the observed changes was that they were reflective of an increased total collagen content of the heart, however further work could be performed to investigate this further given that an altered energetic state is expected in the heart failure state.

The diagnostic accuracy of the custom-built single point fibre-optic probe-based time resolved spectrofluorometer in its discriminative ability of healthy from DOX-HF hearts was 75.5% for detection of the DOX-HF disease state. This remains somewhat disappointing, especially when compared to the diagnostic accuracy seen in the myocardial infarction heart failure model. In doxorubicin chemotherapy cardiomyopathy a diffuse interstitial fibrosis is one of the pathological hallmarks, however from the histological assessment of the PSR-staining shows that fibrosis is not uniformly spread throughout the heart. It might therefore be possible to improve the diagnostic accuracy by sampling a greater number of measurements from across the anatomical regions of the heart.

6.5 Myocardial infarction-heart failure model

Chapter 6 described the application of a compact instrument combining time-resolved spectrofluorometry and diffuse reflectance spectroscopy to explore the potential of these label-free optical readouts to detect the structural and metabolic changes in an established myocardial infarction heart failure model.

The results revealed changes in the autofluorescence consistent with both structural and metabolic alterations at different stages of disease progression, not only in the anatomical area of infarction but also in remodelled remote myocardium. Changes in the structure of the myocardium are the result of collagen deposition as part of the wound-healing process following infarction. The initial phase of collagen deposition occurs within hours in the area of infarction with reconfiguration of the extracellular matrix to form a non-contractile scar. Subsequently there is further collagen deposition within two days and continuing until three months throughout the heart including in areas remote to the infarction. This process is as a result of the remodelling of the heart caused from altered biomechanics with altered stress patterns within

the myocardium as well as changes in sympathetic activation and activation of the neurohumoral system post myocardial infarction. (W. M. Blankesteijn et al. 2001)

Given the long fluorescence lifetime of collagen relative to NADH and FAD, the most predominant fluorophores in cardiac tissue, these structural alterations are characterised by an increase in the mean autofluorescence lifetime of all spectral detection channels of the custom built time-resolved spectrofluorometer used in this thesis. This was most pronounced in channels 1 and 2, where the shorter emission wavelength bands collected collagen emission more efficiently. Given the large increase in collagen content in scar (372% increase at the 16 weeks timepoint in the LV anterior wall / 'scar') changes in the autofluorescence signal due to metabolic alterations were likely masked at the later timepoints. However statistically significant decreases in the short lifetime τ_1 of the autofluorescence decays associated with NADH and FAD were observed and this is unable to be explained by an increase in collagen content. These changes where observed at all timepoints in the areas remote to the myocardial infarction and were seen in all regions of the heart at the earlier timepoints, when collagen deposition is less extensive. Overall this gives weight to the argument that they reflect altered metabolism or metabolic remodelling of the heart post myocardial infarction. Furthermore, the pattern of a decrease in the short lifetime τ_1 was observed in the *ex vivo* Langendorff model following oxygen deprivation, further supporting the hypothesis that it represents alteration of the metabolic state of the myocardium post myocardial infarction. It is interesting to note that the parameters providing the highest discrimination were lifetime related parameters, and classifications that included the use of time-resolved measurements had greater diagnostic accuracy compared with classifications that used spectroscopic measurements alone.

Given the aim to create a new cardiac diagnostic tool, it was encouraging to see that the diagnostic accuracy for identification of MI-HF demonstrated excellent discriminative capability, very clearly in the areas of infarction, but also in remote regions to the infarction where the changes in tissue properties might be considered to be more subtle, particularly at earlier stages of disease progression.

6.6 Towards *in vivo* measurements in man

The results of application of the custom-built single point fibre-optic probe-based time resolved spectrofluorometer demonstrated successful acquisitions from the beating heart and the ability to detect second-by-second changes in the autofluorescence signature upon changes such as hypoxia or glucose deprivation, as well as excellent discriminative ability between MI-HF and control hearts even in areas remote to the area of infarction. As such, towards the end of the experimental period of the PhD work began on look at the possibilities for translation of this technology into making epicardial recordings in man. The goal of this first-in-man study would be to assess whether making time-resolved autofluorescence measurements in cardiac

procedures is viable and practical. Working with Dr João Lagarto from the Photonics Group, we spent some time taking into account the practicalities of this as a future undertaking along with clinical and technical staff from the Royal Brompton Hospital. Following discussions with consultant cardiologists and cardiac surgeons, it became apparent that epicardial measurements of a patient undergoing valve surgery requiring the use of cardiopulmonary bypass would be a good target for initial first-in-man study. Firstly the surgical procedure is relatively long and the patients are usually low-risk surgical candidates therefore an additional couple of minutes undertaken to obtain autofluorescence measurements would not be considered an unreasonable burden on the study patient. Secondly the patient would be expected to have a relatively 'uniform' myocardium, without the scarring or regional ischaemia that might be encountered in patients undergoing coronary artery bypass grafting. Thirdly, the difference between a heart beating normally prior to going onto cardio-pulmonary bypass compared to when the heart is "on pump" during cardio-pulmonary bypass would be expected to be accompanied by large change in metabolic status and as such would potentially offer the greatest target to attempt to detect differences in the autofluorescence signature.

A new system was assembled and mounted on a clinically-approved trolley for ease of deployment and transportation within the operating theatre, so that the device would be permitted to enter the operating theatre environment at the Royal Brompton Hospital. In order to obtain autofluorescence measurements in an operating theatre environment, lighting is a very important issue to address. In all the laboratory experiments conducted in this thesis, the lighting in the room was turned off during acquisitions to permit acquisitions in extremely low light conditions to reduce the background to a minimum in the autofluorescence signal. In an operating theatre, it would be unacceptable to turn the lighting down significantly whilst the patient is anaesthetised on the operating table. Therefore an alternative method to reduce the effect of the presence of the background light would be necessary to make it possible to record autofluorescence decays. Consideration on how to achieve this led to development of a custom-built stainless steel sheath with a cylindrical shaft sitting on top of conical-shaped base that covers and excludes background lights from the area of the surface of the heart (see figure 6.1). The conical-shaped base makes contact with the surface of the heart and its shape is designed to shield the area of interest being studied from background light. The fibre-optic probe sits within the cylindrical shaft which includes a glass window at its base surrounded by two O-rings, so that the fibre optic probe is never in direct contact with the heart or blood and the distance between the tip of the probe and the surface of the heart is fixed at 3 mm.



Figure 6.1 Photograph of the fibre optic probe stainless steel sheath

The second consideration is that of concern regarding exposure to UV radiation. Exposure to UV radiation has been shown to produce biological damage in the DNA of human cells (De Laat et al. 1997) and can promote the development of tumours in animal models.(Horneck 2000) The risk of malignant transformation is greater at shorter wavelengths, especially the UVB and UVC range of the spectrum, i.e. up to 315 nm.(Ahmed et al. 1993; Lam et al. 1993) Therefore approval for the use of the device in man will require demonstration that it doesn't pose a significant risk to the patient.

Approximately 98% of the solar UV exposure comes from the UVA range, i.e. from 315 to 400 nm, for which our skin has evolved to provide protection against the potential harmful effects. However, the effects of UV light exposure to the internal organs remains unclear owing to the fact that they are not exposed to UV light in the course of normal life. Because the wavelength used in our system falls within the UVA range, we compared the dose provided by our system against that received during exposition to sunlight. The average UV power used in acquisitions is typically around 1 μW at the sample. At 3 mm from the sample and considering 3 consecutive acquisitions of 1 second duration each, the corresponding average dose delivered to the sample is 78 $\mu J/cm^2$, which is equivalent to the UV dose of less than 10 seconds exposition to indirect sunlight through a north facing window during the morning of a clear sunny summer day in London. We note that a number of operating theatres worldwide have windows and they use daylight illumination for some degree of room lighting and clearly in this situation the UV light dose delivered to internal organs in such conditions in a standard open-heart procedure would be greater than that delivered as a result of a protocol autofluorescence measurements using our device. As the heart is a post-mitotic organ, the ability for heart cells to reproduce is low and thus the development of primary cardiac tumours is extremely rare. (Lam et al. 1993) Overall it would seem extremely unlikely that the UV light delivered by our system in the course of measurement

of autofluorescence lifetime could induce malignancies in the heart. In order to mitigate the risk further however, it was decided that participant patients to be selected for the study would be aged 65 or older.

Maintaining aseptic technique during surgery is essential. It is envisaged that the fibre optic probe would be able to enter the sterile field by the use of a use of a commercially available sterile cover, similar to those used during surgery to cover the transoesophageal echocardiography probe. The custom built sheath would be sterilised in the same way as a medical instrument. The surgeon or the surgical assistant would open the sterilised sheath into a sterile field using aseptic technique and would receive the fibre-optic probe within a sterile cover. Using aseptic technique the probe could then be secured within the sheath and the sterile cover would be secured on the shaft of the sheath by the use of clips or ties. At the Royal Brompton Hospital, like many other hospitals around the country, the sterilisation of surgical appliances has been outsourced to private contractors. Unfortunately the contractor in question stated that they are unable to sterilise any device that is not CE-mark approved (Conformité Européenne / "European Conformity" – confirmation of a product meeting EU safety, health and or environmental standards relevant to the product) and herein the project hit a hiatus, whereupon the focus was upon investigation of an alternative provider of sterilisation services acceptable to the hospital not requiring these conditions, or the possibilities of obtaining CE mark approval for the sheath.

At the current time, work towards establishing a first-in-man safety study with *in vivo* autofluorescence measurements in man is on-going.

6.7 Limitations

Owing to absorption and scattering of both the excitation light and emitted fluorescence, the custom-built single point fibre optic probe time-resolved spectrofluorometry instrument is the most sensitive to autofluorescence signal emitted from the epicardial surface of the myocardium. This clearly could be disadvantageous in disease processes that vary with depth within the myocardium. In future potential investigative or clinical applications of this technology, there could be incorporation of the fibre-optics into a cardiac catheters or pacing wires and this would facilitate *in vivo* measurements during a minimally-invasive procedure that would be most sensitive to the signal emitted from the endocardial surface. Additionally, alteration of the probe geometry with different separation between the illumination and detection fibres could be investigated in the future to adjust the depth of myocardium probed.

One concern regarding autofluorescence intensity and diffuse reflectance spectroscopy measurements from a beating heart is related to the effect of movement artefact causing variation in intensity of the steady state parameters resulting from changes in probe-heart

surface distance affecting optical absorption. Additionally variable pressure applied by the probe to the epicardial surface could theoretically affect the blood content within the tissue on contact, again affecting optical absorption. Changes in the optical absorption will influence the measured fluorescence intensity and diffuse reflectance spectrum most strongly. Ratios of the fluorescence signal between different spectral detection channels will also be affected due to the change in absorption between channels. The fluorescence lifetime data was acquired over a relatively narrow spectral band however and is inherently ratiometric. Therefore, while the pressure of the probe tip may influence the mean depth that is probed, it should not greatly influence the fluorescence decay recorded provided that the tissue structure is homogenous over the volume probed. Overall, we achieved relatively small standard deviations on the fluorescence lifetime parameters obtained with the control models (e.g. from AMC hearts in the MI-HF model) which suggests that any variation in lifetime caused by variations in probe pressure is small. An acquisition time of 1 second was chosen for each laser excitation as this spans several cardiac cycles in the rat – typically 6 heart beats per acquisition - in order to average these effects. In the future, if this model is to be applied to study man, or other species with a slower average heart rate, then it would be important to consider the effect of the number of cardiac cycles during the acquisition time. In addition, three repeat measurements at each spatial location within a region of interest were performed to achieve an average over multiple applications of the probe tip to the tissue surface to control for potential variations in the pressure of probe tip application.

6.8 Final remarks

In summary, the work presented in this thesis aimed has demonstrated the potential of autofluorescence lifetime measurements to be applied to the study of heart disease and specifically heart failure. It was shown, for the first time, that it is possible to make measurements on a second-by-second basis from the surface of the beating heart in both *ex vivo* and *in vivo* models. Furthermore the custom-built single point fibre-optic probe-based time resolved spectrofluorometer used in this thesis was able to discriminate healthy and diseased tissue in heart disease in models of post-myocardial infarction heart failure (MI-HF) and chemotherapy cardiomyopathy (DOX-HF). In the *ex vivo* Langendorff model, it appeared possible to track characteristic changes in the autofluorescence signature associated with altered metabolic states on a second-by-second basis. In the MI-HF model, changes in the autofluorescence signature appeared to reflect both structural changes and the altered metabolic state in this model.

The overall motivation of the work is to develop an instrument that would be of use clinically to readout myocardial metabolic and structural status as a 'virtual biopsy' or indeed to track metabolic changes in the heart as a 'metabolometer'. The work presented in this thesis constitutes a first step towards the implementation of autofluorescence lifetime metrology as a label-free diagnostic tool in heart disease. Once the autofluorescence signatures that accompany

the structural, functional and metabolic aberrations in other cardiac disease states have been further characterized, this approach could be applied either during open-chest procedures, or via incorporation of fibre-optic probes into coronary angiography or electrophysiology catheters, or even incorporation into pacemaker leads. Initial translational work needs to confirm whether the contrast observed in animal studies is reproducible in the human heart. Provided that the clinical viability of this instrument is verified in man it possible to envisage that autofluorescence lifetime measurements could find wide application in cardiac diagnosis and cardiac monitoring. For example, epicardial autofluorescence measurements could track the metabolic state of the heart during heart surgery; incorporation of the fibre-optic probe into cardiac catheters could potentially add additional diagnostic information in the work up of a heart failure patient of unknown aetiology undergoing coronary angiography; or incorporation of the fibre-optic probe into an electrophysiology catheter to identify areas of scar during an ablation procedure. The structural changes of fibrosis can be observed with other modalities such as LGE-CMR however autofluorescence spectroscopy techniques could be performed without the need of contrast agents and additionally their relative portability means could be used during the procedure to provide immediate feedback to the clinician. Once the autofluorescence signatures that accompany the structural, functional and metabolic changes in heart disease are fully, characterized this would add a completely novel set of diagnostic information to tomorrow's clinicians.

References

Ahmed, F.E. et al., 1993. DNA damage, photorepair, and survival in fish and human cells exposed to UV radiation. *Environmental and molecular mutagenesis*, 22(1), pp.18–25. Available at: http://www.ncbi.nlm.nih.gov/pubmed/8393402.

Alberts, B. et al., 2008. *Molecular Biology of the Cell (5th ed.)* 5th editio., Garland Science.

Alsaad, A.M.S. et al., 2012. Chronic doxorubicin cardiotoxicity modulates cardiac cytochrome P450-mediated arachidonic acid metabolism in rats. *Drug Metabolism and Disposition*, 40(11), pp.2126–2135.

Alshabanah, O. a et al., 2010. Doxorubicin toxicity can be ameliorated during antioxidant L-carnitine supplementation. *Oxidative medicine and cellular longevity*, 3(6), pp.428–433.

Arai, A.E. et al., 1999. Myocardial oxygenation in vivo: optical spectroscopy of cytoplasmic myoglobin and mitochondrial cytochromes. *The American journal of physiology*, 277(2 Pt 2), pp.H683-97.

Ardeshirpour, Y. et al., 2014. In vivo fluorescence lifetime imaging for monitoring the efficacy of the cancer treatment. *Clinical cancer research : an official journal of the American Association for Cancer Research*, 20(13), pp.3531–9. Available at: http://www.ncbi.nlm.nih.gov/pubmed/24671949.

Arola, O.J. et al., 2000. Acute doxorubicin cardiotoxicity involves cardiomyocyte apoptosis. *Cancer Research*, 60(7), pp.1789–1792.

Ashjian, P. et al., 2004. Noninvasive in situ evaluation of osteogenic differentiation by time-resolved laser-induced fluorescence spectroscopy. *Tissue engineering*, 10(3–4), pp.411–20. Available at: http://www.ncbi.nlm.nih.gov/pubmed/15165458.

Babior, B.M., 1999. NADPH oxidase: an update. *Blood*, 93(5), pp.1464–76.

Balaban, R.S., 2002. Cardiac energy metabolism homeostasis: Role of cytosolic calcium. *Journal of Molecular and Cellular Cardiology*, 34(10), pp.1259–1271.

Becker, W. et al., 2004. Fluorescence Lifetime Imaging by Time-Correlated Single-Photon Counting. *Microscopy Research and Technique*, 63(1), pp.58–66.

Becker, W., 2010. The bh TCSPC Handbook. *Scanning*, (800), pp.1–566. Available at: http://www.becker-hickl.de/handbook.htm.

Bell, R.M., Mocanu, M.M. & Yellon, D.M., 2011. Retrograde heart perfusion: the Langendorff

technique of isolated heart perfusion. *Journal of molecular and cellular cardiology*, 50(6), pp.940–50. Available at: http://www.ncbi.nlm.nih.gov/pubmed/21385587 [Accessed July 26, 2012].

Bers, D.M., 2006. Altered cardiac myocyte Ca regulation in heart failure. *Physiology (Bethesda, Md.)*, 21(17), pp.380–387.

Bers, D.M., 2002. Cardiac excitation contraction coupling. *Nature*, 415, pp.198–215.

De Beule, P.A.A. et al., 2007. A hyperspectral fluorescence lifetime probe for skin cancer diagnosis. *The Review of scientific instruments*, 78(12), p.123101.

De Beule, P. a a et al., 2007. A hyperspectral fluorescence lifetime probe for skin cancer diagnosis. *The Review of scientific instruments*, 78(12), p.123101. Available at: http://www.ncbi.nlm.nih.gov/pubmed/18163714 [Accessed April 25, 2012].

Blacker, T.S. et al., 2014. Separating NADH and NADPH fluorescence in live cells and tissues using FLIM. *Nature Communications*, 5(May), p.3936. Available at: http://www.nature.com/doifinder/10.1038/ncomms4936.

Blankesteijn, W.M. et al., 2001. Dynamics of cardiac wound healing following myocardial infarction: Observations in genetically altered mice. *Acta Physiologica Scandinavica*, 173(1), pp.75–82.

Blankesteijn, W.M. et al., 2001. Dynamics of cardiac wound healing following myocardial infarction: observations in genetically altered mice. *Acta physiologica Scandinavica*, 173(1), pp.75–82.

Blatt, E. et al., 1981. Viscosity and temperature dependence of fluorescence lifetimes of anthracene and 9-methylanthracene. *Journal of Physical Chemistry*, 85(19), pp.2810–2816. Available at: http://www.scopus.com/inward/record.url?eid=2-s2.0-0347200041&partnerID=tZOtx3y1.

Bovelli, D. et al., 2010. Cardiotoxicity of chemotherapeutic agents and radiotherapy-related heart disease. *Annals of oncology : official journal of the European Society for Medical Oncology / ESMO*, 21(5), pp.v277-NaN-6.

Brazhe, N.A. et al., 2013. In Situ Raman Study of Redox State Changes of Mitochondrial Cytochromes in a Perfused Rat Heart V. Lionetti, ed. *PLoS ONE*, 8(8), p.e70488. Available at: http://www.ncbi.nlm.nih.gov/pmc/articles/PMC3757006/.

Bugger, H. et al., 2011. Uncoupling protein downregulation in doxorubicin-induced heart failure improves mitochondrial coupling but increases reactive oxygen species generation. *Cancer*

Chemotherapy and Pharmacology, 67(6), pp.1381–1388.

Butte, P. V et al., 2013. Diagnosis of meningioma by time-resolved fluorescence spectroscopy. *Journal of biomedical optics*, 10(6), p.64026. Available at: http://www.pubmedcentral.nih.gov/articlerender.fcgi?artid=2981341&tool=pmcentrez&rendertype=abstract.

Cancer Research UK, U., Breast cancer mortality statistics Cancer Research UK. Available at: http://www.cancerresearchuk.org/cancer-info/cancerstats/types/breast/mortality/.

Caorsi, V. et al., 2013. Non-linear optical microscopy sheds light on cardiovascular disease. *PloS one*, 8(2), p.e56136.

Cardinale, D. et al., 2010. Anthracycline-induced cardiomyopathy: clinical relevance and response to pharmacologic therapy. *Journal of the American College of Cardiology*, 55(3), pp.213–20. Available at: http://www.ncbi.nlm.nih.gov/pubmed/20117401 [Accessed September 12, 2012].

Chorvat, D. et al., 2010. Rejection of transplanted hearts in patients evaluated by the component analysis of multi-wavelength NAD(P)H fluorescence lifetime spectroscopy. *Journal of biophotonics*, 3(10–11), pp.646–52. Available at: http://www.ncbi.nlm.nih.gov/pubmed/20635425 [Accessed March 23, 2013].

Chorvat, D., Kirchnerova, J., Cagalinec, M., Smolka, J., Mateasik, A., et al., 2005. Spectral unmixing of flavin autofluorescence components in cardiac myocytes. *Biophysical journal*, 89(6), pp.L55-7. Available at: http://www.pubmedcentral.nih.gov/articlerender.fcgi?artid=1367005&tool=pmcentrez&rendertype=abstract.

Chorvat, D., Kirchnerova, J., Cagalinec, M., Smolka, J., Mateasik, a, et al., 2005. Spectral unmixing of flavin autofluorescence components in cardiac myocytes. *Biophysical journal*, 89(6), pp.L55-7. Available at: http://www.pubmedcentral.nih.gov/articlerender.fcgi?artid=1367005&tool=pmcentrez&rendertype=abstract [Accessed March 8, 2013].

Chorvat, D. & Chorvatova, a, 2006. Spectrally resolved time-correlated single photon counting: a novel approach for characterization of endogenous fluorescence in isolated cardiac myocytes. *European biophysics journal : EBJ*, 36(1), pp.73–83.

Chorvat, D. & Chorvatova, a., 2009. Multi-wavelength fluorescence lifetime spectroscopy: a new approach to the study of endogenous fluorescence in living cells and tissues. *Laser Physics Letters*, 6(3), pp.175–193. Available at: http://doi.wiley.com/10.1002/lapl.200810132

[Accessed March 27, 2013].

Cicchi, R. & Pavone, F.S., 2011. Non-linear fluorescence lifetime imaging of biological tissues. *Analytical and bioanalytical chemistry*, 400(9), pp.2687–97. Available at: http://www.ncbi.nlm.nih.gov/pubmed/21455652 [Accessed March 23, 2013].

Cleutjens, J.P. et al., 1995. Collagen remodeling after myocardial infarction in the rat heart. *The American journal of pathology*, 147(2), pp.325–38. Available at: http://www.pubmedcentral.nih.gov/articlerender.fcgi?artid=1869816&tool=pmcentrez&rendertype=abstract.

Coda, S. et al., 2014. Fluorescence lifetime spectroscopy of tissue autofluorescence in normal and diseased colon measured ex vivo using a fiber-optic probe. *Biomedical optics express*, 5(2), pp.515–38. Available at: http://www.osapublishing.org/viewmedia.cfm?uri=boe-5-2-515&seq=0&html=true.

Cohn, J.N., Ferrari, R. & Sharpe, N., 2000. Cardiac remodeling-concepts and clinical implications: A consensus paper from an International Forum on Cardiac Remodeling. *Journal of the American College of Cardiology*, 35(3), pp.569–582.

Cortassa, S. et al., 2009. Control and regulation of integrated mitochondrial function in metabolic and transport networks. *International Journal of Molecular Sciences*, 10(4), pp.1500–1513.

Cove-Smith, L. et al., 2014. An integrated characterization of serological, pathological, and functional events in doxorubicin-induced cardiotoxicity. *Toxicological Sciences*, 140(1), pp.3–15.

Czamara, K. et al., 2015. Raman microspectroscopy of human aortic valves: investigation of the local and global biochemical changes associated with calcification in aortic stenosis. *Analyst*, 140(7), pp.2164–2170. Available at: http://dx.doi.org/10.1039/C4AN01856G.

Czarnecki, C.M., 1984. Animal models of drug-induced cardiomyopathy. *Comparative Biochemistry and Physiology. Part C, Comparative*, 79(1), pp.9–14.

Demirkaya, E. et al., 2009. Cardioprotective roles of aged garlic extract, grape seed proanthocyanidin, and hazelnut on doxorubicin-induced cardiotoxicity. *Canadian journal of physiology and pharmacology*, 87(8), pp.633–640.

Doenst, T., Nguyen, T.D. & Abel, E.D., 2013. Cardiac metabolism in heart failure: Implications beyond atp production. *Circulation Research*, 113(6), pp.709–724.

Doenst, T., Nguyen, T.D. & Abel, E.D., 2013. Cardiac metabolism in heart failure: implications beyond ATP production. *Circulation research*, 113(6), pp.709–24.

Duchen, B.Y.M.R. & Biscoe, T.J., 1992. Mitochondrial function in type i cells isolated from rabbit arterial. , pp.13–31.

Eyre, D.R., Paz, M. a & Gallop, P.M., 1984. Cross-linking in collagen and elastin. *Annual review of biochemistry*, 53, pp.717–748.

Fallah-Rad, N. et al., 2011. The utility of cardiac biomarkers, tissue velocity and strain imaging, and cardiac magnetic resonance imaging in predicting early left ventricular dysfunction in patients with human epidermal growth factor receptor II-positive breast cancer treated with a. *Journal of the American College of Cardiology*, 57(22), pp.2263–70. Available at: http://www.ncbi.nlm.nih.gov/pubmed/21616287 [Accessed July 19, 2012].

Fatakdawala, H. et al., 2015. Fluorescence Lifetime Imaging Combined with Conventional Intravascular Ultrasound for Enhanced Assessment of Atherosclerotic Plaques: an Ex Vivo Study in Human Coronary Arteries. *Journal of Cardiovascular Translational Research*, 8(4), pp.253–263. Available at: http://dx.doi.org/10.1007/s12265-015-9627-3.

Georgakoudi, I. & Quinn, K.P., 2012. Optical imaging using endogenous contrast to assess metabolic state. *Annual review of biomedical engineering*, 14, pp.351–67. Available at: http://www.ncbi.nlm.nih.gov/pubmed/22607264 [Accessed March 3, 2013].

Gibbs, C.L., 1978. Cardiac Energetics. *Physiological reviews*, 58(1), pp.174–254.

Gill, E.M. et al., 2003. Relationship between collagen autofluorescence of the human cervix and menopausal status. *Photochemistry and photobiology*, 77(6), pp.653–658.

Gray, W.R., Sandberg, L.B. & Foster, J.A., 1973. Molecular model for elastin structure and function. *Nature*, 246(5434), pp.461–466.

Gu, R. et al., 2012. Increased expression of integrin-linked kinase improves cardiac function and decreases mortality in dilated cardiomyopathy model of rats. *PLoS ONE*, 7(2).

Häggblad, E. et al., 2008. Myocardial tissue oxygenation estimated with calibrated diffuse reflectance spectroscopy during coronary artery bypass grafting. *Journal of biomedical optics*, 13(5), p.54030.

Camm, C.W. et al., 2009. The ESC Textbook of Cardiovascular Medicine: Second edition. *Oxford University Press*. Available at: http://dx.doi.org/10.1093/med/9780199566990.001.0001.

Haplen, M., 1957. The dual blood supply of the rat heart. *Am J Anat*, 101, pp.1–16.

Herrmann, G. & Decherd, G.M., 1939. The Chemical Nature of Heart Failure. *Annals of Internal Medicine*, 12(8), p.1233. Available at: http://annals.org/article.aspx?doi=10.7326/0003-

4819-12-8-1233.

Herzig, S. et al., 2012. Identification and functional expression of the mitochondrial pyruvate carrier. *Science (New York, N.Y.)*, 337(6090), pp.93–6. Available at: http://www.ncbi.nlm.nih.gov/pubmed/22628554.

Horneck, G., 2000. Quantification of biological effective environmental UV irradiance. *Advances in Space Research*, 26(12), pp.1983–1994.

Huss, J.M. & Kelly, D.P., 2005. Review series Mitochondrial energy metabolism in heart failure : a question of balance. , 115(3).

Ingwall, J.S., 2009. Energy metabolism in heart failure and remodelling. *Cardiovascular Research*, 81(3), pp.412–419.

Islam, M.S. et al., 2013a. pH dependence of the fluorescence lifetime of FAD in solution and in cells. *International Journal of Molecular Sciences*, 14(1), pp.1952–1963.

Islam, M.S. et al., 2013b. pH Dependence of the Fluorescence Lifetime of FAD in Solution and in Cells. *International journal of molecular sciences*, 14(1), pp.1952–63. Available at: http://www.pubmedcentral.nih.gov/articlerender.fcgi?artid=3565358&tool=pmcentrez&rendertype=abstract [Accessed March 24, 2013].

Ivanová, M. et al., 2012. Chronic cardiotoxicity of doxorubicin involves activation of myocardial and circulating matrix metalloproteinases in rats. *Acta pharmacologica Sinica*, 33(4), pp.459–69. Available at: http://www.pubmedcentral.nih.gov/articlerender.fcgi?artid=4003364&tool=pmcentrez&rendertype=abstract.

J. R. Neely, H Liebermeister, E. J. Battersby, and H.E.M., 1967. Effect of pressure development on oxygen consumption by isolated rat heart. *American Journal of Physiology - Legacy Content*, 212(4), pp.804–14.

J.F.W., H., 1845. On a case of superficial colour presented by a homogenous liquid internally colourless. *Philosophical Transactions of the Royal Society of London*, 135, pp.143–145.

Jang, I.K., 2015. *Cardiovascular OCT imaging*,

Johansson, A. et al., 2011. A spectroscopic approach to imaging and quantification of cartilage lesions in human knee joints. *Physics in medicine and biology*, 56(6), pp.1865–78. Available at: http://www.ncbi.nlm.nih.gov/pubmed/21364258.

Kallaway, C. et al., 2013. Advances in the clinical application of Raman spectroscopy for cancer

diagnostics. *Photodiagnosis and Photodynamic Therapy*, 10(3), pp.207–219.

Kharin, S. et al., 2013. Remodeling of ventricular repolarization in a chronic doxorubicin cardiotoxicity rat model. *Fundamental and Clinical Pharmacology*, 27(4), pp.364–372.

Khavandi (ed), A., 2014. *Essential revision notes for the Cardiology KBA*,

Kierdaszuk, B. et al., 1996. Fluorescence of reduced nicotinamides using one- and two-photon excitation. *Biophysical Chemistry*, 62, pp.1–13.

Kollner, M. & Wolfrum, J., 1992. How many photons are necessary for fluorescence-lifetime measurements? *Chemical Physics Letters*, 200(1–2), pp.199–204.

Konig, K. et al., 2004. Multiphoton autofluorescence imaging of intratissue elastic fibers. , 26, pp.495–500.

Kumarswamy, R. et al., 2012. SERCA2a gene therapy restores microRNA-1 expression in heart failure via an Akt/FoxO3A-dependent pathway. *European heart journal*, 33(9), pp.1067–75.

De Laat, A., Van Der Leun, J.C. & De Gruijl, F.R., 1997. Carcinogenesis induced by UVA (365-nm) radiation: The dose-time dependence of tumor formation in hairless mice. *Carcinogenesis*, 18(5), pp.1013–1020.

Lakowicz, J.R. et al., 1992. Fluorescence lifetime imaging of free and protein-bound NADH. *Proceedings of the National Academy of Sciences of the United States of America*, 89(4), pp.1271–5. Available at: http://www.pubmedcentral.nih.gov/articlerender.fcgi?artid=48431&tool=pmcentrez&rendertype=abstract.

Lakowicz, J.R., 2006. *Principles of Fluorescence Spectroscopy* 13th ed., Springer.

Lakowicz, J.R. & Masters, B.R., 2008. *Principles of Fluorescence Spectroscopy, Third Edition* J. R. Lakowicz, ed., Springer.

Lam, K.Y., Dickens, P. & Chan, A.C., 1993. Tumors of the heart. A 20-year experience with a review of 12,485 consecutive autopsies. *Arch Pathol Lab Med*, 117(10), pp.1027–1031. Available at: http://www.ncbi.nlm.nih.gov/pubmed/8215825.

Li, B.H. & Xie, S.S., 2005. Autofluorescence excitation-emission matrices for diagnosis of colonic cancer. *World Journal of Gastroenterology*, 11(25), pp.3931–3934.

Li, Y.H., Yue, J.C. & Cai, G.P., 1997. Fluorescence characterization of type I collagen from normal and silicotic rats and its quenching dynamics induced by hypocrellin B. *Biopolymers*, 42(2), pp.219–226.

Lindbergh, T. et al., 2011. Improved model for myocardial diffuse reflectance spectra by including mitochondrial cytochrome aa3, methemoglobin, and inhomogenously distributed RBC. *Journal of Biophotonics*, 4(4), pp.268–276. Available at: http://doi.wiley.com/10.1002/jbio.201000048.

Lodish, H. et al., 2008. *Molecular Cell Biology* 6th ed., WH Freeman.

Lyon, A.R. et al., 2009. Loss of T-tubules and other changes to surface topography in ventricular myocytes from failing human and rat heart. *Proceedings of the National Academy of Sciences of the United States of America*, 106(16), pp.6854–9.

Lyon, A.R. et al., 2012. Plasticity of surface structures and β(2)-adrenergic receptor localization in failing ventricular cardiomyocytes during recovery from heart failure. *Circulation. Heart failure*, 5(3), pp.357–65.

Manning, H.B. et al., 2008. A compact, multidimensional spectrofluorometer exploiting supercontinuum generation. *Journal of Biophotonics*, 1(6), pp.494–505. Available at: http://doi.wiley.com/10.1002/jbio.200810051.

Manning, H.B. et al., 2013. Detection of cartilage matrix degradation by autofluorescence lifetime. *Matrix Biology*, 32(1), pp.32–38.

Manning, H.B., 2006. *The expression and cross-linking of collagens*.

Marambio, P. et al., 2010. Glucose deprivation causes oxidative stress and stimulates aggresome formation and autophagy in cultured cardiac myocytes. *Biochimica et Biophysica Acta - Molecular Basis of Disease*, 1802(6), pp.509–518.

Marcu, L. et al., 2000. Characterization of Type I, II, II, IV, and V by time-resolved laser-induced fluorescence spectroscopy R. R. Alfano, ed. *Proceedings of SPIE*, 3917, pp.93–101. Available at: http://link.aip.org/link/?PSI/3917/93/1&Agg=doi.

Marcu, L. et al., 2001. Discrimination of human coronary artery atherosclerotic lipid-rich lesions by time-resolved laser-induced fluorescence spectroscopy. *Arterioscler Thromb Vasc Biol.*, 21(7), pp.1244–50.

Marcu, L., 2010. Fluorescence lifetime in cardiovascular diagnostics. *Journal of biomedical optics*, 15(1), p.11106.

Marcu, L., 2012. Fluorescence lifetime techniques in medical applications. *Annals of biomedical engineering*, 40(2), pp.304–31.

Margoliash, E. & Frohwirt, N., 1959. Spectrum of horse-heart cytochrome c. *The Biochemical*

journal, 71(3), pp.570–572.

Matthews, T.E. et al., 2011. Pump-Probe Imaging Differentiates Melanoma from Melanocytic Nevi. *Science Translational Medicine*, 3(71), p.71ra15-71ra15. Available at: http://stm.sciencemag.org/content/3/71/71ra15.

McGinty, J. et al., 2010. Wide-field fluorescence lifetime imaging of cancer. *Optics Express*, 1(2), pp.627–640. Available at: http://www.pubmedcentral.nih.gov/articlerender.fcgi?artid=3017991&tool=pmcentrez&rendertype=abstract.

Minotti, G. et al., 2004. Anthracyclines : Molecular Advances and Pharmacologic Developments in Antitumor Activity and Cardiotoxicity. , 56(2), pp.185–229.

Monsuez, J.-J. et al., 2010. Cardiac side-effects of cancer chemotherapy. *International journal of cardiology*, 144(1), pp.3–15. Available at: http://www.ncbi.nlm.nih.gov/pubmed/20399520 [Accessed August 21, 2012].

Mycek, M.-A., Schomacker, K.T. & Nishioka, N.S., 1998. Colonic polyp differentiation using time-resolved autofluorescence spectroscopy. *Gastrointestinal endoscopy*, 48(4), pp.390–394.

Nakabayashi, T. et al., 2012. PH dependence of the fluorescence lifetime of enhanced yellow fluorescent protein in solution and cells. *Journal of Photochemistry and Photobiology A: Chemistry*, 235, pp.65–71.

Neubauer, S., 2007. The Failing Heart — An Engine Out of Fuel. *New England Journal of Medicine*, 356(11), pp.1140–1151. Available at: http://www.nejm.org/doi/abs/10.1056/NEJMra063052.

Nickel, A., Löffler, J. & Maack, C., 2013. Myocardial energetics in heart failure. *Basic Research in Cardiology*, 108(4).

Nikolaev, V.O. et al., 2010. Beta2-adrenergic receptor redistribution in heart failure changes cAMP compartmentation. *Science (New York, N.Y.)*, 327(5973), pp.1653–7.

Onizawa, K. et al., 1999. Usefulness of fluorescence photography for diagnosis of oral cancer. *International journal of oral and maxillofacial surgery*, 28, pp.206–210.

Opie, L.H. et al., 2006. Controversies in ventricular remodelling. *The Lancet*, 367(9507), pp.356–367. Available at: http://linkinghub.elsevier.com/retrieve/pii/S0140673606680744.

Palero, J. a et al., 2011. In vivo monitoring of protein-bound and free NADH during ischemia by nonlinear spectral imaging microscopy. *Biomedical optics express*, 2(5), pp.1030–9.

Park, J. et al., 2012. Biochemical characterization of atherosclerotic plaques by endogenous multispectral fluorescence lifetime imaging microscopy. *Atherosclerosis*, 220(2), pp.394–401.

Phipps, J. et al., 2011. Fluorescence lifetime imaging for the characterization of the biochemical composition of atherosclerotic plaques. *Journal of biomedical optics*, 16(9), p.96018. Available at: http://www.scopus.com/inward/record.url?eid=2-s2.0-80455141448&partnerID=tZOtx3y1.

Phipps, J. et al., 2009. Fluorescence lifetime imaging microscopy for the characterization of atherosclerotic plaques. *Proceedings - Society of Photo-Optical Instrumentation Engineers*, 7161, p.71612G. Available at: http://www.pubmedcentral.nih.gov/articlerender.fcgi?artid=2709872&tool=pmcentrez&rendertype=abstract.

Phipps, J.E. et al., 2012. A fluorescence lifetime imaging classification method to investigate the collagen to lipid ratio in fibrous caps of atherosclerotic plaque. *Lasers in Surgery and Medicine*, 44(7), pp.564–571.

Ponikowski, P. et al., 2016. 2016 ESC Guidelines for the diagnosis and treatment of acute and chronic heart failure F. Gerasimos McMurray, John J. V. Aboyans, Victor Achenbach, Stephan Agewall, Stefan Al-Attar, Nawwar Atherton, John James Bauersachs, Johann John Camm, A. Carerj, Scipione Ceconi, Claudio Coca, Antonio Elliott, Perry Erol, Çetin Ezekowitz, Justin Fernández-, ed. *European Heart Journal*, 37(27), p.2129 LP-2200. Available at: http://eurheartj.oxfordjournals.org/content/37/27/2129.abstract.

Pradhan, a et al., 1995. Steady state and time-resolved fluorescence properties of metastatic and non-metastatic malignant cells from different species. *Journal of photochemistry and photobiology. B, Biology*, 31(3), pp.101–12.

Prahl, S., 1999. Optical absorption of hemoglobin. *Oregon Medical Laser Center*, 15, pp.770–774. Available at: http://ieeexplore.ieee.org/ielx5/5564175/5580291/05580316.pdf?tp=&arnumber=5580316&isnumber=5580291\nhttp://ieeexplore.ieee.org/xpl/articleDetails.jsp?tp=&arnumber=5580316&queryText=Monitoring+Patient+Respiration+using+a+Single+Optical+Camera.

Pu, Y. et al., 2013. Native fluorescence spectroscopy reveals spectral differences among prostate cancer cell lines with different risk levels. *Journal of biomedical optics*, 18(8), p.87002.

Querejeta, R. et al., 2004. Increased collagen type I synthesis in patients with heart failure of hypertensive origin: relation to myocardial fibrosis. *Circulation*, 110(1263–8).

R. A. Colyer, C. Lee, and E.G., 2007. A Novel Fluorescence Lifetime Imaging System That Optimizes Photon Efficiency. *Microsc. Res. Tech.*, 213, pp.201–213.

R. M. Bell, M. M. Mocanu, and D.M.Y., 2011. Retrograde heart perfusion: The Langendorff technique of isolated heart perfusion. *Journal of Molecular and Cellular Cardiology*, 50(6), pp.940–950.

Ramrakha, P. & Hill, J., 2008. *Oxford Handbook of Cardiology* P. Ramrakha & J. Hill, eds., Oxford University Press.

Ranji, M. et al., 2006. Fluorescence spectroscopy and imaging of myocardial apoptosis. *Journal of biomedical optics*, 11(6), p.64036. Available at: http://www.ncbi.nlm.nih.gov/pubmed/17212559.

Ranji, M. et al., 2009. Quantifying Acute Myocardial Injury Using Ratiometric Fluorometry. , 56(5), pp.1556–1563.

Richards-Kortum, R. & Sevick-Muraca, E., 1996. Quantitative optical spectroscopy for tissue diagnosis. *Annual review of physical chemistry*, 47, pp.555–606.

Roca-Alonso, L. et al., 2012. Breast Cancer Treatment and Adverse Cardiac Events: What Are the Molecular Mechanisms?. *Cardiology*, 122(4), pp.253–259. Available at: http://www.ncbi.nlm.nih.gov/pubmed/22907032 [Accessed September 4, 2012].

Rosano, G.M.C. et al., 2008. Cardiac metabolism in myocardial ischemia. *Current pharmaceutical design*, 14(25), pp.2551–62. Available at: http://www.ncbi.nlm.nih.gov/pubmed/18991672.

Sayed-Ahmed, M.M. et al., 2010. Inhibition of gene expression of heart fatty acid binding protein and organic cation/carnitine transporter in doxorubicin cardiomyopathic rat model. *European Journal of Pharmacology*, 640(1–3), pp.143–149.

Schenkman, K. a et al., 1997. Myoglobin oxygen dissociation by multiwavelength spectroscopy. *Journal of applied physiology (Bethesda, Md.: 1985)*, 82(1), pp.86–92. Available at: http://www.ncbi.nlm.nih.gov/pubmed/9029202.

Schneckenburger, H., 1992. Fluorescence decay kinetics and imaging of NAD(P)H and flavins as metabolic indicators. *Optical Engineering*, 31(7), p.1447.

Schrijvers, D.L., 2003. Extravasation: a dreaded complication of chemotherapy. *Annals of oncology : official journal of the European Society for Medical Oncology / ESMO*, 14(Supplement 3), p.iii26–iii30.

Shah, A.M. & Mann, D.L., 2011. In search of new therapeutic targets and strategies for heart failure: Recent advances in basic science. *The Lancet*, 378(9792), pp.704–712. Available at: http://dx.doi.org/10.1016/S0140-6736(11)60894-5.

Shah, A.T. et al., 2014. Optical metabolic imaging of treatment response in human head and neck squamous cell carcinoma. *PLoS ONE*, 9(3).

Singal, P.K. & Iliskovic, N., 1998. Current concepts: Doxorubicin-induced cardiomyopathy. *The New England journal of medicine*, (339), pp.900–5.

Skala, M.C., Riching, K.M., Bird, D.K., et al., 2007. In vivo multiphoton fluorescence lifetime imaging of protein-bound and free nicotinamide adenine dinucleotide in normal and precancerous epithelia. *Journal of biomedical optics*, 12(2), p.24014. Available at: http://www.scopus.com/inward/record.url?eid=2-s2.0-34250214344&partnerID=tZOtx3y1.

Skala, M.C., Riching, K.M., Gendron-Fitzpatrick, A., et al., 2007a. In vivo multiphoton microscopy of {NADH} and {FAD} redox states, fluorescence lifetimes, and cellular morphology in precancerous epithelia. *Proceedings of the National Academy of Sciences*, 104(49), pp.19494–19499. Available at: http://www.pnas.org/content/104/49/19494.abstract.

Skala, M.C., Riching, K.M., Gendron-Fitzpatrick, A., et al., 2007b. In vivo multiphoton microscopy of NADH and FAD redox states, fluorescence lifetimes, and cellular morphology in precancerous epithelia. *Proceedings of the National Academy of Sciences of the United States of America*, 104(49), pp.19494–9. Available at: http://www.pubmedcentral.nih.gov/articlerender.fcgi?artid=2148317&tool=pmcentrez&rendertype=abstract.

Spivak, M. et al., 2013. Doxorubicin dose for congestive heart failure modeling and the use of general ultrasound equipment for evaluation in rats. Longitudinal in vivo study. *Medical Ultrasonography*, 15(1), pp.23–28.

Stanley, W.C., Recchia, F.A. & Lopaschuk, G.D., 2005. Myocardial substrate metabolism in the normal and failing heart. *Physiol Rev*, 85(3), pp.1093–1129. Available at: http://www.ncbi.nlm.nih.gov/entrez/query.fcgi?cmd=Retrieve&db=PubMed&dopt=Citation&list_uids=15987803\nhttp://physrev.physiology.org/content/85/3/1093.full.pdf.

Stanley, W.C., Recchia, F. a & Lopaschuk, G.D., 2005. Myocardial substrate metabolism in the normal and failing heart. *Physiological reviews*, 85(3), pp.1093–1129.

Stefanon, I. et al., 2013. Left and Right Ventricle Late Remodeling Following Myocardial Infarction in Rats. *PLoS ONE*, 8(5).

Sugden, M.C. & Holness, M.J., 2003. Recent advances in mechanisms regulating glucose oxidation at the level of the pyruvate dehydrogenase complex by PDKs. *American journal of physiology. Endocrinology and metabolism*, 284(5), pp.E855–E862.

Sun, Y. et al., 2012. In vivo validation of a bimodal technique combining time-resolved fluorescence spectroscopy and ultrasonic backscatter microscopy for diagnosis of oral carcinoma. *Journal of biomedical optics*, 17(11), p.116003. Available at: http://www.ncbi.nlm.nih.gov/pubmed/23117798.

Swain, S.M., Whaley, F.S. & Ewer, M.S., 2003. Congestive heart failure in patients treated with doxorubicin: a retrospective analysis of three trials. *Cancer*, 97(11), pp.2869–79. Available at: http://www.ncbi.nlm.nih.gov/pubmed/12767102 [Accessed July 26, 2012].

Swamy, A. et al., 2011. Cardioprotective effect of ascorbic acid on doxorubicin-induced myocardial toxicity in rats. *Indian Journal of Pharmacology*, 43(5), pp.507–511. Available at: <Go to ISI>://WOS:000295294700004.

Swift, L. et al., 2014. Visualization of Epicardial Cryoablation Lesions Using Endogenous Tissue Fluorescence. *Circulation: Arrhythmia and Electrophysiology*, 7(5), p.929 LP-937. Available at: http://circep.ahajournals.org/content/7/5/929.abstract.

T. J. Pfefer, K. T. Schomacker, M. N. Ediger, and N.S.N., 2002. Multiple-fiber probe design for fluorescence spectroscopy in tissue. *Appl. Opt.*, 41(22), pp.4712–21.

T. Papaioannou, N. Preyer, Q. Fang, H. Kurt, M. Carnohan, R. Ross, A. Brightwell, G. Cottone, L. Jones, and L.M., 2003. Performance evaluation of fiber optic probes for tissue lifetime fluorescence spectroscopy. *Proc. SPIE*, 4958, pp.43–50.

Tadrous, P.J. et al., 2003. Fluorescence lifetime imaging of unstained tissues: early results in human breast cancer. *The Journal of pathology*, 199(3), pp.309–17. Available at: http://www.ncbi.nlm.nih.gov/pubmed/12579532.

Takaseya, T. et al., 2004. Mechanical unloading improves intracellular Ca2+ regulation in rats with doxorubicin-induced cardiomyopathy. *Journal of the American College of Cardiology*, 44(11), pp.2239–46. Available at: http://www.ncbi.nlm.nih.gov/pubmed/15582323 [Accessed April 3, 2012].

Takemura, G. & Fujiwara, H., 2007. Doxorubicin-induced cardiomyopathy from the cardiotoxic mechanisms to management. *Progress in cardiovascular diseases*, 49(5), pp.330–52. Available at: http://www.ncbi.nlm.nih.gov/pubmed/17329180 [Accessed March 19, 2012].

Talbot, C. et al., 2010. Fluorescence Lifetime Imaging and Metrology for Biomedicine. *Handbook of Photonics for Biomedical Science*.

Talbot, C.B. et al., 2011. Application of ultrafast gold luminescence to measuring the instrument response function for multispectral multiphoton fluorescence lifetime imaging. *Optics express*, 19(15), pp.13848–61.

Tang, D.X. et al., 2013. QiShenYiQi pills, a compound chinese medicine, ameliorates doxorubicin-induced myocardial structure damage and cardiac dysfunction in rats. *Evidence-based Complementary and Alternative Medicine*, 2013.

Tang, G.C., Pradhan, a & Alfano, R.R., 1989. Spectroscopic differences between human cancer and normal lung and breast tissues. *Lasers in surgery and medicine*, 9(3), pp.290–295.

Teale, F.W. & Weber, G., 1957. Ultraviolet fluorescence of the aromatic amino acids. *The Biochemical journal*, 65(3), pp.476–482.

Thompson, A.J., 2012. *Developing endoscopic instrumentation and techniques for in vivo fluorescence lifetime imaging and spectroscopy*.

Thompson, A.J. et al., 2012. In vivo measurements of diffuse reflectance and time-resolved autofluorescence emission spectra of basal cell carcinomas. *Journal of biophotonics*, 5(3), pp.240–54. Available at: http://www.ncbi.nlm.nih.gov/pubmed/22308093 [Accessed March 26, 2012].

Thygesen, K. et al., 2012. Third universal definition of myocardial infarction. *European Heart Journal*, 33(20), pp.2551–2567.

Ti, Y., Chen, P. & Lin, W.-C., 2010. In vivo characterization of myocardial infarction using fluorescence and diffuse reflectance spectroscopy. *Journal of biomedical optics*, 15(3), p.37009. Available at: http://www.ncbi.nlm.nih.gov/pubmed/20615038.

Torikata, T. et al., 1979. Lifetimes and NADH quenching of tryptophan fluorescence in pig heart cytoplasmic malate dehydrogenase. *Journal of Biological Chemistry*, 254(9), pp.3516–3520.

Tsutsui, H., Kinugawa, S. & Matsushima, S., 2009. Mitochondrial oxidative stress and dysfunction in myocardial remodelling. *Cardiovascular Research*, 81(3), pp.449–456.

Tuunanen, H. & Knuuti, J., 2011. Metabolic remodelling in human heart failure. *Cardiovascular Research*, 90(2), pp.251–257. Available at: http://cardiovascres.oxfordjournals.org/cgi/doi/10.1093/cvr/cvr052.

Uehlinger, P. et al., 2009. In vivo time-resolved spectroscopy of the human bronchial early cancer autofluorescence. *Journal of biomedical optics*, 14(2), p.24011. Available at: http://www.ncbi.nlm.nih.gov/pubmed/19405741.

Vellick, S.F., 1958. Fluorescence spectra and polirization of glyceraldehyde-3 phosphate and lactic dehydrogenase coenzyme complexes. *Journal of Biological Chemistry*, 233, pp.1455–1467.

Venius, J., Bagdonas, S., Žurauskas, E., et al., 2011. Time-resolved fluorescence spectroscopy of the heart tissues. *Lithuanian Journal of Physics*, 51(4), pp.370–376.

Venius, J., Bagdonas, S., Zurauskas, E., et al., 2011. Visualization of human heart conduction system by means of fluorescence spectroscopy. *Journal of biomedical optics*, 16(10), p.107001. Available at: http://www.ncbi.nlm.nih.gov/pubmed/22029363.

Vishwasrao, H.D. et al., 2005. Conformational dependence of intracellular NADH on metabolic state revealed by associated fluorescence anisotropy. *The Journal of biological chemistry*, 280(26), pp.25119–26. Available at: http://www.ncbi.nlm.nih.gov/pubmed/15863500 [Accessed April 25, 2012].

Visser, A.J.W.G. & van Hoek, A., 1981. The fluorescence decay of reduced nicotinamides in aqueous solution after excitation with a UV-mode locked Ar ion laser. *Photochemistry and Photobiology*, 33, pp.35–40.

Voelkel, N.F. et al., 2006. Right Ventricular Function and Failure: Report of a National Heart, Lung, and Blood Institute Working Group on Cellular and Molecular Mechanisms of Right Heart Failure. *Circulation*, 114(17), pp.1883–1891. Available at: http://circ.ahajournals.org/cgi/doi/10.1161/CIRCULATIONAHA.106.632208.

Weber, K.T., 1989. Cardiac interstitium in health and disease: the fibrillar collagen network. *Journal of the American College of Cardiology*, 13(7), pp.1637–52.

Weber, P. et al., 2012. Tumor cell differentiation by label-free fluorescence microscopy. *Journal of biomedical optics*, 17(10), p.101508. Available at: http://www.ncbi.nlm.nih.gov/pubmed/23223984.

White, S.K. et al., 2012. Characterising the myocardial interstitial space: the clinical relevance of non-invasive imaging. *Heart (British Cardiac Society)*, 98(10), pp.773–9. Available at: http://www.ncbi.nlm.nih.gov/pubmed/22422587 [Accessed March 21, 2013].

Whittaker, P. et al., 1994. Quantitative assessment of myocardial collagen with picrosirius red staining and circularly polarized light. *Basic research in cardiology*, 89(5), pp.397–410.

Wijns, W. et al., 2012. ESC Guidelines for the diagnosis and treatment of acute and chronic heart failure 2012: The Task Force for the Diagnosis and Treatment of Acute and Chronic Heart Failure 2012 of the European Society of Cardiology. Developed in collaboration with the Heart. *European heart journal*, 33, pp.1787–1847. Available at:

http://www.ncbi.nlm.nih.gov/pubmed/22611136\nhttp://www.pubmedcentral.nih.gov/articlerender.fcgi?artid=3690472&tool=pmcentrez&rendertype=abstract\nhttp://www.ncbi.nlm.nih.gov/pubmed/16875962\nhttp://www.ncbi.nlm.nih.gov/pubmed/20802247\nhttp://www.ncbi.nl.

Wild, F. & Ludwig, C., 1846. Ueber die peristaltische Bewegung des Oesophagus, nebst einigen Bemerkungen uber diejeningen des Darms. *Z Rat Med*, 5, pp.76–132.

Yager, J.Y., Brucklacher, R.M. & Vannucci, R.C., 1991. Cerebral oxidative metabolism and redox state during hypoxia-ischemia and early recovery in immature rats. *The American journal of physiology*, 261(4 Pt 2), pp.H1102-8.

Yong, W.H. et al., 2006. Distinction of brain tissue, low grade and high grade glioma with time-resolved fluorescence spectroscopy. *Frontiers in bioscience : a journal and virtual library*, 11, pp.1255–1263.

Zhou, L. et al., 2008. Metabolic response to an acute jump in cardiac workload: effects on malonyl-CoA, mechanical efficiency, and fatty acid oxidation. *American journal of physiology. Heart and circulatory physiology*, 294(2), pp.H954-60. Available at: http://www.ncbi.nlm.nih.gov/pubmed/18083904.

Zimmer, H.G., 1998. The Isolated Perfused Heart and Its Pioneers. *News Physiol Sci.*, 13, pp.203–210.

Zonios, G. & Dimou, A., 2006. Modeling diffuse reflectance from semi-infinite turbid media: application to the study of skin optical properties. *Optics express*, 14(19), pp.8661–74.